DOE/ER/13000--T8

1991 ACTIVITY REPORT

Arthur Bienenstock
Director

Herman Winick
Deputy Director

Katherine Cantwell
Marjorie St. Pierre
Editors

Stanford Synchrotron Radiation Laboratory
A National Users Facility

ABOUT THE STANFORD SYNCHROTRON RADIATION LABORATORY

SSRL is a national facility supported primarily by the Department of Energy for the utilization of synchrotron radiation for basic and applied research in the natural sciences and engineering. It is a user-oriented facility which welcomes proposals for experiments from all researchers.

The synchrotron radiation is produced by the 3.5 GeV storage ring, SPEAR, located at the Stanford Linear Accelerator Center (SLAC). SPEAR is a fully dedicated synchroton radiation facility which operates for user experiments 7 to 9 months per year.

SSRL currently has 24 experimental stations on the SPEAR storage ring. There are 145 active proposals for experimental work from 81 institutions involving approximately 500 scientists. There is normally no charge for use of beam time by experimenters.

Additional information for prospective users can be obtained from SSRL by writing or telephoning Katherine Cantwell at SSRL, SLAC M.S. 69, P.O. Box 4349, Stanford, CA 94309-0210 - telephone (415) 926-3191, e-mail - K@SSRL750.bitnet.

This report summarizes the activity at SSRL for the period January 1, 1991 to December 31, 1991 for research. Facility development through March 1992 is included.

SSRL is operated by the Department of Energy, Office of Basic Energy Sciences, Division of Chemical Sciences. Support for research by SSRL staff is provided by tht Office's Division of Material Science. The SSRL Biotechnology Program is supported by the NIH, Biomedical Resource Technology Program, Division of Research Resources and the Office of Health and Environmental Resources (OHER), Department of Energy.

STANFORD SYNCHROTRON RADIATION LABORATORY

1991 ACTIVITY REPORT

Facility Developments January 1991-March 1992

TABLE OF CONTENTS

Introduction

In 1991, SSRL took a major step forward along the path to its becoming a full-time synchrotron radiation facility. The SPEAR injector was fully commissioned, with the provision of beam to users for experimentation during the last four months of the commissioning process. An injector Operational Readiness Review and a SPEAR Change Analysis were performed, paving the way for the initiation of full functioning of the injector and SPEAR for users in February, 1992.

In spite of the Laboratory's heavy commitment to the injector commissioning, the Operational Readiness Review and the Change Analysis, it joined SLAC in preparing for and successfully facing a thorough review of the sites environmental, health and safety status by a Department of Energy Tiger Team.

In addition, many of the experimental facilities were upgraded significantly. Beam Line 5 went through its final commissioning phase and was made available to users. Three VUV instruments reached extremely high resolution and photons were put through the new 10-1 experimental station for the first time. The double axis goniometers for high precision monochromatic topography and rocking curve measurements in Station 2-2 underwent initial testing, as did a semi-dedicated small angle x-ray scattering station on 4-2. A Laue crystallography station on 10-2 was commissioned and a new SSRL-designed Laue recording camera was constructed, commissioned and utilized for experimentation during the summer of 1991.

Finally, SSRL held a workshop on 4th Generation Light Sources which is likely to have a major influence on its future development. The workshop gave more credence to the concept that large collider rings such as PEP, PETRA, and TRISTAN could be utilized to achieve x-ray brightness 10 to 100 times greater than those anticipated from the 3rd generation rings presently under construction. Also, several orders of magnitude greater brightness at wavelengths of 40 Å and below (as low as 1 Å) could be achieved by constructing Free Electron Lasers on the SLAC linear accelerator. SLAC and SSRL are presently considering the development of these FELs very carefully.

At the time of this writing, the SPEAR/Injector complex has demonstrated its very great capabilities for continued, high-efficiency, high-effectiveness synchrotron radiation production. The Laboratory's instrumentation and staff have met the challenge of full-time operation. SSRL stands prepared to provide the nation with virtually full-time operation in the years to come if sufficient operations funding is provided.

– A. Bienenstock
Director

I LABORATORY OPERATIONS

The laboratory's focus in 1991 was the final commissioning of the accelerator complex with the new 3 GeV injector as its centerpiece and completing the DOE-required ES&H reviews. Completion of these activities in February 1992 opened a new era for SSRL as a fully dedicated, synchrotron radiation source delivering beam to users 7 to 9 months per year.

ACCELERATOR OPERATIONS

1991 Commissioning Run - A successful seven month commissioning run started on February 14, 1991. In the period from February through April, beam was accelerated in the linac and the booster, and routine injector operation was established. April and May were occupied mostly by optimizing injection into SPEAR, studying the best matching conditions for Booster-SPEAR transfer, and improving the SPEAR filling rate.

Since the real test of an injector is its ability to deliver beam on the schedule required by users, the final injector commissioning was carried out with users participating. Users understood that there would be periods when the injector would not be available in order to fix any problems that came up during this commissioning run. On May 27th the first users went on line and through September 18th, 110 separate experiments from 54 different spokespersons were run. During this commissioning run, delivery of beam to users was not always the top priority. Under these circumstances beam was delivered to experimenters ~60% of the scheduled time. In the weeks when delivery to users was top priority the delivery rates were in the mid-eighties.

Users reported very stable beam much of the time. Currents were low through most of the run, but gradually became higher. During the last weeks devoted to accelerator physics 93 mA were regularly injected and stored.

The long run was also a real test of SPEAR's reliability as a storage ring. Only 5% of the total down time was related to SPEAR component failure.

The period from September 18th to 27th was used for accelerator physics studies; in particular, studies of the low emittance lattice. It had been planned to continue with these studies until October 4. Unfortunately, on September 27th a water leak was discovered in a power supply transformer coil. Since this is a complex repair and there was so little of the run left, the run was terminated.

1992 Dedicated User Operation - On February 17, 1992, one year after the beginning of the commissioning run, SSRL began its first user run as a fully dedicated synchrotron radiation facility operating in the low emittance mode. In the first half of the run, February-May 1992, 117 assignments of time involving over 500 scientists were planned.

In the first twelve weeks of dedicated user running an average of 89.8% of the scheduled beam was delivered to users. The average current was approximately 58 mA. Injection of SPEAR occurred once every 24 hours and as of mid-March 1992 was taking 30-45 minutes to accomplish. This delivery rate is significantly higher than ever achieved with the SLAC linac. User operation will continue through September 14, 1992.

This is the first run in the low emittance mode. In this mode the beam appears to be more stable with improved injection and ramping from 2.3 to 3 GeV compared to the previously used optics. For users there is a decrease in horizontal beam size which results in a smaller focus and a brightness comparable to the NSLS.

ES&H REVIEWS

Operational Readiness Review (ORR) - Toward the end of the three year injector construction project, SSRL learned that it would be necessary to carry out an Operational Readiness Review (ORR) before this injector could be used routinely for user runs on SPEAR. This was the first such review of a "low-risk" accelerator facility. After discussions with the DOE, a plan for this review was submitted by SSRL in February, 1991. This plan called for outside reviewers (mostly experts from SLAC who were not involved with the Injector Project) to review all aspects of the injector construction and preparation for operation, with particular emphasis on ES&H. These outside reviews were conducted over a period of several months with participation by members of a DOE team who would do a validation of the Final SSRL Operational Readiness Review.

The outside review resulted in 24 "Issues" (findings that must be resolved before routine operation could begin) and 187 "Concerns" (findings which could be dealt with on a longer time scale). SSRL staff developed Corrective Action Plans to deal with each of these findings and submitted a Final ORR Report to the DOE on September 23, 1991.

A DOE Validation Team reviewed this report and originated 6 additional Issues and 29 additional Concerns in their Validation Report dated December, 1991. By February 16, 1992 SSRL had completed, and the DOE had validated, the corrective actions on all 30 Issues, clearing the way for the start of routine operation for users on February 18th. Work continues on the corrective actions for the outstanding Concerns, and when completed will be validated by the DOE Stanford Site Office.

Tiger Team Review of SLAC/SSRL - A major staff effort from May 1991 through January 1992 was the completion of a site-wide self-assessment, preparation for and support of a visit from a DOE Tiger Team (October 7-November 5, 1991) and participation in the development of Corrective Action Plans for the selfassessment and Tiger Team findings. For matters of ES&H, SSRL functions as a division of SLAC and SSRL staff participated fully in the various activities.

The self-assessment found 1,745 OSHA-type violations at SSRL, none of which were in Category 1 (imminent danger of immediate death or serious physical harm). There were 41 Category 2 violations (potential for causing minor injury, minor occupational illness, or major property damage) all of which have been corrected. Over a third of the remaining less serious code violations (Categories 3 and 4) have been corrected. The remaining corrections will be incorporated into the overall SSRL safety program now being established by the SSRL ES&H Office. The Tiger Team found a total of 132 concerns at SLAC. There were no Category 1 Concerns, and only ten Category 2 concerns, all which have been corrected.

SPEAR Change Analysis Document - The final ES&H review mandated by the DOE was a SPEAR Change Analysis. This review was an analysis of the ES&H issues resulting from the transfer of SPEAR operations from the SLAC linac to the SSRL injector and included changes made to SPEAR as part of the injector project. The SPEAR Change Analysis Document was approved in January.

ACCELERATOR IMPROVEMENTS

Low Emittance - On February 18, 1992 SSRL began operating for users in the new low emittance mode. Utilizing its own injector, SPEAR delivered a low-emittance (130 nm-rad at 3 GeV) beam to users for the start of a run which will last until mid-September, 1992. The first noticeable operational improvement with the low emittance lattice is that the beam is considerably more stable. The stability potentially derives from the fact that the energy dispersion in the radio frequency accelerating cavities is a factor of four less than with the collider optics. This makes the machine much less susceptible to 'synchro-betatron' resonances. The improvement shows up during injection and particularly during the ramping process to higher energy, where the characteristic particle vibration frequencies of the beam change, and synchro-betatron resonances are crossed.

The low-emittance lattice uses stronger focusing, so that the energy dispersion is reduced in the bending magnets. This lower dispersion means a smaller betatron displacement following the emission of radiation. Since the beam emittance is determined by the balancing of this betatron amplitude excitation and radiation damping, a stronger focussing lattice leads to a smaller emittance. For the photon beam, the decrease in horizontal source size results in a focus that is smaller and brighter. The emittance of SPEAR in the new mode has been lowered to 130 nanometer radians from 510 nanometer radians at 3 GeV.

Ion Clearing - Equipment was assembled to clear positive ions, which sometimes are trapped in the circulating electron beam, by a resonant excitation technique, based on work previously done at CERN and at the UVSOR ring in Japan. The equipment was used on several occasions with some success in curing ion trapping problems. It is now available for routine use by the SPEAR operator.

Horizontal-Vertical Coupling Studies - The coupling between horizontal and vertical planes was measured, and the efficiency of the coupling compensation magnets verified. These magnets contribute to minimizing the vertical emittance.

Hardware Improvements - Most of the hardware improvements during the fall 1991 shutdown were directed toward improving safety, the machine protection interlocks, the reliability of the linear accelerator and the booster synchrotron. This program was driven by the findings of the teams performing the Operational Readiness Review. Examples of such improvements in the linear accelerator are the interlock protection of the high voltage system and the cabling and grounding of the variable voltage transformer. The White circuit of the booster synchrotron was improved through insulation improvements and relocations of cables and other components. In SPEAR, maintenance and component replacements were carried out to improve the reliability of the storage ring. Items replaced included the RF supply rectifier diodes, the coils of the transformer providing power to the main bending magnets and the complete set of capacitors.

BEAM AND SPEAR USAGE TABLES

The following tables and graphs contain statistics on SPEAR running, experimental use and characteristics of SSRL stations. For earlier information, consult previous Activity Reports. Table 1 and Figure 1 show the number of SPEAR shifts scheduled and delivered since dedicated running commenced in 1979. Figure 2 shows the details of the 1991 commissioning run. Table 2 and Figure 3 show the use of beam at SSRL for experimental purposes. Table 3 lists the characteristics of the 24 SSRL SPEAR stations.

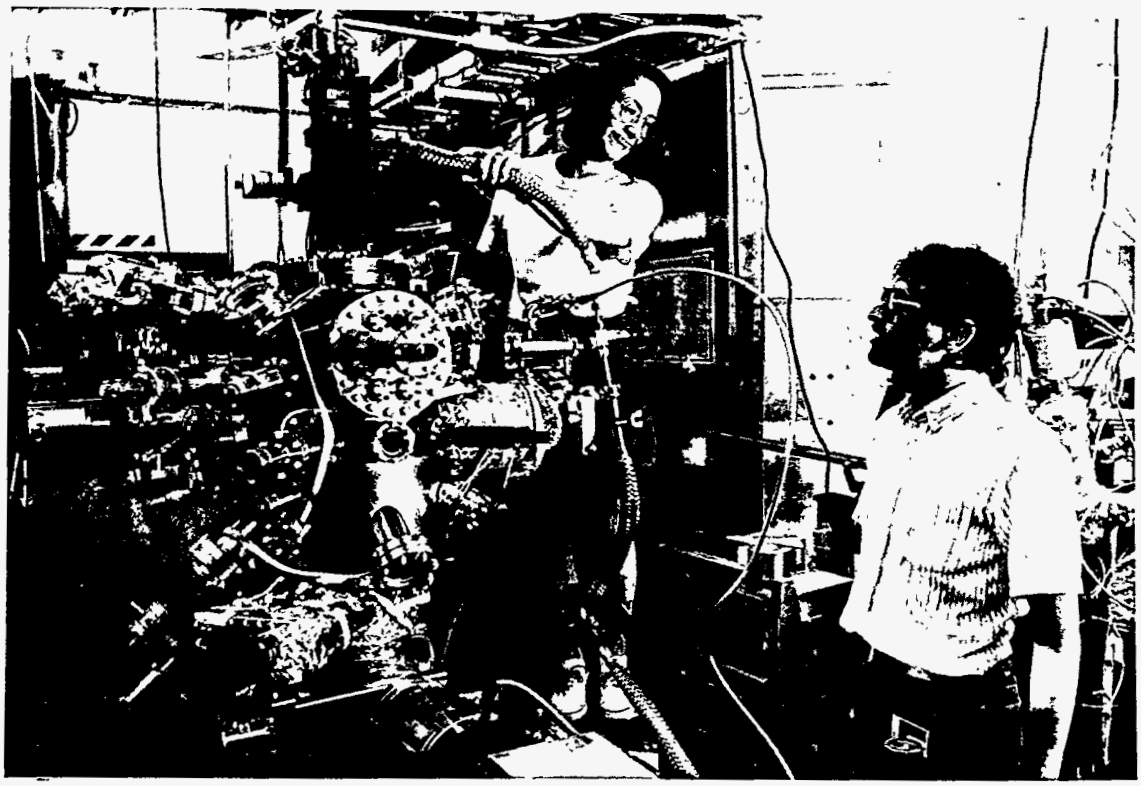

Stanford Unviersity student, Jackeline Pawela (left) and IBM Scientist , Mahesh Samant, using the IBM Surface Science Chamber on Station 8-2 to study molecular oxygen on Ag(110)

TABLE 1

BEAM TIME STATISTICS/DEDICATED TIME

DEDICATED RUN	SCHEDULE HOURS	DELIVERED HOURS	%DELIVERED	
10/20-11/05/79	152	95.3	62	
12/03-12/21/79	352	299.4	85	
02/08-03/05/80	472	366.3	77	
04/16-05/19/80	764	588.2	76	
06/30-07/30/80	726	320.4	44	
09/29-10/14/80	336	194.9	58	
12/02-12/22/80	440	309	70	
01/26-03/03/81	792	600.9	76	
05/16-06/30/81	988	727	73	
11/18-12/21/81	546	363.6	66	
01/08/-02/22/82	748	612.5	81	
03/09-04/26/82	995	830.9	83	
10/15-11/05/82	473	316	66	
12/27-02/22/83	1050	825.6	78	
05/09-06/30/83	1195	960.3	80	
11/07-12/23/83	857	662.8	77	
03/21-04/30/84	835	674.3	80	
01/10-02/21/85	905	606.6	67	
03/15-07/22/85	1502	1056.5	70	
10/14-11/11/85	416	203.7	48	
04/11-06/30/86	1550	1106.5	71	
11/17-12/24/86	752	527	70	
01/02-02/07/87	696	522	75	
03/18-05/02/87	1112	769	69	
10/26-12/24/87	1360	801	59	
01/23-03/17/89	1160	504	43	
04/02-05/02/90	720	536	74	
05/27-09/18/91	2304	1376.5	60	*(Commissioning Run)*

The history of dedicated time at SSRL/SPEAR since its inception in 1979 is shown. Until 1986 SSRL received one-half of the SPEAR operating time in a mode dedicated to synchrotron radiation while the other half was used for colliding beam physics. In 1987 and 1989 there was no high energy physics operation on SPEAR. In 1988 there was no operation for synchrotron radiation science. In the fall of 1990 SPEAR became a dedicated synchrotron radiation source.

FIGURE 1

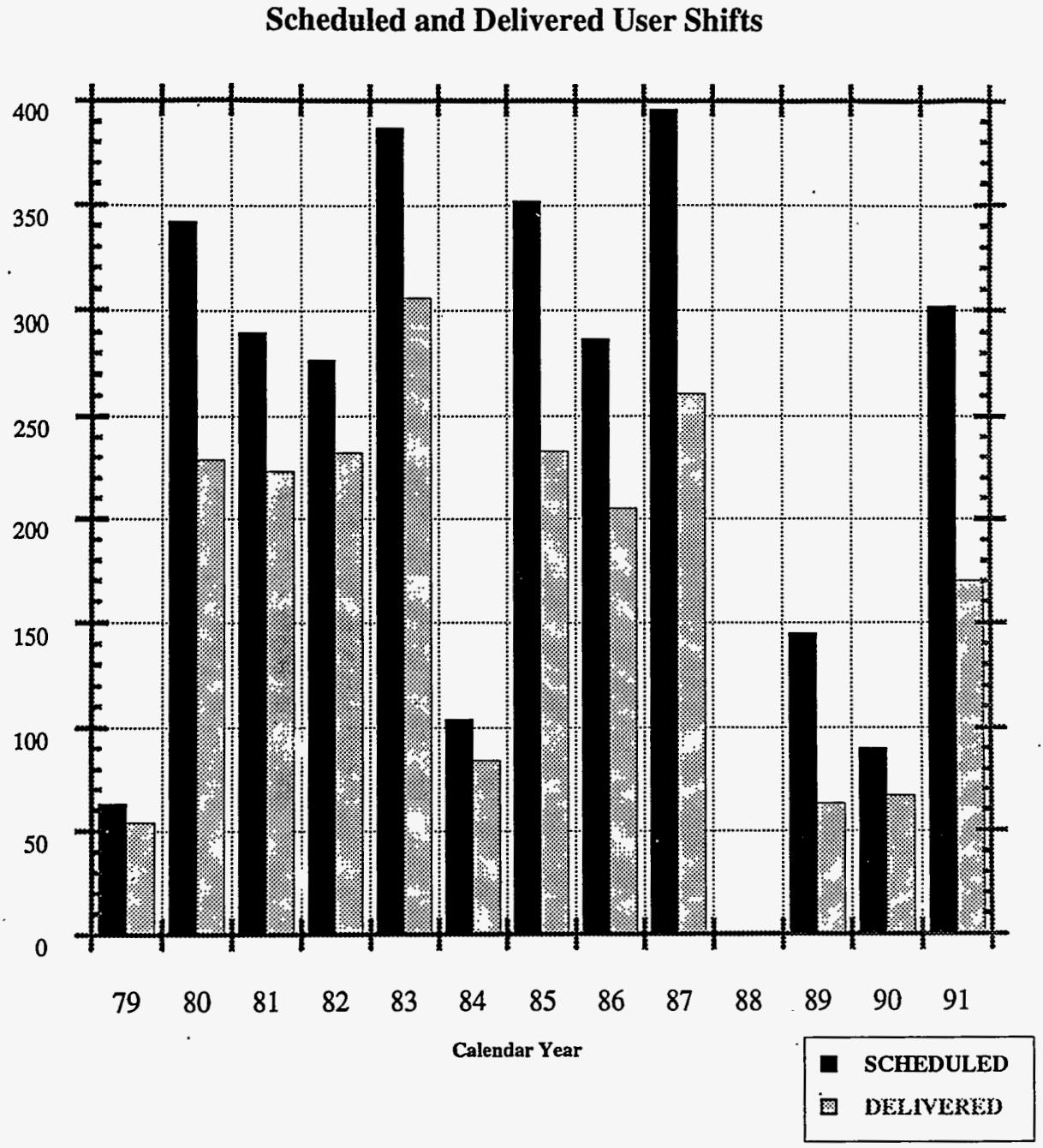
Scheduled and Delivered User Shifts
400
350
300
250
200
150
100
50
0
79
80
81
82
83
84
85
86
87
88
89
90
91
Calendar Year
SCHEDULED
DELIVERED

FIGURE 2

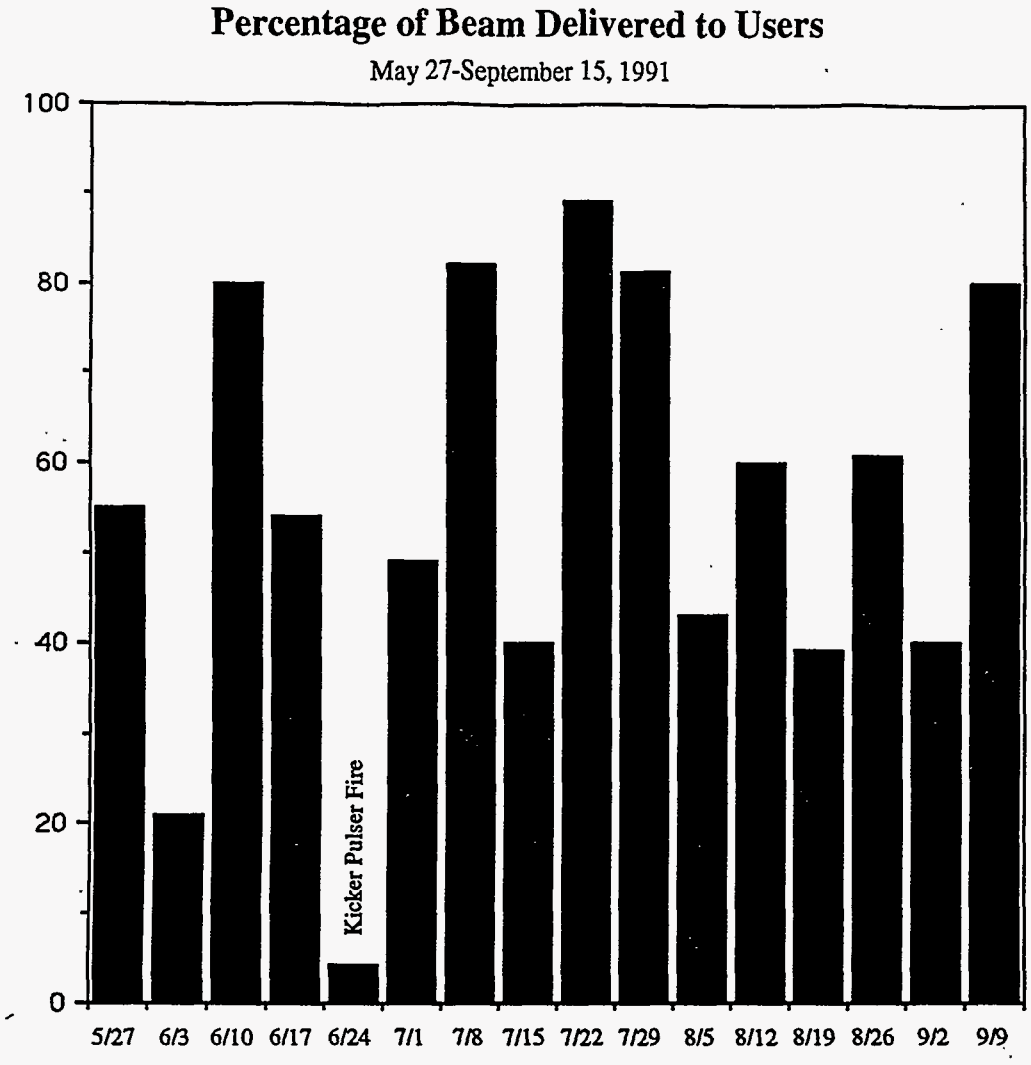

The 1991 run was a commissioning run, and delivery of beam to users was not always the top priority. The user beam delivery statistics, however, are still of interest. For the entire period, including the initial start up, a ten day down time for repair of damage from a small fire, a several week period in August where key staff effort was moved to completing the DOE-required Operational Readiness Review, the beam was delivered to users 60% of the time. What was most encouraging is that in the weeks where user delivery was top priority, and there were no other problems, delivery rates were in the mid-eighties. In particular, three of the five weeks in July were 82%, 89% and 81%.

TABLE 2

USER SHIFTS BY EXPERIMENTAL STATION
Calendar 1991

Experimental Station	5/27-9/18/91	
Beam Line 1		
1-1	76	(34)*
1-2	158	
1-4	**Closed	
1-5	182	
Beam Line 2		
2-1	Closed	
2-2	163	
2-3	121	
Beam Line 3		
3-1	170	
3-2	Closed	
3-3	192	
3-4	129	
Beam Line 4		
4-1	87	
4-2	173	
4-3	159	
Beam Line 5 (only 1 station on 5 can be used at a time)		
5-1		(48)
5-2	51	
5-3	67	
Beam Line 6		
6-1		(170)
6-2	155	
Beam Line 7		
7-1	182	
7-2	167	
7-3	159	
Beam Line 8		
8-1	162	
8-2	158	
Beam Line 10		
10-2	190	
TOTAL Shifts Used	**3118**	
Proposals Run	**117**	

*( ) = *facility characterization time*
** Several stations were closed in 1991 to allow better staff support for users on the operational lines.

In 1991, 2990 8-hour shifts were actually used by experimenters for data taking on the 20 SSRL stations available in 1991. A total of 128 shifts were used by SSRL staff, PRT members and collaborators for characterization, upgradingand commissioning time.

TABLE 3 CHARACTERISTICS OF SSRL EXPERIMENTAL STATIONS

SSRL has 24 experimental stations on SPEAR. 13 of these stations are based on insertion devices while the remainder use bending magnet radiation.

	Horizontal Angular Acceptance (Mrad)	*Mirror Cut Off (keV)*	*Monochromator*	*Energy Range (eV)*	*Resolution ΔE/E*	*Approximate Spot Size HgtxWdth (mm)*	*Dedicated Instrumentation*
INSERTION DEVICES STATIONS							
WIGGLER LINES - X-RAY							
End Stations							
4-2 (8-Pole)							
Focused	4.6	10.2	Double Crystal	2800-10200	$\sim 5 \times 10^{-4}$	1.0 x 3.0	
Unfocused	1.0		Double Crystal	2800-45000	$\sim 10^{-4}$	2.0 x 20.0	
6-2 (54-Pole)							
Focused	2.3	22	Double Crystal	2400-21000	$\sim 5 \times 10^{-4}$	1.0 x 3.0	
Unfocused	1.0		Double Crystal	2400-45000	$\sim 10^{-4}$	2.0 x 20.0	
7-2 (8-Pole)							6-circle Diffractometer
Focused	4.6	10.2	Double Crystal	2800-10200	$\sim 5 \times 10^{-4}$	1.0 x 3.0	
Unfocused	1.0		Double Crystal	2800-45000	$\sim 10^{-4}$	2.0 x 20.0	
10-2 (30-Pole)							
Focused	2.3	22	Double Crystal	2800-21000	$\sim 5 \times 10^{-4}$	1.0 x 3.0	
Unfocused	1.0		Double Crystal	2800-45000	$\sim 10^{-4}$	2.0 x 20.0	
Side Stations							
4-1	1.0		Double Crystal	2800-45000	$\sim 5 \times 10^{-4}$	2.0 x 20.0	
4-3							2-circle Diffractometer
Focused	1.0	Variable	Double Crystal	2800-20000	$\sim 10^{-4}$	0.3 x 20	
Unfocused	1.0		Double Crystal	2800-45000	$\sim 10^{-4}$	2.0 x 20.0	
7-1	1.0		Curved Crystal	6000-13000	$\sim 8 \times 10^{-4}$	0.6 x 3.0	Rotation Camera
7-3	1.0		Double Crystal	2800-45000	$\sim 10^{-4}$	2.0 x 20.0	
VUV/Soft X-Ray Stations							
5 mutli-undulator	1.5		Rowland Circle	10-1200	Δλ =.013-.13Å	6.0 x 8.0	Multiple Grating
6-1			6m SGM	200-1000	$\sim 2 \times 10^{-4}$	$\leq 1 mm^2$	
10-1	2.0		6m SGM	200-1000	$\sim 2 \times 10^{-4}$	$\leq 1 mm^2$	In commissioning
BENDING MAGNET STATIONS							
X-Ray							
1-4	2.0		Curved Crystal	6700-10800	0.3×10^{-3}	0.25 x 0.5	SAS Detector
1-5	1.0		Double Crystal	2800-30000	$\sim 10^{-4}$	3 x 20	Area Detector/CAD-4
2-1 (Focused)	4.8	8.9	Double Crystal	2800-8900	$\sim 5 \times 10^{-4}$	1 x 4	
2-2	1.0-6.1		None	3200-40000		4 x 22 - 4 x 134	
2-3	1.0		Double Crystal	2800-30000	$\sim 5 \times 10^{-4}$	3 x 20	
VUV/Soft X-Ray							
1-1	2.0		Grasshopper	64-1000	Δλ = .1-.2Å	1.0 x 1.0	
1-2	4.0		6m TGM	8-90	$\sim 1 \times 10^{-3}$	1.0 x 2.0	
3-1	2.0		Grasshopper	25-1000	Δλ = .05-2 Å	1.0 x 1.0	
3-2	4.0		Seya-Namioka	5-40	Δλ = .2-6 Å	2 x 7	
3-3	8-10	4.5	UHV Double Crystal (Jumbo)	800-4500	$\sim 5 \times 10^{-4}$	1.5 x 2.5	
3-4	0.6		Multilayer	0-3000	White or $\Delta\lambda/\lambda = .6\%$	2 x 8	Vacuum Diffractometer Litho. Expo.Station
8-1	12		6m TGM	8-180	$\sim 1 \times 10^{-3}$	$\leq 1 mm^2$	Angle Resolved e^- Spectrometer
8-2	5.0		6m SGM	150-1000	$\sim 1 \times 10^{-4}$	$\leq 1 mm^2$	Angle Resolved e^- Spectrometer

II ACCELERATOR PHYSICS

With the start of long periods of SPEAR operating in a dedicated mode and the availability of injection on demand from the new 3 GeV injector, the SSRL accelerator physics program on SPEAR was again active in 1991 following several years where it was very difficult to pursue accelerator studies. SPEAR is now operating six contiguous 8-hour shifts of accelerator physics scheduled at two week intervals. Training of students in accelerator physics remains a strong emphasis with two Ph.D.'s granted in 1991 based on development of the SPEAR low emittance lattice and the injector RF gun design.

Although much of the accelerator physics time in 1991 was dedicated to commissioning the new injector complex, the following on-going programs were initiated.

SPEAR STUDIES

Multi-bunch Instabilities in SPEAR - There are indications that bunch-to-bunch coupling may be a source of beam instability in SPEAR under present operating conditions (total stored current of 80-100 mA in 20 bunches). Since multi-bunch instabilities are expected to become more severe at higher currents, it is important to understand their cause and cure. Building on work previously done at SSRL for a longitudinal feedback system for PEP, a diagnostic tool to characterize longitudinal multi-bunch instabilities in SPEAR was developed during 1991. This tool is the first step toward diagnosing the beam motion and will aid in the design of feedback countermeasures for multi-bunch instabilities. The first performance test for the device on SPEAR was successfully carried out in September of 1991 and the results published in SSRL ACD Note #117.

When coming up for the new users run in February in the lowemittance lattice, SPEAR appeared to suffer much less from beam loss instabilities than it did in the high energy physics lattice. But still, a very rich spectrum of harmonics of the synchrotron frequency, as well as fluctuations in the photon beam intensity and position fluctuations (beam noise), have been observed. This beam noise is reducing the quality of the delivered light beam.

Measurements with the diagnostics tool show that large amplitude longitudinal coherent phase oscillations of the bunches are contributors to the rich harmonics spectrum which, in turn, seems to contribute to some of the high frequency part of the beam noise.

The study of the coherent bunch oscillations is being intensified. The diagnostics tool is being finalized and will soon be available for routine measurements of the modes of longitudinal coupled-bunch oscillations for the operational bunch patterns.

Orbit Simulation Studies - A new orbit simulation program, 'RESOLVE', has been developed in collaboration with SLAC and implemented on SPEAR to aid in calibraiton of magnet strengths, BPM readbacks, and to locate component misalignment errors. The main feature of RE-

FIGURE 4

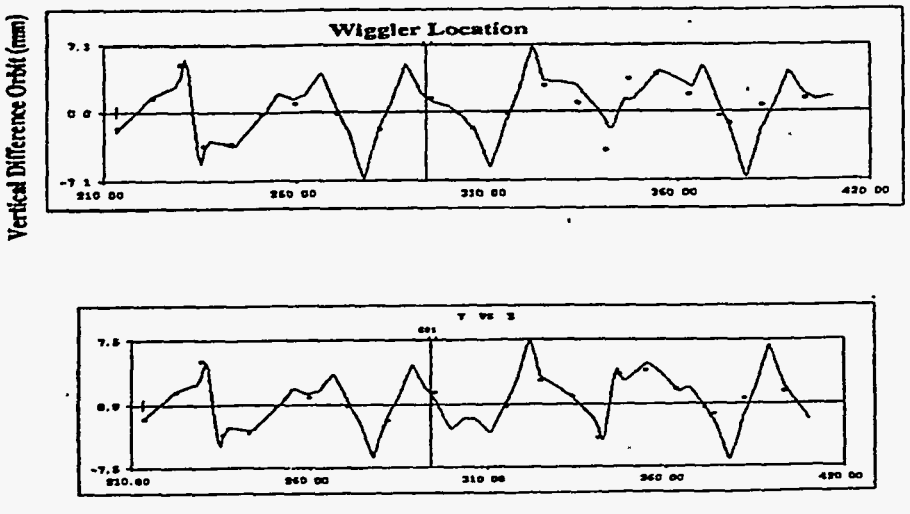

The predicted vertical difference orbit before and after calibration of a wiggler magnet in SPEAR using RESOLVE

SOLVE lies in the ability to "fit" the measured data (absolute or difference orbits) to detect the source of discrepancies between the SPEAR model and the measured beam orbit. In particular, with RESOLVE it is possible to calibrate quadrupole family strengths (to obtain agreement between measured and model tunes), or to calibrate the focusing effects of insertion devices. RESOLVE has also been used to "steer" the photon beam by synthesizing a 14 corrector bump in the South Arc, and to generate 4-magnet bumps for injection steering or steering through the RF cavities. With RESOLVE, the main quadrupole alignment discontinuities in the horizontal and vertical planes have been identified to lie in the East and West Interaction Regions where the quadrupole strengths are high, alignment is critical, and the magnet supports are physically a weak link. By fitting the absolute orbit in the arcs, the photon beam coordinates (x,x',y, y') can be predicted. RESOLVE is now undergoing a further upgrade to allow "comand file" driven operation to speed up the analysis procedrue and will benefit from the efforts of the Beam Position Monitor Task Force to improve the signal to noise ration in the BPM electronics. Figure 4 shows the predicted vertical difference orbit before and after calibration of a wiggler manget in SPEAR using RESOLVE.

SPEAR Lattice with Low Momentum Compaction - A study of short-bunch operation by reduction of the momentum compaction factor was initiated for SPEAR in collaboration with UCLA, LBL, and A. Hofmann, CERN. In principle, short bunch operation could lead to emission of coherent radiation, short-pulse synchrotron light experiments or very low beta colliders. The present project envisions design and operation of a new lattice to lower the momentum compaction factor by an order of magnitude or more, and to investigate the operational aspects and physical properties with such short electron bunches. A new optics that requires no hardware changes except for a different connection of the sextupole magnets, was experimentally investigated. This optics is based on the principle of letting the dispersion function oscillate between positive and negative values, leading to a very small momentum compaction function. The lowest positive value achieved was 0.001. A negative value of -0.005 was also obtained. The experimental results so far are encouraging. A small current (less than 1 mA) was captured, indicating that the lattice is stable. This is believed to be the first demonstration of stored beam with negative momentum compaction in an electron accelerator. The lifetime is still very short (a few minutes), and this prevents the accumulation of higher current. It is believed that the reason for the short lifetime is the large excursion of the still uncorrected orbit. Present studies are aimed at accumulating enough current to be able to measure and correct the orbit.

Modified Sextupole Design Studies - Studies of modified sextupole magnets to improve dynamic aperture and modified octupole magnets to induce tune spread while preserving dynamic aperture are continuing. In each case, the coefficients characterizing the modified field structure were optimized based on pre-selected (analytic) field functions that could be conformally mapped on to iron pole pieces. Present plans are to extend the range of possible field functions for modified sextupole studies in SPEAR by introducing differential algebra techniques.

FEL STUDIES

During 1991 accelerator physicists at SSRL and a group at KEK in Japan pursued theoretical exploration of the use of large circumference, high energy colliders such as PEP and TRISTAN to produce very high levels of coherent power at short wavelengths by Self Amplified Spontaneous Emission (SASE). The PEP ring has features which make it very suitable for this use. These include its large circumference (2.2 km), long straight sections (up to 117 m), and low bending magnet field (0.07 T at 3.5 GeV). The single pass approach to a short wavelength FEL eliminates the need for the optical cavity normally used in an FEL. The lack of availability of normal incidence reflectors now sets the short wavelength limit of conventional FELs. If successful, the SASE would produce picosecond pulses of coherent, short wavelength (around 40 Å) light with a peak power of several hundred megawatts and an average power up to about one watt. Wavelengths around 40 Å are particularly interesting because they lie within the "water window" between the carbon and oxygen absorption edges. This makes the 40 Å wavelength range most appropriate for biological imaging.

The SASE approach requires that a low emittance, high peak current electron bunch with low energy spread radiate in a long (20-60 m) undulator. The interaction of the light and the electron bunch travelling together through the undulator builds up a density modulation in the electron beam at the desired optical wavelength in a single pass. When the bunch density modulation and the optical field intensity reach the threshold level, stimulated coherent radiation emission grows exponentially in the last part of the undulator. The coherent power level ultimately saturates due to the energy spread induced in the electron beam by the radiation process.

The necessary emittance (given by the wavelength/2π) for wavelengths around 40 Å can be reached by operating PEP at about 3-3.5 GeV, a fraction of its maximum energy (15 GeV), in low emittance optics. Extra emittance reduction

is provided by damping wigglers or the long FEL undulator itself. Further study is needed to develop techniques for satisfying the other requirements; namely achieving high enough peak current with an acceptably small energy spread in the electron beam.

With the removal of PEP from operation due to a SLAC budget reduction, FEL studies shifted to the use of the SLAC linac as a driver of short wavelength FELs. It appears that with the use of recently developed, high-brightness, photocathode electron guns, it should be possible to drive a "water window" (23-44 Å) FEL by operating SLAC at energies up to 10 GeV. With improved guns and the use of the full SLAC 50 GeV linac capability, it should be possible to reach 1 Å. Studies of such FELs began in 1991 and were a main subject of the Workshop on 4th Generation Light Sources held at SSRL on February 24th through the 27th, 1992 (see Chapter IV).

ULTRASHORT PARTICLE AND PHOTON PULSES

Detailed studies and simulations for the RF gun developed as the electron source for the 3 GeV SPEAR injector showed that the beam is spread over only a very small longitudinal beam emittance. This makes it possible to manipulate the phase space distribution such that very short bunches can be produced. Simulations show that such an RF gun, in connection with a magnetic compression system, is capable of producing electron bunches as short as 30 to 50 f-sec rms. Such bunches, while passing though a magnetic field, emit photons at wavelengths equal to and longer than the electron bunch length; in this case at wavelength of 10 μm and longer. The intensity is very high since this radiation is emitted coherently and scales like the square of the number of particles rather than linearly as does ordinary synchrotron radiation. To exploit this effect, a test facility including an RF gun, a magnetic compression system and a 40 MeV linac with associated equipment has been assembled and experimentation is expected to begin in late 1992. Based on present design parameters a photon flux of 2×10^{19} photons/sec/100%BW in a wide spectrum from 10 μm to the mm range which, in this frequency range, exceeds greatly the photon flux available from any other source including storage rings.

III EXPERIMENTAL FACILITIES

Experimental stations at SSRL are of two types: general facility stations and participating research team (PRT) stations. General user stations have been funded by various government agencies, principally the DOE, NIH and NSF and are open to the user community on a competitive basis for most of their operating time. In addition to experimental stations there are facilities such as sample preparation laboratories, dark rooms, computer terminal rooms and a machine shop available to users.

SSRL has three operational PRTs with a fourth in the final phases of commissioning a beam line. All existing PRTs are three part collaborations, with SSRL as one of the parties. The two outside institutions receive two-thirds of the available beam time while the other third is for SSRL general users. The PRT arrangements are for a three year period. Renewal is based on review by an *ad hoc* committee, appointed by the Stanford University Dean of Research, which considers the quality of the research achievements, contributions to graduate student education and contributions to the SSRL user community.

The major beam line support staff activity during the past year was directed toward supporting the May-September 1991 run, beam line maintenance and upgrades, support of the injector commissioning, preparation for the Tiger Team visit in October 1991 and support of the user run which began Feburary 17, 1992. The beam line maintenance and upgrade activities were directed not only at increased capability but also to increase reliability. This increased reliability bore fruit in the May-September 1991 run and resulted in very reliable running due to a very low incidence of accidental beam losses caused by equipment failure. Close coordination between the user scheduling process and the requirements of the user support staff resulted in a schedule which allowed us to provide a high level of user support even though the beam line support staff remained constant.

EXPERIMENTAL STATIONS

There are 13 x-ray stations located on six beam lines at SSRL. Two of these are PRT lines (wiggler lines 6 and 10). The other 11 are SSRL facility stations. Of the facility lines, two (Beam Lines 4 and 7) have wigglers as sources for six stations and the other two (Beam Lines 1 and 2), serving five stations, have bending magnet sources.

There are currently ten VUV or soft x-ray stations at SSRL. Five of these facilities were built by PRTs and the general user community has access to one-third of the time on these lines. The facilities being scheduled for users are: two TGMs (1-2 and 8-1), two grasshopper monochromators (1-1 and 3-1), one Seya-Namioka monochromator (3-2), one in-vacuum double crystal monochromator (3-3), one SGM (8-2), the lithography/optics line (3-4), and a mutli-undulator line (5-1,-2,-3). One PRT branch line, 6-1 is in the final stages of commissioning and another, 10-1, is just starting the commissioning phase.

VUV LINES

In 1991 and early 1992 the VUV beam lines underwent a period of both extended use and new developments.

Station 3-3 – The Beam Line 3-3 UHV crystal monochromator (JUMBO), which is over 10 years old, is the subject of renewed user interest as a result of successful experiments in two areas. First, using Si monochromator crystals, backscattered standing wave experiments were performed on metal monolayers on Si and GaAs. Second, it was shown that by using an existing aperture in the beam line, it is possible to perform magnetic circular dichroism measurements in the 3 keV photon energy range using InSb monochromator crystals. This work, as well as the work using circular polarization below 1 keV, has important applications in the area of magnetic and magneto-optical recording.

Station 3-4 – The Beam Line 3-4 lithography line was used for novel x-ray microscopy experiments employing a hollow field emission tip as the imaging element as well as for studies which used a low background pressure of oxygen to continuously clean optical elements.

Beam Line 5 – Beam Line 5 went through it's final commissioning phase and made available to users who performed studies of: diamond surfaces, spin resolved PES of Gd on Fe, and high temperature superconductors at high resolution. In all of these cases, the beam line's high resolution and flux made the work possible. Further beam line characterization work, using a new windowed gas cell, was done to confirm that the monochromator exceeds its design resolution for the two and four degree gratings.

Station 6-1 – On May 22, 1991, the Lawrence Berkeley Laboratory PRT collected the first N_2 1s-Πi^* photo-absorption resonance data from the 6-1 Spherical Grating Monochromator. The spectrum has the highest resolution of any collected with this instrument and is comparable with the best in the world at this energy. [See Figure 5.]

Station 8-1 – Although toroidal grating monochromators (TGM) have been in routine use for a number of years, they have been noted for high output fluxes rather than for high resolution. Recent photoionization work on the 8-1 TGM

FIGURE 5

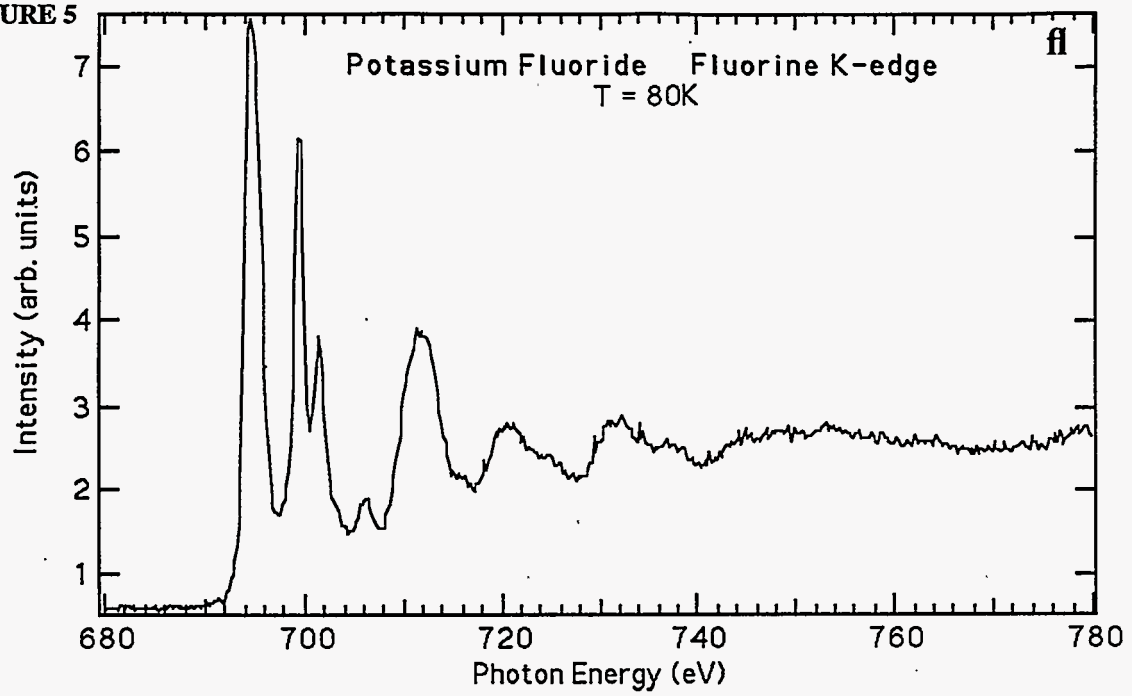

Spectrum from Station 6-1

High-resolution photoabsorption spectrum of single-crystal potassium fluoride: VUV radiation from the LBL Spherical Grating Monochromator was oriented with the polarization direction along the [110] crystallographic direction. The combination of high photon flux and high resolution allowed the detection of several previously unobserved resonances near the fluorine K-edge. The narrow states observed at lower energies, and possibly the broader states at higher energies, are core-level excitons.

FIGURE 6

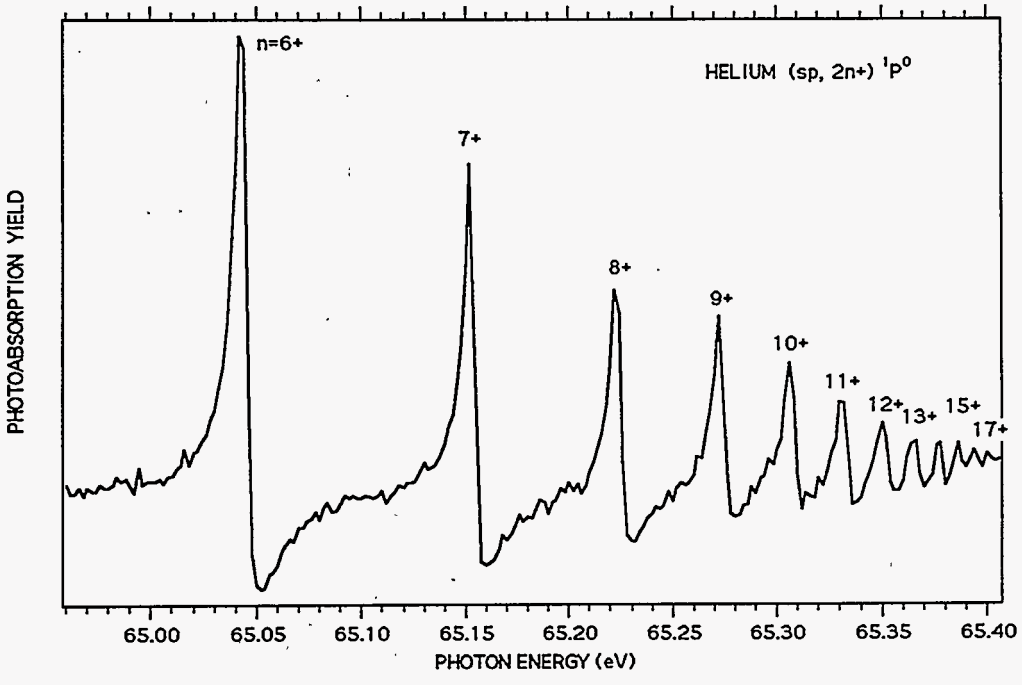

Spectrum from Station 8-1

Autoionizing states of double-excited He below the N=2 threshold of He^+, showing only the $n \geq 6$ region. The spectrum was taken using entrance and exit slits of 15 microns, with a resolving power of $E/\Delta E = 13{,}000$.

has achieved a resolution of 12 meV at 67 eV, which was limited by the smallest possible vertical slit opening of approximately 40 microns. A set of entrance and exit slits, based on the design of the Station 6-1 spherical grating monochormator, have been fabricated as a collaboration between LBL, SSRL and LLNL, and were installed at the end of March. An absolute calibration of intensity using high quantum efficiency Si-based photodiode as a function of resolution is also under way. [See Figure 6.]

Station 8-2 – Resolution studies on Station 8-2 showed that this 55 m spherical grating monochromator has a resolving power of 7,500-10,000 at the nitrogen K-edge, thus making it one of the highest resolution VUV/SXR lines in use. Gas-phase measurements at the carbon and oxygen K-edges also exhibited excellent energy resolution. In addition, magnetic circular dichroism studies were performed on magnetic multilayers using circularly polarized light in the 700 eV region which was obtained by directing the off-axis radiation through the beam line by a simple manipulation of the input optics. Since then, a new input aperture located in front of the first mirror has been fabricated and installed in collaboration with IBM and LLNL. This aperture will selectively allow left circular, right circular or plane polarized radiation to pass through the beam line without moving the input optics thus making it possible to remotely choose the handedness of the polarization in a reproducible manner. In addition, the IBM group has developed a set of magnetic multilayers which give a well defined absorption response when illuminated with circularly polarized radiation, making them ideal as polarimeters. These samples have been installed on the beam line for routine use as polarimeters.

Station 10-1 – On the afternoon of March 12, 1992 photons were put throught the new 10-1 experimental station for the first time. The station employs a SGM with water cooled optics and entrance slits which will allow full use of the high fluxes coming from the wiggler source and yield state of the art resolutions from 150 eV to 1500 eV.

The 10-1 branch line was built as a collaboration between SSRL, the IBM Almaden Research Center and the Surface Structures and Reactivity Thrust of the Stanford Center for Materials Research. The branch line was built on the LLNL/UC PRT wiggler line, which also includes Station 10-2. This branch line will give spectral resolutions on the order of 10,000 at 500 eV, as with similar systems at SSRL. In addition, since the branch line is on a high power wiggler beam line, it will achieve very high intensities making possible a number of experiments, especially in the 500-1200 eV range which have not been readily possible at SSRL. Research that will be undertaken as part of an IBM/Stanford CMR collaboration includes high resolution NEXAFS studies on precursor states on surfaces. The Stanford CMR effort will include work in the area of diamond thin film growth using a novel sequential reactor technique developed in the Stanford Materials Science Department.

X-RAY LINES

The work on the x-ray beam lines was also characterized by extensive use as well as the addition of new experimental capabilities. A number of the developments on the x-ray lines relate to the SSRL structural molecular biology program and are described in more detail in the following section on "Biotechnology Projects and Developments".

Station 2-2 – The double axis goniometers for high precision monochromatic topography and rocking curve measurements in Station 2-2 underwent initial testing. In addition, standard x-ray topography using white light was used to study the defect structure and strains in the following materials: YB_{66} crystals (an R&D-100 award was won for the soft x-ray monochromator application of these crystals), Si-$TaSi_2$ composites which is useful for new electronic devices (obtained from GTE), integrated circuit sensors, thin Mo films sputtered on Si and also III-V compounds.

Station 2-3 – Station 2-3 was used for x-ray microscopy experiments in the 8-10 keV range using zone plates. The high efficiency of the zone plate collection optics allows the use of a bend magnet source to achieve resolutions potentially as high as 1 μm.

Station 4-2 – A semi-dedicated small angle x-ray scattering (SAXS) station on 4-2 successfully underwent initial commissioning during the spring run.

Station 6-2 – Station 6-2 has been modified to accept a new water-cooled, high vacuum monochromator which is currently being fabricated. The significance of this modification is two-fold. First, it will allow operation with a single thin Be window after the monochromator and will permit photon energies as low as 2.1 keV to be reached. Second, since this also results in the removal of the Be windows in front of the monochromator (the differential pumping system from 10-2 is being used to isolate the monochromator from the SPEAR vacuum), any limitations on the SPEAR current due to Be window heating are completely eliminated. The net result will be an improvement in flux over the 2-3 keV region of between 1-2 orders of magnitude (depending on energy).

Station 10-2 – Station 10-2 saw heavy use with a number of exciting experiments performed during the past year. These experiments included high spatial resolution x-ray tomography and *in-situ* studies of GaAs CVD growth using grazing incidence x-ray scattering. The extensive modifications to Station 10-2 during the previous year which provided a white light capability on this beam line were commissioned and tested.

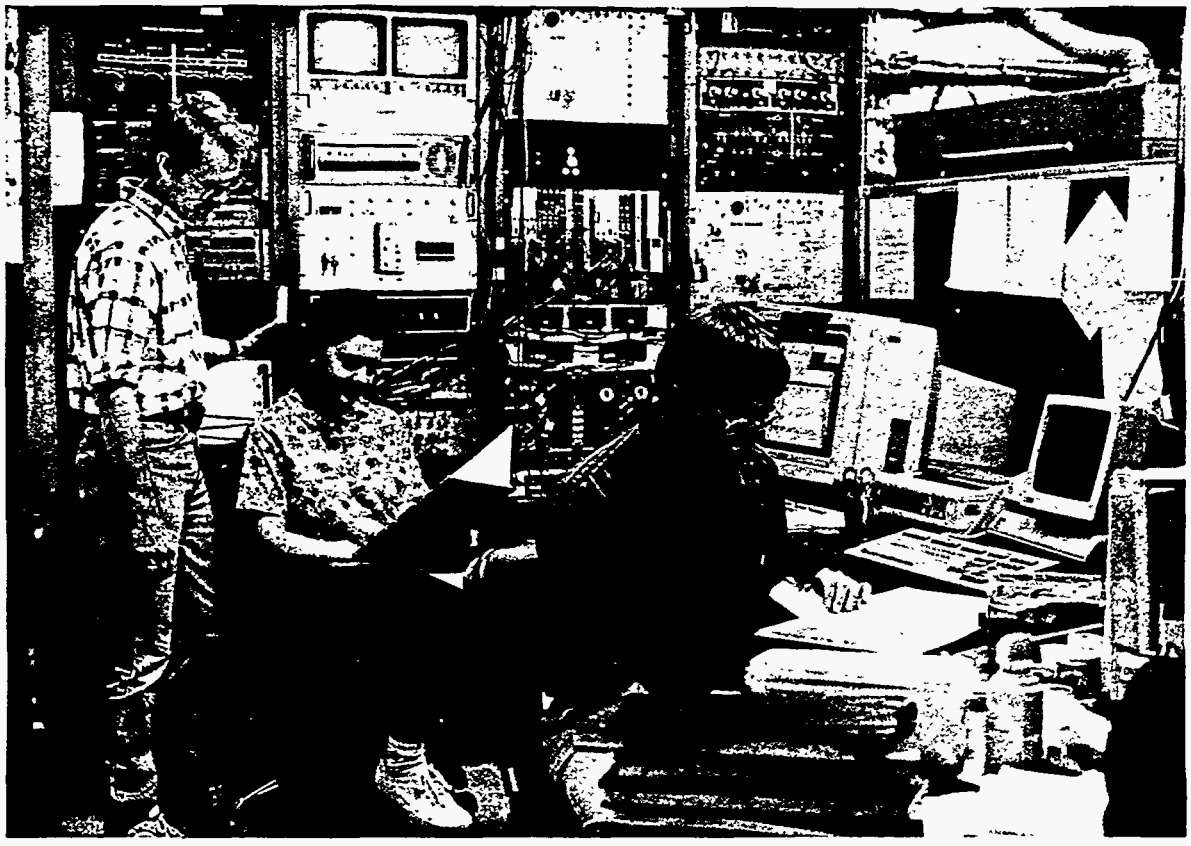

Brian Stephenson (IBM Yorktown Heights), Patrizia Imperatori (Consiglio Nazionale delle Ricerche) and Paul Fuoss (AT&T Bell Laboratories) working on Station 10-2. The group is studing in situ x-ray analysis of organiometallic vapor phase epitaxy.

The UCLA PRT group has taken a lead role in the acquisition and installation of a new multi-circle diffractometer for the rear hutch. The diffractometer is a standard Huber 4-circle augmented by a second 440 goniometer behind the 2θ axis which can support positioning optics, light sources or spectrometers to monitor and/or photo-excite the sample. The diffractometer is mounted on an SSRL Huber table which includes horizontal and vertical positioning and rotation about the vertical axis. The incident and diffracted beam can be defined using stepper-motor driven slits, and a Ge solid stated detector can be used for detecting the scattered radiation. All the equipment has been installed in the hutch. The first diffraction pattern using the goniometer is expected in May 1992.

BIOTECHNOLOGY PROJECTS AND DEVELOPMENTS

The primary purpose of work in this area is to further develop and make available specialized instrumentation for experimentation in structural molecular biology (SMB). These efforts are supported primarily by funds from the NIH Biomedical Resource Technology Program (BRTP) and the DOE Office of Health and Environmental Research (OHER). Additional funding for instrumentation has recently been provided by the NSF. The scientific and technological focus includes the applications of synchrotron radiation to protein crystallography and anomalous scattering, small-angle x-ray scattering, and x-ray absorption spectroscopy.

Protein Crystallography

Laue Crystallography Station on 10-2 – The development of instrumentation for Laue crystallography has proceeded very rapidly at SSRL. Station 10-2 was modified to accept white light over the preceeding year and the line was commissioned with this new mode of operation in 1991. Further, a new SSRL-designed Laue recording camera was constructed, commissioned and utilized for experimentation during the summer of 1991. This camera incorporates water-cooled components and a fast timing shutter (down to the few millisecond time regime). Film was used as the initial recording medium and Laue exposures were obtained in 600-800 milliseconds/frame. [See Figure 7.]

More recently, the capability of recording Laue images with imaging plates has been added. A new Fuji BAS2000 off-line scanner has been purchased using funding from the NSF and installed at SSRL. This is an extraordinary system with 10-50 times higher sensitivity than film and much wider dynamic range (~ 10^5 vs. 10^2 for film). The 10-2 Laue station has recently been operated using image plates as the detector and exposures of protein crystals were made in the few millisecond/frame time regime. Besides crystallography, the IP system will find applicability in other experiments such as time-resolved x-ray scattering.

FIGURE 7

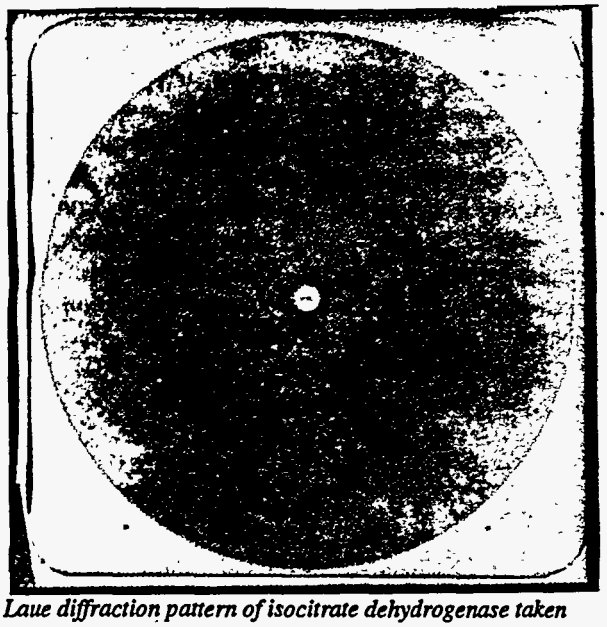

Laue diffraction pattern of isocitrate dehydrogenase taken on Station 10-2 by a collaboration between SSRL and UC Berkeley.

Imaging Plate on the Rotation Camera Station (7-1) – A dedicated imaging plate recording/readout system (purchased from MAR Research) has replaced film as the medium for data collection on this station. This IP system has sensitivity and dynamic range characteristics similar to the Fuji system mentioned above, but is a self-contained "turn-key" system. The MAR system has been in use on the line since the beginning of the February 1992 run. It has resulted in a remarkable improvement in capability as well as improved efficiency of protein data collection for the outside community of protein crystallography users of this station.

Advanced Computer Graphics Workstations – Two VAXstation 4000s were delivered in early 1992 and will provide computational support for the two imaging plate systems (MAR Research and Fuji) and for crystallographic computing in general. Complete data reduction software will be implemented for processing imaging plate data in the future. This step represents a very significant advance over film. With the film medium, SSRL users could only take away developed images and had to process the data "off-site" in their home laboratories. The IP/workstations combination will allow our users to do data reduction "on-site" and thus enable much better determination of data quality while still present at SSRL.

X-ray Absorption Spectroscopy

Modifications to Station 6-2 for XAS Measurements in the 2.1-4.0 keV Region – A new in-vacuum water-cooled monochromator for Station 6-2 has been designed and fabricated. The new monochromator, together with a differentially pumped section, will provide for operation of the beam line with only a single thin exit Be window. When complete this coming fall (1992), this station will provide very high intensity (about 10^2 higher than currently available) for XAS studies in the 2.1 - 4.0 keV region.

XAS on Station 7-3 – SSRL is now operating station 7-3 in a mode dedicated to XAS utilization with the primary component being for structural molecular biology applications. This mode was used with great success during the summer 1991 run and is continuing to be successful in the current extended 7 month run. There is a permanent setup of a motorized optical alignment rail, a liquid He cryostat, and a 13-element Ge solid state detector array which are used by the SMB groups. Operation is much more efficient, user friendly and optimizes use of staff time while minimizing wear-and-tear on delicate instrumentation.

VAXstation 4000 for XAS Analysis – A new VAXstation 4000 has been received and is being set up adjacent to the 7-3 station. Software will be put on this station for XAS data reduction and analysis, thereby providing users the very important capability of assessing data quality while still "on-line". This will greatly improve efficiency of beam time use because it will be possible to evaluate signal-to-noise as data averages are being built up, and to examine questions such as changes in sample integrity during the actual course of the experiments.

Array Detectors and Future Developments – Fluorescence detection equipment is now available to general users at SSRL for study of dilute samples with concentrations as low as about 1 millimolar. In particular, there are two 13-element high resolution Ge array detector systems which are supported by SSRL scientific and technical staff for use in both biological and non-biological applications.

A next-generation, HgI_2 array detector prototype was successfully tested during the summer 1991 run (this work is a joint project with Xsirius Inc.). This detector, based on a 20 element HgI_2 array, performed very well, giving an energy resolution of around 275 eV/element at 7 keV. The array has now been equipped with fully hybridized, computer-controlled electronics and will be used in production data collection during the summer of 1992. This array

already represents a significant advance over the 13 - element Ge detector array systems already in use at SSRL and other synchrotron laboratories.

Small Angle X-ray Scattering

Quasi-Permanent Small Angle Scattering Station – During the spring-summer, 1991 run, a new quasi-permanent station for the small-angle scattering camera was commissioned. This station, in the rear of the 4-2 hutch (including a new optical table) allows the camera to be permanently aligned, thereby minimizing setup time and providing a "user-friendly", stable and efficient station.

Improvements to Small Angle Scattering Camera – During the December 1991 shutdown, many components of the SAXS camera were improved. A much more reliable and flexible high-vacuum scattered beam flight path was designed, fabricated and assembled. The camera can be configured with a variable path length with data being recorded using one of three detector systems; i) a 20 cm one-dimensional PSD system (purchased from Biologic), ii) a quadrant detector (EMBL design) or iii) imaging plates scanned with the new Fuji BAS2000 IP system (described above). This new camera system was successfully used with recent scattering studies on Station 10-2.

Instrumentation for Time-Resolved Studies – Instrumentation for rapid-mixing has been developed for carrying out time-resolved small angle scattering measurements into the millisecond time regime. Included are control electronics and software. The time scale is on the order of 10-50 milliseconds.

The Structural Molecular Biology Beam Line 9

SSRL has begun the conceptual design on a new multipole, high intensity wiggler beam line on SPEAR which would be fully dedicated to structural molecular biology research. This beam line would provide very high brightness radiation to experimental stations configured for protein crystallography (Laue and monochromatic), x-ray absorption spectroscopy, and x-ray small angle scattering/diffraction. The location for this insertion device-based beam line would fall mostly in an existing building at SSRL (building 120). A parallel expansion of the floor and mezzanine space around the building, to accommodate important user setup and work areas for structural molecular biology experiments is also being planned.

SSRL staff scientist, Michael Soltis (left) discussing the use of the new imaging plate diffraction camera system for protein crystallography data collection with users from the Stanford University Department of Cell Biology.

SPECIAL PROJECTS

Crystal Cooling Project – Based on prior experience with microchannel water cooling of silicon monochromator crystals, SSRL staff have worked with engineers from Rockwell Power Systems, a subsidiary of Rocketdyne Corporation, to modify their pin-post cooling technique (functionally similar to the microchannel method) to produce a marketable cooled monochromator crystal. Ways have been found to minimize the strain introduced during their pin-post machining process, and low-power x-ray tests indicate that high-quality strain-free crystals containing integral pin-post water cooling channels can be produced. Rockwell Power Systems is now constructing a prototype high-power monochromator crystal intended for extended tests and service at a high-power wiggler beam line at the Cornell High Energy Synchrotron Source. Similar devices should give improved performance at SSRL's high-power wiggler Beam Lines 6 and 10. This project is led by John Arthur of the SSRL Photon Research and Operations Group.

Adjustable Phase Insertion Device – The goal of this project was to design, build, and test an undulator based on the notion that its magnetic field could be adjusted not by varying its gap, but by varying the longitudinal phase between its jaws. Based on a theoretical study and a detailed numerical simulation, such a device was constructed from SmCo magnets borrowed from the PEP 1B undulator. The adjustable phase undulator (APU) was placed on the Beam Line 5 undulator mover in November, 1991, and tested early in 1992. The effects of the APU on the electron beam in SPEAR, particularly at injection, were studied and the x-ray spectra generated were characterized.

The APU was tested at the minimum gap allowed by the Beam Line 5 undulator mover; its jaws were moved longitudinally by one half of the 77 mm period. Trim coil compensation to null the effect of tuning on the horizontal electron beam steering showed that the APU required only minimal change of compensation over its entire range, as compared to any of the other Beam Line 5 undulators when their gap is varied. Studies with a pinhole camera and sensitive measurements by other SPEAR users also showed very small effects on the SPEAR beam. Also, SPEAR injection into the APU moved to the 'out of phase' position was trouble-free; neither ramping nor lifetime were affected by the presence of the device. Finally it was shown that the x-ray spectra produced by the APU were the same as those produced when the device's gap was varied, except for a redshift due to the SPEAR beam being off-axis vertically.

An APU is much simpler to build than a comparable adjustable gap device, it interferes with the electron beam less, and it generates similar x-ray spectra. This design should be an interesting option for future insertion devices. This project is led by Roger Carr of the SSRL Photon Research and Operations Division, who received an R&D 100 award for this work.

SUPPORT FACILITIES

Computer Systems – All x-ray stations are now under microVAX control and employing the MIDAS and SUPER software packages for XAS and diffraction, respectively. The 1991 run saw the first production use of the

IV WORKSHOPS AND MEETINGS

WORKSHOP ON FOURTH GENERATION LIGHT SOURCES

A Workshop on Fourth Generation Light Sources (*i.e.*; future machines which would significantly exceed the performance level of sources now in operation or construction) was held at SSRL from February 24-27, 1992 with support provided by the DOE Division of Materials Research. There were 146 registered participants from 48 institutions in 10 countries. The workshop was chaired by Max Cornacchia and Herman Winick of the SSRL staff.

The workshop provided the opportunity for several somewhat distinct groups of accelerator and insertion device specialists to interact. In addition to those involved with developing storage rings and linacs as light sources, there were also many who were developing these for high energy physics purposes, where there is also a need to reduce electron beam emittance and increase current. In many cases, people working on similar problems met for the first time and were able to compare solutions.

Ideas were presented for future light sources with improved brightness, coherence, peak power, pulse duration, and polarization. Sources discussed ranged from compact superconducting storage rings to the use of multi-kilometer colliders as light sources and included free electron lasers operating down to 1 Å, new rings with more than 1 km circumference and the use of ultra-low emittance, ultra-high energy proton beams from the SSC. Several new concepts were presented, including storage ring lattices that would reach an emittance 100 times lower than third generation rings, modified electron optical elements to enlarge dynamic aperture, a linac energy recovery scheme, a photon storage ring, and short period plasma wigglers.

The workshop was charged with the following tasks:

- *evaluate directions for fourth generation sources in the light of what has been learned from facilities now in operation and construction as well as expected scientific needs*

- *identify fundamental limits of fourth generation sources*

- *suggest research and development activities toward development of fourth generation sources*

A full report on the workshop is now in preparation and will be available through Todd Slater at SSRL. A summary of some of the high points from each of the working groups, is given below, with the caveat that the most important results of the workshop will only become clear in the future when some of the ideas are implemented.

1. Sources based on storage rings

The basic approaches and technology now being used in the design and construction of third generation storage ring light sources can be extended in fairly straightforward ways to the design and construction of rings with about an order of magnitude lower emittance.

To reach diffraction limits at hard x-ray wavelengths, further reduction in emittance is required. New approaches to the design of such rings were reviewed including new lattices and rings with very large circumferences, as well as the use of damping wigglers and modified sextupoles. The use of combined function magnets with strong gradients, coupled with locally corrected chromaticity, is also a promising approach to achieving very low emittance.

Large collider rings such as PEP, PETRA and TRISTAN, with their long straight sections and low emittance capability, offer extreme capabilities and could serve as prototypes and test-beds for future rings as well as drivers for short wavelength FELs reaching the "water window" around 30-40 Å.

Specialized rings to achieve very short pulse lengths (quasi-isochronous or low alpha rings), down to 1 ps and possibly less, appear feasible and are of interest for colliders as well as light sources. The advantages of using a "top-up" mode to achieve essentially constant stored beam current (and therefore constant power loading on beam line optical components) with very frequent injection was discussed, with urging that this be tested on existing rings.

2. Sources base on linacs

Short wavelength FELs appear feasible using recently developed low-emittance laser-driven photocathode guns as injectors to linear accelerators. Guns delivering 1 nC of charge in less than 10 ps, with normalized emittance of 4 mm-mrad are now in operation. Guns expected to reach 1.5 mm-mrad and/or higher charge are nearing completion. Pulse compression techniques can reduce pulse length to less than 1 ps, boosting peak current to over 1000 Å.

During the workshop the basic parameters for several FELs operating at 1000 Å or below were determined and presented, including examples using the SLAC linac to drive FELs at 40 Å if equipped with a presently available photocathode gun and at 1 Å with an improved gun. These short wavelength linac-based FELs will deliver sub-picosecond pulses with saturated peak power levels in the gigawatt range and average spectral brightness up to 10^{22} photons/

s/mm²/mrad²/0.1% bandwidth.

Examples were also presented illustrating the benefit of "beam conditioning" to relax the emittance requirement and reduce the wiggler length needed to reach saturation in an FEL.

Challenges that must be addressed include the development of reliable, high duty-factor, low emittance photocathode guns and techniques for preserving emittance during beam transport, acceleration and pulse compression.

3. Insertion Devices

The approaches being used and the mechanical and magnetic tolerances being achieved for undulators on third generation sources are close to adequate for sources with about an order of magnitude lower emittance. To achieve tighter tolerances, improved measurement techniques appear to be necessary.

Significant advances have been made in theoretical efforts to predict and reduce field errors. However, accurate brightness predictions for high performance undulators on 3rd and 4th generation rings will require new codes which more fully account for real magnetic fields and real electron beam properties. Utilization of these beams for experiments will require improvements in beam line optics.

Presentations were made on the advantages of recently tested devices such as the in-vacuum undulator at the Accumulator Ring at KEK and the adjustable phase undulator at SSRL. Among the new, mostly untried, ideas discussed were: new versions of helical undulators requiring no constraints in the horizontal beam direction; micropole devices with gaps of the order of 1 mm; undulators using RF fields; field synthesizers to make arbitrary and variable polarization; Compton backscattering using high powered lasers to reach high photon energy with low electron energy; plasma undulators to achieve period lengths between lasers and micropole undulators and very long undulators with 1000 or more periods to provide narrow band radiation without a monochromator.

Alan Jackson from the ALS (center) talks with John Galyada, APS (left) and Ewan Paterson, SLAC.

Workshop photos by T. Nakashima, SLAC

Bob Batterman, Cornell (left) and Ed Rowe (Wisconsin)

Denis McWhan (NSLS) and Paul Fuoss (AT&T Bell Laboratories)

Burton Richter, SLAC and Lee Teng, Argonne

1991 USER'S MEETING

The 18th Annual User's Meeting was held on November 7-8, 1991 and featured talks and posters on research done during the commissioning of the new booster/injector synchrotron. There were 17 scientific talks and 25 posters given in the areas of VUV, x-ray, instrumentation, and biotechnology. The conference was chaired by Roger Carr (SSRL) and Paul Fuoss (AT&T Bell Laboratories). Logistical arrangements were handled by Shirley Robinson and Michelle Kearney of the SSRL User Research Administration group.

In the VUV area, J. Tobin (LLNL) spoke about studies of magnetic thin films and Y. Wu (IBM Almaden) presented the results of magnetic dichroism experiments with circularly polarized off-axis bend magnet radiation. H. Tang (UC Irvine) spoke about spin polarized photoemission studies of Gd on tungsten, which were done on the newly commissioned soft x-ray multiundulator on Beam Line 5. Z. Hussain (LBL) reviewed high resolution soft x-ray spectroscopy now becoming feasible with the new SGMs on stations 6-1 and 8-2, which have resolving powers up to 10,000.

In the hard x-ray area, A. Payne (Stanford) spoke about *in-situ* studies of sputtered films, and D. Kisker (IBM) described *in-situ* studies of OMVPE GaAs growth. P. Allen (LANL) discussed advances in dispersive XAFS.

In the biotechnology field, D. Eliezer (Stanford) described small angle scattering experiments to determine the radius of gyration of the FeMo cofactor in nitrogenase. J. DeWitt (Stanford) spoke about EXAFS on methane monooxygenase and V. Yachandra (LBL) presented the results of EXAFS on the manganese centers of the photosynthetic reaction center. J. Kinney (LLNL) discussed tooth decay studied by x-ray tomography.

Instrumentation talks included a description of SSRL's expanded crystallography capacity by M. Soltis (SSRL) and a talk by C. Stahle (Stanford) on a liquid helium calorimetric x-ray detector; L. Terminello (LLNL) spoke on high resolution spectroscopy on the new LLNL SGM (Station 8-2). R. Bionta (LLNL) described hard x-ray phase zones plate lenses. G. Hirsch (Hirsch Assoc.) presented the first data from a novel photoelectron microscope and Z. Rek (SSRL) gave an update on the development of YB_{66} for soft x-ray monochromators.

V SSRL ORGANIZATION

SSRL is organized into three functional divisons: the Accelerator Research and Operations Division (AROD), the Photon Research and Operations Division (PROD) and the Computing and Administration Resources Division (CARD). The functions of the AROD Division are to operate, maintain and develop the booster and SPEAR as well as performing research on these and future machines. The functions of the PROD Division are beam line managment, beam line development, research using the synchrotron radiation and user support. The CARD group provides central computing services for scientific research, user data collection and administrative purposes as well as business services, contract management, personnel and facility administration. The current organization chart is shown on the following page.

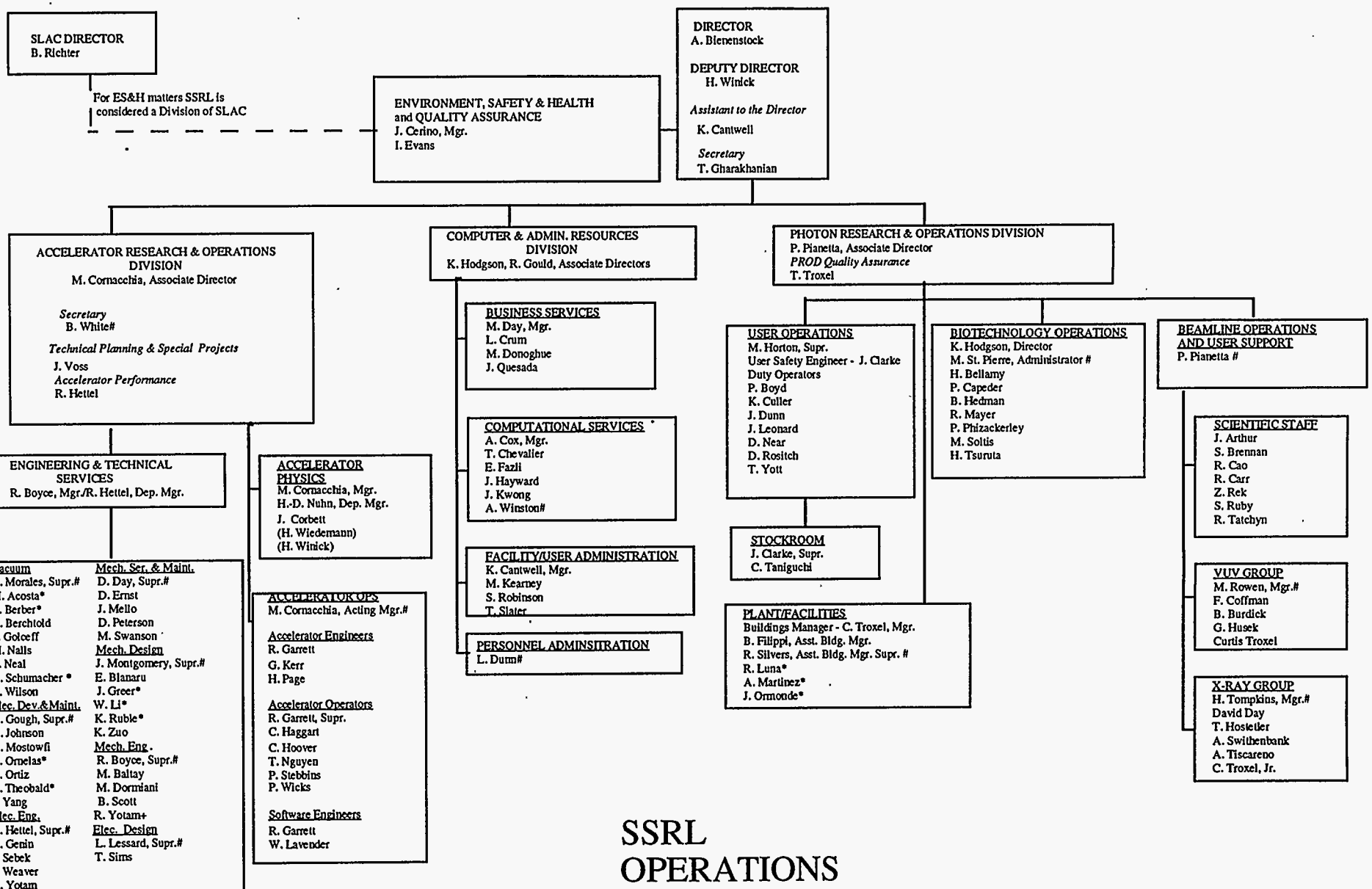

SSRL OPERATIONS ORGANIZATION

Group Safety Coordinator
( ) Primary Responsibility Elsewhere
* Denotes Contract Worker

SSRL EXPERIMENTAL STATIONS
RESPONSIBLE PERSONNEL

BRANCH LINE		RESPONSIBLE PERSON(S)
1-1	Grasshopper	F. Coffman
1-2	TGM	M. Rowen
1-4	SAS	H. Tompkins
1-5	Unfocused Bend Magnet	H. Tompkins
1-5 ES2	Area Detector	P. Phizackerley/H. Bellamy
2-1	Focused Bend Magnet	H. Tompkins
2-2	White Radiation	Z. Rek
2-3	Unfocused Bend Magnet	H. Tompkins
3-1	Grasshopper	F. Coffman
3-2	Seya - Soft X-ray	F. Coffman
3-3	Jumbo - Soft X-ray	M. Rowen
3-4	Lithography	P. Pianetta
4-1	8-Pole Wiggler	H. Tompkins
4-2	8-Pole Wiggler	H. Tompkins
4-3	8-Pole Wiggler (Materials Diffraction)	H. Tompkins
5	Mutli-Undulator	R. Carr/F. Coffman
6-1	54- Pole Wiggler - SGM	R. Tatchyn *(SSRL)*, P. Heimann *(LBL)*
6-2	54- Pole Wiggler	J. Arthur *(SSRL)*, G. George *(EXXON)*, P. Ross *(LBL)*
7-1	8-Pole Wiggler (Rotation Camera)	P. Phizackerley/M. Soltis
7-2	8-Pole Wiggler (Scattering)	S. Brennan
7-3	8-Pole Wiggler	H. Tompkins
8-1	TGM	M. Rowen *(SSRL)*, J. Tobin *(LLNL)*
8-2	SGM	M. Rowen *(SSRL)*, J. Tobin *(LLNL)*
10-1	SGM	M. Rowen *(SSRL)*, J. Stohr *(IBM)*, P. Pianetta *(Stanford)*
10-2	31- Pole Wiggler	S. Brennan *(SSRL)*, J. Wong *(LLNL)*, M . Nicol *(UCLA)*

INSTRUMENTATION/FACILITY RESPONSIBILITIES

MATERIALS DIFFRACTOMETER: S. Brennan, H. Tompkins
PERKIN-ELMER CHAMBER: M. Rowen
VG SAMPLE CHAMBER: M. Rowen
AREA DETECTOR: P. Phizackerley, H. Bellamy
ROTATION CAMERA: P. Phizackerley, M. Soltis
CAD-4 DIFFRACTOMETER: M. Soltis
COMPUTER SYSTEMS and SOFTWARE: T. Cox
7-2 SPECTROMETER: S. Brennan, H. Tompkins
Bldg 131 SAMPLE PREPARATION LABORATORY: R. Mayer, B. Hedman
Bldg 120 SAMPLE PREPARATION LABORATORY: P. Pianetta, M. Rowen
DARKROOMS: M. Soltis, Z. Rek
EXAFS EQUIPMENT: B. Hedman, R. Mayer
SAS CAMERA (BIOTECH): H. Tsuruta
EXAFS CONSULTANT: B. Hedman
SCATTERING CONSULTANTS: S. Brennan. J. Arthur
TOPOGRAPHY EQUIPMENT: Z. Rek
RAPID TURNAROUND EXAFS FACILITIES: B. Hedman, R. Mayer

SSRL ADVISORY BOARDS

PROPOSAL REVIEW PANEL

A main task of the Proposal Review Panel is the review and rating of scientific proposals to SSRL based largely on reports obtained from outside (non-panel) referees. During 1991 the panel met on January 3 and June 27 and rated the new proposals which had been received in September 1990 and March, 1991.

As of January 1, 1992 SSRL had received a total of 2,172 proposals of which 103 are presently active.

The Proposal Review Panel meets twice yearly, generally in June and January. Deadlines for receipt of proposals for consideration at the next meeting are the first of September and the first of March each year.

The panel members in 1991 were:

Biology Sub-panel
Don Engelman, Yale University
William Orme-Johnson, MIT
Douglas Rees, Cal Tech

Materials Sub-panel
Howard Birnbaum, University of Illinois
G. Slade Cargill, IBM
Russell Chianelli, EXXON
Peter Pershan, Harvard University

VUV Sub-panel
Warren Grobman, IBM *(Chair)*
Torgny Gustafsson, Rutgers University
Victor Henrich, Yale University

SCIENCE POLICY BOARD

The Science Policy Board reviews all aspects of SSRL operation, development and plans for the future. It reports to Stanford University President, Donald Kennedy. The Board met once during this reporting period, on April 12-13, 1991. Members of the 1991 Board were:

Craig Barrett, Intel Corporation
Praveen Chaudhari, IBM
Marvin Cohen, University of California
Robert Dynes, University of California
Wayne Hendrickson, Columbia University
Ed Knapp, Los Alamos National Laboratory
Venkatesh Narayanamurti, Sandia National Laboratory *(Chair)*
William Orme-Johnson, MIT
Yves Petroff, LURE
Andrew Sessler, LBL

SSRL USERS ORGANIZATION

Members of the Executive Commitee of the SSRLUO were elected at the 18th Annual SSRL Users Group Meeting as follows:

C. Richard Brundle, IBM-Almaden
George Brown, UC Santa Cruz
Stephen Cramer, UC Davis/LBL
David Eliezer, Stanford University
Charles Fadley, UC Davis/LBL
Paul Fuoss, AT&T Bell Laboratories *(Chair)*
Jeff Kortright, Lawrence Berkeley Laboratory
Brad Pate, Washington State University, *(Ex-Officio)*
James Tobin, LLNL *(Vice-Chair)*
Stephanie Yoshikawa
Katherine Cantwell *(Secretary-SSRL Liaison)*

VI EXPERIMENTAL PROGRESS REPORTS

MATERIALS PROPOSALS

VUV PROPOSALS

BIOLOGY PROPOSALS

MATERIALS PROPOSALS

X-RAY ABSORPTION SPECTROSCOPY OF ION SORPTION COMPLEXES AT AQUEOUS/MINERAL INTERFACES

Peggy A. O'Day[1], Ning Xu[1], Charalambos J. Papelis[2], Per Persson[1], John R. Bargar[1], Steven N. Towle[1], Singfoong Cheah[1], James O. Leckie[2], George A. Parks[1], and Gordon E. Brown, Jr.[1]

(1) School of Earth Sciences, (2) Dept. of Civil Engineering
Stanford University, Stanford CA. 94305

INTRODUCTION

The uptake of ions from aqueous solutions by solid substrates can occur by a variety of sorption processes that control transport and partitioning in diverse contexts such as contaminant and radionuclide migration in groundwater, electrochemical and corrosion processes, ore deposition, solar energy conversion, and enhanced oil recovery. Characterization and understanding of the molecular structure and bonding of sorbed ions in simplified systems is critical in order to accurately describe and predict the behavior of these species in more complex natural systems. Fluorescence-yield x-ray absorption spectroscopy (XAS) is one of the few spectroscopic methods that can provide quantitative structural information of *in situ* species at concentrations representative of natural conditions[1]. Our objective is to determine how the coordination chemistry of sorbate ions and the surface structure of sorbent minerals influence the types of surface complexes that form in different sorbate/sorbent systems.

Our previous investigations include EXAFS and XANES studies of selenate and selenite complexes chemisorbed on α-FeOOH (goethite)[2], Pb(II) on γ-Al_2O_3[3] and α-FeOOH[4], Co(II) on γ-Al_2O_3, TiO_2 (rutile), $Al_2Si_2O_5(OH)_4$ (kaolinite), α-SiO_2 (quartz), and $CaCO_3$ (calcite)[5-9], and aqueous Np(V) on α-FeOOH[10]. For much of our previous sorption work, Co^{2+} was chosen as the sorbate ion because its solution chemistry is relatively well understood and it does not form significant polymeric species in solution over the pH ranges we examined (5-8)[11]. Our choice of a single type of sorbate ion (aqueous Co^{2+}) on sorbents with different surface structures (γ-Al_2O_3, TiO_2 (rutile), and $Al_2Si_2O_5(OH)_4$ (kaolinite)), all at similar sorbate loadings, permitted us to examine the effects of the mineral surface on the types, structures, and sizes of Co sorption complexes that form. In the past year, we have completed XAS studies of Co sorption on kaolinite, quartz, and calcite, and have initiated several new studies (described below) to investigate specific interactions between aqueous species and mineral substrates.

EXPERIMENTAL

XAS data were collected at SSRL during two sessions, July-August and August-September, 1991, on beamline IV-3 (wiggler field = 18 kG) using a Si(220) monochromator. X-ray absorption spectra were collected at the Co, Ti, Zn, Cu, Se, and Cd K-edges and the Pb L_{III}-edge. Fluorescence spectra of sorption samples were collected using a Lytle-type dectector; transmission spectra were collected for solid model compounds and aqueous $ZnCl_2$ solutions. In general, sorption samples are prepared by equilibration of pH-adjusted solutions with powdered solids for 24-72 hours to achieve at least 90% uptake of the ion of interest from solution. After removal of excess supernatent solution, XAS samples are sealed in teflon sample holders with mylar windows and run as wet pastes under ambient conditions. Edge spectra of supernatent solutions show little signal from the element of interest; thus, the minor amount of solution remaining in contact with sorption samples produces no significant spectral component. EXAFS spectra are analyzed using empirical phaseshift and amplitude parameters derived from crystalline, well-characterized model compounds to determine distances, coordination numbers, and relative Debye-Waller factors.

Co(II) SORPTION ON KAOLINITE, QUARTZ, AND CALCITE

Co(II) sorption as a function of surface coverage was studied by EXAFS analyses on three different natural kaolinites and on ground quartz (Minusil). Co surface sorption densities (Γ) ranged from 0.26 to greater than 10 μmol m^{-2} on kaolinite, and from 0.77 to 10 μmol m^{-2} on quartz. EXAFS spectra were also collected on kaolinite and quartz samples equilibrated with solutions in which the thermodynamic solubility of $Co(OH)_2$ was purposely exceeded. Analyses of XAS spectra indicate that sorbed Co at all surface coverages is octahedrally coordinated by first-shell oxygen atoms at 2.06 to 2.08 (± 0.01) Å and is

not oxidized to Co(III). At Γ of 0.26 to 0.31 μmol m^{-2}, EXAFS analyses of Co sorbed to three different kaolinites suggest that Co bonds to the surface as both outer-sphere and inner-sphere mononuclear sorption complexes. With increasing Co surface coverage, the appearance of second-neighbor Co atoms at distances of 3.12-3.15 Å (Figure 1) suggests the formation of multinuclear surface complexes at relatively low surfaces coverages (Γ= 0.51 - 1.2 μmol m^{-2}) corresponding to about 3 - 7% of a monolayer of closest-packed, oxygen-ligated Co atoms. Both solution studies and EXAFS analyses suggest a predominance of inner-sphere over outer-sphere complexes in this range of surface coverage. Low average coordination numbers (generally < 1) for second-shell Al and Si indicate that Co is bonded directly to the mineral surfaces, but also suggest that there is not significant diffusion of Co into the mineral structure. With increasing Co surface coverage on both kaolinite and quartz, the average number of second- and fourth-neighbor Co atoms surrounding a central Co increases, suggesting the formation of large, three-dimensional multinuclear surface complexes that grow in average size with increasing Co sorption. Distances, coordination numbers, and Debye-Waller factors derived from EXAFS analyses show that the local structure around Co in these complexes is similar but not identical to that of Co in either freshly precipitated or aged $Co(OH)_2$(s). At high surface coverages, EXAFS data suggest several possibilities: (1) the formation of a disordered phase of $Co(OH)_2$(s), (2) small particles of $Co(OH)_2$(s) in which edge effects become significant, or (3) a $Co(OH)_2$(s)-like species in which epitaxy with the oxygen atoms of the mineral surface leads to contraction of the surface phase hydroxide structure.

XAS data were collected for sorption samples of Co sorbed to calcite prepared at two initial Co concentrations (10^{-4} M and $2x10^{-5}$ M), two pH's (pH=7.4 and 8.5) and two different controlled calcite saturation indexes (CSI=Log([Ca^{2+}][CO_3^{2-}]/K_{SP})=0.95 and 0.60). A comparison of the EXAFS spectra of these sorption samples shows two different distinctive "beat" patterns (Figure 2). Co EXAFS spectra of the samples prepared at low pH are identical to those for a solid solution of 2500 ppm Co in calcite, while the EXAFS spectrum of the sorption sample prepared at high pH shows significant differences. However, none of the "beat" patterns of these spectra is similar to that of Co-solid phase — $Co(OH)_2$, $CoCO_3$, or $Co_2(OH)_2CO_3$. This preliminary result suggests that $(Ca,Co)CO_3$ solid solution forms on calcite surface at lower pH value, but a structurally-different surface coprecipitate, or even a mixture of a coprecipitate and a Co-solid surface precipitate, might have formed at the higher pH value. Further quantitative data analysis will provide testing of this hypothesis and give more structural information to differentiate sorption features among samples prepared at lower pH's.

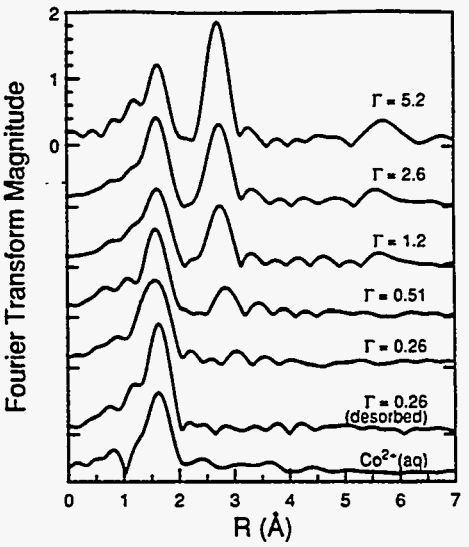

Figure 1. Radial structure functions (uncorrected for phase shift) for Co(II) sorbed to Dry Branch kaolinite at sorption densities (Γ, μmol m^{-2}) shown compared to 12 mM aqueous Co^{2+} (bottom spectrum). Note the appearance of a second shell peak at Γ = 0.51.

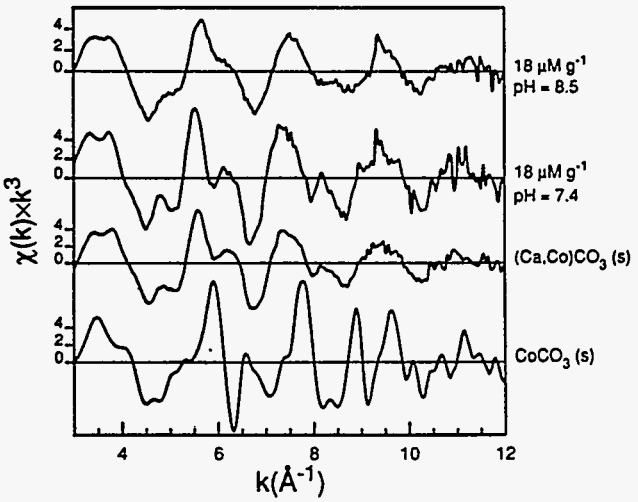

Figure 2. Normalized, background-substracted EXAFS spectra for Co(II) uptake on calcite by coprecipitation at two different pH's (top spectra) compared to Co solid model compounds (bottom spectra).

SELENITE AND Cd(II) SORPTION ON ALUMINUM OXIDES

To enhance our understanding of the partitioning of toxic species, we have collected x-ray absorption spectra of selenite and Cd(II) sorbed at aluminum oxide/water interfaces. The sorbents studied include two different, high surface area amorphous aluminum oxides (ALCOA CP-5, $Al_2O_3 \cdot 0.5\ H_2O$, and ALCOA C-33, $Al_2O_3 \cdot 0.1\ H_2O$), α-Al_2O_3 (corundum), and γ-$Al(OH)_3$ (gibbsite). The

concentrations of aqueous Na_2SeO_3 and $Cd(NO_3)_2$ were 10^{-3} and 10^{-4} M. For both cadmium and selenite sorption samples, surface coverages corresponding to the lower concentration (10^{-4} M) were 1.2 μmol m^{-2} for amorphous Al_2O_3 and 1.1 μmol m^{-2} for gibbsite and corundum. The higher selenite concentration (10^{-3} M) resulted in surface coverages of 4.6, 2.2, and 3.1 μmol m^{-2} for CP-5, C-33, and corundum respectively. Cadmium is believed to form a precipitate at the higher concentration studied. Analyses of the EXAFS data for the SeO_3^{2-} sorption samples indicate that the Se-O distances (1.69 Å) and Se coordination numbers (3 oxygens) are constant irrespective of sorbent and that the complexes are mononuclear (Figure 3). The Cd XAS data are consistent with $Cd(II)O_{5-6}$ species [d(Cd-O) = 2.04 - 2.14 Å] that become increasingly similar to the Cd environment in $CdCO_3$ (otavite) [d(Cd-O) = 2.29 Å] at the highest cadmium concentration studied (10^{-3} M). These results help explain the observed strong partitioning of aqueous SeO_3^{2-} and Cd(II) on alumina.

STRUCTURE OF $ZnCl_2$ (aq)

In previous studies, aqueous solutions of zinc chloride have displayed anomalous behavior. Both thermodynamic and transport properties of this system are different from those of aqueous solutions of alkaline-earth and transition-metal halides. Previous fluorescence XAS study of aqueous Zn as a function $ZnCl_2$ concentration and Zn:Cl ratio[12] suggests a transition from an inner-sphere tetrachloro complex to an outer-sphere aquo complex near concentrations of 1 M. In order to elucidate the structural changes occurring in solution, we collected EXAFS transmission spectra of five solutions in the range 0.5 to 2.0 M. Also, the effects of pH and ionic strength were studied. The data are presently being analyzed.

Cu(II) SORPTION ON SiO_2 IN THE PRESENCE OF 2,2-BIPYRIDINE

The presence of organic ligands plays an important role in the speciation and sorption of metal ions in natural waters. It has been suggested that ternary metal-ligand-surface complexes form in the presence of organic ligands and thus, form surfaces species that are distinct in their structure and bonding properties from aqueous metal surface complexes[13]. Preliminary XAS fluorescence spectra were collected on Cu(II) sorbed to amorphous SiO_2 (Aerosil 300) in the presence of 2,2-bipyridine at a sorption density of 10^{-5} mol g^{-1}, corresponding to a surface coverage of about 0.03 μmol m^{-2}. From analyses of the EXAFS spectra, we hope to establish whether Cu is bonded as an inner-sphere or outer-sphere complex and examine changes in bond strength as a function of pH in the presence and absence of organic ligands.

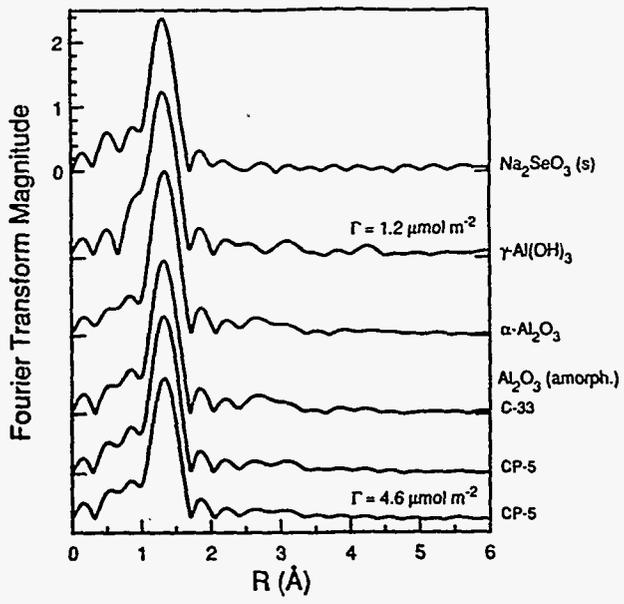

Figure 3. Radial structure functions (uncorrected for phase shift) for selenite sorbed to three amorphous Al_2O_3 solids and α- and γ-Al_2O_3 at the sorption densities (Γ) shown, compared to Na_2SeO_3 solid model compound (top spectrum).

Pb(II) SORPTION ON α-Al_2O_3 AND ZnS_2

The concentration and transport of toxic Pb(II) in natural waters is controlled primarily by sorption processes at mineral surfaces. Previous EXAFS study of Pb(II) sorbed onto high surface area powders of γ-Al_2O_3[3] indicates that Pb is coordinated by three first-shell oxygen atoms and that both Pb and Al atoms occur in the second coordination shell around Pb, suggesting a direct bond between sorbed Pb and oxygen atoms of the mineral substrate. However, little is known about which reactive sites on mineral surfaces take part in sorption and how they influence the structure of the surface complex. We have begun studies of Pb sorption on a different polymorph of Al_2O_3 (α-form, corundum) and on a sulfide mineral (ZnS_2, wurtzite) in order to evaluate how the structure of the mineral substrate, irrespective of composition for α- and γ-Al_2O_3, affects the local Pb coordination environment. Preliminary absorption spectra were collected on samples of Pb^{2+} sorbed onto high surface area corundum (α-Al_2O_3) powder at two different sorption densities, 0.1 and 0.9 μmol m^{-2}, and on ground ZnS_2. Analyzable spectra were collected for Pb/α-Al_2O_3 samples and data reduction is currently in progress. However, Pb/ZnS_2 spectra suffered from such strong background fluorescence originating from the sulfide substrate that the data cannot be analyzed quantitatively. In future work on this system, we will use a multi-channel array detector instead of a Lytle detector in order to eliminate background fluorescence.

GRAZING-INCIDENCE EXAFS OF Co(II) ON SINGLE CRYSTAL TiO_2

In our past studies of ion sorption onto high surface area powders, it was difficult to determine which crystallographic surfaces and thus, which surface sorption sites, are taking part in surface complexation reactions with aqueous ions. As an extension of our previous study of Co(II) sorption on powdered TiO_2 (rutile)[7], we are collecting EXAFS spectra of Co sorbed to particular crystallographic surfaces of single crystal wafers of TiO_2 using a grazing incidence geometry. Grazing incidence geometry allows us to optimize surface sensitivity and to examine individual surface orientations, as well as offering advantages in signal-to-noise[14].

Initially, EXAFS spectra were collected at the Ti K-edge of clean TiO_2 crystals of (110) and (001) orientations. Crystals (about 1 cm^2) were prepared by cutting and polishing surfaces to optically flat and cleaning of all polishing residues, as indicated by x-ray photoelectron spectroscopy (XPS). Co(II) was sorbed from a solution of 10^{-3} M $Co(NO_3)_2$ at pH 6.5 onto single TiO_2 crystals. A surface coverage of Co of about 0.3 of a monolayer of oxygen-ligated Co atoms was estimated from XPS measurements. We attempted to collect Co K-edge x-ray absorption spectra on the (001) oriented surface, however, a variety of experimental difficulties prevented us from obtaining useful data. Some of these problems, such as fine tuning the alignment, were solved, but others were more intractable, such as excessive background fluorescence from Ti in the substrate. Future experiments will employ a better optimized system for alignment and an array detector to eliminate background fluorescence.

ACKNOWLEDGEMENTS

This research was supported in part by NSF grants EAR-8805440 and EAR-9105015. We gratefully acknowledge the staff of SSRL and Britt Hedman for valuable assistance during data collection, and Graham George (Exxon Research and Engineering Co.) for use of his EXAFS data reduction software.

REFERENCES

[1] Brown, G.E., Jr. (1990) Spectroscopic studies of chemisorption reaction mechanisms at oxide/water interfaces. In: *Mineral-Water Interface Geochemistry, Reviews in Mineralogy*, Vol. 23, eds. M.F. Hochella, Jr. and A.F. White, Washington, DC: Mineralogical Society of America, 309-363.

[2] Hayes, K.F., Roe, A.L., Brown, G.E., Jr., Hodgson, K.O., Leckie, J.O., and Parks, G.A. (1987) In-situ x-ray absorption study of surface complexes: selenium oxyanions on α-FeOOH. *Science* 238, 783-786.

[3] Chisholm-Brause, C.J., Hayes, K.F., Roe, A.L., Brown, G.E., Jr., Parks, G.A., and Leckie, J.O. (1990) Spectroscopic investigation of Pb(II) complexes at the γ-Al_2O_3/water interface. *Geochim. Cosmochim. Acta* 54, 1897-1909.

[4] Roe, A.L., Hayes, K.F., Chisholm-Brause, C.J., Brown, G.E., Jr., Parks, G.A., and Leckie, J.O. [1991) X-ray absorption study of lead complexes at α-FeOOH/water interfaces. *Langmuir* 7, 367-373.

[5] Chisholm-Brause, C.J., O'Day, P.A., Brown, G.E., Jr., and Parks, G.A. (1990) Evidence for multinuclear metal-ion complexes at solid/water interfaces from x-ray absorption spectroscopy. *Nature* 348, 528-531.

[6] Chisholm-Brause, C.J., Brown, G.E., Jr., and Parks, G.A. (1991) *In-situ* EXAFS study of Co(II) sorption on g-Al_2O_3 at different adsorption densities. In: *X-ray Absorption Fine Structure*, ed. S.S. Hasnain, Ellis Horwood Ltd. Publ., 263-265.

[7] Chisholm-Brause, C.J. (1991) *Spectroscopic and equilibrium study of Co(II) sorption complexes at oxide/water interfaces.* Ph.D. Dissertation, Stanford University, Stanford, CA., 155 pp.

[8] O'Day, P.A., Brown, G.E., Jr., and Parks, G.A. (1991) EXAFS study of aqueous Co(II) sorption complexes on kaolinite and quartz surfaces. In: *X-ray Absorption Fine Structure*, ed. S.S. Hasnain, Ellis Horwood Ltd. Publ., 260-262.

[9] Xu, N., Brown, G.E., Jr., Parks, G.A., and Hochella, M.F., Jr. (1990) Sorption mechanism of Co^{2+} at the calcite-water interface. (abstr.) *Abstr. Program Geol. Soc. Amer. Ann. Mtg.*

[10] Combes, J.-M., Chisholm-Brause, C.J., Brown, G.E., Jr., Parks, G.A., Conradson, S.D., Eller, P.G., Triay, I., Hobart, D.E., and Meier, A. (1992) EXAFS spectroscopic study of neptunium (V) sorption at the a-FeOOH/water interface. *Environ. Sci. Technol.* 26, 376-382.

[11] Baes, C. F., Jr. and R. E. Mesmer (1986) *The Hydrolysis of Cations*, N. Y.: Wiley and Sons, 489 pp.

[12] Parkhurst, D. L. (1985) *The Application of EXAFS and Mean Activity Coefficient Data to Ion Association Models for the Zinc-Chloride System*, MS Thesis, Stanford University, Stanford, CA.

[13] Schindler, P.W. (1990) Co-adsorption of metal ions and organic ligands: Formation of ternary surface complexes. In: *Mineral-Water Interface Geochemistry, Reviews in Mineralogy*, Vol. 23, eds. M.F. Hochella, Jr. and A.F. White, Washington, DC: Mineralogical Society of America, 281-307.

[14] Heald, S.M., Chen, H., and Tranquada, J.M. (1988) Glancing angle extended x-ray fine structure and reflectivity studies of interfacial regions. Phys. Rev. B 38, 2, 1016-1026.

APPLICATION OF HIGH RESOLUTION CALORIMETRIC X-RAY DETECTORS TO COMPTON SCATTERING EXPERIMENTS

Caroline K. Stahle
Stanford University, Department of Materials Science and Engineering, Stanford, CA 94305

Douglas Osheroff
Stanford University, Department of Physics, Stanford, CA 94305

Richard L. Kelley, S. Harvey Moseley, Andrew E. Szymkowiak
NASA / Goddard Space Flight Center, Greenbelt, MD 20771

COMPTON SCATTERING

Compton scattering, the inelastic scattering of x-rays from electrons, is a method of measuring a function called the Compton profile, which is the projection of the electron momentum distribution of the target material along the scattering vector. This measurement of electron momenta provides a means of evaluating calculations of electron wavefunctions. Compton scattering data can be reduced to such a Compton profile if the impulse approximation is valid, which requires that the energy transfered to the electrons in scattering be much greater than their binding energies.

It is customary to use atomic units when discussing Compton scattering. The free electron Fermi momentum for many solids is about 1 au. The breadth of a Compton profile is of this order. To see the detailed structure of a Compton profile, a momentum resolution of better than 0.1 au is desirable. Compton scattering experiments have tended to fall into two classes, x-ray and gamma-ray experiments. The x-ray experiments have used radiation from 10 KeV to 20 KeV, combined with focussing crystal optics and a position sensitive detector, to obtain momentum resolutions near 0.1 au. The gamma experiments have involved using radioactive sources and solid state detectors with resolutions in the hundreds of eV. Typically achieving no better than a momentum resolution of 0.5 au, those who have pursued this class of Compton experiments traded resolution for the advantage of working at higher energy, the ability to study heavier materials while yet still having the impulse approximation be valid and not losing signal due to absorption in the sample. While many valuable experiments of both classes have been performed, the need for better resolution, particularly for the higher energy experiments, is clear. The gross features, born of atomic physics and crystal geometry, could be seen, but the more subtle solid state physics, such as correlation effects, lay beyond the resolution limit. This motivated a search for detectors which would permit high resolution, high energy Compton scattering measurements.

The detector energy resolution that corresponds to a particular momentum resolution in the final data depends on the incident x-ray energy and the scattering angle. For a scattering angle of 150° and incident photon energy 40 KeV, which puts the Compton peak at 35 KeV, 0.1 au corresponds to a resolution of 46 eV at the peak of the profile. Compton cross sections are weak, so the count rate limit of a Compton spectrometer need not be particularly high. Compton profiles require a minimum of about 10^6 counts, so the count rate can not afford to be arbitrarily low. Detectors with counting rates of 100 counts per second able to resolve 35 KeV photons to 35 eV would have a significant impact on Compton scattering research. We have investigated whether calorimetric x-ray detectors could be made to meet those specifications.

CALORIMETRIC X-RAY DETECTORS

Calorimetric x-ray detectors are devices which determine x-ray energies by measuring the heat deposited by individual photons. A calorimeter consists of an absorber in which the energy of the x-ray is converted to heat and a thermometer to measure the resulting increase in temperature. The ensemble is thermally isolated except for a weak thermal link to a heat sink to permit recovery after a photon is detected. The combined heat capacity of absorber and thermometer is minimized in order to maximize responsivity. Calorimeters are operated at temperatures near 0.1 K in order to reduce both thermal fluctuations and the value of the heat capacity.

The calorimeters discussed in this report used doped semiconductor thermistors for thermometers. Details of the theory and development of such resistive calorimeters have been described in several articles. [1-4] The resistance of the thermistor decreases sharply with increasing temperature at cryogenic temperatures. The thermistor and a load resistor of comparable magnitude are connected in series and a constant bias voltage is placed across them. An increase in the temperature of the calorimeter is associated with a drop in the voltage across

the thermistor. This is the signal, which is sent through a series of low-noise amplifiers. The absorber could be no more than the semiconductor into which the thermistor is implanted, or it could be a separate thermal mass in good thermal contact with the thermistor. The electrical connections to the thermistor also form the thermal link to the heat sink.

We have worked with implantation doped silicon thermistors fabricated at Goddard Space Flight Center in monolithic arrays of twelve devices. Each detector had an active area of about 1 mm × 0.25 mm, which was suspended by four silicon legs, each 20 mm wide and 2 mm long. A thermistor had been formed in the active area by ion implanting phosphorus compensated with boron. Electrical paths down two of the legs, from the thermistor to bonding pads in the surrounding frame, were created by doping degenerately with phosphorus.

For the best performance, a calorimetric x-ray detector needs to have an absorber separate from the semiconductor in which the thermistor is implanted, yet is in good contact with the thermistor. This is a result of the way thermalization proceeds in a material with a band gap. The energetic electron excited by x-ray absorption loses energy rapidly through scattering from other electrons, and in a semiconductor this involves both the transfer of energy to phonons and the creation of electron-hole pairs. At low temperatures, these free carriers become localized in impurity states in the gap. The lifetime of a trapped carrier is essentially infinite at these temperatures, keeping the energy associated with these electon-hole pairs from ever entering the phonon system and being detected. Variations in the initial partition of energy between phonons and trapped carriers causes a spread in pulse heights for a given incident photon energy. The choice of the absorbing material is constrained by the need for rapid and complete thermalization, efficient absorption of high energy x-rays, and low heat capacity. Thermalization problems rule out insulators and most semiconductors. The large electronic specific heat of normal metals rules them out as practical alternatives. That leaves narrow gap semiconductors and superconductors. The calorimeter program at Goddard Space Flight Center has successfully used HgTe crystals for absorbers, affixed with epoxy to silicon thermistors. It is with such a device that 7.3 eV resolution of 6 KeV x-rays has been attained. [4] The low Debye temperature of HgTe, and small gap semiconductors in general, limits the volume which can be used to an amount acceptable for low energy x-rays, but not for energies near 40 KeV. Several superconductors with high Debye temperatures seem attractive candidates because their absorption per unit heat capacity can be quite a bit larger than for the narrow gap semiconductors. The energy gap in a superconductor is small, typically an meV, so one might expect thermalization to proceed as well as in HgTe, but the process in superconductors is a bit more complicated.

Thermalization following the absorption of an x-ray photon in a superconductor involves breaking Cooper pairs into quasiparticles. [5] One expects in a short time to have a phonon population with a broad distribution of energies resulting from inelastic electron scattering and a population of quasiparticles of energy Δ and higher (where 2Δ is the energy gap). [6] At temperatures much less than the critical temperature, T_c, quasiparticle lifetimes are expected to be long. Phonons of energy 2Δ and higher are consumed in the breaking of Cooper pairs, tying up a fraction of the deposited energy in the long-lived quasiparticles which result. In these detectors the thermal time constant, several milliseconds, is long compared with the lifetime of a 2Δ phonon against pair breaking; thus a phonon generated when two quasiparticles recombine is more likely to break another pair than to escape the system. This phonon bottleneck slows thermalization, reducing both detector responsivity and the permissible count rate. One can attempt to circumvent this difficulty by creating recombination sites, areas where the gap is reduced by the proximity of a normal metal or magnetic material. Quasiparticles which scatter inelastically in these regions become trapped. [7] The quasiparticle density in the trap becomes greater than in the bulk, enhancing the recombination rate. Phonons emitted from recombination in the trap have less energy than the gap in the bulk and cannot contribute to the breaking of Cooper pairs. With this model, a superconductor seems a reasonable candidate for an absorber for use with high energy x-rays, as long as quasiparticle recombination sites are provided.

We investigated Re, Ta, and Sn absorbers and various schemes for introducing such recombination sites. While results from Re and Ta were disappointing, better performance was achieved with devices with 0.2 mm × 0.5 mm × 25 μm, 99.999% pure Sn absorbers affixed to them. The sensitivity was about a factor of two less than anticipated. After peaking, the signal pulse decayed with an initial time constant of 3 ms, followed by a tail characterized by a time constant of 30 ms. Quasiparticle recombination schemes had no effect on this characteristic pulse shape. Using an analog data acquisition system, spectra of Ba fluorescence lines were acquired using the Sn devices. The full width at half maximum of the Ba Kα lines, 31.82 KeV and 32.19 KeV, was 90 eV, based on the local slope of the calibration curve at those energies. Figure 1 shows such a spectrum. The measured noise levels would have predicted a FWHM of 40 eV at that point in the spectrum, so the resolution was far from noise limited. A possible source of the excess broadening is thermalization noise in the superconductor, intrinsic variations of pulse shape for a given photon energy, perhaps correlated with the position in the superconductor at which the photon is absorbed. An alternative cause could be small variations in the device temperature due to changes in the level of background power into the device of order 10^{-15} W.

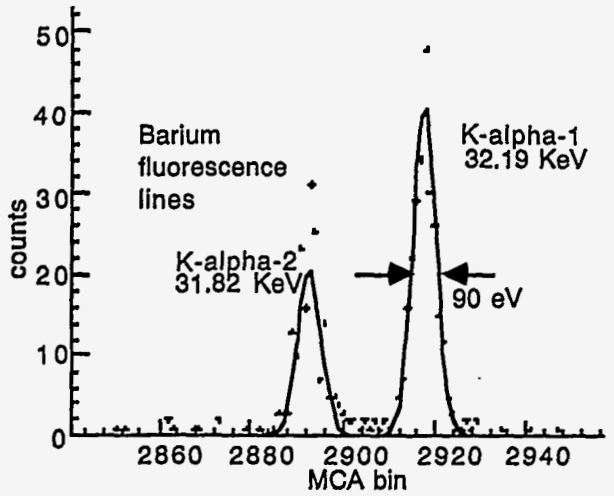

Figure 1 -- Fluorescence spectrum measured with Sn device

That attempts to create quasiparticle recombination sites had no effect suggests either that the traps were ineffective or that recombination was proceeding adequately in the bare superconductor. If the sites were ineffective, due to a low probability that quasiparticles reach the traps or inelastically scatter within them, the unexpected long tails in these pulse shapes could be indicative of a recombination bottleneck. If recombination were proceeding unimpeded in the bare superconductor, due to an excess of quasiparticles above the theoretical population caused by trapped flux or impurities, the long tails could simply be the result of the greater heat capacity associated with this excess of quasiparticles. Further investigations will address the origin of these long recovery times.

APPARATUS

The extremely low operating temperatures were achieved with the use of a small $^3He/^4He$ dilution refrigerator. The mixing chamber, which is the part of the refrigerator which serves as the heat sink, was regulated near 60 mK for most of the device studies. The He dewar admitted x-rays into the refrigerator through a series of windows which shielded the cold elements from thermal radiation.

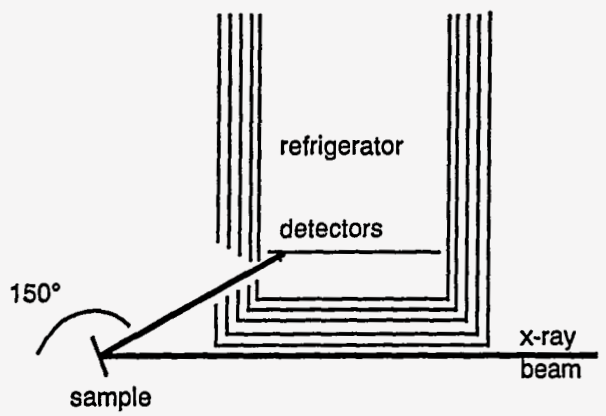

Figure 2 -- Scattering geometry for Compton experiment

There were two data acquisition systems. An analog system was employed for all the device characterization studies. This filtered the amplified signal and fed the output to a multi-channel analyzer. A digital system was used in parallel with the analog system during the Compton experiments. This digitized the individual pulses for later processing. The apparatus had room enough to wire up two separate channels, so two detectors could be operated simultaneously.

COMPTON EXPERIMENT

It was decided that the 90 eV resolution of the Sn devices was adequate to perform a preliminary Compton experiment. The spectrometer system was transported to the Stanford Synchrotron Radiation Laboratory, where it was installed in the forward section of the large experimental hutch on wiggler branch line 4-2. Compton profiles for the (100) and (111) directions of silicon were acquired at a scattering angle of 150° and incident beam energy of 40748 eV. Figure 2 illustrates the scattering geometry.

During data acquisition at the synchrotron, drift of spectral lines on the time scale of several hours was apparent. This contrasted with our previous data acquisitions which typically could be acquired overnight without significant broadening. The 90 eV result was such an acquisition. It is not clear whether this greater instability was due to the environment of the synchrotron or to a disruption to the apparatus experienced during the move. We expected that, with the digital acquisition system incorporated into the apparatus at that time, we would be able to correct for drift. In order to calibrate the drifting spectrum, fluorescence was measured from a target composed of powders of La_2O_3, CeO_2, Pr_6O_{11}, and Nd_2O_3. Placing this at the sample holder and tuning the beam energy above the Nd K-edge, the Kα and Kβ fluorescence lines of La, Ce, Pr, and Nd were incident upon the detectors. These span the range from 33 KeV to 43 KeV, allowing a calibration function to be fit over the exact range of interest for the Compton spectra. The Pr $K\beta_1$ line, at 40748 eV, was chosen as the reference for the elastic line in the Compton spectra. The calibration files and the Compton profiles were corrected for drift in such a fashion that the common 40748 eV line in each file was assigned the same pulse height. Then the calibration function derived from the fluorescence lines could be applied to the Compton data.

After processing the digitized pulses, including digital filtering and drift correction, the final resolution at the center of the Compton peak was 180 eV. This

corresponds to a momentum resolution of 0.4 au. We have not yet found an explanation for this degradation. A more serious limitation was the low number of total counts in each of the two profiles, 10^5, an order of magnitude less than the minimum desirable. Because of the long tails on the Sn pulses, the count rate had been limited to one count per second per detector. Figure 3 shows the raw data for the (100) direction, the (111) data being quite similar. Figure 4 shows the difference between the (100) and (111) profiles. These profiles were obtained from the measured Compton spectra through the established procedures for Compton analysis, using the Ribberfors [8] expression for relating the relativistic cross section to the Compton profile. The gross features of the anisotropy agree with that measured by Reed and Eisenberger [9], but the need for better statistics is clear.

ASSESSMENT

Interest in using calorimetric x-ray detectors for Compton scattering originated in their potential for extremely high resolution. In the experiment described, that potential was not met, but not because of any fundamental limitation. Further study of the materials of these detectors promises to improve the resolution. Research should focus on determining the origin of the excess broadening and eliminating it.

Count rate limitations present a more serious restriction. The biggest limitation to the count rate for the particular devices used for this Compton experiment was the presence of long tails. It is reasonable to expect that, with further investigations, devices will be made that are efficient for high energy x-rays and do not have long tails with time constants in the tens of milliseconds; however, it is unrealistic to expect, because of the constraints on heat capacity and thermal conductivity, that the tolerable count rate will ever exceed a hundred counts per second. For Compton scattering, a count rate of that order is

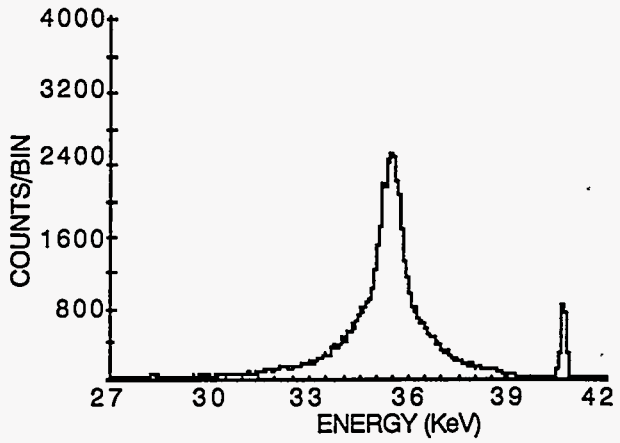

Figure 3 -- Compton spectrum for Si (100)

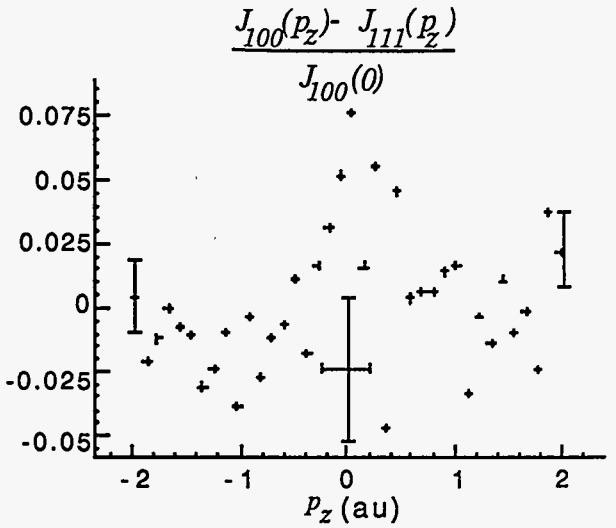

Figure 4 -- Difference of silicon Compton profiles, J, for the (111) and (100) directions, as a function of the component of momentum, p, along the scattering vector, z.

enough to acquire adequate statistics in one profile in several hours. Use of an array can increase the total count rate when the limit in individual detectors can no longer be improved.

REFERENCES

[1] S. H. Moseley, J. C. Mather and D. McCammon, J. Appl. Phys. 56 (1984) 1257

[2] D. McCammon, S. H. Moseley, J. C. Mather and R. F. Mushotzky, J. Appl. Phys., 56 (1984) 1263

[3] D. McCammon, B. Edwards, M. Juda, P. Plucinsky, J. Zhang, R. Kelley, S. Holt, G. Madejski, S. Moseley and A. Szymkowiak, "Thermal Detection of X-rays" in Low Temperature Detectors for Neutrinos and Dark Matter III, eds., L. Brogiato, D. V. Camin and E. Fiorini (Editiones Frontieres, Gif sur Yvette Cedex, 1990) p. 213

[4] D. McCammon, W. Cui, M. Juda, P. Plucinsky, J. Zhang, R. L. Kelley, S. S. Holt, G. M. Madejski, S. H. Moseley and A. E. Szymkowiak, Proc. PANIC XII -- Nucl. Phys. A527 (1991) 821c

[5] A. Gilabert, Ann. Phys. Fr. 15 (1990) 255

[6] J. J. Chang and D. J. Scalapino, Phys. Rev. B 15 (1977) 2651

[7] N. E. Booth, Appl. Phys. Lett. 50 (1987) 293

[8] R. Ribberfors, Phys. Rev. B 12 (1975) 3136

[9] W. A. Reed and P. Eisenberger, Phys. Rev. B 6 (1972) 4596

EXAFS SPECTROELECTROCHEMISTRY: STRUCTURE OF METALS IN AMALGAMS

R.C. Elder and William R. Heineman

Department of Chemistry
University of Cincinnati
Cincinnati, Ohio 45221-0172

The use of x-ray absorption spectroscopy (eg. XANES, EXAFS) has provided a new look at electrochemical reactions. (1-3) An extremely useful electrochemical technique, anodic stripping voltammetry, utilizes the fact that certain metals (eg. In^{3+}, Tl^{+}, Cd^{2+}, Zn^{2+}, Ga^{3+}, Sn^{2+}, Pb^{2+}, Bi^{3+}) preconcentrate by amalgamation and diffusion in a mercury electrode at a reducing potential. Detection limits can be improved by three orders of magnitude when subsequent oxidation by a linear potential scan or a differential voltammetric pulse is applied.

The characteristics of amalgams have been exhaustively analyzed by a variety of techniques. (4-7) Solubilities of selected metals are reported in Table 1, column 2. Most of these metals will form complexes as solid alloys with mercury at low temperatures. (4,5) For Na, K, and Mg metal-mercury amalgamation occurs in the liquid, as well as a solid alloy phase. (4 p.158) Similarly, for In and Tl a metal-mercury amalgam is formed at room temperature over a variety of compositional ranges for the relative metal/mercury content in the amalgam. (4 p.169-170) For Cd, Ba, Au and Ag, a metal-mercury interaction survives at a room temperature but is assumed to result from solid phase precipitates suspended within the amalgam. (4) Finally, the metals Zn, Sn, Pb and Bi are assumed to be randomly distributed as free atoms in amalgams above 0°C. (4) Based upon electrochemical measurements, it has been proposed that several $metal_1$-$metal_2$ complexes will

TABLE 1: Feasibility of EXAFS Studies with Various Amalgams.

Metal	Amount in Amalgam[a] (mMoles/cm3)	Edge Energy[b]	(keV)	Penetration Depth[c] (μm)
Hg	67.0	L1	14.8	
		L2	14.2	
		L3	12.3	
In	67.0	K	27.9	3.83
Tl	28.0	L3	12.6	0.92
Cd	6.0	K	27.7	3.74
Zn	3.9	K	9.6	1.03
Ga	2.6	K	10.3	1.30
BA	0.32	K	37.4	10.13
Sn	0.68	K	29.2	4.36
Pb	0.98	L3	13.0	1.00
Bi	0.90	L3	13.4	1.08
Na	3.64	K	1.0	0.06
K	1.31	K	3.0	0.13
Au	0.09	L3	11.9	2.21
Ag	0.04	K	25.5	2.99
Mg	1.72	K	1.3	0.06

[a] This value was calculated from the density of mercury at room temperature (13.5 g/cm^3) and the solubility of the metal in mercury (% weight) from reference 5.

[b] Values obtained from Viegel, W.J., Photon Cross Section from 0.1 KeV to 1 MeV for Elements Z=1 to Z=94, Atomic Data Tables, 5, 51-111 (1973).

[c] Penetration depth into pure mercury at a given edge energy such that the transmittance (I/I_0) was 0.8.

form in amalgams. (4,7) The solubility of intermetallic compounds in mercury is frequently low and the solid phase separates. (4,5 p.63) Interestingly, most of the structures for these complexes are not know. Although x-ray diffraction has been used to estimate structural parameters in these amorphous matrices, (8) to our knowledge, we are the first to investigate amalgams with EXAFS.

Our ability to study amalgams via EXAFS spectroscopy is fundamentally limited by absorption of the solvent (mercury). As shown in Table 1, the penetration depth of X-ray photons into pure mercury at the specified energy, such that transmittance is equal to 0.8, is on the order of micrometers. Based on Table 1, useful EXAFS measurements with saturated amalgams of In, Tl, Cd, Zn, Sn, Ba and Ga should be feasible and may be possible with Pb and Bi.

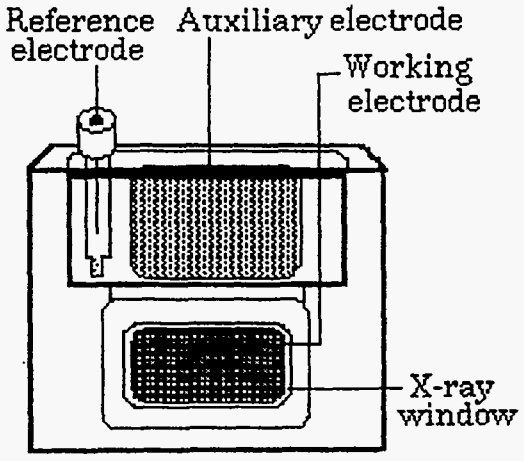

Figure 1: The Spectroelectrochemical Solution Cell for Analysis of EXAFS.

For EXAFS measurements, potential control of a static solution is necessary to maintain amalgamation of mercury and metal being observed. Solution cells used in EXAFS generally utilize a thin-layer configuration which enables exhaustive and rapid electrolysis. (1) EXAFS analysis of amalgams created by in situ deposition of mercury and metal onto a reticulated vitreous carbon electrode (RVC) has proven quite troublesome. A new solution cell, Figure 1, has been developed to solve such problems as hydrogen gas evolution from acidic solutions that becomes entrapped in the RVC.

Our original investigations have proven that EXAFS is a useful spectroelectrochemical technique for amalgam studies. Figure 2 shows the absorption spectrom of amalgamated mercury and thallium at a maximum solubility of two thallium atoms per five mercury atoms. The thallium L3-edge (A) is approximately 300 eV above the mercury L3-edge (B). The EXAFS regions of the metals show little structure; as a result, further experimentation is needed to elucidate the coordinated environment of each metal. XANES regions of pure mercury metal and mercury amalgamated with indium in Figure 3 gives no apparent differences in edge energies, but a slight difference in the absorption edge rise is noticeable.

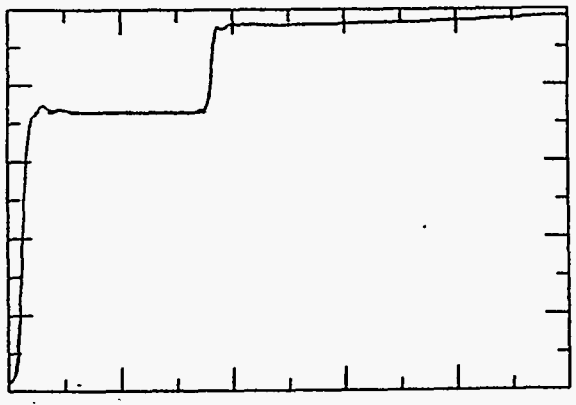

Figure 2: The absorption spectrum of the thallium-mercury amalgam. (A) The thallium L3-edge, 12.6 KeV. (B) The mercury L3-edge, 12.3 KeV.

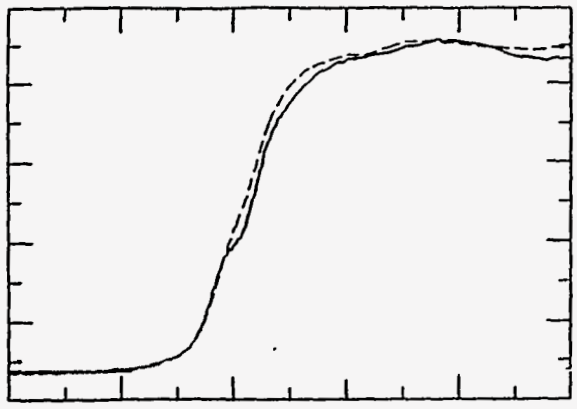

Figure 3: The mercury XANES spectra of pure mercury metal (solid line) and the mercury-indium amalgam (dashed line).

ACKNOWLEDGEMENTS

Support for this project is from the AFOSR (88-0089). The work reported her is largely that of Robert O. Rigney and Drs. Ying Ping Deng and David H. Igo. All data were measured at SSRL beamline 4-2.

REFERENCES

1) Dewald, H.D.; Elder, R.C.; Heineman, W.R., Anal. Chem., **1986**, 58, 2968.

2) Sharpe, L.R.; Heineman, W.R.; Elder, R.C., Chem. Rev., **1990**, 90, 705.

3) Igo, D.H.; Elder, R.C.; Heineman, W.R.; Dewald, H.D., Anal. Chem., **1991**, 63, 2535.

4) Kovolsky, M.; Zebreva, A., Intermetallic Compounds in Amalgams, in Progress Polarography, Vol. 3, (Zumen, P. and Meites, L., ed.) Wiley-Interscience, New York, 1972, pp. 157-194.

5) Trotman-Dickenson, A.F. (ed.), Comprehensive Inorganic Chemistry, Vol. 3, Pergamon Press, London, 1973, pp. 283-285.

6) Vydra, F.; Stulik, K.; Lulakova, E., Electrochemical Stripping Analysis, Halsted Press, New York, 1976.

7) Heineman, W.R.; Mark, H.; Wise, J., Electrochemical Preconcentration, in Laboratory Techniques in Electroanalytical Chemistry, (Kissinger, P. and Heineman, W. eds.), Marcel Dekker, New York, 1984, pp. 499-538.

8) Smallman, R.E.; Frost, B.R.T.; Acta Met., **1956**, 4, 611.

EXAFS STUDIES OF(100) III-V SEMICONDUCTOR SURFACES TREATED WITH $[Ru^{II}(NH_3)_5(H_2O)]^{2+}$

S. R. Lunt, S. T. Nguyen, T.L. Longin, G.A. Shreve, A. G. Sykes, A. Bansal,
G. M. Miskelly, M. J. Sailor, and N. S. Lewis*

Division of Chemistry and Chemical Engineering
California Institute of Technology
Pasadena, CA 91125

A major theme of the Lewis group research concerns the fundamental chemistry that happens at semiconductor/liquid interfaces. One important focus in our ongoing study of the chemical processes that occur at these interfaces has been the investigation of the nature of the recombination sites at semiconductor surfaces, in particular those of Group III-V semiconductors. Previous work in our group has found that several transition metal complexes that bind to the surface of GaAs. This binding produces remarkable passivation of surface recombination in which the metal species function as electrocatalysts for hole transfer into solution.[1,2] Subsequent investigations of the reaction of well-defined Co(II) and Co(III) coordination complexes with the GaAs(100) surface using a variety of surface-sensitive techniques such as XPS, RBS, XAS, and SEXAFS has led to the unequivocal identification of the resulting surface species as an extended layer of $Co(OH)_2$.[3] Cobalt is however, a unique case: surface analysis has shown that coordination complexes of Ru(II), Cr(III), and Rh(III) all react with (100) GaAs in very different manners from the analogous Co(II) and Co(III) complexes; this result is striking given that the electrocatalytic behaviors of these surface-bound metal species are all very similar to the bound cobalt species. In view of these different observations, it is clear that more structural data are needed before the interactions between GaAs and transition metal systems other than cobalt are understood. From these studies, a general structure-function relationship for all electrocatalysts should emerge that supplements our current understanding of charge transfer processes at the GaAs semiconductor/liquid interface. This knowledge should allow the design of more efficient photovoltaic cells based on this junction.

Of all the other transition metal complexes investigated in our laboratory, the reaction of $[Ru^{II}(NH_3)_5(H_2O)]^{2+}$ and GaAs is particularly interesting. Preliminary XPS and RBS experiments have shown that submonolayer coverages of Ru result when GaAs(100) is exposed to a solution of this compound. Also, since the ammine ligands are less labile than the aquo ligand, this compound is expected to react with the GaAs surface in a selective fashion by substitution of the aquo ligand with a surface atom. The unique chemistry of this system, coupled with the low coverage of bound Ru make this system ideally suited for a comprehensive study using SEXAFS. Such experiments are crucial in our investigation because they provide us with important structural data such as the oxidation state of the metal present on the surface as well as its coordination sphere.

During our most recent run, we continued our attempt to elucidate the structure of the surface-bound Ru species in the reaction of GaAs(100) with $[Ru^{II}(NH_3)_5(H_2O)]^{2+}$. Because Ga and As are similar in their scattering power, we had also planned to study the interaction of $[Ru^{II}(NH_3)_5(H_2O)]^{2+}$ with InAs and GaP surfaces. $[Ru^{II}(NH_3)_5(PPh_3)]^{2+}$ and $[Ru^{II}(NH_3)_5(AsPh_3)]^{2+}$ were used as models for the interaction of the $Ru(NH_3)_5^{2+}$ core with III-V semiconductor surfaces. To provide calibration for the oxidation state of surface species, powder XAS spectra of $[Ru^{II}(NH_3)_6]Cl_2$ and $[Ru^{III}(NH_3)_6]Cl_3$ were also obtained. Finally, a powder XAS spectrum of $RuSe_2$ was collected as model for a Ru center surrounding by heavy scatterers.

Model complexes were synthesized according to literature procedures.[4] $[Ru^{II}(NH_3)_6]Cl_2$ and $[Ru^{III}(NH_3)_6]Cl_3$ were obtained from Aldrich Chemical Co. and used as received. XAS spectra of the model complexes were obtained in transmission mode on powder samples (10% complex : 90% BN

w/w). The samples were sealed under inert atmosphere using Mylar tape. SEXAFS experiments were conducted only on GaAs and InAs(100) surfaces. (Unfortunately, repeated problems with our experimental set up in addition to intermittent beam crashes prevented collection of data for the GaP sample). The $[Ru^{II}(NH_3)_5(H_2O)]^{2+}$ was dissolved in 0.1M H_2SO_4(aq) to make a 0.01M solution. Each 1"x1" etched wafer of the semiconductor was exposed to this solution for 40 minutes. The etching of the semiconductor surface and subsequent exposure of this surface to the [Ru] solution was performed under an argon atmosphere, and the wafer was then placed in a Kapton-covered cell which was continually purged with argon during the course of the SEXAFS data collection. XPS analysis of a control sample before the experiment showed a very small amount of surface oxide that could be attributed to the air exposure during transfer to the XPS analysis chamber. Due to an instrumental problem, a post-SEXAFS XPS analysis could not be performed to check for surface oxidation after data collection.

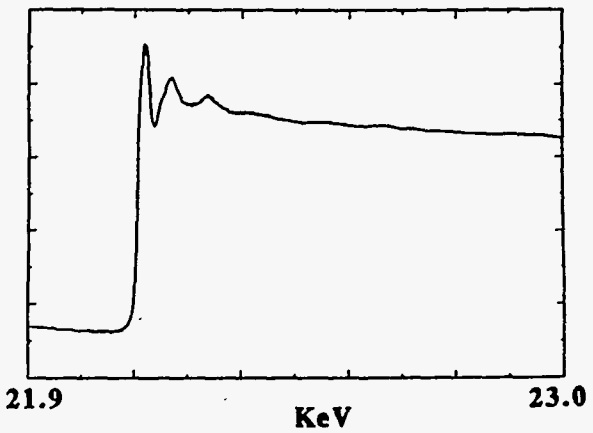

Figure 1 X-ray absorption data taken at room temperature for $[Ru^{II}(NH_3)_6]Cl_2$. The data was collected in transmission mode.

The transmitted X-ray signals from the powder samples were detected via the use of a gas ionization detector. The Ru K_α fluorescence data from the SEXAFS experiments were collected by a solid state Ge detector at a low angle to surface normal. The raw data for the $[Ru^{II}(NH_3)_6]Cl_2$ model and the Ru-exposed GaAs are shown in figures 1 and 2. The resulting spectra were analyzed using $[Ru^{II}(NH_3)_6]Cl_2$ as a first approximation model to determine scattering amplitudes and phase factors. The chemical shift data indicate that the oxidation state of Ru on InAs remains +2 while that of the species on GaAs changes to either +1 or 0. This observation is very puzzling in light of the initial data that we had obtained from a prior run. Preliminary fits of the first shell for Ru on GaAs do not match well at high k values, indicating that there maybe several heavy scatterers (such as Ga or As) in the coordination sphere of the Ru. Although the InAs data looked very promising at first, a closer investigation revealed abnormal variations in the background from one spectra to another that prevented achieving an acceptable signal to noise ratio so that the SEXAFS data could be analyzed. The average of some of these spectra for InAs is shown in figure 3.

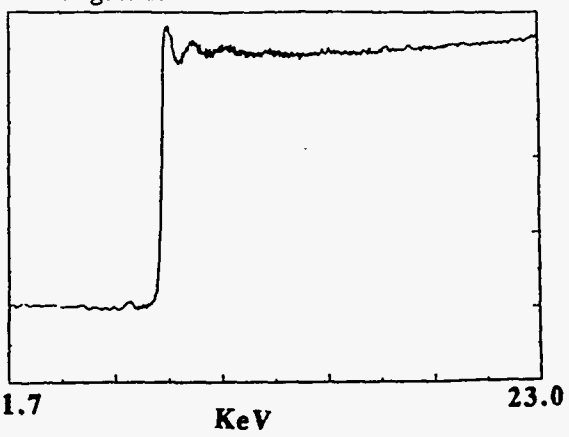

Figure 2 X-ray absorption data taken at room temperature for (100) GaAs which had been exposed to $[Ru^{II}(NH_3)_5(H_2O)]^{2+}$. The data was collected in fluorescence mode.

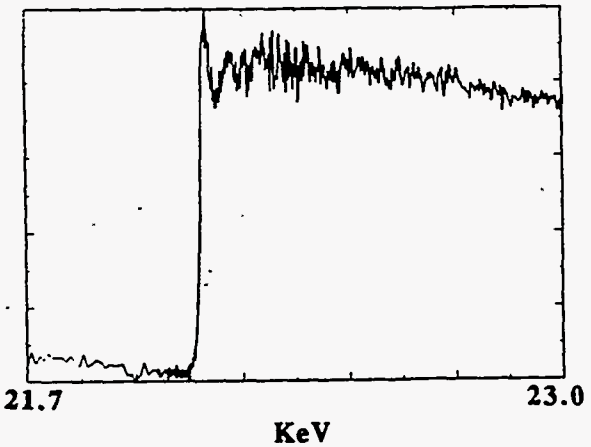

Figure 3 X-ray absorption data taken at room temperature for (100) InAs which had been exposed to $[Ru^{II}(NH_3)_5(H_2O)]^{2+}$. The data was collected in fluorescence mode.

At present, our available experimental data require additional runs to completely elucidate the surface chemistry in this system. If $[Ru^{II}(NH_3)_5(H_2O)]^{2+}$ reacts with all of the different III-V semiconductor surfaces in the same manner, then a comparison of the SEXAFS spectra of Ru on GaAs, InAs, and GaP should reveal the bonding mode of Ru on the (100) surface of these

semiconductors. If Ru-As is the primary bonding mode, the SEXAFS of InAs and GaAs should be identical to each other but different from that of GaP. On the other hand, if Ru-Ga is the primary binding mode then the SEXAFS of GaP and GaAs should be very different from that of InAs. Lastly, if the main binding mechanism of Ru to III-V semiconductor surfaces is through a surface oxygen bridge, the SEXAFS would be identical for all three surfaces. We look forward to our next run when more reliable data can be obtained, particularly due to the availability of a more stable and brighter beam from the new injector.

Acknowledgements

We would like to thank G. Ryba and B. Tsai of Caltech for help in this research. Helpful discussions with Drs. B. Hedman and A. Cox of SSRL are gratefully acknowledged. We thank Drs. T. Chevalier and A. Winston for their help with computers and Mr. Hal Tompkins and his staffs for their help with the electronic equipment during our experiments. Material were kindly provided by Dr. D. Miller of Penn State University (InAs) and Dr. L. Joyce of Semia Corp. (GaP). We also thanks Dr. J. Gordon of IBM Almaden for the use of equipment and many helpful discussions.

References

1. a) Tufts, B. J.; Abrahams, I. L. ; Santangelo, P. G.; Ryba, G. N.; Casagrande, L. G.; Lewis, N. S. *Nature (London)* **1987**, *326*, 861. b) Tufts, B. J.; Abrahams, I. L. ; Casagrande, L. G.; Lewis, N. S. *J. Phys. Chem.* **1989**, *93*, 3260.
2. Abrahams, I. L. ; Casagrande, L. G.; Rosenblum, M. D.; Rosenbluth, M. L.; Santangelo, P. G.; Tufts, B. J.;.Lewis, N. S. *Nouv. J. Chem.* **1987**, *11*, 157.
3. Tufts, B. J.; Abrahams, I. L. ; Caley, C. E.; Lunt, S. R.; Miskelly, G. M.; Sailor, M. J.; Santangelo, P. G.; Lewis, N. S.; Hedman, B. M.;Roe, A. L.; Hodgson, K. O. *J. Am. Chem. Soc.* **1990**, *112*, 5123.
4. a) $[Ru^{II}(NH_3)_5(H_2O)]^{2+}$ was synthesized according to Kuchner, C. G.; Taube, H. *J. Am. Chem. Soc.* **1976**, *98*, 689. b) $[Ru^{II}(NH_3)_5(PPh_3)]^{2+}$ and $[Ru^{II}(NH_3)_5(AsPh_3)]^{2+}$ were synthesized according to a modification of the procedures reported by DeRezende, J. M.; Franco, D. W. *Trans. Met. Chem.* **1987**, *12*, 267-270. c) $RuSe_2$ was made following a procedure by Murray, J. J.; Heyding, R. D. *Can. J. Chem.* **1967**, *45*, 2675 and Bennett, S. L.; Heyding, R. D. *Can. J. Chem.* **1966**, *44*, 3017.

In Situ X-Ray Studies of OMVPE Growth

P.H. Fuoss, F.J. Lamelas and P. Imperatori
AT&T Bell Laboratories

D.W. Kisker and G.B. Stephenson
IBM Research Division

S. Brennan
Stanford Synchrotron Radiation Laboratory

The past ten years have seen remarkable progress in understanding the atomic level mechanisms of epitaxial growth and, in particular, the growth of semiconductor crystals by ultra-high vacuum deposition techniques such as molecular beam epitaxy (MBE). A common assumption is that this extensive knowledge is directly transferable to non-UHV processes such as organometallic vapor phase epitaxy (OMVPE). However, detailed theories of these processes have not been developed and only sketchy experimental results are available for OMVPE growth.[1] [2]

In situ x-ray analysis holds great promise for the detailed understanding of these technologically important processes. Over the last four years and, particularly, in 1991, great strides were made in developing techniques to allow such *in situ* analysis.

1. Experimental Techniques

During 1991, our experiments concentrated on the OMVPE growth of GaAs using tertiarybutylarsine (TBAs) and trimethylgallium (TMG) as the organometallic source materials. The growth was performed in a specially designed reactor that has been described elsewhere.[3] This reactor must grow high quality semiconductor films while simultaneously allowing the transmission of x-rays through a wide angular range. For our reactor, this is done by having a small incident beryllium window and a large beryllium window for monitoring the x-ray fluorescence and the x-rays diffracted by the surface. The necessary sample rotations are coupled into the reactor through a differentially pumped rotary seal. This reactor is mounted inside a portable gas cabinet along with the gas handling system, temperature baths, etc. so that it is easily installed at the synchrotron radiation source.

The x-ray absorption and x-ray scattering measurements were performed on BL 10-2 with the 15 period hybrid wiggler operating at 1.4 Tesla. During these experiments, a typical stored current was ≈40 mA at 3.0 GeV. During this experiment, a monochromator heating problem, since corrected, was observed which made the incident flux current independent above 20 mA. We expect that with the use of the new SPEAR low-emittance lattice and stored currents of 100 mA will increase our signal rates by an order of magnitude.

Both the surface sensitive x-ray absorption measurements and the x-ray scattering measurements were performed in a grazing incidence geometry where the incident beam was totally reflected from the surface at a small grazing angle of ≈0.2°. The GIXS geometry and surface sensitive x-ray scattering have been reviewed extensively.[4]

The x-ray data were collected with CAMAC data acquisition modules and a MicroVAX II computer running the VMS operating system and the SSRL implementation of the "SUPER" diffraction program.[5] Deadtime in this system was ≈50 msec per point which limited our time-resolved measurements. Current implementations have reduced this deadtime to ≈10 msec. This improvement should increase our effective count rate by a factor of two.

2. Experimental Results

The experimental results described here will be presented in two sections. First we will describe preliminary work using x-ray absorption spectroscopy to investigate the gas phase dynamics and adsorption of TBAs onto InP (001) surfaces. The second part will discuss time-resolved x-ray scattering studies of the layer-by-layer homoepitaxial growth of GaAs.

The complicated gas flows and potential chemical reactions in the vapor are two of the significant differences between chemical vapor deposition and UHV techniques. This problem has been studied extensively but a simple, non-invasive probe has not been developed.[1] The use of x-ray absorption analysis holds great promise in this area.

Figure 1 shows the As K_α fluorescence from the gas phase of our reactor during switching transients. This fluorescence rate data shows the relative concentration of As in the reactor. The decay of the As signal can be accurately fit by assuming the reactor is well-mixed. Such information can easily be obtained with a spatial resolution of ≈0.1mm×0.1mm×1cm (the last dimension is along the x-ray beam) and should allow detailed chemical mapping of gas phase hydrodynamics.

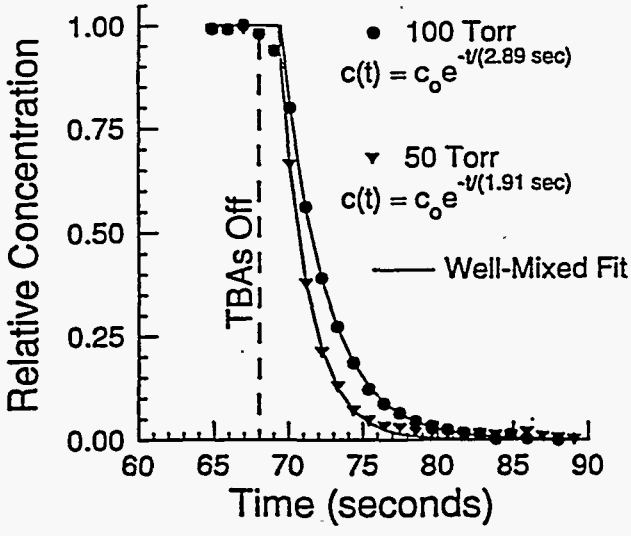

Figure 1: The decay of the arsenic concentration in the reactor following the shutoff of the TBAs flow is shown here. The data points are determined from the As K_α fluorescence and the fit assumes a well mixed reactor nozzle.

X-ray absorption spectroscopy can also be used to analyze surface adsorption and stoichiometry of atoms on surfaces. Figure 2 shows the fluorescence signal from As adsorbed on an InP (001) surface. Under a constant flow of TBAs the signal rate is constant at 150°C. When the temperature is raised to 220°C the slope becomes positive indicating that As is being adsorbed. (The sharp downward discontinuity at each temperature change is due to small motions of the sample.) Adsorption continues until 250°C where As starts desorbing from the InP surface. This and x-ray scattering results show that TBAs decomposes on the InP surface at ≈200°C, a surprisingly low temperature when compared to the dissociation temperature of ≈450°C observed for TBAs in a H_2 carrier gas.[6]

In addition to these fixed energy experiments, x-ray spectroscopies such as EXAFS and NEXAFS can be used to probe the chemical state of the reactant vapor and for atoms on surfaces. It is still unclear whether these techniques can be widely applied to such high temperature processes but we have been able to monitor

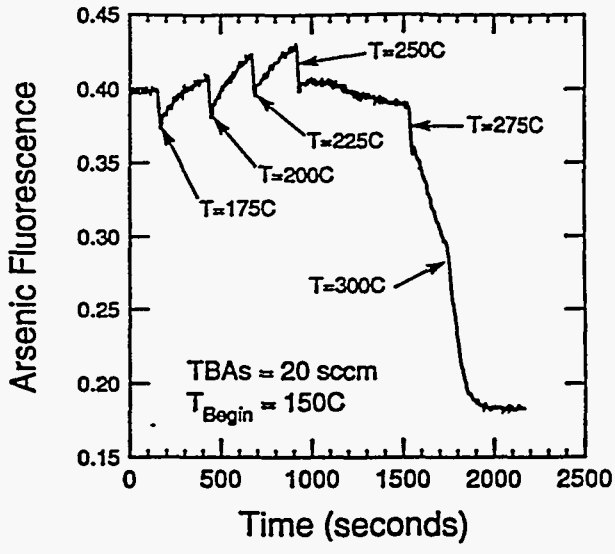

Figure 2: The As K_α fluorescence signal from an InP(001) substrate during dosing with TBAs. Note that the rate of change of the As K_α fluorescence increases until 250°C and then starts to fall. These and x-ray scattering results show that TBAs is decomposing on the InP surface at low temperatures and is being desorbed at higher temperatures. For comparison, TBAs decomposes at ≈450°C in the gas phase.

the chemical state of Ga at concentrations appropriate for OMVPE growth at room temperature.

A technique which has matured faster is the use of x-ray scattering to probe surface structures during OMVPE growth. Figure 3 shows data from a time-resolved experiment looking at homoepitaxial growth at 540°C. This measurement is monitoring the bulk-forbidden, (110) anti-Bragg reflection. Since this reflection is forbidden because of destructive interference from successive GaAs bilayers (a Ga layer and an As layer), it has maximum strength for a filled, atomically smooth surface and zero intensity if the surface of the substrate consists of half-filled layers.

Thus, Figure 3 can be interpreted as follows. Initially, the (1,1,0.04) reflection has a strong intensity showing that the surface is atomically abrupt. During the entire growth run, the TBAs source is on and, ten seconds into the experiment, the TMG source is turned on. After a latency of ≈2 seconds for gas to flow through the piping, the TMG partial pressure starts to build and successive layers of GaAs are grown. Twenty seconds into the run the TMG is turned off and growth is exponentially turned off as the reactor purges. The surface is left in a mixed state where different regions of the sample are at different phases of a growth cycle because of non-uniform growth. This disorder slowly anneals out and

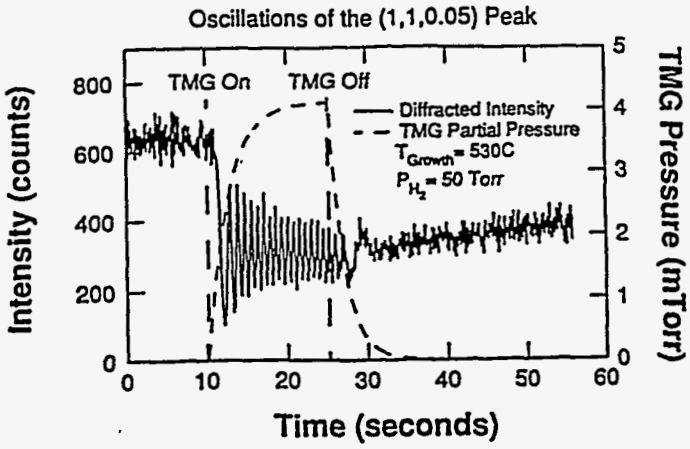

Figure 3: X-ray intensity oscillations of the (1,1,0.05) diffraction peak during a typical growth run at 540°C. The dashed line shows the partial pressure of TMG reaching a peak of 4 mTorr. The partial pressure of TBAs was a constant 150 mTorr and the total reactor pressure was 50 Torr. Twelve atomic bilayers or 34Å of GaAs were grown in this cycle.

the x-ray intensity recovers to its initial value after five minutes (only the initial portion of the recovery is shown here).

Figure 4 shows similar patterns for different growth temperatures. At 520°C the growth rate is 48 layers/minute and increases rapidly with temperature, saturating at 90 layers/minute at higher temperature. This temperature dependence suggests that growth is being limited by surface chemical reactions and not by mass transport to the surface at low temperature.

This hypothesis can be tested by measuring the growth rate dependence on TMG partial pressure while keeping the TMG/TBAs ratio constant. Figure 5 shows that the growth rate dependence on TMG partial pressure is accurately fit by a Langmuir-Hinshelwood model.[7] That is, the TMG is saturating the available surface sites and this saturation is limiting the growth rate. Since chemical reactions in the vapor would not show this dependency, this result shows that surface chemical reactions are limiting growth in this process variable range.

The final example of results obtained in 1991 is given in Figure 6. This figure is a contour plot of diffuse scattering obtained near the GaAs (110) peak during the first cycle of growth in Figure 3. This diffuse scattering comes from the growing islands that nucleate, grow to a characteristic size and then gradually coalesce. The peak at $\theta=\pm 0.8°$ at a time of 0.9 seconds into the run shows that the nucleation of islands is not random. That is, the positions of the nuclei are correlated, presumably by

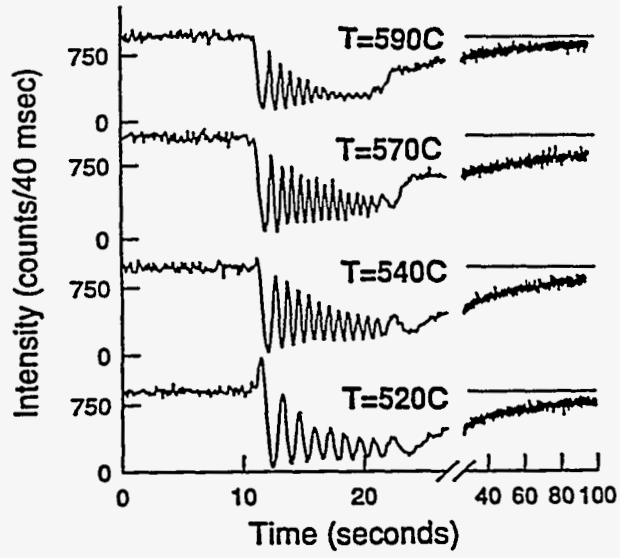

Figure 4: X-ray intensity oscillations of the (1,1,0.05) diffraction peak at the series of temperatures. Note the qualitative change in the onset of growth between 520°C and 540°C. At 520°C there is a consistent increase in the diffracted signal as growth starts while at higher temperatures the signal almost always decreases as growth starts. Note also that the growth rate is significantly slower at 520°C.

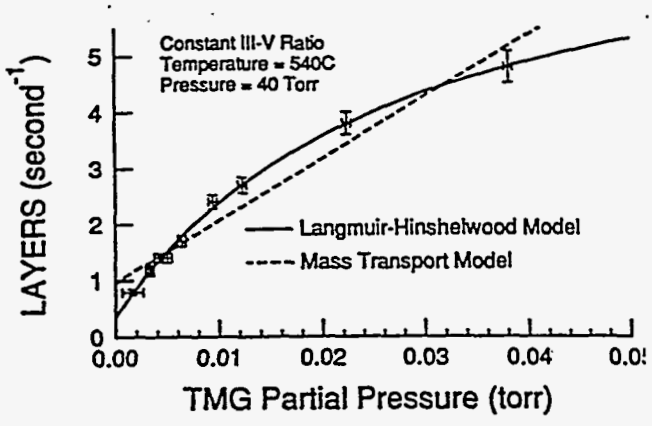

Figure 5: A plot of the growth rate versus TMG partial pressure for growth with a constant TBAs/TMG ratio. The growth rate is clearly not the linear increase predicted by mass transport and is instead accurately fit by a Langmuir-Hinshelwood theory. This shows that surface chemical reactions are limiting the growth rate.

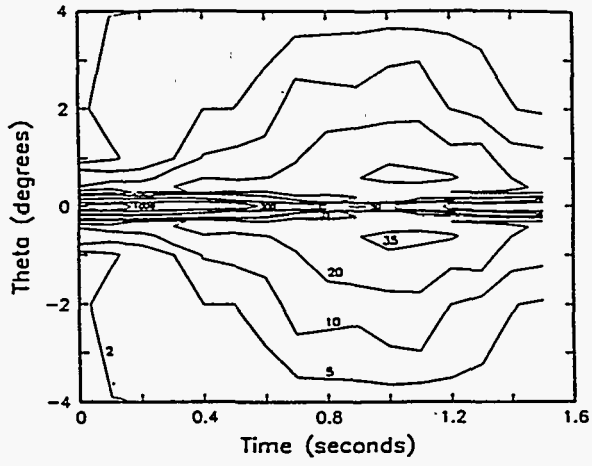

Figure 6: The diffuse scattering associated with the (1,1,0.05) diffraction peak during the first cycle of growth. These data are a composite of ten growth runs at different, fixed values of $\Delta\theta=\theta_{110}-\theta$. The inset shows the peak intensity versus time.

depletion or denuded zones around existing nuclei.

3. Summary of Current Accomplishments

These results described in this paper are only a small fraction of those obtained in three weeks of experiments at SSRL. In addition, we have examined surface cleaning and preparation processes with and without TBAs stabilization for both InP (001) and GaAs (001) surfaces. We have determined the surface reconstructions present on those surfaces over a wide range of temperatures and gas flows. For example, we found that the structure of the GaAs(001) arsenic stabilized surface was the same as that found in MBE experiments but, unlike MBE, this reconstruction disappeared during growth.[8] We have examined the kinetics of alternate layer and migration enhanced epitaxies. And, finally, we have performed a time-resolved, x-ray diffuse scattering study monitoring the size and distribution of islands during layer-by-layer growth.[9] The ability to obtain such wide-ranging information about the microscopic mechanisms of OMVPE growth demonstrates the power of x-ray analysis for the *in situ* analysis of growth.

1. G.B. Stringfellow, *Organometallic Vapor Pha Epitaxy: Theory and Practice* (Academic Press, S Diego, 1989).
2. Andrew Zangwill, *Physics at Surfaces*, (Cambrid University Press, New York, 1988).
3. S. Brennan, P.H. Fuoss, J.L. Kahn and D.W. Kisk Nucl. Instr. and Meth., A291, 86(1990).
4. P.H. Fuoss and S. Brennan, Ann. Rev. Mater. Sc 20, 365(1990).
5. S. Brennan, Rev. Sci. Instrum. 63, 992 (1992).
6. R.M. Lum, J.K. Klingert and D.W. Kisker, J. Ap Phys., 66, 652(1989).
7. T.R. Olmstead and Klavs F. Jensen, Chemistry Materials, 2, 39(1990).
8. F.J. Lamelas, P.H. Fuoss, P. Imperatori, D. Kisker, G.B. Stephenson and S. Brennan, Submit to Applied Physics Letters, 1992.
9. P.H. Fuoss, D.W. Kisker, F.J. Lamelas, G Stephenson, P. Imperatori and S. Brenn Submitted to Phys. Rev. Lett., 1992.

POLARIZED S K-EDGE XAS STUDIES OF BIS(ETHYLENETHIOUREA)GOLD(I) CHLORIDE HYDRATE: A MODEL FOR THE METAL-SULFUR INTERACTION IN PHOTOGRAPHIC MATERIALS

Jane G. DeWitt,[1] Teresa A. Smith,[2] Britt Hedman,[3] and Keith O. Hodgson[1]

[1] Department of Chemistry, Stanford University, Stanford, CA 94305
[2] Eastman Kodak Co., Imaging Research Laboratories, Rochester, NY 14650
[3] Stanford Synchrotron Radiation Laboratory, Stanford University, Stanford, CA 94309

Introduction

Several crucial elements of the photographic system including spectral sensitizing dyes, surface modifying agents, and chemical sensitization centers contain sulfur atoms incorporated in species on the surface of the photoactive silver halide microcrystals. These centers are involved in surface electron and energy processes and are, therefore, of general interest for their photophysical properties.

Sulfur K-edge x-ray absorption spectroscopy has been used to characterize a variety of compounds relevant to the photographic system [1,2]. Measurements on merocyanine and cyanine dye samples revealed sharp absorption edge features which are characteristic of the electronic and geometric environment of the S atoms. The white-line feature in spectra of metal-sulfur complexes is much more intense than that in the spectra of the corresponding non-metal-complexed ligands, suggesting that the interaction between sulfur and metal atoms in the photographic system can be followed by using XAS.

Polarized single-crystal XAS studies can be used to determine the orientation-dependence of absorption edge features in anisotropic centers. Oriented single-crystal spectra of representative merocyanine and cyanine dye nuclei have shown that these features are polarized along specific molecular bonds and can therefore be used to determine the orientation of dye molecules in well-characterized systems [1,2].

As part of our ongoing project to characterize the interaction between sulfur and metals in photographic samples, we have measured the sulfur K-edge x-ray absorption spectrum of bis(ethylenethiourea)gold(I) chloride hydrate [3], both as a powder and as an oriented single-crystal, and the powder spectrum of the ligand, ethlyenethiourea. These studies will provide insight into the nature of the interaction between the sulfur and metal atoms.

Experimental

Spectra were measured at room temperature and detected as excitation fluorescence using a N_2-filled Stern/Heald/Lytle detector [4]. The data were collected on the focused 54-pole wiggler beamline 6-2 in low magnetic field mode (5 kG) at SSRL using a Si(111) double-crystal monochromator. SSRL was operated in dedicated mode (3.0 GeV, and 40 - 90 mA). Harmonic rejection was achieved by detuning the monochromator 25% at 2740 eV. Air absorption of the incident beam was minimized by using a He beam path. Pre-oriented single crystal data were measured using a sample holder with χ fixed at 180° and full ϕ rotation. Solid samples were measured as finely ground thin powders on mylar tape.

Results and Discussion

Our previous studies of photographic dye molecules have shown that the presence of a terminal S, such as the thione group of merocyanine dye nuclei, is characterized by a pre-edge feature at ~ 2471 eV [1]. Single crystal polarized XAS studies of 2-thiohydantoin, which contains a thione group, showed that the 2471 eV feature is polarized perpendicular to the C=S bond and therefore involves a transition to a S $p\pi^*$ orbital [1]. This feature shifts to higher energy and becomes less resolved from the white-line feature with increasing negative charge on the terminal sulfur atom. In the powder spectrum of ethylenethiourea, the feature attributed to the presence of the terminal sulfur occurs at 2472.1 eV (Figure 1).

In spectra of metal-sulfur complexes, the pre-edge feature is absent, suggesting a direct interaction between the metal and the terminal S occurs through the S $p\pi^*$ orbital [1]. In addition, the white-line feature of the ligand increases in intensity and broadens, sometimes splitting

into two features [1]. Both of these trends are seen in the powder spectrum of the bis(ethylenethiourea)gold(I) (Figure 1). Upon complexation with gold, the 2472.1 eV feature is no longer resolved from the white-line feature at 2473.4 eV, the white-line feature increases in intensity, and a shoulder appears at 2475.1 eV.

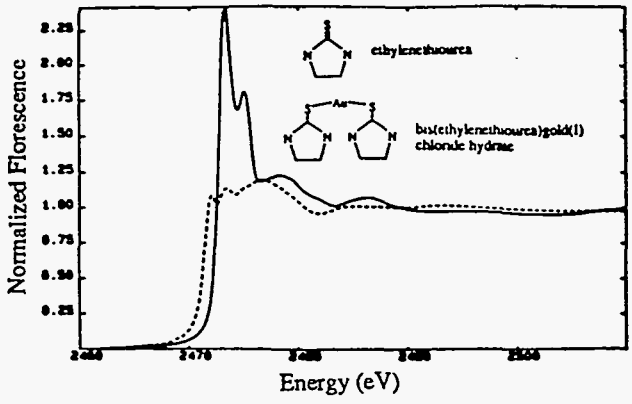

Figure 1. The S K-edge spectra of bis(ethylenethiourea)gold(I) chloride hydrate (—) and ethylenethiourea (– – –).

Polarized XAS studies of bis(ethylenethiourea)gold(I) provide additional insight into the nature of the interaction of the metal ion and the terminal sulfur group. The single-crystal oriented spectra are compared to the powder spectrum in Figure 2. The polarization vectors were defined as follows: X was defined to be in the plane of the ring along the average C-S_{thione} bond, Z was defined to be the average of the ligand plane normals, and Y, defined to be the cross-product of X and Z, is directed roughly along the S-Au-S bond. As a result of this definition, the Y polarization will have some X character in it.

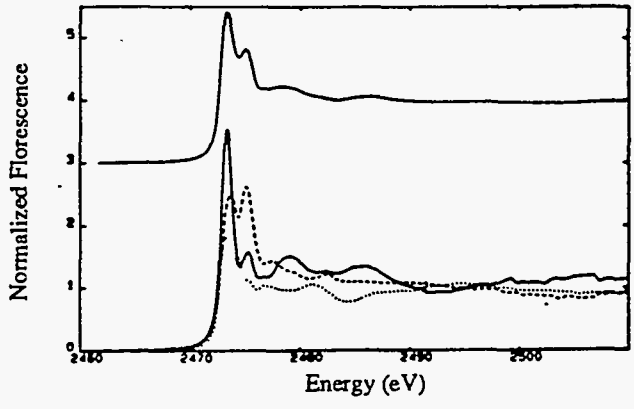

Figure 2. The powder spectrum (top) of bis(ethylenethiourea)gold(I) chloride hydrate and the single-crystal spectra (bottom) corresponding to polarization along X (– – –), Y (—) and Z (· · · ·).

The 2473.4 eV feature is polarized primarily in the plane of the ring system. The feature in the Y-polarized spectrum occurs at 2473.4 eV, but in the X-polarized spectrum, the feature occurs at slightly higher energy, 2473.8 eV. This split contribution to the white-line feature accounts for the broadening to the high energy side seen in the powder spectrum. This suggests that the white-line feature can be attributed to transitions to two final states, one with with Au-S σ^* character and one with C-S σ^* character. There is some contribution to the 2473.4 eV feature from the Z, or out-of-plane, orientation. No contribution to the white-line feature is seen in the Z-polarized spectrum of 2-thiohydantoin, therefore the contribution seen in bis(ethylenethiourea)gold(I) is due to the metal-terminal S interaction. We cannot say at this time if the feature in the Z-polarized spectrum is a new feature or simply the 2472.1 eV thione feature shifted to higher energy as a result of complexation with the metal ion. The shoulder in the powder spectrum at 2475.1 eV is strongly polarized along the X direction, suggesting that this feature arises from transitions to a final state with predominantly C-S σ^* character. The small shoulder at this energy seen in the Y-polarized spectrum is probably due to the X character in that orientation. The Y-polarized spectrum has very strong EXAFS features due to the interaction between the metal and sulfur atoms. These studies will help us determine the nature of the interaction between sulfur-containing compounds and metal halide microcrystals on surface samples.

Acknowledgements

This work is supported by research funds from Eastman Kodak Company. The data were measured at the Stanford Synchrotron Radiation Laboratory which is supported by the Department of Energy, Division of Materials Sciences and Division of Chemical Sciences, and by the National Institutes of Health, Biomedical Resource Technology Program, Division of Research Resources.

References

1. DeWitt, J. G.; Smith, T. A.; Hedman, B.; Hodgson, K. O. *Stanford Synchrotron Radiation Laboratory Activity Report*, **1989**, 60.
2. DeWitt, J. G.; Smith, T. A.; Hedman, B.; Hodgson, K. O. *Stanford Synchrotron Radiation Laboratory Activity Report*, **1990**, 55.
3. Jones, P. G.; Guy, J. J.; Sheldrick, G. M. *Acta Cryst.*, **1976**, *B32*, 3321.
4. (a) Stern, E.; Heald, S. *Rev. Sci., Instrum.*, **1979**, *50*, 1579. (b) Lytle, F. W.; Greegor, R. B.; Sandstrom, D. R.; Marques, E. C.; Wong, J.; Spiro, C. L.; Huffman, G. P.; Huggins, F. E. *Nucl. Instr. and Meth.*, **1984**, *226*, 542.

DIRECT SCATTERING STUDIES OF LIQUID SURFACES

J.L. Kahn
Department of Physics, Stanford University

P.H. Fuoss, F. Lamelas
AT&T Bell Laboratories, Murray Hill, New Jersey

1. INTRODUCTION

As electronic devices get smaller and smaller, surfaces become increasingly important to our understanding of these devices. The structure of thin layers and surfaces has become a field of great interest. We are studying a monolayer of liquid lead on a germanium (111) surface. We hope to gain insight into how a crystalline surface affects the structure of a very thin liquid layer.

The Pb/Ge(111) phase diagram has been studied extensively by LEED[2], RHEED[3], and x-ray scattering[4]. The earlier x-ray studies see evidence of a monolayer liquid but do not go into detail of the structure of the liquid . We hope to be able to more clearly describe the liquid structure, and to understand more about the effect of a crystal structure on a thin liquid overlayer.

2. EXPERIMENT

The reasons for choosing Pb/Ge(111) are several. Firstly, the mutual solid solubility of Pb and Ge are negligible[5], so the lead stays on the surface. Also, the desorption of Pb is small at the temperatures used (below 250° C) although care must be used at higher temperatures. We periodically cooled the sample to check the Pb coverage to ensure minimal evaporation. Another reason to use this system is the relative ease of preparing clean, flat Ge(111) surfaces and keeping the Pb/Ge(111) uncontaminated in vacuum. The reactivities of both are less than that for aluminum, the last surface melting material we tried. The earlier work, particularly that of Grey[4], has been immeasurably helpful for knowing how much lead has been deposited on the substrate. Finally, the strength of Pb as a scatterer helps to raise the count rate for just a single monolayer of liquid.

This experiment was performed at the NSLS AT&T Bell Laboratories beamline X16A. The surface diffractometer is described in detail elsewhere[6]. The important features of the UHV chamber are its surface capabilities. The Pb can be deposited in the same vacuum system with the x-rays. Both Auger spectroscopy and low energy electron diffraction (LEED) help assure a clean and ordered sample. For the x-rays, the grazing incidence geometry is crucial for surface sensitivity of one monolayer.

A germanium crystal, oriented to within 0.1° of the (111) surface, was mounted in the X16A UHV surface diffractometer, with a base pressure of about 5×10^{-10} torr. The Ge substrate was first cleaned by alternating cycles of Ar sputtering and annealing at 750°. When clean, the sample showed no oxygen or carbon above background using Auger spectroscopy, and the clean germanium c(2x8) room temperature reconstruction was seen with LEED. This was checked with the x-rays. Then, we deposited about 2 monolayers of lead from an evaporator at a rate of about 1 monolayer per minute. After a quick anneal at 250°, a c($\sqrt{3}$x$\sqrt{3}$) reconstruction was seen with both LEED and the x-rays. The Ge c(2x8) reconstruction disappears as soon as Pb is deposited, and doesn't reappear until annealing again. By heating the sample to desorb lead, and checking the relative intensities of several of the c($\sqrt{3}$x$\sqrt{3}$) reconstruction peaks, we could tune the Pb coverage by comparison with the work done by F. Grey[4]. The experiment was performed at a

coverage of about 1.25-1.30 Pb atoms per Ge atom, which has a low enough melting temperature to avoid excessive Pb evaporation. (See Figure 1.) After melting the Pb, occasional checks for no evidence of the c(√3x√3) reconstruction show that we have not lost enough lead to raise the melting point.

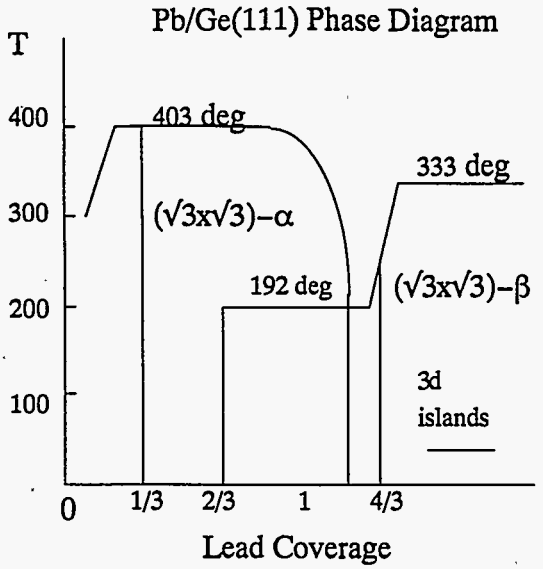

Figure 1: The Pb/Ge(111) phase diagram. There are two c(√3x√3) phases. In the region of this experiment, the melting temperature changes rapidly with temperature.

Using a grazing angle of 0.17°, which is below the critical angle for both Pb and Ge at the energy used, 11 keV, we scanned the surface to look for liquid-like scattering. (See Figure 2) There is clear evidence of a monolayer of liquid, with a first peak at 2.05 inverse angstroms. This peak can be seen in all directions of reciprocal space in the plane, although it appears to have a six fold modulation, presumably caused by the substrate. Unfortunately, a second peak cannot be clearly resolved. We have not finished all analysis and more data is needed further out in reciprocal space before the liquid structure can be well described.

3. FUTURE PLANS

We hope to finish our study of the Pb/Ge(111) system during an SSRL run on beamline 10-2 in May. Using an energy above the Ge k-edge we will be able to monitor the fluorescence. This will automatically normalize the data, solving a problem we are currently having. Also, the Beamline 10 wiggler should provide an order of magnitude greater count rate than the NSLS X16 bending magnet.

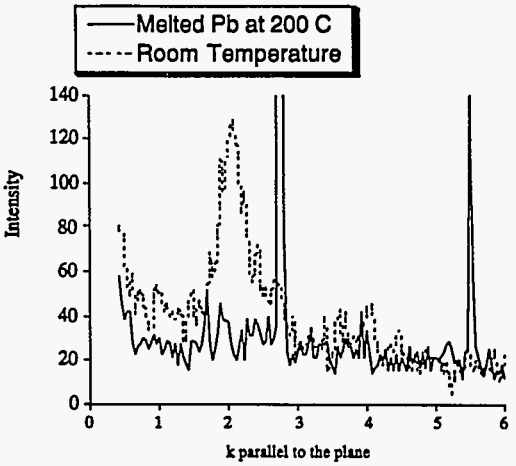

Figure 2. The dashed line is the intensity at room temperature. Note the sharp peaks near 2.8 and 5.6 inverse angstroms. These are caused by the Pb reconstruction. The dashed line shows the melted Pb intensity, with first peak at 2.05 inverse angstroms.

Further experiments include comparisons of Pb/Ge(111) to Pb on other Ge surfaces and Pb on various Si surfaces. From these experiments we should be able to understand better the effect a crystalline substrate has on a thin liquid. With this better understanding we may be able to return to the surface melting problem and learn about a fundamental property of many surfaces.

REFERENCES

[1] For examples, see: U. Breuer, O. Knauff, H.P. Bonzel, Phys. Rev. B, **41**, p.10,848-51 (1990); Joost W.M. Frenken, Peter M.J. Maree, J. Friso van der Veen, Phys. Rev. B, **34**, p.7506-16, (1986).

[2] G. Le Lay, Z. Imam, Surf. Sci. **154**, p.90-98 (1985); G. Le Lay, J.J. Metois, Appl. Surf. Sci. **17**, p.131-135 (1983); J.J. Metois, G. Le Lay, Surf Sci. **133**, p. 422-442.

[3] T. Ichikawa, Sol. Stat. Comm. **46**, (1983).

[4] F. Grey thesis, Riso National Laboratory, Denmark.

[5] M. Hansen, Constitution of Binary Alloys, p. 771 (1958) McGraw Hill.

[6] P.H. Fuoss and I.K. Robinson, Nuc. Instr. and Methods, **222**, p.164 (1984).

Sn-related DX centers in $Al_xGa_{1-x}As$

T.M. Hayes, J. Pant,* J. Zhang, and K. Pansewicz
Physics Department, Rensselaer Polytechnic Institute, Troy NY 12180-3590

D.L. Williamson
Physics Department, Colorado School of Mines, Golden CO 80401

P. Gibart
Laboratoire de Physique du Solide et Energie Solaire, CNRS, Valbonne, France

T.N. Theis and T.F. Kuech†
IBM T.J. Watson Research Center, Yorktown Heights NY 10598

Si, Se, Sn, and Te are all suitable electron donors in GaAs. When Al is substituted for Ga to form $Al_xGa_{1-x}As$ ($x > 0.2$), however, deep electron levels are formed rather than the desired shallow donor levels. These are called "DX centers." Their formation greatly reduces our ability to produce highly conducting n-type $Al_xGa_{1-x}As$ and they are widely regarded as *the* most significant impediment to the design of many useful devices based on these materials.

The electronic properties of DX centers have been characterized extensively. The large discrepancy between thermal and optical excitation energies (~1 eV) is attributed to the (occupied) DX center differing from the ionized donor site by a change in the configuration of the neighboring atoms. There has been controversy about whether the electronic properties can be explained by a small change in atom positions, or require a large lattice distortion. Experimental resolution of this question is hampered by the necessity of keeping the number of dopants below ~5×10^{18} cm^{-3}. Dopant concentrations in excess of this level lead to self-compensation and/or to the formation of impurity complexes rather than the desired isolated shallow donor or acceptor levels. The structure of isolated dopants can be determined only at lower concentrations where they dominate the distribution of dopant sites. To our knowledge, only x-ray absorption fine structure (XAFS) spectroscopy can address this structural question directly for such dilute systems.

At the start of this research program, we believed that we need only be able to distinguish between two alternative models for the DX center: nearly all the nearest neighbors of the Sn atoms are at a distance similar to the Ga-As distance; nearly all the neighboring atoms are at a distance larger by *several* tenths of an Angstrom. Measurement of an XAFS spectrum with a sufficient ratio of signal to noise to answer that question despite a donor concentration < 5×10^{18} cm^{-3} seemed technically feasible given the favorable situation of a large Z donor (Sn) in a smaller Z matrix (Al, Ga, and As).

The theoretical situation was changed in 1988 when Chadi and Chang proposed that the DX center associated with Si or S dopants in GaAs and $Al_xGa_{1-x}As$ is a negatively charged dopant atom with only three nearest neighbors [Phys. Rev. Lett. 61, 873 (1988)]. Photoexcitation of this DX center yields two conduction electrons. When ionized (i.e., positively charged), the dopant has four neighbors at the usual distance for a substitutional shallow donor site. This model can explain nearly all observed features of DX centers without elaborate

further assumptions, and has consequently become a widely favored model.

In the Chadi-Chang model, the structural differences between the positively-charged ionized donor and the negatively-charged deep center are much more subtle than in previous models for the DX center. Specifically, the only predicted change is in the *number* of nearest neighbors of the dopant: three for the negatively-charged DX configuration instead of four for an ionized shallow donor site. The distance to the nearest neighbors is essentially identical. Furthermore, even if *all* of the dopant atoms are electrically active, one half of the donors must be ionized in the ground state, giving up their electrons to the other half of the Sn dopants (which become negatively charged). Thus, the principal difference between the ground state and a state where all of the Sn atoms are in ionized shallow donor sites is a change of 12.5% in the *number* of nearest neighbors. It is well known to be very difficult to obtain the number of neighbors accurately from an XAFS spectrum, especially in a dilute system, in which the ratio of signal to noise is necessarily low. We believe nonetheless that we have designed this experiment well enough to distinguish readily between a 12% change and no change. Detection of a uniform dilation of the neighbors by a few tenths of an Angstrom would, of course, be *much* easier.

In response to the new theoretical situation, our collaborators at IBM produced two new samples in the winter of 1988/89: Sn-doped $Al_xGa_{1-x}As$ with x=0.0 and 0.22. The Sn doping level was adjusted to obtain the largest concentration of electrically active dopants while avoiding the formation of other Sn impurity configurations. The resulting dopant concentrations were believed to be in the range of 2 to 3×10^{18} cm^{-3}. The sample with x=0.22 was designed so that we could measure the Sn dopant environment in both configurations in one sample. This ought to enable the most precise measurement of any differences. Specifically, if we assume for the moment that the Chadi-Chang model is correct, we could place half of the Sn dopant atoms in the DX state by holding that sample in the dark at ~80 K. After collecting many XAS spectra in that state, we could cool the sample to ~20 K and use light-emitting diodes to photoexcite the DX centers, producing a persistent-photoconductivity (PPC) sample with nearly all Sn dopants in the positively-charged shallow donor configuration. The spectra from these two configurations of the *same sample* could be compared directly to quantify differences in Sn environment.

Unfortunately, the relative change of 12.5% in number predicted by the Chadi-Chang model is reduced further by multiplication by the fraction of Sn atoms which are electrically active. The number of active sites can be determined by Hall effect measurements. SIMS is the customary technique to measure the total concentration of Sn atoms, active and inactive. It can also be measured directly from the K-edge step height in our XAS spectrum and from the total signal in the Mössbauer spectra. From the latter two measurements, we have found that SIMS measurements on these materials frequently indicate much lower concentrations of Sn atoms than are actually present, and therefore suggest a misleadingly high fraction of electrically active dopants. Specifically, SIMS indicated that the Sn concentration was 2 to 3×10^{18} cm^{-3} in these samples, while the XAS spectra indicated quite clearly that there were in excess of 10^{19} cm^{-3} Sn atoms. The fraction of electrically active Sn dopants was therefore only ~15%, rather than the anticipated ~70%, and the change in the number of nearest neighbor atoms predicted by the Chadi-Chang model was under 2% rather than nearly 9%. It would be difficult to measure a 2% change in number with any confidence.

Our collaborators at IBM produced a new series of presumably optimal samples in the spring of 1990: Sn-doped $Al_xGa_{1-x}As$ with x=0.11, 0.23, and 0.28. The resulting dopant concentrations were again believed to be in the range of 2 to 3×10^{18} cm^{-3}. The sample with x=0.23 was designed so that we could measure the Sn dopant environment in both

configurations in one sample, while the x=0.11 and 0.28 samples were expected to have most of the Sn atoms in either shallow donor sites or DX centers, respectively. In April 1990, we were able to measure the x=0.11 and 0.28 samples only, and those measurements were made at very low photon flux. The XAFS data from the x=0.28 sample was much too noisy to analyze, but the Sn K-edge step heights did suggest appropriate concentrations of Sn atoms in both samples. The Fourier transform ϕ of the Sn K-edge XAFS from the x=0.11 sample is shown in fig. 1a.

We returned to SSRL in June 1991 and were able to measure XAFS spectra from all three samples before a fire at the accelerator ended our experiments. Analysis of that data has revealed that, although the x=0.11 and 0.28 samples do have 2 or 3×10^{18} cm^{-3} Sn, the important x=0.23 sample has nearly 2×10^{19} cm^{-3} Sn. The photoexcited carrier density in that sample is only ~2×10^{18} cm^{-3}, suggesting that only ~10% of the Sn atoms are ionizable. This reduces the change in the number of Sn nearest neighbors predicted for that sample by the Chadi-Chang model to an undetectable 1%.

The Sn K-edge XAFS data from the x=0.28 sample are again too noisy. The ϕ's from the data from the x=0.11 and 0.23 samples measured in the dark at ~80 K are shown in figs. 1b and c. The three prominent structural peaks in fig. 1a are approximately in the positions expected for the neighbors of a substitutional donor in a zincblende lattice, 2.27, 3.75, and 4.47 Å. That is not true for either of figs. 1b or c. In both cases, a new peak has arisen to the immediate right of the nearest neighbor peak (at 2.27 Å). It is obvious that the Sn environment in the x=0.11 sample has changed during the 14 months between measurements. The peaks in the ϕ from the x=0.23 sample are similar to those from the x=0.11 sample, but are not identical. We do not yet have a model for the Sn environment in these "aged" samples. We also observed slight changes in the ϕ from the x=0.23 sample when measured at ~20 K in the PPC condition, but these changes are

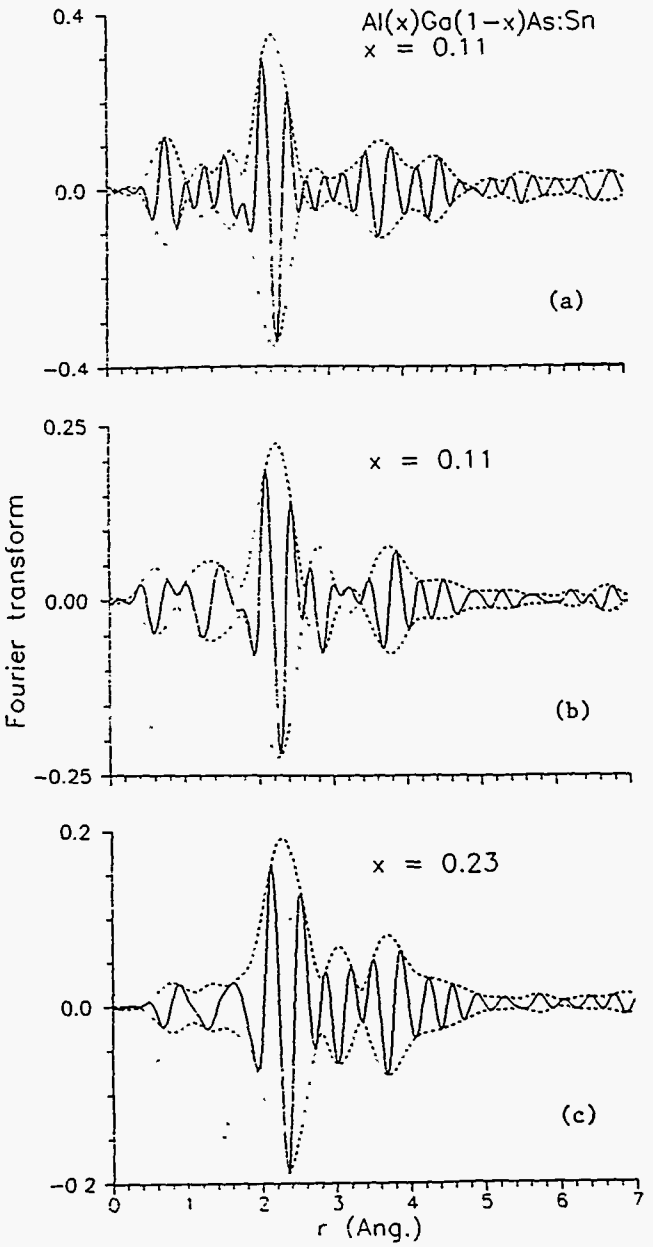

Fig. 1. The real part (solid line) and the magnitude (dashed line) of the Fourier transform of the extended fine structure $k\chi$ on the Sn K-shell absorption of (a) $Al_{0.11}Ga_{0.89}As$ doped with ~3×10^{18} cm^{-3} Sn, measured in April 1990, (b) the same sample measured in June 1991, and (c) $Al_{0.23}Ga_{0.77}As$ doped with ~2×10^{19} cm^{-3} Sn, measured in June 1991, all held at ~80 K. The data were transformed using a square window with final state electron momentum k between 2.8 and 14 $Å^{-1}$, broadened by convolution with a Gaussian of half-width 0.5 $Å^{-1}$.

quite difficult to quantify when we don't yet understand the underlying structure.

We are responding to this information by preparing a new set of samples for use in April 1992, in which the dopant concentration *will* be controlled to levels chosen to minimize the fraction of Sn in electrically inactive sites. Furthermore, we are hoping to avoid grinding our samples to a fine powder, which may well have contributed to the evolution of the Sn environment with time, by designing a new sample holder in which the sample orientation can be oscillated during the measurement. This approach has been used by G.S. Cargill, amongst others, to reduce or eliminate the very large features due to Bragg diffraction which can make useless the XAS spectrum from a single crystal sample.

Acknowledgements: This research is supported by NSF Grant Nos. DMR-9006956 and DMR-8902512. The measurements were made at SSRL which is funded by the DOE Office of Basic Energy Sciences and the NIH Biotechnology Resource Program.

*On leave from the Physics Department, Devi Ahilya Vishwavidyalaya, Indore 452001, India.
†Presently at the University of Wisconsin.

ANOMALOUS SMALL-ANGLE X-RAY SCATTERING STUDIES OF AMORPHOUS METAL–GERMANIUM ALLOYS

Marybeth Rice
Stanford University, Department of Electrical Engineering, Stanford, CA 94305

Arthur Bienenstock
Stanford Synchrotron Radiation Laboratory, Bin 69, P.O. Box 4349, Stanford, CA 94309

Soichi Wakatsuki
Laboratory of Molecular Biophysics, Oxford, U.K. OX13QU

INTRODUCTION

Small-angle X-ray scattering (SAXS), a standard tool for detecting and characterizing phase separation, often yields ambiguous results when applied to sputtered amorphous thin films. SAXS can arise from simple density fluctuations such as those associated with vacancies, voids and cracks, or from the electron density fluctuations associated with chemical composition modulation or phase separation. Both are likely components of sputtered amorphous thin films. Hence it is often difficult, if not impossible, to unravel the true nature of the intermediate or long range structure of an amorphous sample even with the aid of SAXS since different types of electron density fluctuations are indistinguishable. Here, SAXS is combined with the anomalous dispersion effect to remove this ambiguity[1] and to detect and characterize composition modulation in sputtered amorphous metal-germanium (a-M_XGe_{100-X}) thin films.

In particular, these experiments use anomalous small-angle X-ray scattering (ASAXS) to investigate the structure of a-Fe_XGe_{100-X}, a-W_XGe_{100-X}, and a-Mo_XGe_{100-X} samples as a function of metal concentration. These three systems all exist in the amorphous state over a composition range extending from pure a-Ge to approximately 70 atomic % metal. Across this range the structure changes from an open, covalently bonded semiconductor to a densely packed metal. Electronic changes accompany the structural changes. A semiconductor-metal transition is seen in all three systems at approximately 15 atomic percent metal. The a-Fe_XGe_{100-X} system also exhibits a ferromagnetic transition near 40 atomic % Fe and the a-Mo_XGe_{100-X} system becomes superconducting at 13 atomic % Mo. The purpose of this investigation is to discover whether these transitions proceed via homogeneous alloy formation or through phase separation.

EXPERIMENTAL

The data presented here were collected on the National Synchrotron Light Source (NSLS) beamline X14A in December 1989 using the SSRL Biotechnology Resource's SAXS camera equipped with a position sensitive quadrant detector[2]. Data were collected on a-Fe_XGe_{100-X} samples with 0, 5, 12, 18, 27, 30, 33, 44, 49, and 65 atomic % Fe, on a-W_XGe_{100-X} samples with 8, 20, 40, 42, and 55 atomic % W, and on a-Mo_XGe_{100-X} samples with 2, 4, 8, 14, 25, 42, and 65 atomic % Mo. Data were collected at 200, 100, 30, 20, and 10 eV below the absorption edge of each element in the a-Fe_XGe_{100-X} and a-W_XGe_{100-X} samples and at 200, 100, 30, 20, and 10 eV below the Ge edge in the a-Mo_XGe_{100-X} samples. Data collection at the Mo edge for the a-Mo_XGe_{100-X} samples was attempted but was unsuccessful. The argon gas in the position sensitive quadrant detector was more efficiently ionized by the fluorescent Ge X-rays from the a-Mo_XGe_{100-X} samples than by the elastically scattered X-rays at 20 keV. The Ge fluorescence swamped the elastic signal at the Mo edge.

The region of reciprocal space probed by these experiments ranges from $s (= 2\sin\theta/\lambda) = 0.01$ to $s = 0.1$ $Å^{-1}$. The data shown here are scaled by the intensity of the transmitted beam, are background subtracted, are corrected for the aperture of the quadrant detector, divided by the solid angle, divided by the sample thickness, and corrected for the cumulative detector responses. This procedure put the intensity of the ASAXS for all the samples on a relative scale but not on an absolute scale.

To put the ASAXS on an absolute scale, further experiments were performed in August 1991 on SSRL beamline IV-2 using the SSRL Biotechnology Resource's SAXS camera equipped with a linear position sensitive detector. Lupolen was used as a standard to put the data on an absolute scale. Data were retaken on several of the a-Fe_XGe_{100-X} samples under the same conditions as the data taken for the lupolen standard to obtain the value of the absolute intensity. The results of this undertaking are not complete and will be presented elsewhere.

RESULTS AND DISCUSSION

The most striking result of these experiments is that number density of Ge atoms is uniform across the sample for all samples with less than 30 atomic % metal. The SAXS arises from fluctuations in the number density of metal atoms. Data from the a-$Fe_{12}Ge_{88}$ sample are representative of this regime and are shown in Figures 1 and 2.

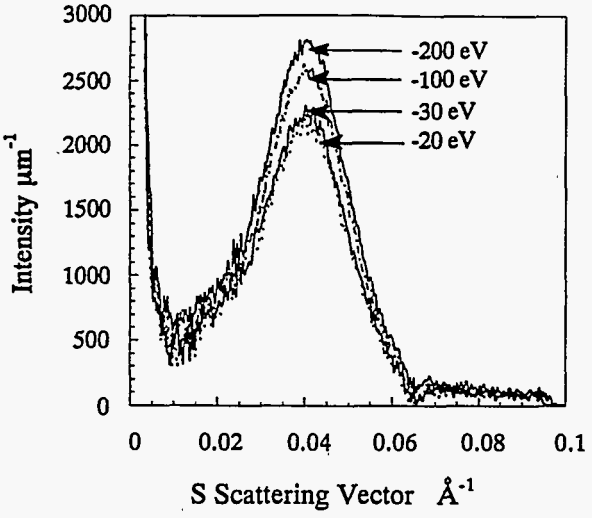

Figure 1. The intensity of scattered radiation at incident photon energies of 200, 100, 30, and 20 eV below the Fe K-absorption edge in a-$Fe_{12}Ge_{88}$. The intensity of scattered radiation decreases as the absorption edge is approached.

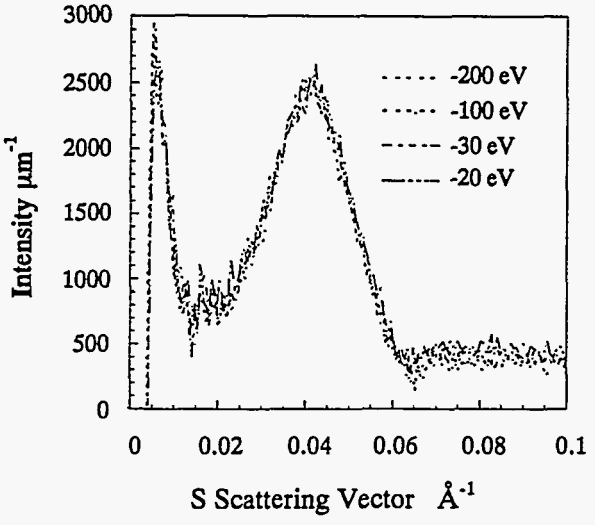

Figure 2. The intensity of scattered radiation at incident photon energies of 200, 100, 30, and 20 eV below the Ge K-absorption edge in a-$Fe_{12}Ge_{88}$. The intensity of scattered radiation remains constant as the absorption edge is approached.

The intensity of the SAXS peak decreases as the metal edge is approached from lower energies. The constant intensity of the SAXS peak with changing scattering factor near the Ge edge indicates that Ge is not contributing to the SAXS. Evidence that this is a physically reasonable result is offered by the analogous crystalline (c-) equilibrium systems. The number density of Ge atoms in c-MGe_2 and pure c-Ge is nearly identical. If the SAXS peak was caused by voids the intensity would decrease at both the metal and the Ge edges as each edge was approached from lower energies.

All three systems also exhibit, in the composition range $0<x<30$, a shift of the SAXS peak to smaller values of s with increasing metal concentration. This shift of the peaks toward smaller s with increasing x is accompanied by an increase in the intensity of the peaks. This is illustrated in Figure 3 for the a-Fe_xGe_{100-x} system.

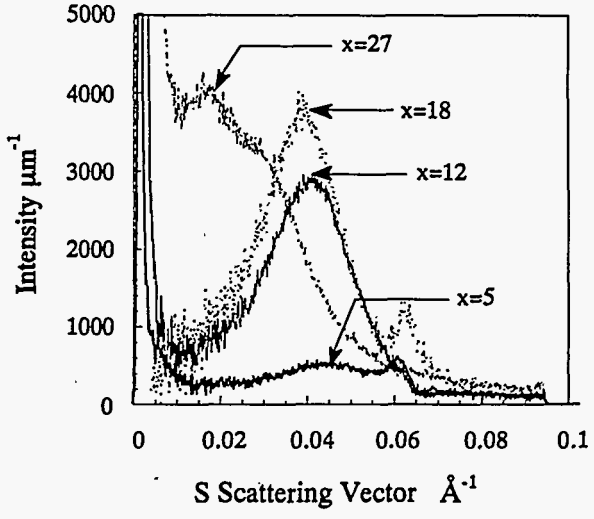

Figure 3. The variation of peak position and intensity in a-Fe_xGe_{100-x} for x values of 5, 12, 18, and 27. As the Fe content increases the peak intensity increases and the peak position decreases. The small peak near s=0.065 is due to imperfect subtraction of the kapton substrate.

These data indicate that there is very fine scale composition modulation, as opposed to cracks or voids, in the low metal concentration regime of these three systems and that the size scale of the composition fluctuations increases with increasing metal concentration.

For the a-Fe_xGe_{100-x} samples with more than 33 atomic % Fe, the X-ray absorption near-edge structure (XANES) studies of Lorentz, Bienenstock, and Morrison[3] indicate large scale phase separation into an a-$FeGe_2$-like material and an a-Fe_3Ge-like material. The ASAXS results reported here corroborate this finding.

With the assumption of large scale phase separation, the SAXS intensity, I, is related to the electron density, ρ, through the expression

$$Q = \int_0^\infty s^2 I(s)\, ds \;=\; 1/N \int_V (\rho - \rho_0)^2 dV \qquad (1)$$

where ρ_0 is the mean value of the electron density, so that $(\rho-\rho_0)$ is the deviation of the electron density from the background, and Q is the integral of the SAXS intensity over reciprocal space.

With the notation N is the number of atoms in the volume, V is the volume, f_A and f_B are the scattering factors for elements A and B, respectively, and m is the fraction of A atoms in the material, ρ_0 can be expressed as

$$\rho_0 = (N/V)\left[m f_A + (1-m) f_B\right]. \qquad (2)$$

For a binary alloy that is phase separated into two phases the electron density in phase 1 will be given by

$$\rho_1 = (N_1/V_1)\left[m_1 f_A + (1-m_1) f_B\right] \qquad (3)$$

while the electron density in phase two will be given by

$$\rho_2 = (N_2/V_2)\left[m_2 f_A + (1-m_2) f_B\right], \qquad (4)$$

where the subscripts 1 and 2 refer to the values of the variables in phases 1 and 2 respectively.

By denoting the volume fraction of the sample occupied by phase 1 as c, the integral in equation (1), which is really the sum of two integrals:

$$\begin{aligned} Q &= (1/N)\int_V (\rho - \rho_0)^2 dV \\ &= (1/N)\left\{\int_{V_1} (\rho_1 - \rho_0)^2 dV_1 + \int_{V_2} (\rho_2 - \rho_0)^2 dV_2\right\} \end{aligned} \qquad (1)$$

can be evaluated as

$$Q = (1/N)\left\{cV(\rho_1 - \rho_0)^2 + (1-c)V(\rho_2 - \rho_0)^2\right\}. \qquad (5)$$

Since ρ_0 is obviously also equal to $[(c)\rho_1 + (1\text{-}c)\rho_2]$, equation (5) can now be expressed as

$$Q = (V/N)c(1-c)(\rho_1 - \rho_2)^2. \qquad (6)$$

This equation can be expressed in terms of f_A and f_B by use of equations (3) and (4) giving

$$Q = (V/N)c(1-c)\cdot \left\{\begin{aligned}&\left[(N_1/V_1)(m_1) - (N_2/V_2)m_2\right] f_A + \\ &\left[(N_1/V_1)(1-m_1) - (N_2/V_2)(1-m_2) f_B\right]\end{aligned}\right\}^2. \qquad (7)$$

If the a-Fe_xGe_{100-x} samples with 33<x<75 are phase separated into a-$FeGe_2$ and a-Fe_3Ge, as indicated by the XANES analysis of Lorentz, et al., then the ASAXS intensity will, according to equation (7), decrease as the energy approaches the Fe edge from below and will increase as the energy approaches the Ge edge from below.

This behavior is seen for the a-$Fe_{49}Ge_{51}$ sample as shown in Figures 4 and 5. Unfortunately there is a large parasitic scattering peak in these data sets that extends from approximately s=0.02 to approximately s=0.004, and obscures the lowest angle scattering. At the Fe edge this parasitic peak overlaps the actual SAXS peak so that the SAXS peak appears as a shoulder on the parasitic peak. Disregarding the data below s=0.05 because of parasitic contamination, one can see that the intensity of the SAXS peak decreases as the energy approaches the Fe edge and increases as the energy approaches the Ge edge.

Application of the phase separation model expressed in equation (7) to this sample yields a decrease in ASAXS intensity at the Fe edge that exceeds the increase in intensity at the Ge edge. This is also seen in the data presented in Figures 4 and 5. The increase in intensity at the Ge edge in a-$Fe_{49}Ge_{51}$ is slight compared to the decrease in intensity at the Fe edge.

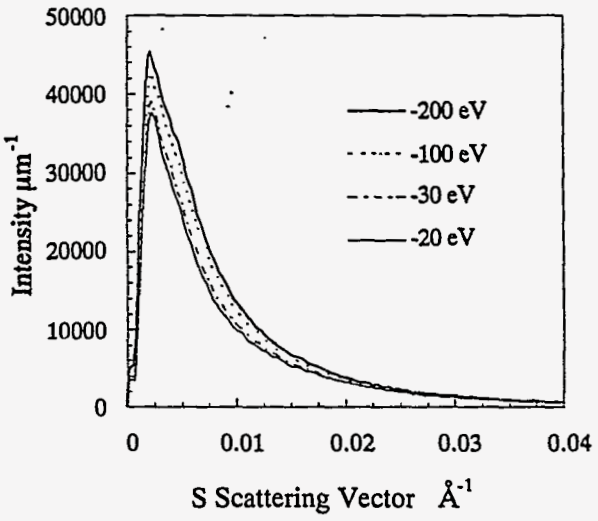

Figure 4. The intensity of the scattered radiation at incident photon energies of 200, 100, 30, and 20 eV below the Fe absorption edge in a-$Fe_{49}Ge_{51}$. The intensity of scattered radiation decreases as the absorption edge is approached.

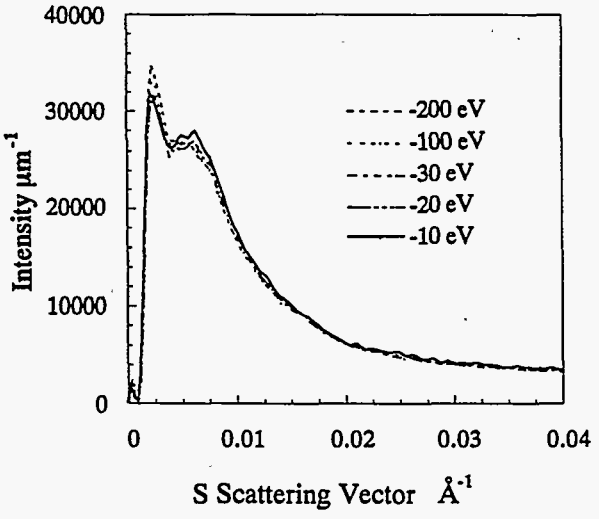

Figure 5. The intensity of scattered radiation at incident photon energies of 200, 100, 30, 20, and 10 eV below the Ge K-absorption edge in a-$Fe_{49}Ge_{51}$. The intensity of scattered radiation increases as the absorption edge is approached.

These data support a model of phase separation into a-$FeGe_2$ and a-Fe_3Ge in the a-Fe_xGe_{100-x} system for Fe concentrations between 33 and 72 atomic %. For metal concentrations of less than 33 atomic % these data indicate very fine scale composition modulation with the Ge number density remaining uniform across the sample. This can also be seen with equation (7) which models the composition modulation as phase separation into two distinct phases. The ASAXS intensity at the Ge edge can only remain constant in equation (7) as the Ge scattering factor changes if the coefficient of the Ge scattering factor is zero. Setting this coefficient equal to zero means that the number density of Ge atoms in phase 1 is the same as the number density of Ge atoms in phase 2.

A more general mathematical description of scattering from amorphous systems given by Rice, Wakatsuki, and Bienenstock[4] that does not make requirements on the number, size, or distribution of phases also shows that the Ge number density must be uniform across the sample if the ASAXS remains constant with changing Ge scattering factor. The more general approach includes continuous composition modulations such as those seen in spinodal decomposition or very fine scale phase separation where the interface between phases may be as large in spatial extent as the phases themselves.

If the SAXS was caused by voids there would two distinct phases: the homogeneous alloy and the voids. In this case equation (7) would apply and would reduce to

$$Q = (V/N)\left[c(1-c)\right]\left\{(N_1/V_1)\left[m_1 f_A + (1-m_1) f_B\right]\right\}^2. \quad (8)$$

As stated above, and seen in equation (8), the ASAXS intensity will decrease beneath the absorption edge of each element in the sample if the SAXS arises from voids.

ASAXS has been used here to show that there is fine scale composition modulation, as opposed to cracks and voids, in a-Fe_xGe_{100-x}, a-W_xGe_{100-x} and a-Mo_xGe_{100-x} thin films with low metal concentrations. The size scale of the modulations increases with increasing metal content. In the metal rich regime of a-Fe_xGe_{100-x} the ASAXS data are consistent with large scale phase separation into a-$FeGe_2$ and a-Fe_3Ge.

ACKNOWLEDGEMENTS

This research is supported by the Department of Energy through the Office of Basic Energy Science and the NIH, Biotechnology Resource Program, Division of Research Resources. This work benefited significantly from AB's participation in the US/France Seminar on Anomalous Scattering sponsored by the NSF and the CNRS. Michel Koch kindly lent us his linear position sensitive detector for the August run and was a valuable resource for information on data reduction. Special thanks go to Gene Ice, Paul Zshack and Mark Egbretson for help on NSLS beamline X14A, to Nanna Gillis, David Eliezer and Michael Regan for help with equipment set-up and data collection and to Tad Slowikowski and Jiri Husek for brilliant last minute machining and design help.

REFERENCES

1 Work establishing the efficacy of this technique is described in, for example, O. Lyon, J. J. Hoyt, R. Pro, B. E. C. Davis, B. Clark, D. de Fontaine, & J. P. Simon, *J. Appl. Cryst.* **18** (1985) 480.

2 M. Rice & S. Wakatsuki, SSRL Report PROD-UG-SAS **09/91-R01** (1991).

3 R. D. Lorentz, A. Bienenstock, & T. I. Morrison, In preparation. (1992). and R. D. Lorentz, PhD thesis, Stanford University, CA, USA (1987).

4 M. Rice, S. Wakatsuki, & A. Bienenstock, *J. Appl. Cryst.* **24** (1991) 598.

LOCAL ATOMIC STRUCTURE OF HIGH TEMPERATURE SUPERCONDUCTORS

F. Bridges and G.G. Li
Department of Physics
University of California, Santa Cruz
Santa Cruz, CA 95064

J. B. Boyce
Xerox Palo Alto Research Center
Palo Alto, CA 94304

T. Claeson
Physics Dept.
Chalmers Univ. of Technology
Gothenburg, Sweden

1. INTRODUCTION

Much discussion on the relationship between structure and superconductivity has occurred[1,2]. One aspect of this is the location of the atoms, the starting point for all evaluations. Here we review our results for the $BaPb_{1-x}Bi_xO_3$ (BPBO) system and for Zn and Co local environments in substituted $YBa_2Cu_3O_7$ (YBCO).

1. BPBO and BKBO

The superconductivity of the perovskite-type oxide $BaPb_{1-x}Bi_xO_3$ (BPBO) has acquired renewed interest with the advent of the high temperature superconductors. It may be considered as the archetype of oxide superconductors. The superconducting transition temperature of the $BaPb_{0.75}Bi_{0.25}O_3$ is relatively high[3] ($T_c \approx 13K$) despite the fact that the carrier density and the density of electron states at the Fermi level are much smaller than in the superconducting metals with similar T_c's. The low density of states and the high T_c imply an exceptionally strong electron-phonon coupling or perhaps another coupling mechanism. The latter possibility has been strengthened by the discovery of the related high T_c superconductor,[4] $Ba_{1-x}K_xBiO_3$ (BKBO), which displays transition temperatures as high as 30 K. It would be surprising if the superconductivity in the two differently doped $BaBiO_3$ compounds were different in origin.

An important hint at a possible relationship between superconductivity and the structure of these systems is the existence of a charge density wave in $BaBiO_3$. Two different Bi sites and two distinctly different Bi–O distances separated by 0.18 Å have been found in $BaBiO_3$.[3,5,6] An accepted model is that frozen breathing Bi–O modes induce a distortion of the perovskite structure and give rise to a static charge density wave (CDW). The transformation to a doubled unit cell, with an energy gap at the Fermi surface and a semiconducting state, is thought[7] to be of the Peierls type. Alloying with Pb or K should destroy the long range order of the CDW and restore metallic conductivity. However, the semiconducting state remains until 65% of the Bi atoms have been replaced by Pb or until 30% of the Ba has been replaced by K.

From the XAFS[8], two separate Bi–O distances have been determined in $BaBiO_3$. The values agree well with those from neutron diffraction and also with the values obtained in other XAFS studies[9–11]. Upon alloying $BaBiO_3$ with Pb, a two-distance Bi–O distribution remains. Our results indicate that Bi tends to keep the same O environment in the alloys (including the variation in the Bi–O bond lengths) that it has in the end-point compound $BaBiO_3$ leading to a local CDW with a short coherence length. For K doping of $BaBiO_3$ however, XAFS studies[9–11] give two

Bi–O distances for the semiconducting alloys, but only one distance (with a large static disorder) for the superconducting alloy.

A semiconducting energy gap has been determined by optical measurements[12]; It decreases with the addition of Pb but an optical pseudogap persists even in the metallic state. (For the K–doped alloys, on the other hand, there is no pseudogap in the metallic state[13].) This would support our picture of two different Bi–O distances and local charge density fluctuations in space (and possibly in time) in the metallic state for Pb–doped, but not K–doped alloys.

Our structural results correlate well with the pseudogap picture as shown in Fig. 1. This implies that the local Bi–O distances and the optical gap have a similar origin, namely, a local CDW. Generally, one would expect a CDW to be detrimental to superconductivity. It would localize charge and prevent the formation of Cooper pairs in k–space[14]. Our results suggest that a local, rather than a long–range, CDW exists in the superconducting state of BPBO and not in BKBO. This may account, in part, for the difference in T_c in the two materials.

2. YBCO:Zn and YBCO:Co

Substitution on the Cu sites in YBCO has been used as a probe to investigate the importance of Cu in these materials[15,16]. Early studies focussed on the role of the chains versus planes, while more recent investigations have considered dopants, such as, Fe, to be potential pinning centers for enhancing J_c. The two dopants considered here -- Zn and Co -- both[16] suppress T_c significantly, but the suppression for Zn dopants[17] is surprisingly larger than for Co. The amount of T_c suppression varies considerably in the literature, particularly for Zn. The substitution site of Zn dopants is still under debate although many investigators indicate that the Zn substitutes mainly at the Cu(2) site. In addition, it has been proposed that a series of thermal anneals can move the Co dopants from the (chain) Cu(1) site (the accepted substitution site for Co in bulk material) to the Cu(2) plane site[18,19].

We have made a detailed XAFS study of Zn substituted YBCO to address the question of the substitution site and to determine the local disorder. We have found that the Zn site is significantly distorted; the nearest neighbor O atoms in the plane are about 2.02 Å away, compared to 1.94 Å in YBCO. The second neighbor environment is also distorted, but, unlike the Co system[20], it is not disordered. The peaks corresponding to the second and third neighbors are shifted in position relative to pure YBCO but the amplitude is not diminished significantly. Our analysis suggests that Zn occupies a distorted Cu(2) site with the Zn displaced out of the plane towards the Cu(1) site; this lengthens the Zn-Y bond and shortens the Zn-Ba bond length. We propose that this distortion leads to a localization of the charge carriers in the CuO_2 layers and hence to a suppression of T_c. We have also found that many samples contain a significant amount of small ZnO particles. When the T_c suppression is corrected for the amount of Zn in these particles, the T_c suppression for different samples is much more consistent.

Our early XAFS study[20] indicated that the Co(1) site in YBCO is badly distorted. We have recently revisited this system in view of the proposal[18,19] that Co can be moved from the Cu(1) site to the Cu(2) site by a series of thermal anneals. We have studied 12 samples with Co concentrations of 5, 8, 10, 11, and 30%, and with different thermal processing. Measurements were made at both the Cu and Co K-edges. The distortion of the Co(1) site in the "as made" material is similar to that observed earlier. Our results for the annealed samples show little change in the XAFS spectra, indicating that not much Co has moved from the Cu(1) to the Cu(2) site, less than 20%; however, the thermal anneals do decrease the amplitude of the further neighbor multi-peak for the Co data somewhat. The change in the data corresponds to a larger width parameter for the Co-Ba peaks, indicating more static disorder in the thermally treated samples.

REFERENCES

1. For a review, see, for example, J. D. Jorgensen, Physics Today, 44, 34 (1991), and references contained therein.
2. See, for example, High Temperature Superconductors, M. B. Brodsky, R. C. Dynes, K. Kitazawa and H. L. Tuller, Editors (Materials Research Society, Pittsburgh, 1988); and High Temperature Superconductors II, D. W. Capone II, W. H. Butler, B. Batlogg and C. W. Chu, Editors (Materials Research Society, Pittsburgh, 1988).
3. D. E. Cox and A. W. Sleight, Acta Cryst. B 35, 1 (1979).
4. R. J. Cava, B. Batlogg, J. J. Kajewski, R. Farrow, L. W. Rupp, Jr., A. E. White, K. Short, W. F. Peck, and T. Kometani, Nature 332, 814 (1988);and L. F. Mattheiss, E. M. Gyorgy, and D. W. Johnson, Jr., Phys. Rev. B 37, 3745 (1988).
5. C. Chaillout, A. Santoro, J. P. Remeika, A. S. Cooper, G. P. Espinosa, and N. Marezio, Solid State Comm. 65, 1363 (1988).
6. Shiyou Pei, N.J. Zaluzec, J.D. Jorgensen, B. Dabrowski, D.G. Hinks, A.W. Mitchell, and D.R. Richards, Phys. Rev. B 39, 811 (1989).
7. L. F. Mattheiss and D. R. Hamann, Phys. Rev. B 28, 4227 (1983).
8. J. B. Boyce, F. G. Bridges, T. Claeson, T. H. Geballe, and J. M. Remeika, Phys. Rev. B 41, 6306 (1990); and J. B. Boyce, F. G. Bridges, T. Claeson, T. H. Geballe, G. G. Li, and A. W. Sleight, Phys. Rev. B 44, 6961 (1991).
9. S.M. Heald, D. DiMarzio, M. Croft, M.S. Hegde, S. Li, and M. Greenblatt, Phys. Rev. B 40, 8828 (1989).
10. O. Durmeyer, E. Beaurepaire, J.P. Kappler, C. Hornick, and M. Drillon, J Less–Common Met. 164&165, 934 (1990).
11. S. Salem–Sugui, Jr., E.E. Alp, S.M. Mini, M. Ramanathan, J.C. Campuzano, G. Jennings, M. Faiz, S. Pei, B. Dabrowski, Y. Zheng, D.R. Richards, and D.G. Hinks, Phys. Rev. B, 43, 5511 (1991).
12. S. Tajima, S. Ushida, A. Masaki, H. Takagi, K. Kitazawa, S. Tanaka, and A. Katsui, Phys. Rev. B 32, 6302 (1985); and S. Tajima, S. Uchida, A. Masaki, H. Takagi, K. Kitazawa, S. Tanaka, and S. Sugai, Phys. Rev. B 35, 696 (1987).
13. H. Sato, S. Tajima, H. Takagi, and S. Uchida, Nature 338, 241 (1989); and Physica C 162–164, 1121 (1989).
14. T. M. Rice and L. Sneddon, Phys. Rev. Lett. 47, 689 (1981); and E. Jurczek and T. M. Rice, Europhysics Lett. 1, 225 (1986).
15. Y. Maeno, T. Tomita, M.Kyogoku,S. Awaji, et al., Nat. 328, 512 (1987).
16. J. M. Tarascon, P.Barboux, P.F.Miceli. L.H. Greene et al, Phys. Rev. B 37, 7458 (1988).
17. B. Jayaram, S. K. Agarwal, C. V. Rao, and A. V. Narlikar, Phys. Rev. B 38, 2903 (1988).
18. E. Takayama-Muromachi, Y. Uchida, and K. Kato, Jpn. J. Appl. Phys. 26, L2087 (1987).
19. S. Katsuyama, Y. Ueda, and K. Kosuge, Mater. Res. Bull. 24, 603 (1989).
20. F. Bridges, J. B. Boyce, T. Claeson, T. H. Geballe, and J. M. Tarascon, Phys. Rev. B 39, 11603 (1989).

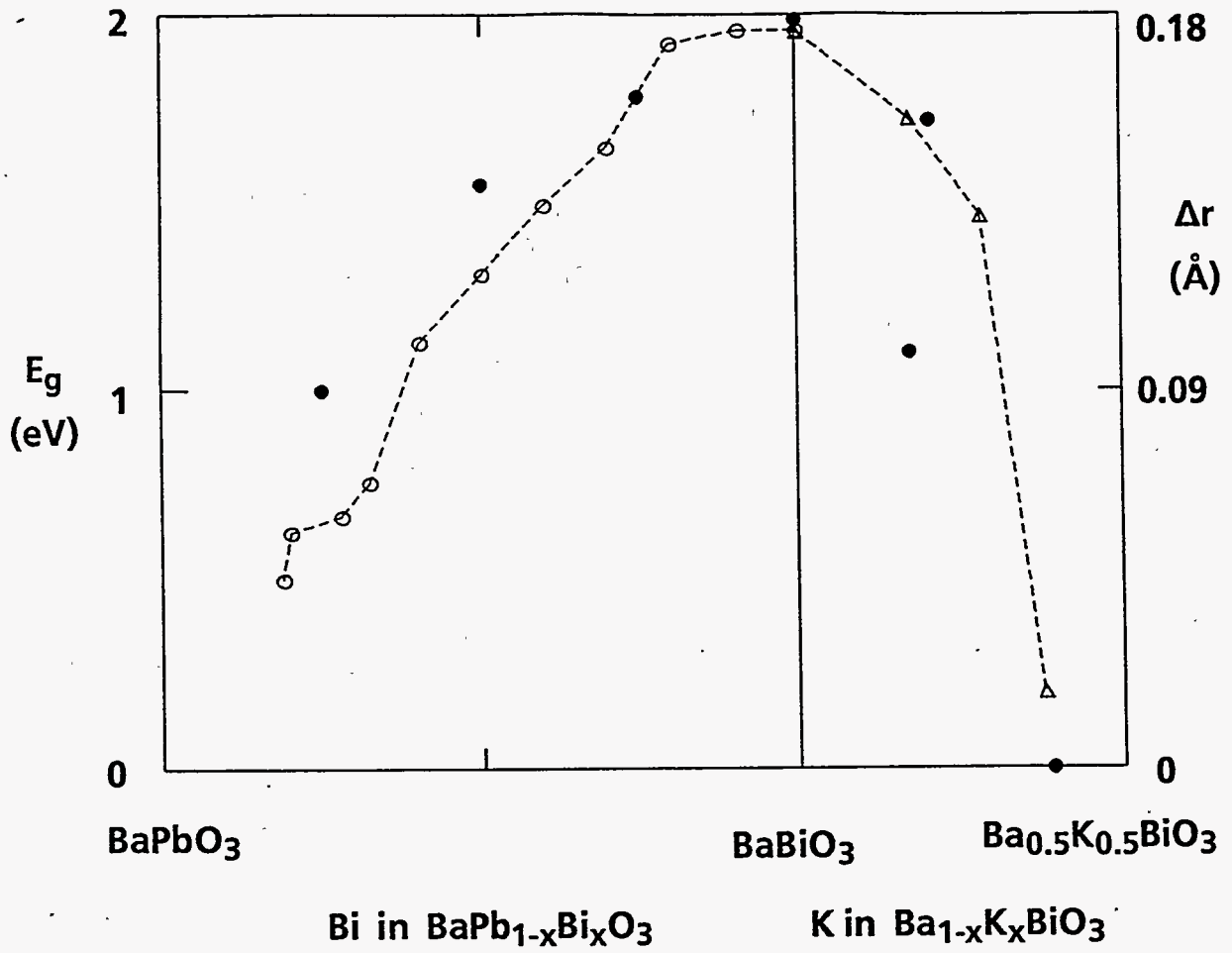

Fig. 1. The optical gap in $BaPb_{1-x}Bi_xO_3$ and $Ba_{1-x}K_xBiO_3$ from Refs. 12–13 and the separation, Δr, (filled circles) between the long and short Bi–O distances from XAFS, plotted on the same scale.

DETERMINATION OF STRAIN DISTRIBUTIONS IN ALUMINUM THIN FILMS AND LINES AS A FUNCTION OF TEMPERATURE USING GIXS

Paul R. Besser, Ramnath Venkatraman, John C. Bravman
Department of Materials Science and Engineering, Stanford University, Stanford, CA 94305

Sean Brennan
Stanford Synchrotron Radiation Laboratory, Menlo Park, CA 94025

Abstract

Using synchrotron grazing incidence X-ray scattering (GIXS), we have measured elastic strain distributions with depth as a function of temperature in Al thin films of various thicknesses on oxidized silicon and in Al-0.5%Cu on Ti lines. Stress gradients have been calculated directly from the strain gradients measured as the films were cycled from room temperature to 400°C and back. For all samples examined, much of the stress arising from thermal expansion differences between the Al and the Si substrate is relaxed during the first few minutes at elevated temperatures. Disregarding minor surface relaxation effects that depend on the film thickness, it is shown that there are no gross stress gradients in planar Al films in the range of temperatures considered. For the case of patterned lines, the width direction of the line supports essentially no stress throughout the thermal cycle.

I Introduction

The variation of stress with thermal cycling in planar Al thin films on Si has been extensively studied and documented [1]-[2]. The stress is commonly obtained using substrate curvature techniques which give the average value of the stress in the film. Due to the variety of deformation processes that could take place in Al thin films at elevated temperatures, it could be hypothesized that there may be large strain gradients through the film thickness at those temperatures. [3] For example, consider an Al thin film on a Si substrate that has been heated to an elevated temperature and in which significant equibiaxial stresses has been induced. The grain structure is known to be columnar. The tractions on the grain boundaries can be relaxed by grain boundary diffusion. A local relaxation at the grain boundaries would then result in a large strain gradient extending from the film-substrate interface to the top of the film. Using grazing incidence x-ray scattering (GIXS), Doerner and Brennan [4] showed that the surface of aluminum films of thicknesses 0.25 μm and 0.6 μm cooled to room temperature is relaxed with respect to the bulk. As part of this work, a series of experiments are being performed on planar Al films with the aim of determining the magnitude of strain gradients at elevated temperatures.

In the integrated circuit industry, these uniform films are lithographically patterned to produce metal lines. As the number of active devices per unit chip area increases, the fabrication and performance of the interconnects themselves pose greater difficulties. The build-up of stresses in lines during deposition and processing has understandably been the subject of much research in recent years. We and other authors have used volume-average x-ray methods to measure stresses in excess of 400 MPa in Al-Cu lines.[5] Voiding, an important reliability concern in the integrated circuit industry, is observed in passivated lines as a method of relaxation of these large hydrostatic stresses. Determination of the distribution of the stress through the thickness of the lines will lead to a better understanding of the relaxation and failure mechanisms operating. The techniques developed for measuring strain gradients in planar films have been applied, with some geometry considerations, to lithographically patterned lines of aluminum. The result is a method for measuring strain distributions through the thickness of unpassivated Al alloy lines.

A brief description of the GIXS technique is provided along with the materials used and the experimental strategy. Stress distributions calculated from measured strain distribution as a function of depth at different temperatures are presented.

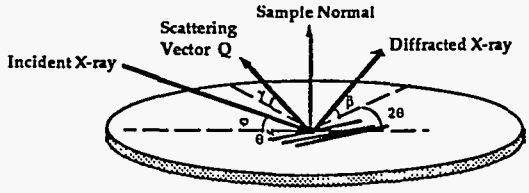

Figure 1: Schematic of the GIXS geometry.

II Experimental Techniques

Uniform films and lines have been examined in these experiments. The films used were: i) Three thicknesses of Al-0.5%Cu : 0.1 μm 0.5 μm and 1.0 μm, ii) a 1.0 μm thick Al-1%Si film and iii) a 0.6 μm thick pure Al film with and without an anodic oxide coating. All films were obtained by room-temperature sputter-deposition onto oxidized Si(100) substrates. The metal lines were fabricated by lithographically patterning a sputter-deposited blanket film of 1.0 μm thick Al-0.5%Cu on a 1000 Å Ti barrier layer. The patterning produced arrays of parallel 1.25 μm wide lines and 1.25 μm wide spaces. Diffraction experiments were performed at SSRL on a focused wiggler beamline using X-rays at 8700eV. A heating stage for thermal cycling was designed for use on the four-circle Huber diffractometer that was used for the experiments. The films were thermally cycled between room temperature and 400°C, and stress relaxation was monitored as a function of time at different depths in the film at several set temperatures. This was done both when the films were in compression (during heating) and in tension (during cooling).

Stress as a function of depth was determined using GIXS. Over the past years GIXS has been used extensively to study the structure of thin films and interfaces [8,9]. It utilizes the principle of total external reflection (TER). For most materials, the index of refraction is less than unity at X-ray energies. According to Snells Law, X-rays going from a material of higher index of refraction (air) to one having a lower index (the diffracting material) will be perfectly reflected below a certain critical angle of incidence. The critical angle of incidence for TER is typically less than a degree; X-rays striking the sample at less than this angle only penetrate a small depth into the material. For the diffraction conditions and samples used in these experiments, the penetration depth is only 50 Å below the critical angle of 0.22°, while it is roughly 6000 Å at 0.4°.

The scattering geometry used in these scans is shown in Figure 1. X-rays are incident at some small angle ϕ relative to the sample surface and θ relative to the diffracting planes. The scattered X-rays are detected at some angle β relative to the sample surface.

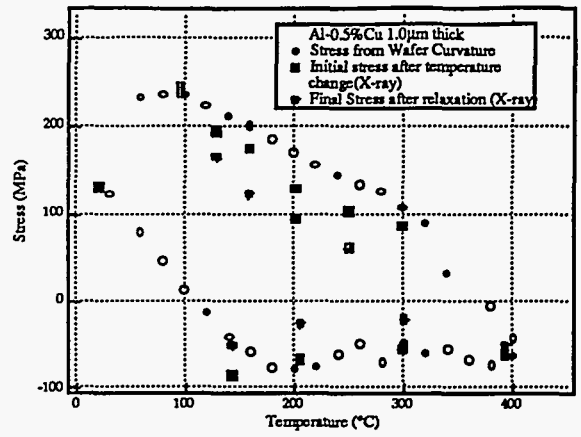

Figure 2: Stress-temperature data as measured by wafer curvature and X-ray diffraction for unifrom Al-0.5%Cu film.

The scattering vector Q is inclined slightly relative to the sample plane. Since this inclination angle is less than a degree, the planes participating in the scattering event are essentially perpendicular to the sample surface. All samples examined had a strong {111} fiber texture. Diffracted peaks from {422} planes perpendicular to the film were favored over the {220} since they occur at higher values of 2θ, leading to increased accuracy in determining lattice spacings. Different values of angles of incidence were chosen to obtain average d spacings over different depths of film. The 2θ peaks are scanned and fitted for peak positions. These scans were not symmetrical $\theta - 2\theta$ scans.

Since the uniform films were subject to a equal biaxial stress state, measurement of the in-plane strain fully defined the stress state of the film. For the samples with lines, two measurements of the strain were required to fully define the strain state; one with the scattering vector along the length of the line and one with the scattering vector oriented along the width of the line.[6]

III Results and Discussion

A Uniform Films

Figure 2 summarizes the thermal history for the 1.0μm Al-0.5%Cu film. There are three sets of data of stress vs. temperature corresponding to: i) the stress as measured by the wafer curvature technique, ii) the stress measured by X-ray diffraction immediately after a temperature change and iii) the stress to which the film was allowed to relax at each temperature. The wafer curvature and the X-ray measurements were performed on films obtained from the

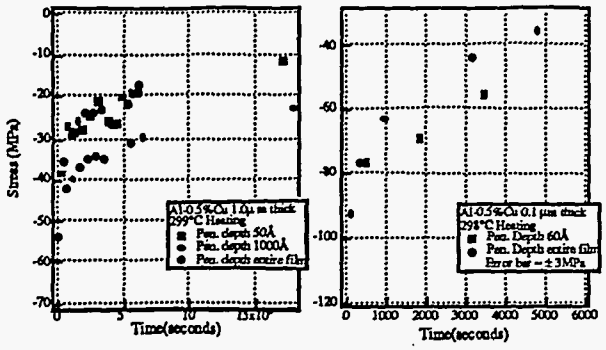

Figure 3: Stress relaxation with time at 298°C for (a) 1.0μm and (b) 0.1 μm thick Al-0.5%Cu .

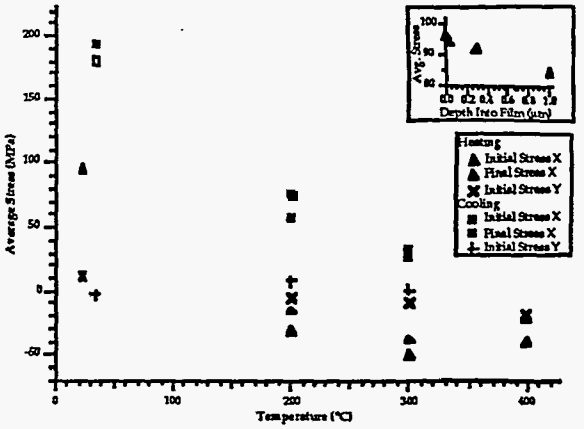

Figure 4: Initial and final values of stress for lines as a function of temperature.

same sputtering run and both sets of measurements correspond to the first thermal cycle. The difference between the stress as measured by the wafer curvature technique and as measured by X-ray diffraction arises from the different thermal histories of the two samples.

The results of the stress relaxation experiments are seen to be thickness dependent. As the films were heated to temperatures greater than 100°C stresses are compressive and relaxation is seen to occur uniformly at all levels in the film. For all films it was found that, below 200°C, the surface of the film maintained a slightly higher value of stress with respect to the bulk. In thicker films, this condition reverses between 200°C and 300°C and the surface relaxes with respect to the bulk. After this happens, the surface remains relaxed at all temperatures during the first and subsequent thermal cycles. Figures 3 (a) and (b) show the stress relaxation data at different penetration depths at 298°C during the heating cycle for the 1.0μm and 0.1μm thick Al-0.5%Cu films. From Figure 3(a), it is clear that the top 50 Å of the 1.0μm thick sample is relaxed with respect to the bulk. It remains relaxed throughout the thermal cycle. Similar behavior was observed also for the 1.0m thick Al-1%Si film. We observed different behavior in films thinner than 0.6μm. The surface of thinner films (0.1μm by example in Figure 3(b)) is more stressed relative to the bulk of the film at 298°C and remains so throughout the thermal cycle. It is important to note that the stress values plotted here are the values averaged over the X-ray penetration depth and hence a plot of actual stress as a function of depth in the film will exhibit a sharper stress drop near the surface. These results are similar to those reported by Doerner and Brennan [4] in that they observed relaxation at the top surface of the film for smaller film thicknesses, i.e. 0.26μm and 0.6μm. This could very well be due to the well-known sensitivity of the film characteristics to differing impurity levels caused by film deposition conditions. Also, their films were annealed for 30 minutes at a temperature (450°C), 50°C higher our annealing temperature. We observed no surface relaxation with respect to the film bulk for films thinner than 0.6μm. In spite of the qualitative differences seen with respect to strain gradients between relatively thick and thin films, it is safe to generalize that there are no gross strain gradients in Al films on Si even at elevated temperatures.

B GIXS of Lines

The thermal cycle of the paterned line samples is shown in Figure 4 . This plot shows the temperatures at which the stress relaxation was observed during heating and cooling. The initial and final values of stress along the length of the line are shown with ϕ large enough to sample the entire depth. For the width of the line, only the initial values of stress are shown since little relaxation occured in this direction. The lines are in compression during heating and in tension upon cooling. At room temperature (inset to Figure 4), the average stress distribution along the length of the line is shown as a function of depth. The stress at the surface of the film is 15% greater than the stress in the bulk of the film.

Figure 5 shows the calculated stress relaxation profiles for two temperatures of interest, namely 200°C during heating and 200°C during cooling. Three depths of the film are shown in each plot for each line direction. As with uniform films, most of the stress relaxation occurs in the first few minutes of observation. This rapid relaxation can still be seen both in heating and in cooling. The slope of the stress/time plot at 200°C reduces significantly after 30 minutes. It is apparent (and expected)[6] that the width direction of the line supports essentially no stress at any tempera-

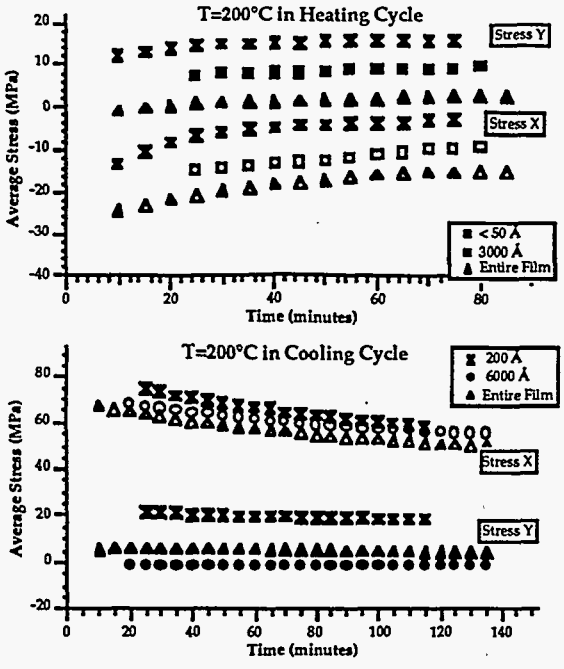

Figure 5: Stress relaxation curves for Al-0.5%Cu lines 200°C during heating and cooling.

ture during the thermal cycle. Notice that the surface of the film is relaxed relative to the bulk upon heating; however, upon cooling, the surface is in a higher state of stress relative to the bulk. This trend is still being investigated. The native oxide of Al is not believed to be responsible since it should be present at all temperatures. The formation of the intermetallic $TiAl_3$ (accompanied by a volume reduction of 0.22%[7]) was observed during the relaxation at 399°C using offset Bragg-Brentano X-ray scans. It remains during the cooling cycle. This formation, however, does not explain the stress behavior since the surface of the lines were at a higher state of stress than the bulk at room temperature before thermal cycling.

IV Summary and Conclusions

Grazing incidence X-ray scattering (GIXS) was used to measure elastic strain as a function of film depth at different temperatures during thermal cycling in Al and Al alloy thin films of various thicknesses and in Al alloy lines. The experiments consisted of monitoring the stress relaxation as a function of time at different depths in the film at a particular temperature. It was found that for films 1.0μm thick the surface of the film relaxed with respect to the bulk during the first heating between 200°C and 300°CFor films 0.6μm and thinner, such a relaxation was not observed and in fact, the surface always maintained a slightly higher value of stress as compared with the bulk. However, it can be generalized that any deviation from a uniform stress through the film thickness takes place only near the very surface of the film. In the case of Al-0.5%Cu on Ti lines, it was found that the surface of the line is relaxed relative to the bulk upon heating, but the surface is in a higher state of stress than the bulk upon cooling (as it was initially). It was observed that the width direction of the line supports essentially no stress through the thermal cycle.

V Acknowledgements

The authors would like to acknowledge the support of Semiconductor Research Corporation under contract SRC 90-SP-101. Support for S. Brennan is provided by the Department of Energy (DOE) Office of Basic Energy Sciences. These experiments were performed at SSRL, which is supported by the DOE, Division of Chemical Sciences. We gratefully acknowledge Professors W.D. Nix and Paul Flinn for insightful discussions. We thank Intel Corporation for providing the samples used in the experiment.

References

[1] A.K. Sinha and T.T. Sheng. *Thin Solid Films*, 48:117–126, 1978.

[2] R. Venkatraman et al. *Journal of Electronic Materials;* 19:1231–1238, 1990.

[3] R. Venkatraman, P.R. Besser, S. Brennan and J.C. Bravman *MRS Symposium Proceedings*, Volume 239, Pittsburgh, PA, 1991.

[4] M.F. Doerner and S. Brennan. *Journal of Applied Physics*, 63:126–131, 1988.

[5] B. Greenbaum, A.I. Sauter, P.A. Flinn, and W.D. Nix. *Applied Physics Letters*, 58(17):1845–1847, 1991.

[6] P.R. Besser, R. Venkatraman, S. Brennan and J.C. Bravman *MRS Symposium Proceedings*, Volume 239, Pittsburgh, PA, 1991.

[7] D.S. Gardner and P.A. Flinn. *Journal of Applied Physics*, 67:1831–1844, 1990.

XAFS STUDIES OF PEROVSKITES UNDER PRESSURE

R. Ingalls
Physics Department, University of Washington, Seattle WA
E. D. Crozier
Physics Department, Simon Fraser University, Burnaby, B.C. Canada
B. Houser
Physics Department, Eastern Washington University, Cheney, WA

Introduction

Our group has been measuring the XAFS of various materials under high pressures for a number of years. Pressure is generated in a polycrystalline boron-carbide-anvil cell to avoid Bragg peaks which generally are present when a diamond-anvil cell is used. The pressure is determined from the EXAFS of a calibrant such as copper or an alkali metal halide placed in the presure cell together with the sample. General information obtained by this method includes the pressure dependence of various bond lengths and their mean square deviations. Careful analysis of multiple scattering effects can also shed light on pressure induced bond-bending, especially prevalent in perovskite related materials.

Rhenium Troxide

During the summer 1991 run we conducted a difficult experiment on rhenium trioxide, measuring the Re k-edge XAFS under pressure while at liquid nitrogen temperature. The multiple scattering peak in the fourier transform of rhenium trioxide XAFS is very sensitive to atomic vibrations, which tend to mask information on the high-pressure phase transition this compound undergoes. The importance of our latest measurement was in supressing atomic vibrations sufficiently to separate thermal effects on the absorption spectrum from structural effects. One problem we unexpectedly faced was that, at the low temperatures of the experiment, the pressure calibrant (rubidium chloride) remained in its low pressure phase, for which we have no equation of state measurements. Although this was an important finding and one which we shall pursue (See Proposal 2141) it did complicate the determination of pressures reached during the pressurization process. Another difficulty was an unusually high number of monochromator crystal glitches in the incident beam which we attribute to possible earthquake effects.

High T_c Superconductors

We have also continued our studies of pressure-induced structural changes in high T_c superconductors. Initial x-ray diffraction studies suggested that pressure causes a monotonic compression of the lattice parameters without producing any structural changes in the unit cell of $YBa_2Cu_3O_x$ and $La_{1.85}Sr_{0.15}CuO_{4-y}$. However for perovskite-like structures, phase transitions are difficult to detect by x-ray diffraction. For the second compound above, our results at room temperature† indicate that the Cu-O octahedra are rotated from the 180° position and the consequent change in the electronic structure near the Fermi energy should be included in theory. For the 1-2-3 compound, our analysis of the EXAFS‡indicated that the Cu-O-Cu bonds begin to bend at about 10 kbar. However in this case the analysis is complicated by focussed multiple scattering and we were unable to distinguish whether bending occurs in the linear chains, the puckered sheets, or both.

To resolve this point we have now taken pressure dependent data at 77 K on two samples of the 1-2-3 type material, one with linear chains (x = 6.95) and one with our chains (x = 6.10). Analysis is in progress.

Since we had the same calibrant and monochrometer crystal as in the rhenium trioxide experiment, we intend to repeat both studies with a pressure calibrant more suitable for low temperature work. This is planned for March 1992.

†N. Alberding, K. R. Bauchspiess, J. M. Tranquada, R. Ingalls and E. D. Crozier, Physica B158, 498 (1988).

GLITCH FEATURES IN EXAFS DATA; I. TEST OF THE MODEL FOR LINEARLY TAPERED SAMPLES

F. Bridges, G.G. Li, and Xun Wang
Department of Physics
University of California, Santa Cruz
Santa Cruz, CA 95064

J. B. Boyce
Xerox Palo Alto Research Center
Palo Alto, CA 94304

Double crystal monochromators, used to obtain high energy resolution for synchrotron x-ray sources, have the undesirable feature that over certain small energy ranges, the flux changes rapidly both in intensity and in spatial distribution, as a result of multiple reflections[1-3]. These effects are usually called "crystal glitches". In EXAFS measurements, over an energy range which includes one or more of the "crystal glitches", unwanted features also occur in the EXAFS spectra which we refer to as "EXAFS glitches". They persist in ratioed data, even for the ideal case of perfectly linear detectors and no harmonics, whenever any sample inhomogeneities exist. Since some inhomogeneities are always present, EXAFS glitches are intrinsic to data collected using crystal monochromators.

We have recently developed a model [4] which explains why glitches do not ratio out when there is some nonuniformity in the sample. This arises from an energy dependent change in the spatial distribution of the flux across a slit. If the flux is higher at the thick part of the sample, the effective average thickness will be higher; conversely, if the flux is highest at the thin part of the sample, the sample will appear thinner on average. A change of the spatial distribution of flux with energy will then not ratio out.

The simple model we developed made some specific predictions about a glitch when the sample's thickness varies linearly across the slit. We have studied two glitches using linear tapers of aluminum and plexiglas to check some of these predictions.

In Fig. 1 we show the complicated beam profile observed for a range of energies from 6766 to 6771 eV. Here we plot the flux through a 0.2mm slit as a function of vertical table position y. To show the relative spatial structure more clearly, we have subtracted the data at 6765 eV for each trace. A prominent feature clearly moves across the beam profile as the energy is increased. This feature, a dip in amplitude followed by an increase in amplitude, is the result of multiple scattering and interferences effects. For a 1 mm high slit about the central position (indicated by the vertical dotted line) a significant variation in the distribution of the flux across the slit occurs as the energy is increased. Similar, but less detailed data were collected for a second glitch for energies from 9976 to 9980 eV.

The model presented earlier [4] made the following predictions for a glitch, assuming that the multi-diffraction feature in the beam profile could be described by a symmetric dip, with a width that was roughly 1/2 that of the beam profile.

1. The glitch would have both positive and negative lobes (like a dispersion signal); the two lobes would be of equal height for a symmetric dip.

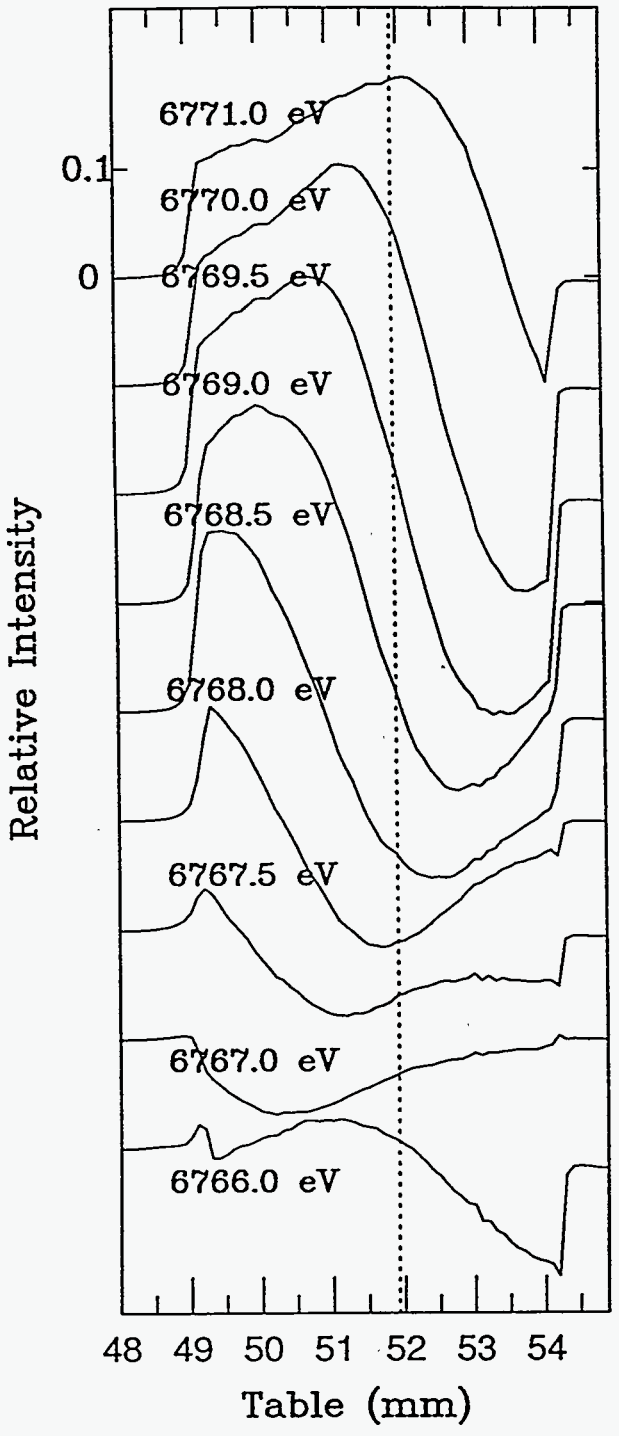

Fig. 1. The intensity across the beam in the vertical direction relative to the data at 6765 eV. The slits were 0.2mm in width, and measurements were taken every 0.2 mm in table height.

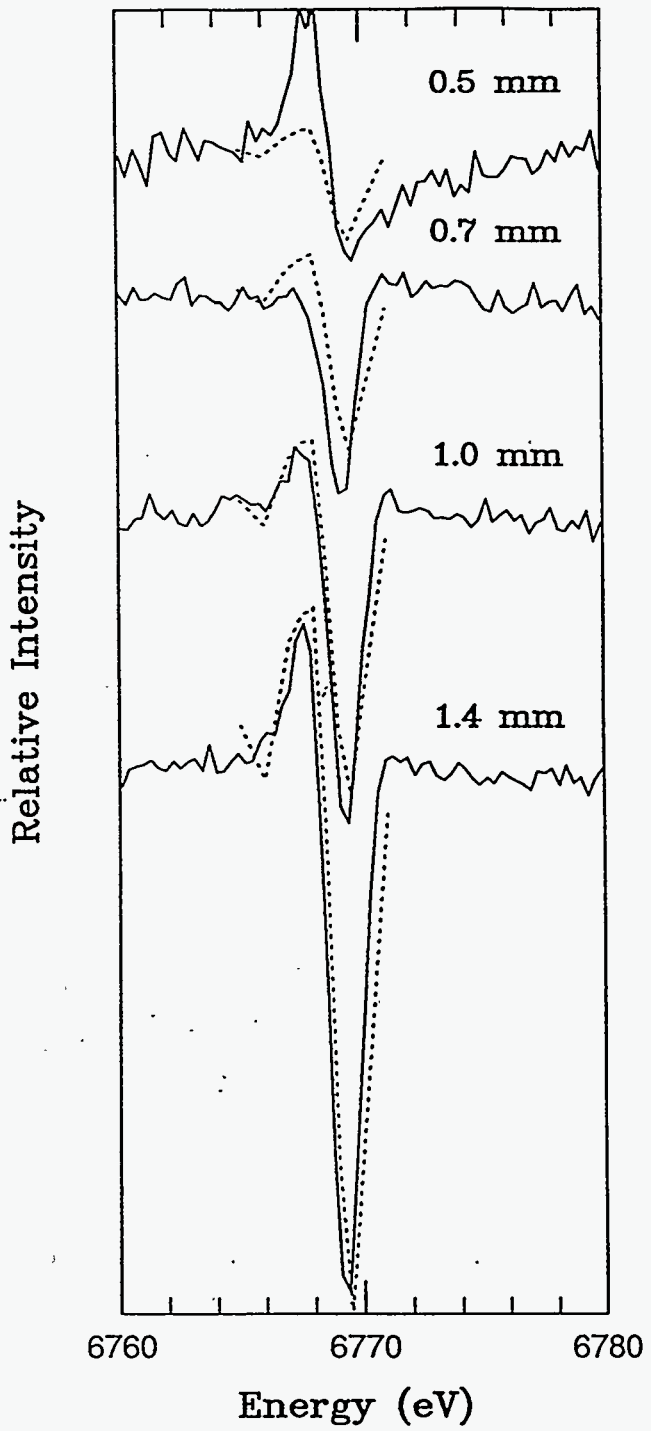

Fig. 2. The glitch from a wedge sample at 6770 eV for slit heights from 0.5 to 1.4 mm. The glitch is inverted when the wedge is inverted. The dotted lines are the calculations from the glitch model [4].

2. The sign of the glitch (i.e., whether it first increases or first decreases) changes when a wedge shaped sample is inverted. Consequently, if one adds together the two spectra for a sample with the wedge up and for the wedge down, the glitch amplitude should cancel if the same part of the wedge is in the x-ray beam.

3. The magnitude of the glitch depends on the slit height.

We have compared the glitches observed using wedge-shaped samples to the glitch structure calculated from our model. The agreement is good; the glitch is inverted when the wedge is inverted and the glitch amplitude increases with the slit height. A detailed comparison of the observed glitch with the prediction from our model is shown in Fig. 2. In this case we have not assumed that the dip in the beam had any particular shape; instead we used the data of fig. 1 directly. A paper on this work has been submitted to Nucl. Instrum Meth. Phys. Res. This work was supported in part by NSF grant number DMR-90-04325.

References

1. Z. U. Rek, G. S. Brown and T.Troxel, "EXAFS and Near Edge Structure III." Ed. K.O. Hodgson, B. Hedman and J. E. Penner-Hahn. (Springer-Verlag, Proc. in Phys. 2 (1984)) p. 511.

2. K. R. Bauchspiess and E. D. Crozier, ibid, p.514.

3. G. Van Der Lann and B. T. Thole, Nuc. Instru. & Meth. Phys. Res. A263, 514 (1988).

4. F. Bridges X. Wang and J. B. Boyce, Nucl. Instrum. & Meth. Phys. Res. A307, 316 (1991).

HIGH PRESSURE TRANSITIONS VIA XAFS

R. Ingalls and F. Wang
Physics Department, University of Washington, Seattle WA

E. D. Crozier
Physics Department, Simon Fraser University, Burnaby, B.C. Canada

Introduction

Our group has been measuring the XAFS of various materials under high pressures for a number of years. Pressure is generated in a polycrystalline boron-carbide-anvil cell to avoid Bragg peaks which generally are present when a diamond-anvil cell is used. The pressure is determined from the EXAFS of a calibrant such as copper or an alkali metal halide placed in the presure cell together with the sample. General information obtained by this method includes the pressure dependence of various bond lengths and their mean square deviations. However, the biggest changes in the XAFS with high pressure always occurs at a phase transition, such as we chiefly report here for the case of metallic iron.

Study of the bcc to hcp Transition in Iron

The diffusionless (martensitic) bcc to hcp (α to ϵ) transition occurs at about 120 kbar at room temperature, although there is a large two-phase region and considerable pressure hysteresis. X-ray diffraction studies have shown that in the two phase region c/a for ϵ iron is different from what it is at the same presure when single phase (i.e. obtained by lowering the pressure and taking advantage of the hysteresis). This may be due to some sort of epitaxy between the phases, or else, perhaps to the existance of some brief intermediate phase.

We are currently analyzing data on this system taken in July 1991. The pressure was determined using a copper calibrant. Fig.1 shows several XAFS spectra of the k-edge of iron before during and after the transition, namely at atmospheric pressure, 140kbar and 160 kbar. In the last case there may yet be a small fraction of the α phase present, which will be checked in a future run. Figure 2. shows the XAFS oscillations obtained from the data of Fig. 1 and Fig.3 shows the associated Fourier transforms. The similarity between the data for the hcp phase and that for metallic copper which is fcc (cubic close-packed) is quite striking. Detailed analysis of the measured radial distribution functions is currently in progress. This is complicated in part because of the occurance of overlapping peaks

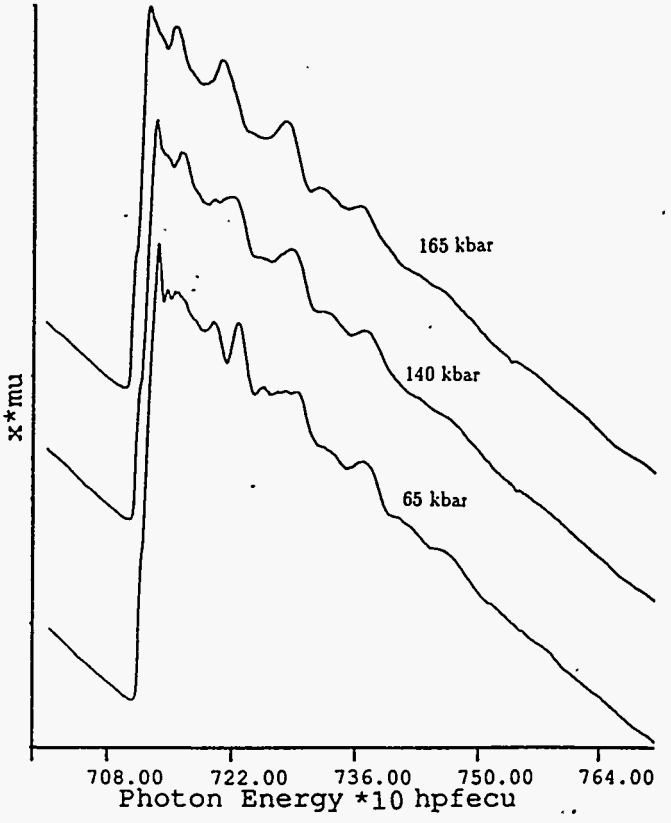

FIGURE 1. k-edge XAFS data of metallic iron

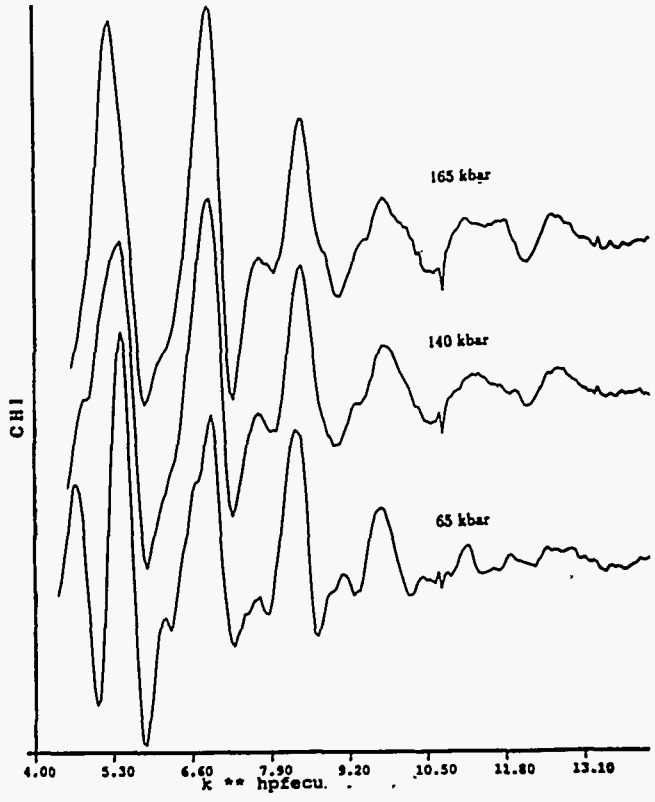

FIGURE 2. EXAFS from Fig.1

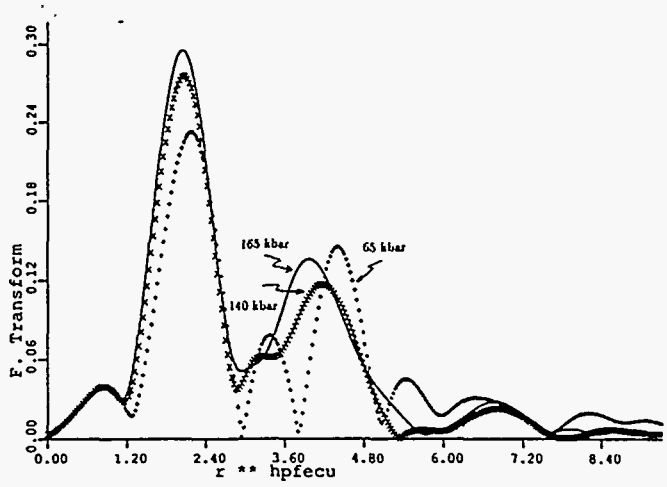

FIGURE 3. Fourier transforms of the data of Fig.2

from nearby shells and multiple scattering. Further work will also include studying the high pressure phase after the pressure is partially reduced.

Other Systems

In a second series of experiments the XAFS of the alkali-metal halide, rubidium chloride was studied at both high pressure and low temperature. At room temperature, this material undergoes a sharp transition from the sodium chloride to cesium chloride structure at about 5 kbar. However, at liquid nitrogen temperature,from the marked change observable in the XANES, we find the transition to be quite sluggish with a mixed phase region evident. We plan to repeat this study with a copper calibrant. Copper is less compressible, but has no known pressure induced phase changes. In the present case, the rubidium chloride was intended to be the calibrant (!), the main samples being perovskite related compounds (see Prop. 2126).

ANISOTROPIC PHASE SEPARATION IN AMORPHOUS FE-GE ALLOYS

M.J. Regan
Department of Applied Physics, Stanford University, Stanford, CA 94305

A. Bienenstock
Stanford Synchrotron Radiation Laboratory, Bin 69, P.O. Box 4349, Stanford, CA 94309

INTRODUCTION

Simple descriptions of most amorphous alloys focus on characterizing the short-range order, while assuming that the material is chemically homogeneous. Phase separation is, however, endemic in the quasi-equilibrium states of such materials. When they are vapor-deposited, the state of separation achieved is limited by kinetics. Past experiments of Rice *et al.*[1] and Lorentz *et al.*[2] show that phase separation of some kind exists throughout most of the composition range ($0<x<75$) of sputtered a-Fe_xGe_{100-x} films. This separation is both scientifically and technologically important, as it plays an important role in determining the films' physical properties. Hence, one hopes to be able to control and manipulate phase growth through either deposition procedures or thermal treatments.

This report is the result of a program designed to better understand the state of chemical homogeneity in a-Fe_xGe_{100-x} films. By varying growth parameters and checking for anisotropy, we are able to show that the deposition conditions affect amorphous phase growth and that the phases are not packed isotropically but rather depend quite significantly on the film surface. Moreover, since the alloy experiences magnetic and metallic transitions with changes in composition, the structural results may play a significant role in interpreting these other properties.

EXPERIMENT

Magnetron (MS) and triode (TS) sputtered films were grown at different rates and power settings. Sputtering is a physical deposition process that occurs when an atom (e.g. Ar) strikes a target material (Fe, Ge). With sufficient kinetic energies, the Ar atoms eject target atoms which are subsequently collected on a substrate table. MS utilizes a magnetron source to localize an Ar plasma near the target, whereas TS relies on a thermionic emission tip to seed the plasma with electrons. A consequence of the TS, however, is to place more energy in the deposit due to the additional electron flux. Unless noted by TS, the sample was magnetron sputtered.

Data were collected at the semi-permanent small-angle scattering beamline 4-2. By employing the anomalous dispersion effect, we can distinguish between phase separation and voids and/or related defects. Previous experiments were performed on samples held perpendicular to the x-ray beam, so that the scattering vector lies in the plane of the sample. Consequently, only those correlations in electron density projected onto the sample surface plane were observed. By tilting the sample by angle ω, the scattering vector rotates out of the surface plane, and we test for correlations projected onto the plane at angle ω with respect to the surface plane (ω=0).

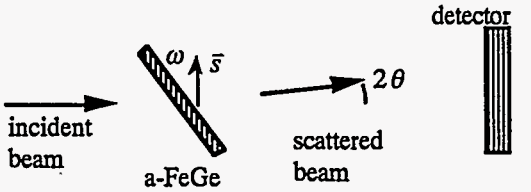

Figure 1. Scattering geometry for ASAXS tilt experiment.

The kapton supported films have been background subtracted as well as normalized per absorption and thickness.

RESULTS

Rice *et al.* have shown that the quasi-equilbrium phase separated state in the region $0<x<33$ is most likely a mixture of a-Ge and an amorphous intermetallic, a-$FeGe_2$. Since the Ge number density is essentially the same in a-Ge as a-$FeGe_2$, Rice observes changes in scattering at the Fe-edge (as it is approached from below) but not at the Ge-edge. For $x>33$, however, one expects changes at the Fe and Ge-edges if the samples are also phase separated, but it has been difficult previously to observe the change at the Ge-edge.

During the initial run in July, we observed the Ge-edge shift and, thus, confirmed previous work by Lorentz *et al.* Figure 2 shows that the scattering pattern moves subtly upward as the x-ray energy approaches the Ge K-edge and steadily downward as the energy approaches the Fe K-edge. This provides further evidence to the conclusions of

Lorentz that the 33<x<75 samples are phase separated into regions of a-$FeGe_2$ and an Fe-rich phase (likely a-Fe_3Ge), where the number densities of Fe and Ge vary with phase. A low energy scan (4500 eV) is also shown to illustrate that there exists a well-defined peak at small $s=2sin\theta/\lambda$ (but is obscured at the higher energies due to parasitic scattering).

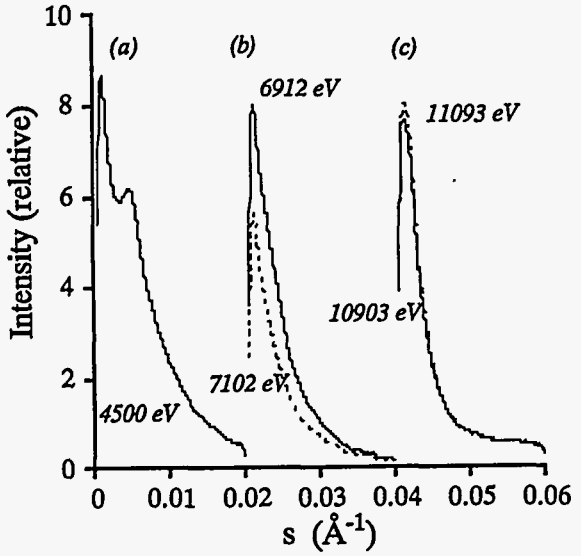

Figure 2. ASAXS experiment performed on a-$Fe_{49}Ge_{51}$ (TS) at various energies. Data are on a relative scale, and the magnitude of scattering from (a), (b), and (c) should not be directly compared.

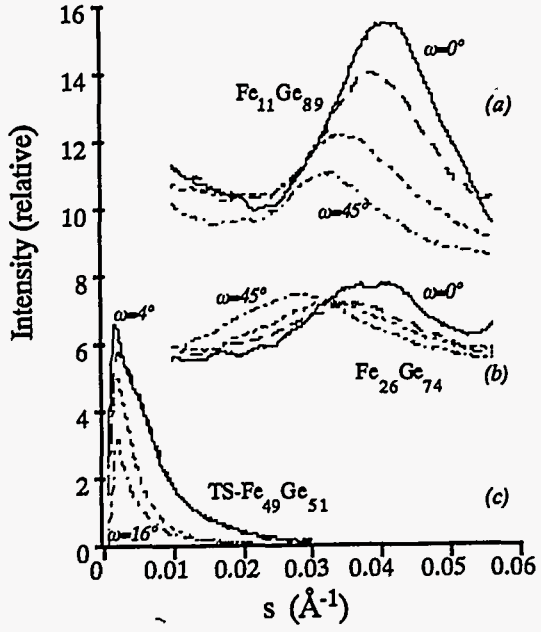

Figure 3. Tilt experiment results. In (a) and (b), the sample is tilted ω=0°, 15°, 30°, 45°. In (c), sample tilted ω=4°, 8°, 12°, 16°. TS sample (c) is not on the same scale as (a), (b).

During the extended portion of the run, we studied newly deposited MS films. Figure 3 shows the results of the tilt experiment for three different compositions, x=11, 25, 49_{TS}. In each case, as the sample is tilted the scattering pattern shifts inward and decreases in amplitude. This is a real effect and has profoundly influenced our thinking. We are still not certain as to the primary cause of the scattering, whether due to interparticle interference effects, heterogeneous isolated particles, or early-stage spinodal decomposition. However, the tilt experiments do show that the films are not the result of a purely two-dimensional growth process. That is, the data suggest that non-trivial correlations exist in the direction of growth (ω=90°); otherwise, we would observe a shift outward rather than inward with sample tilt. Newly planned experiments in a grazing-incidence mode will test for these correlations during the next run.

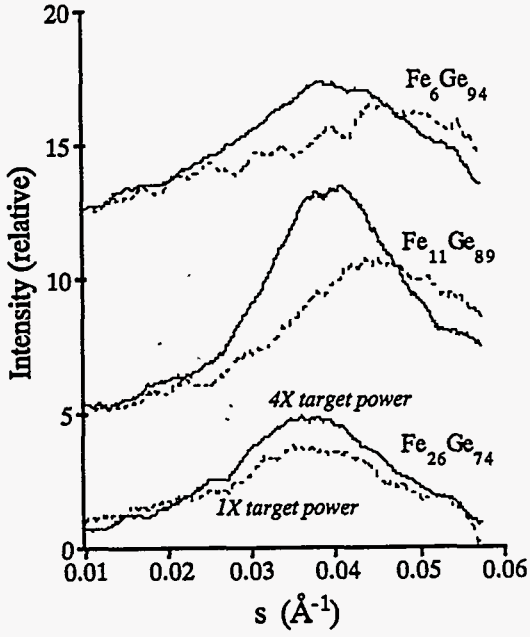

Figure 4. SAXS from samples prepared by varying the power delivered to the sputtering target.

Figure 4 allows one to compare the x-ray scattering from samples that vary both in composition and deposited power flux (related to the adatom's energy and the overall deposition rate). Samples grown at 4 times the target power show a more "advanced" state of phase separation; that is, the samples exhibit a longer correlation length (~1/s)--likely related to the composition modulations and/or particle effects--and occur at a greater magnitude. The scattering amplitude of the $Fe_{11}Ge_{89}$ sample is greatest, consistent with phase separation into a-Ge and a-$FeGe_2$.

CONCLUSIONS

We have used ASAXS to better characterize the chemical homogeneity of a-Fe_xGe_{100-x} films. The scattering results provide evidence that phase separation occurs throughout a wide composition range and that deposition conditions are crucial to the resulting film morphology. Moreover, the tilt experiment shows that a surface-induced structural anisotropy exists. In future work we plan to perform *in-situ* anneals as well as to help determine in what way the anisotropy is related to the surface.

ACKNOWLEDGEMENTS

This research is supported by the Department of Energy through the Office of Basic Energy Science and the NIH, Biotechnology Resource Program, Division of Research Resources. Special thanks to M. Rice and A.P. Bienenstock for help with ASAXS camera alignment and data collection, D. Eliezer and H. Tsuruta for help with camera set-up, P. Capeder and the SSRL X-Ray Staff for help on beamline 4-2, to R. Mayer for table assembly and alignment.

REFERENCES

[1]M. Rice, S. Wakatsuki, and A. Bienenstock, J. Appl. Phys. **24** (1991) 598-602.
[2]R.D. Lorentz and A. Bienenstock, manuscript in preparation (1992). R.D. Lorentz, PhD thesis, Stanford University (1986).

THE EFFECT OF ADSORBED ARSENATE ON THE STRUCTURE OF FERRIHYDRITE DURING AGEING

G.A. WAYCHUNAS[1], C.C. FULLER[2], B.A. REA[2] AND J.A. DAVIS[2]

[1]Center for Materials Research, Stanford University, Stanford, CA 94350-4045
[2]Water Resources Division, U.S. Geological Survey, Menlo Park, CA 94025

Introduction

Our initial work on arsenate adsorption and coprecipitation with ferrihydrite has shown that the tetrahedral arsenate group attaches itself to the ferrihydrite surface by linking to the apices of adjacent FeO_6 octahedra within polymerized octahedral chains forming a binuclear bidentate inner-sphere complex [1,2]. This complex is strongly bound and, if formed in large enough concentrations on the surface during coprecipitation, markedly reduces further polymerization of the resulting ferrihydrite [3]. It is also well known that adsorbed complexes slow the transformation of ferrihydrite into goethite and hematite, but the structural details of the inhibition process are unknown.

During the latest experimentation periods our studies focused on the effect of adsorbed and coprecipitated arsenate on the transformation of ferrihydrite upon ageing. For comparison we also examined the transformation of ferrihydrite samples prepared without arsenate. Samples were prepared with ageing times of from two hours to seven weeks.

Experimental Details

As K-edge and Fe K-edge EXAFS data were collected on beam line 4-1. Samples studied at the As K-edge were moist precipitates held in 1-2 mm thick teflon holders with kapton windows. Samples examined at the Fe K-edge were very thin smears on kapton tape. Data was collected simultaneously in fluorescence and transmission mode, and an extra ionization chamber was used to record an energy calibration standard spectrum during every data scan. All data was collected at room temperature.

Results

Figure 1 shows the Fourier-transformed Fe K-EXAFS for pure ferrihydrite samples of varying age. There is a clear increase in the amplitude of the second (Fe-Fe shell) peak with ageing. The extracted curve-fitting analysis parameters are shown in figures 2 and 3. These results indicate that Fe-O-Fe

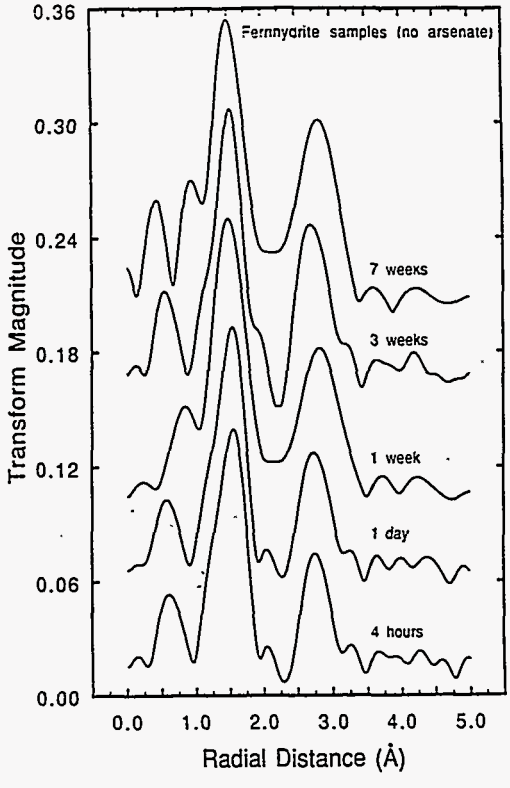

Figure 1. Fourier Transforms of Fe-K edge EXAFS spectra from aged pure ferrihydrite samples. The peak at ca. 3.0 Å is due to second neighbor Fe-Fe correlations. Uncorrected for phase shift effects.

polymerization is occurring during the ageing process. For the youngest ferrihydrite samples there is little polymerization, and the structure consists of very short single FeO_6 octahedral or dioctahedral chains (all octahedra sharing edges) with minimal cross linking (corner sharing between octahedra on nearby chains). With ageing the chains lengthen, dioctahedral chains

become abundant, and cross linking occurs. The seven week sample has Fe-Fe distances closely in agreement with those from bulk goethite (α-FeOOH) which has a dioctahedral chain structure with all chains cross linked, though the total coordination numbers are reduced, probably a consequence of small crystallite size.

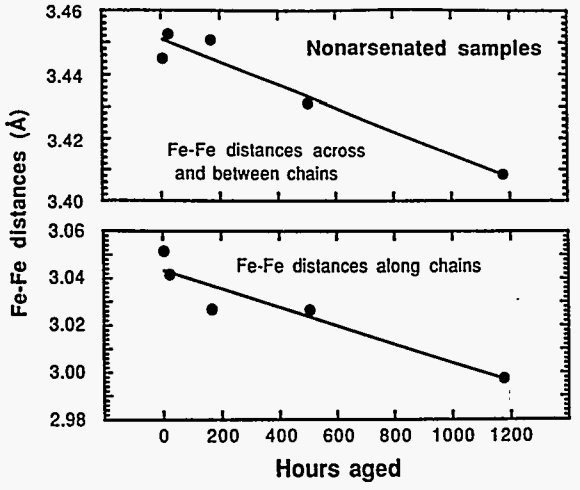

Figure 2. Refined interatomic distances for pure ferrihydrite samples.

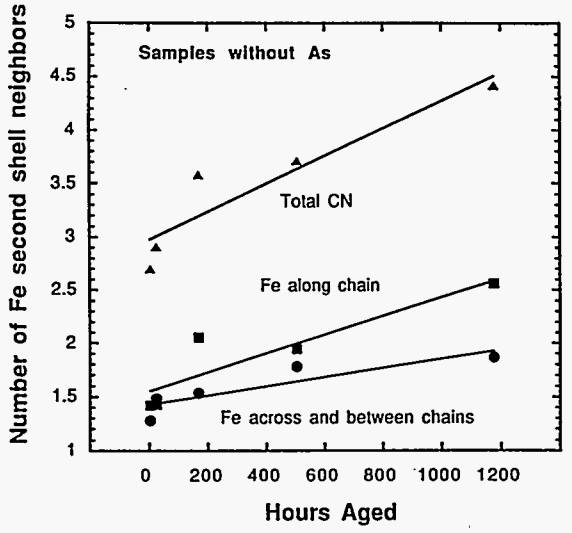

Figure 3. Refined coordination numbers for pure ferrihydrite samples.

In coprecipitated samples with 0.2 As/Fe we see a greatly different trend with ageing. Figure 4 shows that there is very little change in the second transform peak with sample age. It remains the same size as that of the youngest pure ferrihydrite sample. The parameters plotted in figures 5 and 6 clarify this finding. There is a change in Fe-Fe coordination number, but it is small compared to that in the pure ferrihydrite samples. The Fe-Fe distances are also nearly invariant with age. These observations indicate that the arsenated samples have reduced Fe-O-Fe polymerization relative to the unarsenated ones. In particular, the number of Fe-Fe neighbors along the dioctahedral chains are the same initially, but progress much less with sample age, while the numbers of across-chain and interchain Fe-Fe neighbors are strongly reduced in all arsenated samples.

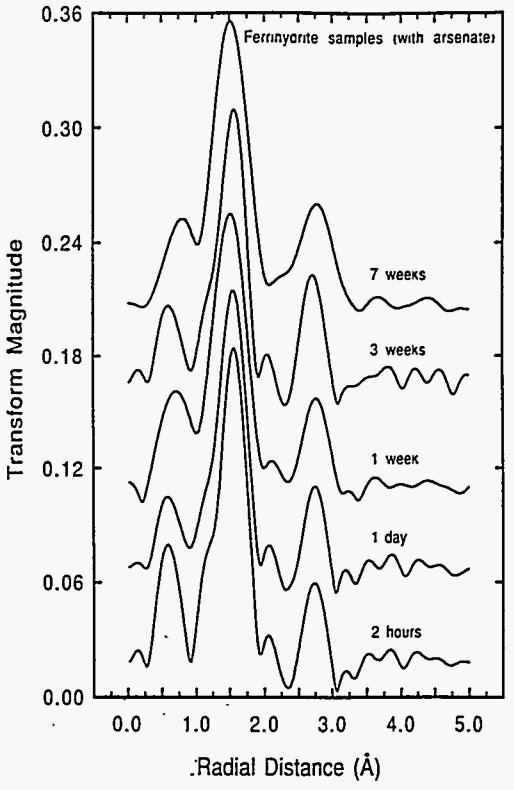

Figure 4. Fourier Transforms of Fe-K edge EXAFS spectra from aged arsenated ferrihydrite samples. The peak at ca. 3.0 Å is due to second neighbor Fe-Fe correlations. Uncorrected for phase shift effects.

Our analysis of these variations suggests that the presence of arsenate while ferrihydrite is polymerizing retards further polymerization. Chain cross linking is stopped completely, and dioctahedral chain length is reduced. This follows from the geometry of the arsenate complexes. They occupy the positions where dioctahedral chains would bind to one another to form more polymerized species. Evidently, the binding of arsenate during the initial stage of polymerization stops this chain linking process and retards chain growth, even at moderate levels of arsenate loading.

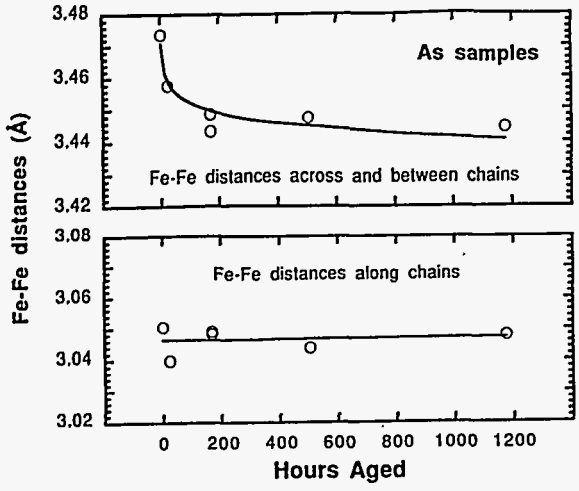

Figure 5. Refined interatomic distances from arsenated ferrihydrite samples.

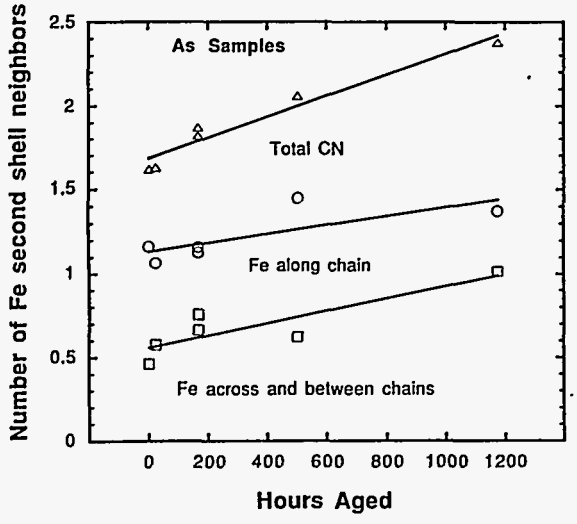

Figure 6. Refined coordination numbers from arsenated ferrihydrite samples.

In classical crystal growth this would be termed surface poisoning. However, single chain growth should not be retarded significantly, as arsenate appears to form no complexes involving the edges of single FeO_6 octahedra. Thus single chain Fe-O-Fe polymers may be dominant in highly arsenated ferrihydrites.

Natural samples

Our findings are particularly significant because natural ferrihydrites frequently contain large amounts of adsorbed or complexed impurities, especially silica, SiO_2, that can have large effects on transformation kinetics [4]. Hence the cycling of adsorbed species in the environment is related not only to the nature of the adsorbed species and the amount of ferrihydrite, but also the degree to which ferrihydrite transformation and solubility are affected by particular adsorbates. At present we are examing the effect of silica on ferrihydrite structure and transformations, as well as the structure of natural samples containing significant arsenate.

References

1. G.A. Waychunas, B.A. Rea, C.C. Fuller and J.A. Davis, X-Ray Absorption Fine Structure, ed. S. Samar Hasnain, Ellis Horwood New York, 215-217, 1991.
2. G.A. Waychunas, J.A. Davis, C.C. Fuller and B.A. Rea, SSRL Activity Report 1990, 48-49.
3. G.A. Waychunas, B.A. Rea, C.C. Fuller and J.A. Davis, submitted to Geochimica et Cosmochimica Acta.
4. R.K. Vempati and R.H. Loeppert, Clays and Clay Minerals 37, 273-279, 1989.

TOTAL REFLECTION X-RAY FLUORESCENCE SPECTROMETRY OF METAL SAMPLES USING SYNCHROTRON RADIATION AT SSRL.

Project leader: W.F.Sommer[c]

Authors:

F.Hegedüs[a],P.Wobrauschek[b],W.F.Sommer[c],R.W.Ryon[d],Ch.Streli[b],P.Winkler[a],
P.Ferguson[c],P.Kregsamer[b],R.Rieder[b],M.Victoria[a],A.Horsewell[e]

(a) Paul Scherrer Institute,Villigen,Switzerland
(b) Atominstitut der österreichischen Universitäten,Vienna,Austria
(c) Los Alamos National Laboratory,U.S.A.
(d) Lawrence Livermore National Laboratory,U.S.A.
(e) Risö National Laboratory,Roskilde,Denmark

ABSTRACT

In this experiment it was demonstrated that a TXRF spectrometer, using monoenergetic synchrotron radiation as the primary X-ray source, is suitable to measure the the concentration of transmutational elements in Cu and Fe metal matrices.

In a typical irradiation of copper with 590 MeV protons or with spallation neutrons, where the damage dose is 0.4 dpa,the calculated concentration of transmutational elements is Ni:25; Co:8; Fe:8 µg/g.

The results show that the minimum detectable concentration is lower than these values. The energy of the synchrotron radiation was set just below the K-edge energy of the matrix element, eliminating therefore the large peak due to the matrix. As an example, in the case of Cu (Z=29) matrix, the minimum detectable concentration of Ni (Z=28) was as low as 3 µg/g.

In order to check systematically the possible geometric arrangements of beam direction - reflector position - detector position a new vacuum chamber was designed and tested. It provides all technical components for remote control of the adjustment procedure to align the reflector in total reflection geometry. Two ways of positioning the reflector in the beam, vertical to the plane of polarization and parallel to that plane were investigated, to find the best excitation condition and lowest limits of detection. A few pg corresponding to a concentration of ng/g of samples where the matrix can be easily removed as in aqueous or acidic solutions and 50 ng/g concentration of metals in a light matrix as in oil were found as detection limits.

1. INTRODUCTION

A program is in progress at PSI and at LAMPF to study radiation damage in first wall materials of future fusion reactors. The program uses the Proton IRradiation EXperiment (PIREX) at the PSI 590 MeV ring accelerator and the LAMPF spallation neutron source (LASREF). The effects of displacement damage and He produced by the protons or neutrons on microstructure and mechanical properties are being evaluated. During the irradiation, due to nuclear reactions,a considerable amount of transmutational elements are produced and this effect is expected to have an impact on the microstructure and mechanical properties.In a typical irradiation of 1 dpa (displacement per atom) in copper the concentration of transmutational elements could be as high as 60 ppm of Ni, 20 ppm of Co and Fe, 15 ppm of Mn, Cr, V and other elements being produced at lower rate. Due to the uncertainties on the cross sections, the reliability of these calculated values is not too good, therefore it is necessary to measure the concentrations.

Several methods, e.g. mass spectroscopy, XRF and TXRF (with X-ray tube) etc, were tested to measure directly the chemical yield of transmutational elements, but the detection limit, specially for elements next to the matrix, was too high.

Compared to the conventional X-ray tubes, the use of synchrotron radiation, as the primary X-ray source for TXRF spectrometry, offers many advantages: high intensity, natural collimation, linear polarization, energy tunability etc. It has become the most promising method to measure the transmutational elements.

2. AIM OF THE EXPERIMENT

The present measurements had three aims:

The first one was to measure the lowest limit of detection (LLD) and minimum detectable concentration (MDC) of trace elements in copper and iron metal matrices.

The second aim of the experiment was to check the reproducibility of the measurements on samples prepared from the same material. Furthermore, the contamination from cutting tools, the environment, the solvents etc. was also investigated.

The third aim of the experiment was to investigate the effect of the polarized beam.Therefore the fluorescence and scattered X-rays have been detected vertically and horizontally to the plane of polarization.

3. DESCRIPTION OF THE EXPERIMENT

Fig.1 shows the schema of a TXRF spectrometer.The monoenergetic SR beam enters on the surface of the quartz plate with an angle smaller than the critical angle. In this case the beam is totally reflected, i.e. the intensity of the scattered radiation is low. The sample is directly pipetted on the surface of the quartz plate and the elemental composition can be determined by measuring the fluorescence X-ray spectrum induced on it.

FIG.1. PRINCIPLE OF THE TXRF SPECTROMETER

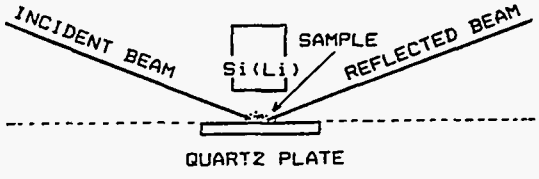

Both main elements of the spectrometer,the beam cut-off slit and the sample holder can be moved vertically and can be rotated by means of remote control with an accuracy of 0.001 mm or 0.2 min respectively. The vacuum chamber was made from one piece of stainless steel by spark erosion, and serves therefore as a solid base to hold the spectrometer elements.

The fluorescence X-ray spectrum is measured by means of a Si(Li) detector (active area: 30 mm2). The detector to sample distance is about 5 mm. The energy resolution of the detector is better than 150 eV.

The TXRF spectrometer was installed at the 10-2 beam line at SSRL. The beam was monochromated by means of a double crystal (Si(III)). In the case of a typical current of 50 mA, the monochromated beam intensity, in the energy range of 7-9 keV, was 2-3 order of magnitude higher than the intensity from a conventional X-ray tube at the sample position.

The incidence angle on the quartz glass was 2 mrad, which is less then the calculated critical angle (4.30 and 3.40 mrad for 7.0 and 8.9 mrad respectively). The incidence angle was determined by measuring the distance between the direct and the reflected beam at 400 mm away from the sample.

The surface of the metal foils, weighing 1.5 to 9 mg, had been cleaned with acetone,then they were dissolved in pure concentrated acids. The samples were prepared by pipetting 5 µl of diluted solution on the centre of a synsil glass plate (d=30 mm,t=3 mm). The liquid was evaporated by heat (hot plate) or by vacuum. The diameter of the spot was between 3 and 4 mm.

80 spectra of copper and 11 spectra of iron samples were measured. The primary beam energy was set just below the K edge energy of the matrix element:8.888 keV for copper and 7.014 keV for iron samples.

4. EVALUATION OF THE MEASUREMENT

4.1. X-RAY SPECTRUM ANALYSIS

The counting time of the measurements was between 500 and 1500 s, this time was needed to get acceptable statistics for the weak peaks. The Ka peak areas have been evaluated by means of the PCRFAN program of the Atominstitut of Vienna.

4.2. CALIBRATION OF THE SPECTROMETER

The detector response vs. energy calibration was made with a series of elements weighing each 1.0 ng. The measured Ka peak areas have been normalized to the Ka peak area of Ti. Fig.2. shows the spectrum of a calibration sample containing 1 ng of Ti, V, Co and Ni.

4.3. MATRIX EFFECT

The minimum detectable concentration (MDC) vs.sample weight was measured with 5.0, 2.0, 0.5 and 0.2 μg samples. It was seen that the optimum weight should be between 0.5 and 1.0 μg. Fig.3. shows the spectrum of the same sample as given in Fig.2. but with 0.2 μg of additional Cu metal matrix.Due to the strong scattering and absorption of the primary beam in the Cu matrix, the Si Ka and the 8.88 keV (primary beam) peaks have increased and the Ti, V, Co, Ni peaks have decreased.

FIG.2. X-RAY CALIBRATION SPECTRUM

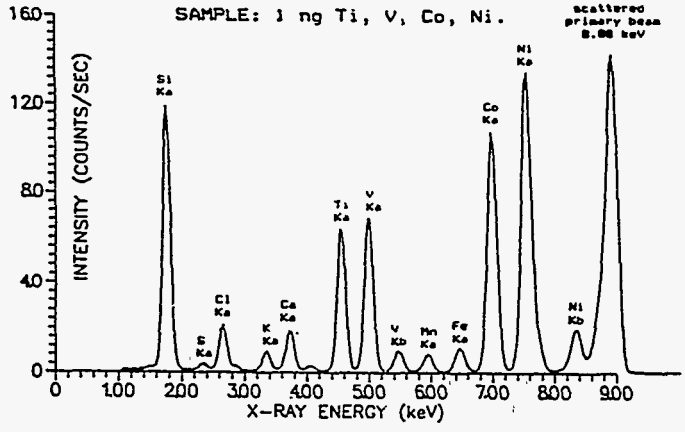

FIG.3. X-RAY CALIBRATION SPECTRUM WITH Cu MATRIX

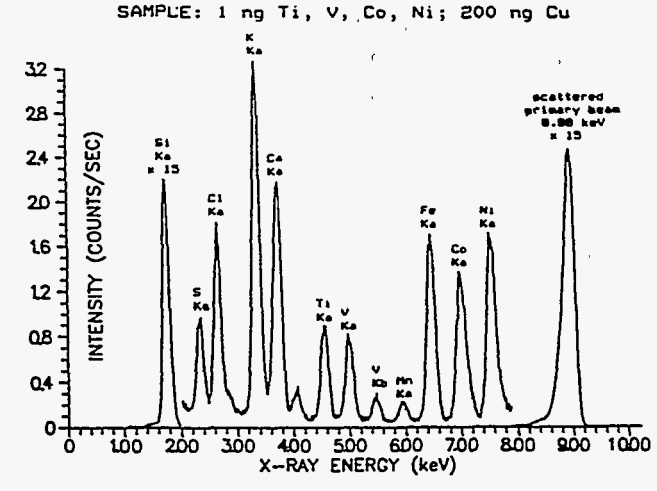

4.4. LOWEST LIMIT OF DETECTION AND CONCENTRATION

LLD (defined as $3*\sqrt{B}*W/AN$, where B:background, W:trace element weight and AN:trace element netto peak area) and MDC (defined as LLD/WS, where WS: sample weight) have been evaluated and are given in Table 1.

Table 1. LOWEST LIMITS OF DETECTION AND CONCENTRATIONS

Element	Matrix	SR energy keV	LLD pg	MDC μg/g
Ti	no	8.880	1.1	----
Ti	Cu:0.2 μg	8.880	2.7	14
Ti	Cu:0.5 μg	8.880	6.2	12
V	no	8.880	1.1	----
V	Cu:0.2 μg	8.880	3.3	16
Cr	Cu:0.5 μg	8.880	2.6	5.2
Fe	Cu:0.2 μg	8.880	1.5	8.0
Fe	Cu:0.5 μg	8.880	1.9	3.8
Fe	Cu:2.0 μg	8.880	19.2	9.6
Co	no	8.880	0.6	----
Co	Cu:0.2 μg	8.880	1.6	7.9
Co	Cu:0.5 μg	8.880	2.5	5.0
Co	Cu:2.0 μg	8.880	24.7	12
Ni	no	8.880	0.5	----
Ni	Cu:0.2 μg	8.880	1.2	6.0
Ni	Cu:0.5 μg	8.880	1.7	3.4
Ti	no	7.014	1.8	----
Ti	Fe:0.2 μg	7.014	2.5	13
Cr	no	7.014	1.5	----
Cr	Fe:0.2 μg	7.014	1.9	10

4.5 CONCENTRATION OF TRACE ELEMENTS AND CONTAMINATION

From each irradiated and unirradiated material several samples have been prepared and measured,then remeasured with Ti internal standard. The weight of the added Ti was between 0.5 and 2.5 ng. The measured trace element concentrations in the irradiated material are much higher than the calculated transmutational concentrations. Specially in the case of a copper matrix, the measured Fe concentrations are 2-3 order of magnitude higher than calculated values. Furthermore the measured trace element concentrations in unirradiated materials are also much higher than the values given by the producer company (e.g. in Cu : Fe < 3 μg/g).

The measurements of empty quartz plates and the used solvents have shown some contamination of mostly iron, which should be taken off from the measured total impurities. The subtracted values are at least one order of magnitude less than the measured concentration values. Therefore it seems the sample itself, very probably its surface, is contaminated.

4.6. COMPARISON OF TWO DIFFERENT GEOMETRIES IN TXRF

To use the polarisation of the SR beam the active volume of the detector has to be situated in the plane of the orbit perpendicular to the beam direction. Placing the reflector in the same plane (horizontal plane),the sample is efficiently excitated because of the natural beam collimation. The fluorescent signal undergoes a strong self-absorption in the sample on its path to the detector. Furthermore the extension of the sample relating to the detector causes long distances for the caracteristic radiation and leads to small solid angles. Arranging the reflector in the vertical plane, the excitation condition is worse compared to the previous case, because most of the primary intensity is blocked by the entrance slits.The vertical divergence is so small, that only about 4 mm in the vertical plane are irradiated with strongly varying intensity and loss of polarization degree. The fluorescent radiation is optimally collected as the path length can be minimized. Therefore no absorption effects are expected in this thin film condition. The results of the polarized beam experiment are given in Table 2.

Table 2.POLARIZED BEAM EXPERIMENT:MEASURED SENSITIVITIES
(extrapolated to a counting time of 1000 s
and to a beam current of 50 mA)

Oil sample: 30 ppm of metals in oil; no matrix removal;
thin film on quartz reflector plate.

DETECTOR	REFLECTOR	LLD (Ni in oil) ng/g	SENSITIVITY cps/(ng/g)
horizontal	horizontal	50	12
horizontal	vertical	150	4

Water sample: 0.1 ppm of metals in water; matrix removal;
3 µl drop on quartz reflector plate.

DETECTOR	REFLECTOR	LLD (Co in water) pg	SENSITIVITY cps/ng
horizontal	horizontal	5	50
horizontal	vertical	3	100

4.7. UNCERTAINTY OF THE MEASUREMENT

The main sources of uncertainty of the measurement are: inhomogenity of the material sample and of the internal standard on the quartz glass plate; reproducibility of the incidence angle and sample position; and counting statistics. In order to estimate the overall uncertainty, a series of measurement have been done with samples prepared from the same solution on different quartz plates. The Ka peak intensities, due to the geometry variation, are not consistent. However by normalizing the Ka intensities to the Ka intensity of the internal standard, the measured values became consistent.

5. CONCLUSION

The use of synchrotron radiation gives impressive results, especially if due to the sample structure, special preparation techniques can not be applied,so the matrix is suppressed either by the polarization effect for low Z elements and by the sharp tunability to an energy value just below the respective absorption edge of the high Z matrix.

In many applications the advantage of a required sample amount of a few micrograms is appreciated especially if radioactive substances are involved.

The results of the experiment confirm that through the use of monoenergetic SR as the primary X-ray source the performance of the TXRF spectrometer was considerably improved. For samples without matrix, the lowest limit of detection was as low as 0.5 pg. In a Cu (Z=29) matrix of 0.5 µg, the minimum detectable concentration of the neighbor element nickel (Z=28) was 3 µg/g, which is two orders of magnitude lower than the results obtained with usual TXRF or with other detection methods.

It can be concluded that this detection method is well suitable to measure the concentration of transmutational elements in irradiated metal samples. However, the problem of decontamination has to be clarified.

ACKNOWLEDGEMENTS

The beam time for this experiment at beam line 10-2 was provided by PRT (Dr.Marvin J.Weber) and is gratefully acknowledged.

The authors would like to express their thanks to the scientific, technical and administrative personal of SSRL for their helpful cooperation.

COMPOSITIONAL ANALYSES OF U.S. AND KUWAITI AEROSOLS

Thomas A. Cahill, Kent Wilkinson, Pat Feeney,
Dan Shadoan, and Bruce Kusko

Air Quality Group, Crocker Nuclear Laboratory (CNL),
University of California, Davis, CA 95616-8569

Compositional analyses of atmospheric aerosols is essential to understanding aerosol sources, transport, transformations, effects (health and welfare), and removal. Yet the mass of aerosol particles that can be collected is usually only on the order of 10 to 100μg, especially at clean, remote sites or in aircraft. Crocker Nuclear Laboratory has pioneered the complete compositional analysis of collected aerosols via a mixture of gravimetric, optical, atomic and nuclear techniques, giving the major and minor components of collected mass to about 0.1ng/m^3 for our remote ground stations around the world. However, this is not good enough for trace elements when one is talking about global scale transport such as from Kuwait to the Mauna Loa Observatory (MLO), Hawaii. We detected a series of unusual aerosol plumes in late February and March 1991, that could be from Kuwait. For positive identification, we wished to see the characteristic V/Ni ratio of Kuwaiti smoke. For this purpose, we participated in NOAA/NCAR flights over Kuwait in May 1991, and analyzed a historic collection of Kuwaiti oils. Finally, we needed better analyses of airborne samples for a major National Park Service (NPS) study of haze aerosols near Mt. Rainier National Park, summer 1990. The anticipation was that the 15keV polarized x-rays of beamline 10-2 at SSRL would give improved sensitivity for K-lines of the important tracer transition metals, V through Br, plus L-lines of heavy metals.

The beamline 10-2 hutch was modified for x-ray fluorescence analysis by a temporary He chamber adequate to displace almost all air, reducing x-ray scatter and the important K-α line of atmospheric krypton. A 30m^2 Si(Li) detector was used to collect data from a variety of thin film foils and National Bureau Standard, Standard Reference Material #1533 and #1477, to make results traceable to primary elemental standards. We made extensive modifications to our aerosol filter supports to avoid scattered primary x-rays. Despite the loss of time associated with these measures during this, our first SSRL run, excellent data were obtained on all types of samples except the liquid oil cells, for which better sensitivity was achieved with 4.5MeV protons at Davis. A factor of 3 improvement was obtained in minimum detectable limits as compared to minimum detectable limits obtained by 5 minute PIXE runs at UCD for transition metals like Ni and As. The high sensitivity particulate areosol samples collected at Mt. Rainier National Park yielded an atmospheric concentration of 7pg/m^3 for Se and nearby elements.

The results obtained over Kuwait were less impressive, since the abundant soils flooded the spectra with strong secondary x-ray lines from elements like iron. Even so, in 3 out of 4 samples, V and Ni were seen at levels of ~50ng/m^3, or about 2ppm of the 1mg collected aerosol. These agreed well with the V/Ni ratio of the combusted oil, showing little fractionation of metals occurred in the (unusual) Kuwaiti combustion process.

Acknowledgements:
We wish to thank all of the Air Quality Group staff who participated in the SSRL runs, and the SSRL staff for assisting us in obtaining He and other supplies on short notice. We wish to especially thank Dick Ryan for scheduling, training, and use of his equipment. This work was performed with support of Contract #CX0001-8-0017-NCS-A.

X-RAY ABSORPTION MEASUREMENTS ON THE SITE DISTRIBUTION OF IRON IN SILICATE PEROVSKITE

E. Knittle, G. Li, C. Closmann, X. Wang and F.G. Bridges
University of California, Santa Cruz

The crystallographic site distribution of iron in the perovskite-structured silicates which comprise the bulk of the Earth's mantle (670 to 2900 km depth in the planet), is important in the understanding the chemical history and evolution of the Earth's interior.[1] In particular, both the limited solubility of Fe in $(Mg_{1-x}Fe_x)SiO_3$ perovskite ($x<0.2$) and the strong partitioning of iron into high-pressure melts relative to coexisting perovskite minerals must ultimately result from the site distribution and valence of iron in this mineral. Therefore, the goal of our study was to clarify the site distribution of iron in $(Mg_{0.88}Fe_{0.12})SiO_3$ in the perovskite structure. The study of such minerals is complicated by the fact that they can only be synthesized at very high pressures (above 25 GPa) and temperatures above 1500 K with maximum sample volumes of 50 micrograms.

The subject of site distribution of iron in $(Mg_{0.88}Fe_{0.12})SiO_3$ in the perovskite structure is controversial. The general crystal chemistry of perovskite-structured silicates is describable as orthorhombic perovskites (the space group is Pbmn) with Si^{4+} in the VI-fold coordinated site bonded with oxygen and the Mg^{2+} is in a distorted VIII-XII-fold coordinated site.[2] If the behavior of Fe^{2+} in this high-pressure mineral is similar to low pressure minerals, then Fe^{2+} would be expected to substitute for Mg^{2+}. In the perovskite structure, that would imply that iron prefers a large, distorted, VIII-XII-coordinated crystallographic site. However, the preference of Fe^{2+} for this site makes it difficult to explain the geochemical behavior of iron at high pressures, especially the strong partitioning of this element into high-pressure liquids. Therefore, on crystal chemical grounds it has been argued that Fe^{2+} must prefer the VI-coordinated site in silicate perovskite, a site which is normally occupied by Si^{4+}.[1]

Previous work on this subject has been limited to two studies utilizing extended x-ray absorption spectroscopy (EXAFS) in a fluorescence geometry and one single-crystal x-ray diffraction study.[3,4] In one of the previous EXAFS studies, the iron was found to be in the VI-site.[3] In the other the authors concluded, based on the near-edge structure alone, that the Fe^{2+} was in the VIII-XII site, a conclusion consistent with single-crystal x-ray data (presented in the same paper).[4] To further complicate matters, the method of synthesis of the high-pressure perovskite minerals was different between the two EXAFS studies, as different high-pressure devices were used.

In our study, we have attempted to improve the quality of the data and therefore solve the problem of site distribution of Fe in $(Mg_{0.88}Fe_{0.12})SiO_3$-perovskite. Two sets of samples, with about 30-50 μg of material each, were synthesized from natural, low-pressure mineral ($(Mg_{0.88}Fe_{0.12})SiO_3$ enstatite) at pressures between 30 and 35 GPa using the diamond anvil cell coupled with laser-heating. One set of samples was doped with a small amount of U^{4+} (our initial hope was also to measure the site distribution of uranium in these minerals; however, our doping concentration of uranium was too low and we were unable to obtain EXAFS spectra of the uranium). The samples were examined both optically and using x-ray diffraction to confirm the presence of single-phase silicate perovskite: based on our observations, we believe these samples to be 90-95% silicate perovskite with the balance being either unreacted starting material or possibley glass. Transmision Fe-K EXAFS and near-edge (XANES) spectra were collected at 77 K for the two different samples using the Stanford Synchrotron Radiation Laboratory (SSRL) Beam Line 10. We note that the quality of our data is superior to that obtained previously (Figure 1). In addition to the silicate perovskite samples, we also measured the spectrum of the low-pressure enstatite starting material for comparison.

The results of our EXAFS experiment are shown in Figure 2. These are the Fourier transforms of the average of three Fe-K EXAFS spectra obtained for the high-pressure perovskite phase without the uranium doping (solid line) and the low-pressure mineral of the same composition (enstatite: dotted line). From neutron diffraction data, Fe^{2+} is known to occupy a VI-fold coordinated site in the low-pressure mineral with an average first-neighbor bond length of 2.04 Å.[5] Qualitatively, the high-pressure mineral appears to have the same first neighbor coordination environment as the low pressure phase, and a different second and third neighbor environment. The Fourier transform results for the high-pressure perovskite phase were fit to obtain an

estimate for the bond length and coordination number using an FeO and a theoretical model compound. The results give a well-defined first neighbor distance for the perovskite of 1.9±0.1 Å with a coordination number of 4±1. We note that the coordination number is probably unreliable and a result of inhomogeneities in the sample material. This first neighbor distance is consistent with Fe^{2+} being present in the VI-fold site of silicate perovskite which, based on x-ray diffraction data, has an expected bond length between the cation and oxygen of 1.8 Å. The Fe^{2+} results are not consistent with being in the larger, distorted VIII-XII-fold site, which would have a range of bond distances between 2.0 and 2.5 Å and would produce a much wider first neighbor peak.

In addition, a qualitative comparison of the pre-edge features of the low-pressure enstatite phase and the high-pressure silicate perovskite show that the amplitude of the perovskite pre-edge feature is similar or slightly smaller than that of enstatite. Although not definitive, this observation suggests that iron occupies a similar or somewhat less distorted crystallographic site in enstatite than in perovskite. Again, this is consistent with occupancy of Fe^{2+} in the VI-fold site in silicate perovskite.

The results for the uranium-doped silicate perovskite samples are somewhat different than for the uranium-free samples. Specifically, the first neighbor environment is significantly broader, by about 50%, than either the low-pressure enstatite phase or the uranium-free silicate perovskite. This result is more consistent with the Fe^{2+} occuping either the distorted VIII-XII-fold site or both this site and the VI-fold site. Although preliminary, our results indicate that the "first" neighbor distance is best fit by considering a range of eight nearest-neighbor distances from 2.0 to 2.5 Å. This is in accord with what would be expected from the bond distances between the cation and anion in the distorted VIII-XII-fold site, based on x-ray diffraction data.

These results are intriguing in that they imply that coupled substitution of several cations can influence the elemental site distributions in silicate perovskite. In the samples without uranium, the iron prefers the VI-fold site. However, in the samples where we believe there is substitution of both Fe^{2+} and U^{4+} into the structure, the Fe^{2+} is found in the VIII-XII-fold site. This implies that the U^{4+} more readily substitutes into the VI-site. If this speculation is correct, then we have potentially solved the discrepancy between the two previous EXAFS studies. Specifically, small differences in trace element chemistry of the perovskites (produced by subtle differences in the synthesis techniques) between the two previous studies may be result in differences in iron partitioning between samples. We note that further work is required to fully document and justify these conclusions, in particular, we must obtain EXAFS spectra for both Fe^{2+} and U^{4+} within the same sample.

References

1. Q. Williams, E. Knittle and R. Jeanloz, in *Perovksites: A Structure of Great Interest in the Earth and Material Sciences*, A. Navrotsky and D.J. Weidner, editors, American Geophysical Union, 1-12, 1989.
2. T. Yagi, H.K. Mao and P.M. Bell, *Phys. Chem. Minerals, 3*, 97-110, 1978.
3. W.E. Jackson, E. Knittle, G.E. Brown and R. Jeanloz, *Geophys. Res. Lett., 14*, 224-226, 1987.
4. J.B. Parise, Y. Wang, A. Yeganeh-Haeri, D.E. Cox and Y. Fei, *Geophys. Res. Lett., 17*, 2089-2092, 1990.
5. N. Morimoto, D.E. Appleman, and H.T. Evans, *Zeits. Kristall., 114*, 120-147, 1960.

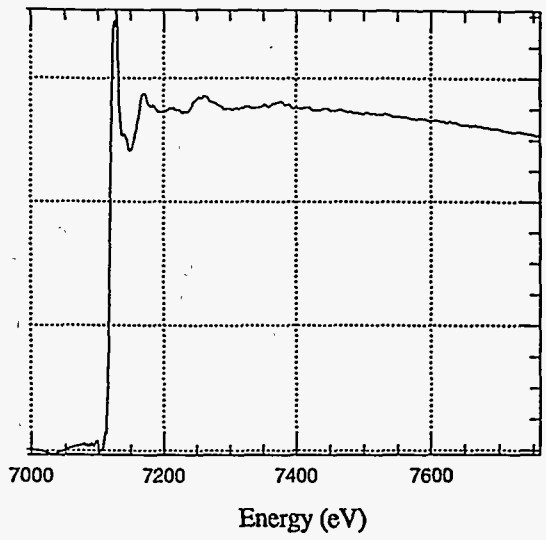

Figure 1. The Fe-K EXAFS spectrum of 50 micrograms of $(Mg_{0.88}Fe_{0.12})SiO_3$ in the high-pressure perovskite structure.

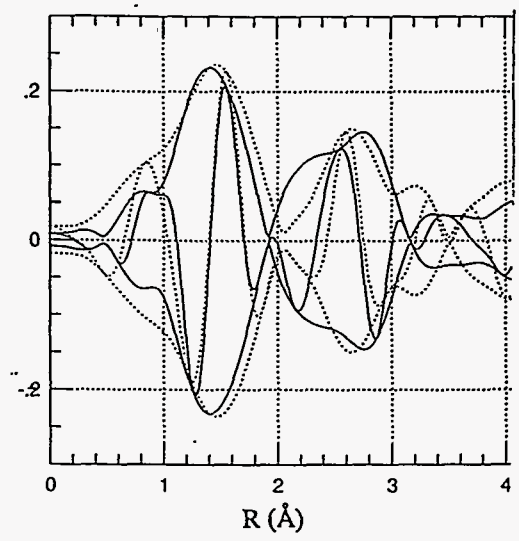

Figure 2. The Fourier transform of the EXAFS data for $(Mg_{0.88}Fe_{0.12})SiO_3$ in the high-pressure perovskite structure (solid line) and low-pressure enstatite structure (dotted line). Note the similarity in first-neighbor environment.

VUV PROPOSALS

NEXAFS OF LANGMUIR BLODGETT AND SELF ASSEMBLED ORGANIC FILMS ON SOLID SURFACES

M. Samant, Y. Wu, B. Hermsmeier, and J. Stöhr

IBM Research Division
Almaden Research Center
650 Harry Road
San Jose, California 95120-6099

The Near Edge X-ray Absorption Fine-Structure Spectroscopy (NEXAFS) data reported here were collected on beam line 8-2. High resolution absorption data at the Carbon edge were obtained from Langmuir Blodgett monolayer of cadmium arachidate on silicon surface and Self Assembled monolayers of docosyl thiols on Au (111) and Ag (111) surfaces. Surface x-ray diffraction studies in the case of self assembled films indicate that individual organic chains within the monolayer films are hexagonally close packed on the (111) oriented surfaces of Au and Ag. The individual chains are typically tilted with respect to the surface normal. NEXAFS data will be used to determine the tilt angles which will be compared to those obtained from x-ray diffraction and other indirect techniques. Figure 1 shows the high resolution NEXAFS data from the Langmuir Blodgett film. Figure 1a and 1b show the result of the NEXAFS scans with the polarization direction of the x-ray beam parallel and at 70° from the sample surface respectively. This is the first report of observation of splitting in the feature corresponding to transition to the antibonding orbitals involving C-H bonds (see the insets in Figure 1). This is exciting as this may allow us to determine whether the tilted organic chains have a preferred spin orientation along their tilt directions. A detailed analysis of these data are presently in progress.

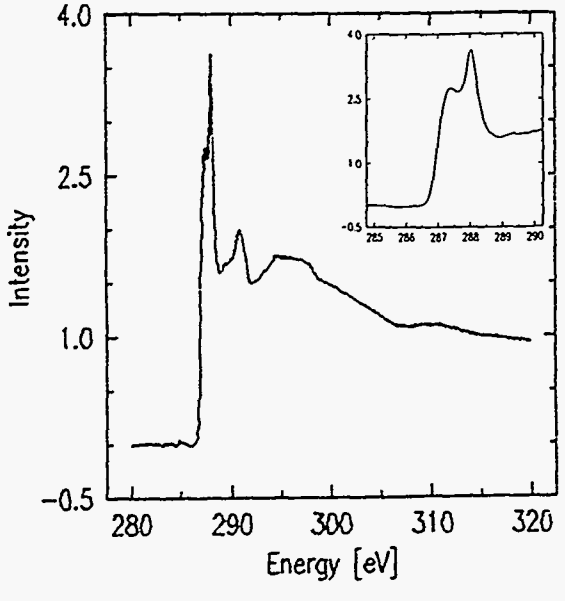

Figure 1a

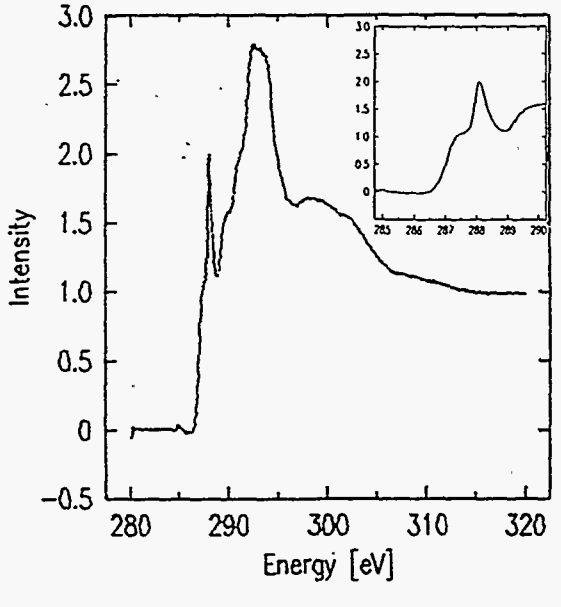

Figure 1b

Fermi Surfaces and Excitation Spectra of High-Temperature Superconductors

Z.-X. Shen, W.E. Spicer, and D.M. King
Stanford Electronics Laboratory, Stanford University, Stanford, CA 94305

In a recent letter to SCIENCE, we discuss the issue of Fermi surface and quasiparticle excitation spectra of high-Tc superconductors.[1] We point out some important experimental facts missing in an earlier article that have significant bearings on the conclusions; We show an experimental example illustrating that the excitation spectra of a metallic cuprate can not be well pictured by band theory and instead is better described as doped insulator.

Fig.1 summarizes our result. We concentrated on the main valence band, in particular the first 2 eV window from E_F. Panel (b) presents the photoemission spectra taken with $k_{//}$ at X point in the two dimensional Brillouin zone. There is a band near the Fermi level which agrees remarkably well with a band calculation as depicted in the inset in panel (a).[2] Besides this band, there is basically no spectral weight (or density of state (DOS)) in the data until a prominent feature near -1.8 eV. This is very different from the calculated DOS shown in panel (a). Even though it is very hard to draw conclusions about the DOS from angle-resolved photoemission data, we believe that the disagreement between the photoemission data and the band calculation depicted in panels (a) and (b) is real based on the following considerations. First, we have searched a very large portion of the Brillouin zone, and we always find a very low density of states for the first 1.8 eV, similar to the situation presented in panel (b). Second, as depicted in the inset, there are many calculated bands in the first two eV window in addition to the one that crosses the Fermi level along Γ-X direction. In principle, the data in panel (b) should be the partial DOS at X point and should reflect many of these flat bands; however, basically none of these bands are present in the experimental data. It is very unlikely that all of them are absent due to selection rule or matrix element effects. Therefore, we suggest that although the band calculation did an excellent job in reproducing the Fermi surface, it did very poorly on the excitation spectra.

Now the question is whether we can find a better explanation for our data. We suggest that, in fact, the $Nd_{1.85}Ce_{0.15}CuO_{4-\delta}$ data can be better explained by the doped insulator picture as illustrated in panels (c) and (d). The parent compound of Nd_2CuO_4 has a charge transfer gap of 1.5 eV,[3] and doping moves the Fermi level into the upper Hubbard band. This explains very naturally why we do not see much spectral weight from -1.8 eV to E_F since it is the energy window of the charge transfer gap. In addition, this picture can account for the valence band satellite observed in this system.[4] The most critical test for this picture is whether it can explain the observed Fermi surface. The Luttinger theorem guarantees the volume of the Fermi surface but not necessarily the shape since it is also influenced by the anisotropy of the system on which the band theory appears to have done a good job. We note that a recent Monte Carlo simulation of the Hubbard model appears to show a Fermi surface and it associate bands that are consistent with experimental data.[5]

Therefore, we argue that our data provides strong support for the doped insulator picture for high-temperature superconductors. The beauty of this picture is that we can understand the Fermi surface and the spectral weight function (or DOS) at the same time. Moreover, we do not have to artificially separate the metallic and insulating cuprates by assuming that they belong to different phases.

Reference:
(1) Z.-X. Shen et al., submitted to Science
(2) This band is not very visible near E_F with $k_{//}$ at X point.(ref.3) However, it is very visible near E_F with $k_{//}$ values where the band is about to cross the Fermi level.
(3) S. Uchida et al., Physica C **162-164**, 1677 (1989)
(4) J.W. Allen et al., Phys. Rev. Lett. **64**, 595 (1990)
(5) A. Moreo et al., Phys. Rev. B **41**, 2313 (1990); D.J. Scalapino, High Temperature Superconductivity Proc., p 314, Bedell, Coffey, Pines, Schrieffer, eds. (Addison Wesley, 1990); In these articles, the authors calculated $\langle n_p \rangle$ for U = 4t (half the band width) and found that on a 16 x 16 lattice, the locus of points where $\langle n_p \rangle = 0.5$ fell on the non-interacting Fermi surface. E. Dagotto et al., preprint; In this article, the authors found on a 4 x 4 lattice that the quasi-particle peak crosses the Fermi surface near the point where the tight binding band crosses.

Figure Caption:
(a) Calculated total DOS. Inset: calculated bands along Γ-X high symmetry direction. The data points are from our experiment. (b) Angle-resolved photoemission data from $Nd_{1.85}Ce_{0.15}CuO_4$ with $k_{//}$ at X point. The energy window of the spectra does not cover the satellite. The satellite is depicted following reference 4. (c) Illustrative picture for the spectra weight of Nd_2CuO_4. The energy difference between the satellite and the empty upper Hubbard band is mianly determined by the Coulomb energy U, and the 1.5 eV insulating gap is mainly determined by the charge-transfer energy. (d) Illustrative picture for $Nd_{1.85}Ce_{0.15}CuO_4$, doping moves E_F into the upper Hubbard band.

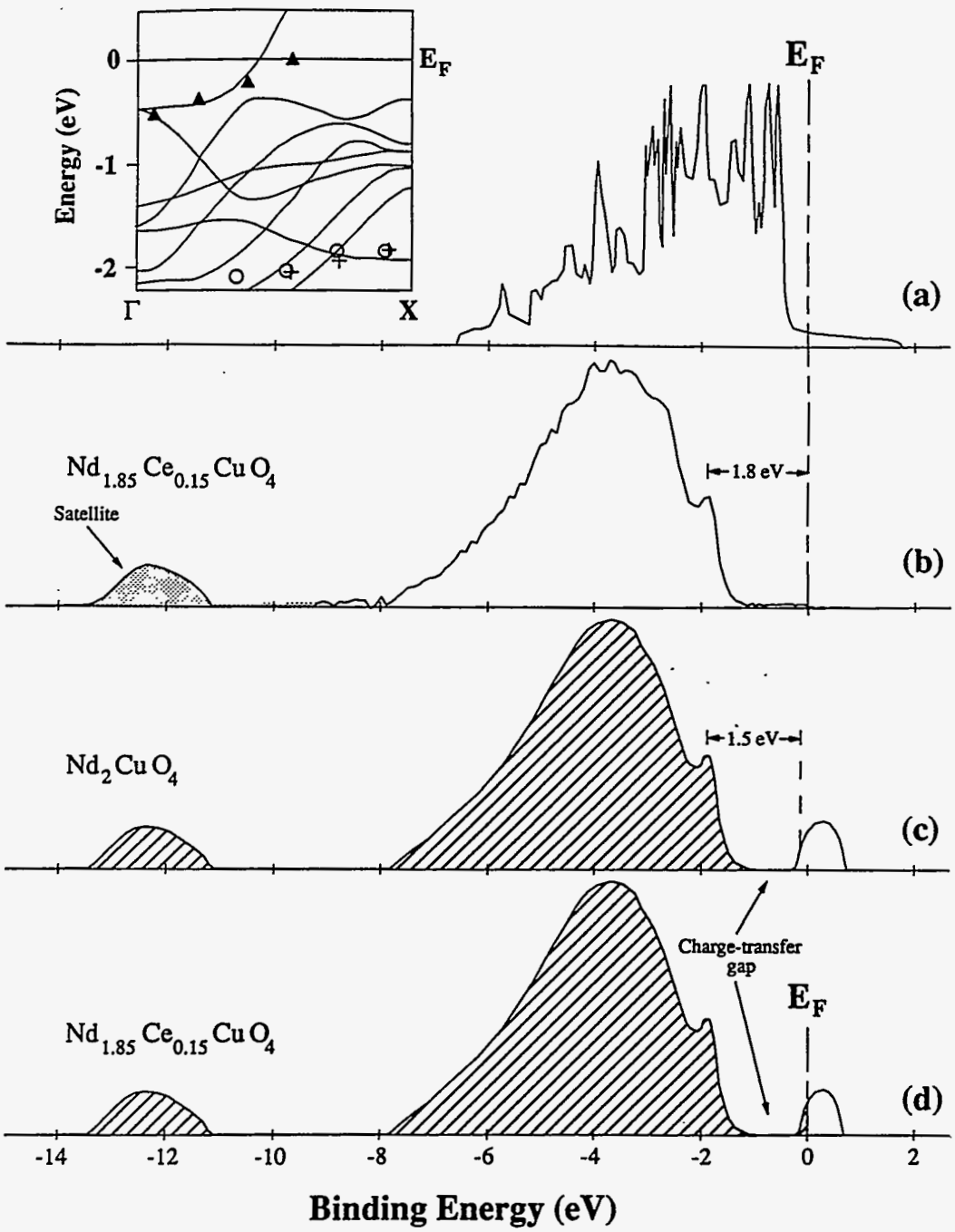

Fermi Surface and Electronic Structure of $Nd_{1.85}Ce_{0.15}CuO_{4-d}$

D.M. King,(1) Z.-X. Shen,(1) D.S. Dessau,(1) B.O. Wells,(1) W.E. Spicer,(1) A.J. Arko,(2) D.S. Marshall,(1) E.R. Ratner,(1) J.L. Peng,(3) Z.Y. Li,(3) and R.L. Greene (3); (1)Stanford Electronics Laboratory and Stanford Synchrotron Radiation Laboratory, Stanford University, Stanford, California 94305, (2)Los Alamos National Laboratory, Los Alamos, New Mexico 87545, (3)Center for Superconducting Research, Department of Physics, University of Maryland, College Park, Maryland 20742

Fermi surface and electronic structure information provide a direct exposition of the physics underlying high temperature superconductivity. Over the past two years, angle-resolved photoemission has played a key role in revealing the Fermi surface and electronic structure of the p-type superconductors. It is well accepted now that, despite the compelling evidence of correlation effects, the Fermi surface of the p-type superconductors agrees well with the LDA calculated Fermi surface [1-4]. The LDA calculated Fermi surface of the p-type superconductors has also been verified by other experimental techniques such as the de Hass van Alphen (dHvA) and positron annihilation experiments [5, 6]. For the n-type superconductors, on the other hand, no experiments have succeeded in revealing Fermi surface information. The positron annihilation experiment is difficult in this case because the positrons do not reside long in the metallic CuO_2 planes, resulting in a very weak signal from the Fermi surface, and the dHvA experiments on cuprate superconductors are nontrivial because of their high critical fields ($H_{c||}$). Angle-resolved photoemission experiments have been performed on n-type superconductors in the past [7]; however, they have not yet succeeded in revealing any Fermi surface information.

We report here our recent angle-resolved photoemission study of the n-type superconductor, $Nd_{1.85}Ce_{0.15}CuO_{4-\delta}$.[8] By using cleaved high quality single crystal samples and providing the necessary experimental conditions, we have succeeded in observing the Fermi surface. Our data clearly shows that a band crosses E_F at approximately the same place in the Brillouin zone as predicted by the LDA calculation. Furthermore, we found that the dispersion of the band near E_F agrees quite well with the LDA calculation. These results are consistent with earlier data from p-type superconductors indicating that the LDA calculation gives a good prediction of the Fermi surface. In addition to the Fermi surface information, we have observed some other interesting aspects of the electronic structure. Despite the LDA calculation's remarkable success in predicting the Fermi surface, we found that it has difficulty describing the distribution of spectral weight. For example, our data shows that aside from the band near E_F, there is virtually no spectral weight until a prominent feature near -2 eV binding energy, in contrast to the LDA prediction for this energy window. It appears necessary to include the coulomb interaction energy, U, into the model to reconcile this spectral weight problem. If we interpret the -2 eV feature as the rim (valence band maximum or VBM) of the parent insulating compound, then within the Mott-Hubbard framework with a charge transfer gap of 1.5 eV [9], we would find that E_F lies inside the upper Hubbard band ($3d^{10}$), which differs from an earlier report [10]. This interpretation of our data is consistent with results from slave-boson mean-field calculations and Monte Carlo simulations of multi- and single-band Hubbard models [11,12].

Fig.1(a) presents angle-resolved photoemission data taken with $k_{||}$ along the Γ-X-Γ high symmetry direction. The k-space locations in the Brillouin zone of the spectra are shown in the inset of Fig.1(a) [13]. The photoemission spectra display distinctive momentum dependent effects, and a band clearly disperses through E_F. To the best of our knowledge, our observation of a band dispersing through E_F is the first time information has been obtained about the Fermi surface of a n-type superconductor, the most relevant part of the electronic structure for understanding the mechanism of superconductivity. We think that there are three essential reasons for our success. First, the samples were of exceptional quality. The Laue diffraction patterns were extremely sharp, indicating excellent crystallinity, and the superconducting transitions were very steep, always less that 2 K according to susceptibility measurements, suggesting a uniform superconducting phase. Second, we found it was essential to use a higher photon energy to observe this dispersive band. For low photon energies (near 20 eV), as was used for band-mapping the p-type superconductors $Bi_2Sr_2CaCu_2O_{8+\delta}$ and $YBa_2Cu_3O_{7-\delta}$, we were unable to observe this feature. Possible explanations for this photon energy dependence include a photoionization cross section effect, notorious for high temperature superconductors [1, 3], and the possibility that we are doping into the Cu 3d upper Hubbard band of the n-type superconductor as we will discuss in detail later. Finally, we found that the band near E_F is much stronger for larger emission angles, corresponding to $k_{||}$ in the second zone in the extended zone scheme, presumably due to matrix element effects. In the same vein, we suggest some possible reasons why the earlier ARPES study failed to observe the Fermi surface: (i) the experiment used thin films which are notorious for surface problems; (ii) the experiment was performed at room temperature, and the oxide surface has been found to be unstable in vacuum at room temperature.

The experimental E versus k relation obtained from the data in Fig.1(a) is plotted in Fig.1(b) (solid triangles) together with the LDA calculated band structure. It is clear that the band near E_F agrees with a calculated band quite well. Although the calculated Fermi surface appears to be somewhat too large, we think the overall agreement is good. This result implies that the n-type superconductor has a Fermi surface, and the Fermi surface is similar to the prediction from the one-electron band calculation. This conclusion is consistent with the results obtained from the p-type superconductors [1-4]. This point is very important in light of the fact that the band near E_F, and thus presumably the Fermi surface, is mainly derived from the correlated 3d bands in the n-type superconductor while the bands at E_F in p-type superconductors are mainly

derived from the O 2p bands. This will put further constraints on theoretical models for the electronic structure and the superconductivity of the cuprates.

Reference:
[1] C. G. Olson *et al.*, Science **245**, 731 (1989).
[2] B. O. Wells *et al.*, Phys. Rev. Lett. **65**, 3056 (1990).
[3] J. G. Tobin *et al.* (to be published).
[4] R. Liu, Phys. Rev. B (preprint).
[5] C. M. Fowler *et al.*, Phys. Rev. Lett. **68**, 534 (1992).
[6] H. Haghihi *et al.*, Phys. Rev. Lett. **67**, 382 (1991).
[7] Y. Sakisaka *et al.*, Phys. Rev. B **42**, 4189 (1990).
[8] D.M. King, et al., Phys. Rev. Lett, submitted
[9] S. Uchida *et al.*, Physica C **162-164**, 1677 (1989).
[10] J. W. Allen *et al.*, Phys. Rev. Lett. **64**, 595, (1990).
[11] C. A. R. Sà de Melo *et al.*, Phys. Rev. B **41**, 6633 (1990).
[12] D. Scalapino, private communication.
[13] S. Massidda *et al.*, Physica C **157**, 571 (1989).

Fig.1. (a) Angle-resolved energy distribution curves, near the Fermi energy, plotted for different angles along the Γ-X direction . The radius of the circles in the Brillouin zone insert represent the ±1° acceptance angle of the analyzer. The solid circles indicate the measured Fermi crossing points along the Γ-X direction. The calculated Fermi surface (x = 0.15) is taken from Massidda et al. [13]. (b) Energy band structure of $Nd_{1.85}Ce_{0.15}CuO_{4-\delta}$ along the Γ-X direction of the Brillouin zone. The peak positions from (a) are plotted along with the calculated energy bands from Massidda et al. [13].

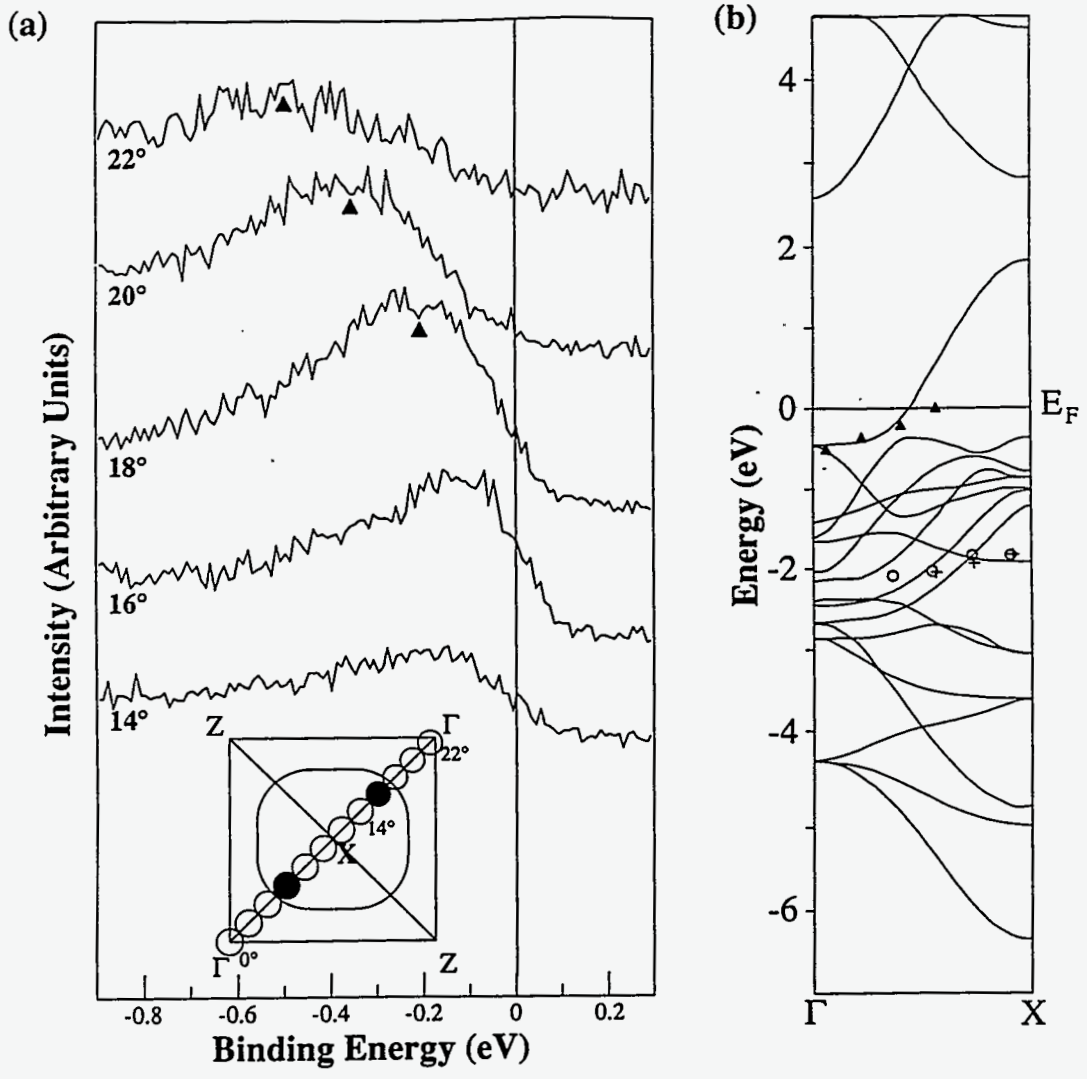

Angle-resolved Photoemission of single crystal C_{60}

Z.-X. Shen, R. Cao, D.S. Dessau, X. Yang, P. Pianetta, D.S. Marshall, B.O. Wells, D.M. King, and J. Terry; Stanford Electronics Laboratories and Stanford Synchrotron Radiation Laboratory, Stanford, CA 94305
D. Elloway, H.R. Wendt, C.A. Brown, Heinrich Hunziker, and M.S. de Vries; IBM Research Division, Almaden Research Center, 650 Harry Road, San Jose, CA 95120-6099

Recently, large quantities of C_{60} molecules have become available, and these molecules condense into a unique form of molecular solid.[1] The fullerene C_{60} has the structure of a truncated icosahedron. 60 equivalent C-atoms occupy the 60 vertices formed by the intersections of 20 hexagonal and 12 pentagonal faces. At room temperature, the C_{60} crystal has a face centered cubic (fcc) or a hexagonal close-packed (hcp) lattice structure.[1-5]

Doping of the C_{60} molecules results in superconductivity with transition temperatures as high as 30 K [6,7]. An important issue for a theoretical understanding of the mechanism of superconductivity in this material is the conduction band width. Due to the repulsive nature of the electrons, a narrow band does not favor the traditional electron-phonon coupling mechanism. The experimental results of the band width are presently controversial. On the one hand, measurements such as IR reflectivity, NMR, critical field, and magnetic susceptibility give band widths of about 80-200 meV [8-10]. This range of band width values were obtained indirectly from the density of states measured in these experiments. On the other hand, the peak widths for both the highest valence band state and the lowest conduction band state range from 800 meV to 1200 meV in the existing photoemission spectra from polycrystalline samples.[11-14] These values of the photoemission peak widths are significantly larger than the energy resolution in the experiments which are typically the order of 100 to 200 meV. If these values from photoemission data are taken as the band widths,[10] then the photoemission results and the results obtained by other measurements differ by about an order of magnitude! We performed the first angle-resolved photoemission study of single crystal C_{60} cleaved in UHV.[15] We found that although the first valence band peak has a width of about 800 meV, it disperses by as little as 50 meV even with substantial changes of electron crystal momentum. This observation provides a possible reconciliation between earlier photoemission results and those obtained by other measurements. We suggest that the peak width one measures from photoemission data may be dramatically modified by final state effects, and thus may not reflect the true band width which is substantially narrower.

Fig.1 is a transmission Laue pattern taken from the single crystal C_{60} with the x-ray beam facing the cleaved surface. This established that the sample we studied was a high quality single crystal. The overall photoemission spectra we took from the single crystal C_{60} are very similar to, and thus verify earlier results from polycrystalline thin films prepared by evaporating C_{60} molecules on various substrates.[11-14] Further, the angle-resolved photoemission data provides additional information regarding the band width of the materials. Fig.2 presents two complementary sets of angle-resolved photoemission data from the single crystal C_{60}. Panel (a) gives off-normal emission data with a photon energy of 25 eV, while panel (c) gives normal-emission data at various photon energies. In the normal-emission case, we fixed the direction of the k vector but changed its amplitude. In the off-normal emission case, we fixed the amplitude of the k vector but changed its direction. In both cases, we change the k vector by relatively small amounts. However, this change is very sizable as compared to the small Brillouin zone size of the C_{60} crystal (approximately 60% and 20% for the off- and normal emission cases, respectively). To first order, the most obvious conclusion from Fig.2 is that there is minimal energy dispersion of the features, i.e., the photoemission features do not move with the change of emission angle or photon energy. The upper bound for the energy dispersion of the first and second photoemission features is 50 meV which is shown more clearly in panel (b). We notice that the first photoemission feature (HOMO) shifts by 50 meV at 6^{o} emission angle, and then shifts back by about 20 meV at 9^{o} emission angle. The experimental conditions during the data collection were very stable and we reproduced the normal emission data after we took the off-normal emission data. Therefore, we believe that the experimental observation is real. However, we can not rule out the possibility that this small shift is caused by a change in the spectral background, or that each photoemission feature contains several states and their relative intensity may change with emission angle and photon energy. In any case, we are confident to say that the energy dispersions of the C_{60} photoemission features are very small, and 50 meV is the upper bound.

It should be noted here that the lack of energy dispersion in the photoemission features of this compound does not necessarily mean that there are no dispersions of individual bands. All the photoemission features resolved contain several bands (e.g., the first feature is five fold degenerate), and the individual bands may disperse differently. We might have a situation that the individual bands have some dispersion while the centroid of these bands is basically non-dispersive. This scenario leads to a change of the width of the photoemission features; however, since we didn't see any sizable changes of the widths of photoemission features, we think the dispersion of individual bands is also small. Another possible explanation for the lack of energy dispersion in our data is the rotational disorder. It is found that the C_{60} molecules spin with high frequencies in the solid.[16] The hopping matrix elements and therefore the band width will be affected by the relative orientations of the C_{60} molecules. Nevertheless, since the trend (say, upwards or downwards) of the energy dispersion in C_{60} solid is determined by the crystal structure, the rotational disorder of the individual molecules will produce many bands with different widths but the same trend. We should still see the "averaged energy dispersion" of these bands if some of them are very dispersive. The fact that we see basically no energy dispersion can not be easily explained by rotational disorder alone. Instead, the individual bands have to be fairly narrow. Therefore, the general conclusion from the angle-resolved photoemission data is that there is very minimal energy dispersion of the features, implying that the solid state effect is very weak and the crystal is basically molecular in nature.

Our angle-resolved data also provides additional information that was not available before: although the photoemission feature width is much wider than our experimental resolution, we see neither a sizable energy dispersion nor a sizable change of the photoemission peak width with substantial changes of crystal momentum. This result puts further constrains on the width of the energy bands. Even though it is difficult to pin down exactly the width of the individual bands, it is reasonable to assert that one can not naively take the width of the photoemission peak as the band width. In addition, we assert that the real band width of the material is substantially narrower than the photoemission peak. Even though a lifetime broadening is unlikely here, photoemission peak could be broadened by final state effects. Such a final state broadening has been observed in other systems before. For example, the very sharp exciton state of F-centers in KI appeared in the photoelectric emission data to have a width of approximately 1 eV at room temperature.[17] The broadening of the exciton state in F-centers was explained by the Franck-Condon final state effects.[18] In the fullerenes, however, the situation is somewhat complicated. For Franck-Condon type of final state effect to be strong, the photohole left behind should be quite localized so that there is a large lattice distortion. Since the photohole left in the HOMO is distributed in the entire molecule, one would not start out expecting a very large lattice distortion. This is consistent with the theoretical calculation that the relaxation energy of the molecule is small. However, a recent high-resolution photoemission experiment from gas phase C_{60} molecules clearly suggests that there is significant geometric distortion.[20] The first photoemission peak from C_{60} gas molecule (thus with no band effect at all) is also very broad. With exceptionally good energy resolution (22 meV), one can even resolve the vibrational structures due to non 0-0 transitions and transitions into Jahn-Teller distortion modes.[20] Therefore, it is very clear that the photoemission peak width can not be simply interpreted as the band width.

References:

1. W. Kratschmer, L.D. Lamb, K. Fostiropoulos, D.R. Huffman, Nature 347, 354 (1990)
2. R.M. Flemming et al., Proc. Mater. Res. Soc. (Boston, 1990) in press
3. P.A. Heiney et al., Phys. Rev. Lett (submitted)
4. Y. Guo, N. Karawasaki, and W.A. Goddard III, Nature 351, 464 (1991)
5. R. Hgeiss, to be published
6. A.F. Hebard et al., Nature 350, 600 (1991); M.J. Rosseinsky et al., Phys. Rev. Lett. 66, 2830 (1991)
7. K. Holczer et al., Science 252, 1154 (1991); K. Holczer et al., Phys. Rev. Lett. 67, 271 (1991)
8. L.D. Rotter et al., preprint
9. R. Tycko et al., Science 253, 884 (1991)
10. A.P. Ramirez, private communication. Susceptibility and critical field measurements also yield a narrow band width (about 7 or 8 times narrower than the photoemission data)
11. J.H. Weaver et al. Phys. Rev. Lett. 66, 1741 (1991)
12. G.K. Wertheim et al., Science 252, 1420 (1991)
13. C.T. Chen et al., Nature 352, 603 (1991)
14. P.J. Benning el al. Phys. Rev. B 44, 1962 (1991)

15. Z.-X. Shen et al., preprint
16. C.S. Yannoni et al., J. Am. Chem. Soc. 113, 319 (1991)
17. L. Apker and E. Taft, Phys. Rev. 79, 964 (1959)
18. see, e.g., articles by M. Lax and C. Herring in Photoconductivity Conference, edited by R.G. Breckenridge et al., published by Wiley and Sons.
19. Hans Peter LÜTHI and Jan ALMLÖF, Chem. Phys. Lett. 135, 357 (1987)
20. P. Baltzer eta al., submitted to Phys. Rev. Lett.

Figure Captions:

Fig.1 Transmission Laue pattern along a cleaved direction of the C_{60} single crystal.

Fig.2 (a) Off-normal emission data from the C_{60} single crystal, the inset (b) shows details of the first two photoemission peaks. (c) Normal-emission data from the C_{60} single crystal.

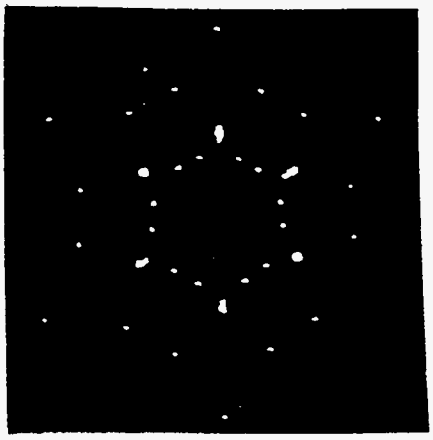

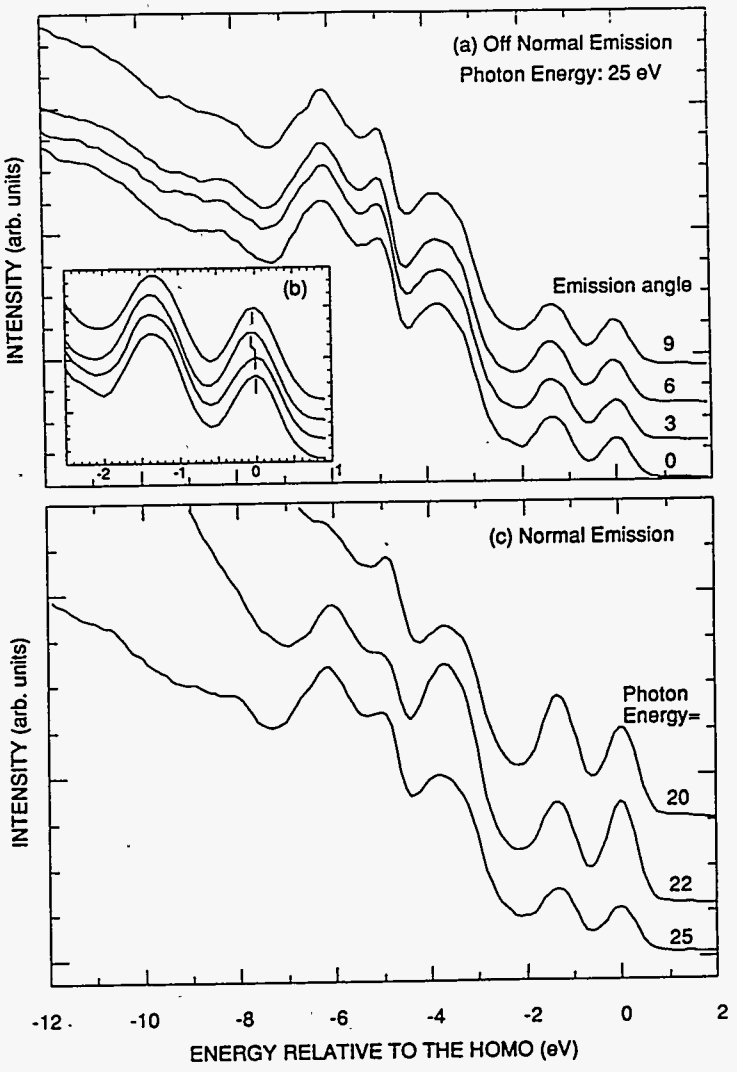

Evidence of Chemical Potential shift with hole doping in $Bi_2Sr_2CaCu_2O_{8+\delta}$

Z.-X. Shen, D.S. Dessau, B.O. Wells
Stanford Electronics Laboratory, Stanford University, Stanford, CA 94305, USA
C.G. Olson
Ames Laboratory, Iowa State University, Ames, IA 50011, USA
D.B. Mitzi, Lou Lombado
Department of Applied Physics, Stanford University, Stanford, CA 94305, USA
R.S. List and A. J. Arko
Los Alamos National Laboratory, Los Alamos, NM 87545, USA

Among the many interesting physical properties of the high-temperature superconductors is their doping mechanism: the superconductors are made by doping antiferromagnetic Mott insulators [1]. Much theoretical and experimental work has been carried out to understand this problem . This includes recent spectroscopic experiments which suggest that new states develop inside the charge transfer gap when the material is doped from an insulator to a metal. In a conventional material where the one-electron picture works well, an important aspect of doping is a chemical potential shift. For the high-temperature superconductors where the simple one-electron band theory is thought to have serious difficulties, it is not obvious whether one should see a chemical potential shift as a function of doping. Experimentally, no clear evidence has been found that suggests a chemical potential shift as a function of doping.

Recently, we presented results of our angle-integrated and angle-resolved photoemission studies of $Bi_2Sr_2CaCu_2O_{8+\delta}$ crystals with different oxygen content.[2] Referenced to the Fermi level, both the valence band and the shallow core levels shift about 0.15-0.2 eV with the oxygen content change. Except for this shift, the line shape of the valence band, the shallow core levels, and even the background were remarkably similar. This result can be best interpreted as a chemical potential shift of about 0.15-0.2 eV with doping. If this interpretation is true, then this result is the first clear evidence for a chemical potential shift in the cuprate superconductors as a function of doping.

Fig.1 presents 120 eV photon energy EDC's of the valence band and some shallow core levels for two $Bi_2Sr_2CaCu_2O_{8+\delta}$ samples with different oxygen contents. The spectra taken from the two samples are almost identical except for a ~ 0.15 - 0.2 eV shift. Referenced to the Fermi level, the valence band and core level features of the high oxygen (hole) content sample shift to lower binding energy with respect to the low oxygen content sample. The Fermi levels of the two samples are the same since they are grounded to the photoelectron spectrometer. The best explanation for this observation is that the chemical potential of the more hole doped sample is lower, just as one would intuitively expect. If this interpretation of the data is correct, then the result in Fig.1 is the first clear evidence for a chemical-potential shift in the cuprate superconductors as a function of doping. The fact that the spectra from the two samples are so similar and the shift is seen in all the features gives us confidence about our interpretation. From this data, we estimate that the chemical potentials of the two samples are shifted by approximately 0.15~0.2 eV as can be more clearly seen in the inset of the figure.

We have also observed similar results in our angle-resolved photoemission data. Fig.2 shows results of our angle-resolved photoemission spectra for the as-grown (thin line) and 12 atm O_2 annealed (thick line) samples. The four sets of data are spectra taken at different parts of the Brillouin zone: normal emission, near where the first band (with the lowest binding energy) crosses E_F along Γ-Y, near where the first band crosses E_F along Γ-X, and near where the first band crosses E_F along Γ-M. Besides some small line shape changes, the main valence band features of the 12 atm oxygen annealed sample shift about 0.2 eV towards the Fermi level. The fact that the shift shows up for all directions sampled is important, as we cannot resolve individual bands in the "spaghetti" of bands which comprise the main valence band. Such changes for any particular direction may be explained by matrix element effects or energy dispersion. However, the fact we see such a shift in all sampled directions and the fact that the line shapes of the spectra of the two samples are so similar makes the chemical potential shift the only sensible explanation of the experimental data. Furthermore, the fact we can reproduce the same result in different experimental set-ups is also very suggestive that the chemical potential shift is the correct interpretation of our data.

This amount of chemical potential shift with doping by annealing our samples in oxygen is also consistent with the estimations from the oxygen content change. The change of oxygen content from as-grown/Ar annealed samples to 12 atm oxygen annealed samples is about 0.06/cell. Assuming the oxygen has a valence of 2^- and using 2.88 per eV per cell total density of states at the Fermi level from a band calculation,[3] we anticipate about 0.1 eV chemical potential shift. If we use the density of states which is

Fig.2 Angle-resolved photoemission data from an as grown (light line) and a 12 atm O_2 annealed $Bi_2Sr_2CaCu_2O_{8+\delta}$ single crystal at different parts of the Brillouin zone. The photon energy used here is 19 eV.

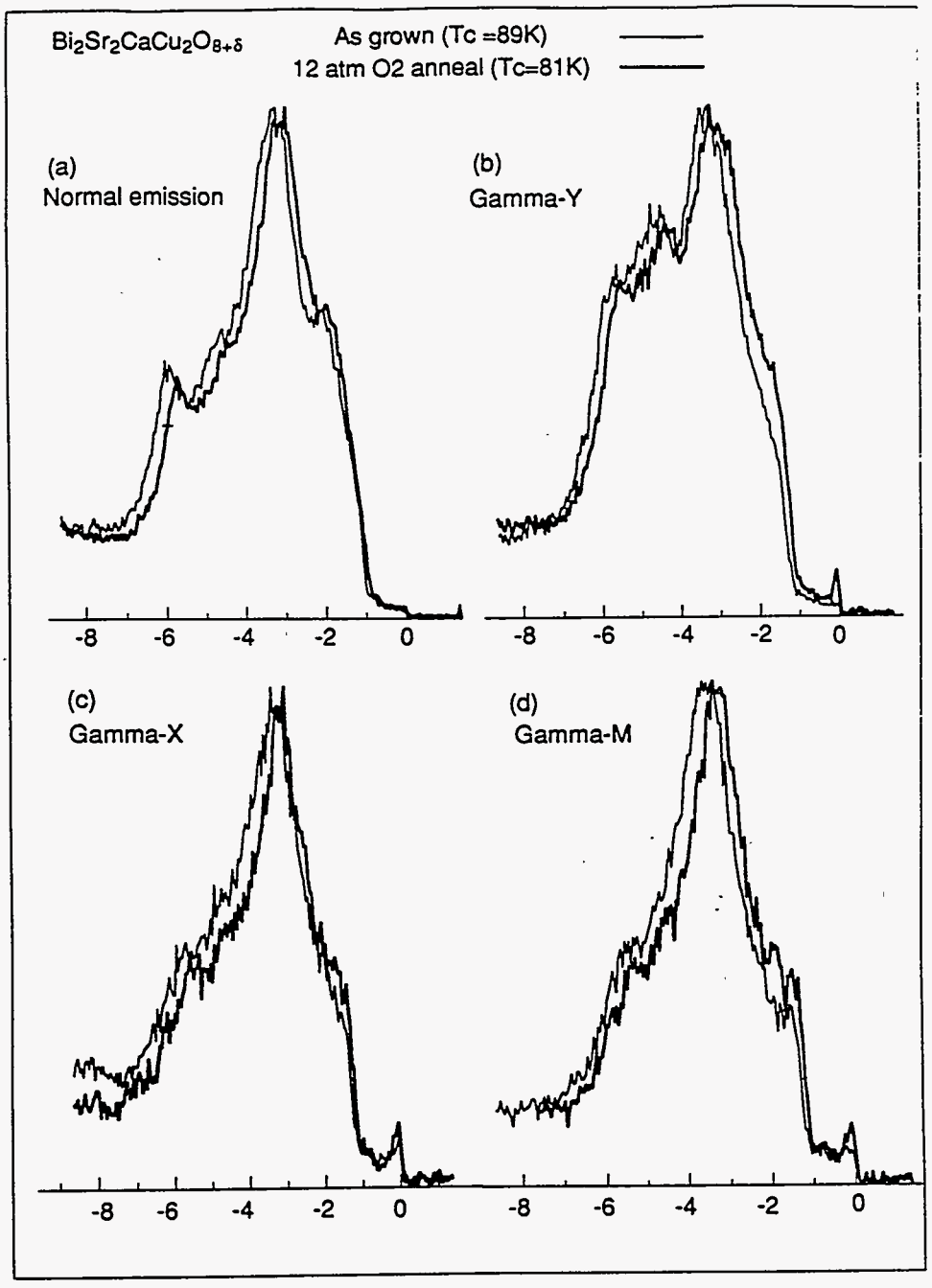

at most half the value of the band calculation as measured by angle-integrated photoemission, [4] we expect about at least 0.2 eV chemical potential shift. On the other hand, if we use the density of states which is two times the value of the band calculation as indicated by magnetic susceptibility measurement or the effective band mass from angle-resolved photoemission,[5, 6] we anticipate a 0.05 eV chemical potential shift. Given the crudeness of these estimations, we think the results of these estimations are consistent with the observed about 0.15 - 0.2 eV chemical potential shift.

Therefore, from our new data and from results in the literature,[2] we now have the following picture of doping for metallic $Bi_2Sr_2CaCu_2O_{8+\delta}$: (i) The chemical potential shifts with hole doping; (ii) The spectral weight at E_F increases with hole doping; (iii) The Fermi surface obeys the Luttinger theorem. This rather "normal" doping behavior in the metallic $Bi_2Sr_2CaCu_2O_{8+\delta}$ can be quite well accounted by the renormalized band approaches[2], and is significantly different from an earlier result nearer the insulating regime where a very minimal chemical potential shift was observed as oppose to what one would intuitively expect [7].

References:

1. J.B. Torrance et al., Phys. Rev. Lett. 61, 1127 (1988); Phys. Rev. B 40, 8872 (1989); and references therein.
2. Z.-X. Shen et al., Phys. Rev. B 44, 12098 (1991)
3. H. Krakauer and W.E. Pickett, Phys. Rev. Lett. 60, 1665 (1988)
4. Z.-X. Shen et al., Phys. Rev. B 38, 7152 (1988)
5. D.B. Mitzi et al., Phys. Rev. B 41, 6564 (1990)
6. C.G. Olson et al., Science 245, 731 (1989)
7. J.W. Allen et al., Phys. Rev. Lett. 64, 595 (1990)

Figure captions:

Fig.1 Angle-integrated photoemission data from an Ar annealed sample (dots) and a 12 atm. O_2 annealed sample (line) at photon energy of 120 eV. Referenced to the Fermi level, the core levels, the valence band, and even the background of the two samples were remarkably well reproduced except an approximately 0.2 eV shift. This data clearly indicates a chemical potential shift as a function of doping: for the oxygen annealed (hole doped) sample, the chemical potential is lowered.

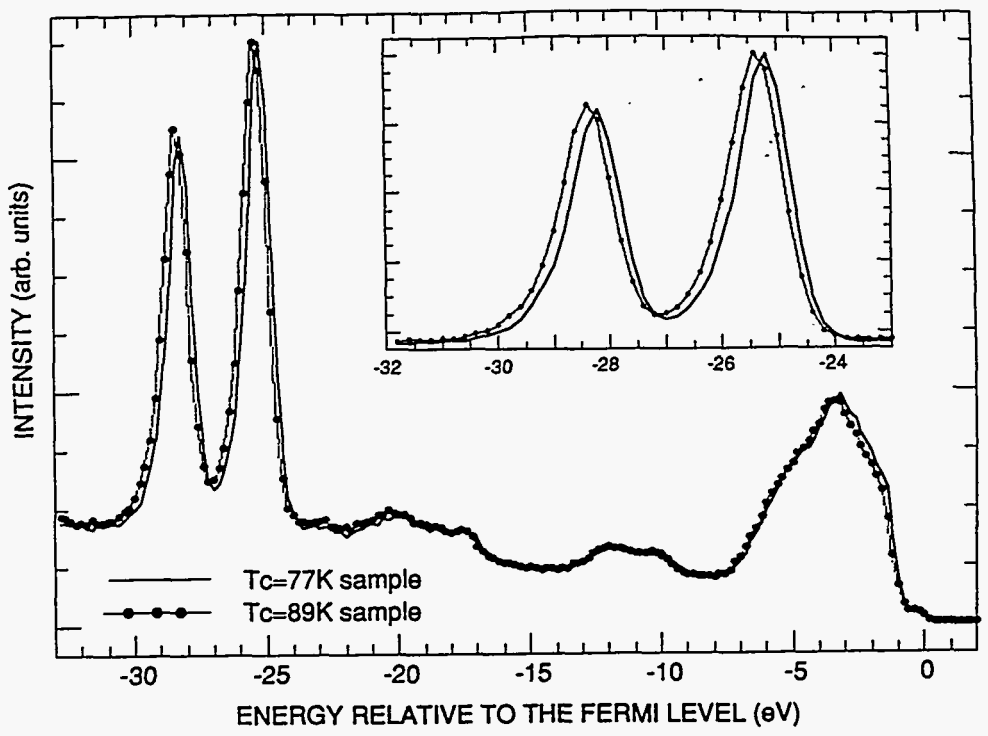

FERMI LEVEL INHOMOGENEITIES ON GaAs(110) SURFACE IMAGED WITH A PHOTOELECTRON MICROSCOPE

Changyoung Kim, Paul L. King, and Piero Pianetta
Stanford Synchrotron Radiation Laboratory
P.O. Box 4349, Bin 99
Stanford, CA 94309

ABSTRACT

A photoelectron microscope operating with a retarding field analyzer can exploit core level energy shifts in order to image Fermi level variations of semiconductor surfaces. Fermi level maps of cleaved n- and p-type GaAs(110) resolved to better than 10 mm indicate lateral variations in the surface Fermi level which are often quite abrupt. In agreement with earlier, lower resolution work [1], Fermi level topography is found to be highly correlated with surface roughness as characterized by SEM, optical microscope and stylus profilometer. Defective fracture surfaces have two distinct characters within SEM resolution: linear defects (steps ledges) that may extend over millimeters and smooth glassy areas. Both types of surface defects shift the Fermi level towards mid-gap. The largest defect derived pinnings encountered to date resut in the Fermi level lying 0.5 eV above the VBM for both n- and p-type GaAs. Low coverage In evaporations have the effect of reducing Fermi level contrast as Fermi levels in formerly unpinned regions move into the gap.

INTRODUCTION

Although there are no intrinsic surface states in the band gap of the cleaved surface of (110) GaAs [2-4], extrinsic surface states are produced by surface defects from cleaving processes. In most experiments utilizing the cleaved (110) surface, qualitative visual tests and measurements of the difference between bulk and surface Fermi levels are carried out. Crystals that are rough or where the surface Fermi level differs from the bulk level by more than 0.1 eV are often recleaved, although experience suggests that the initial cleave-related pinning has little effect on final metal-induced pinning positions. It is, however, difficult to completely exclude the presence of some cleavage defects, and this study has been carried out in part to determine the relationship between cleavage damage and the surface Fermi level and the subsequent behavior of the Fermi level following metallization. From a theoretical perspective, pinning from cleavage defects offers a test to the models proposing to describe the behavior of Schottky barriers. Similar to the experimental observations of irradiated bulk GaAs in which it was shown that the bulk Fermi level moves toward mid-gap for both n- and p-type crystals[5], surface defects introduced by an imperfect cleave provide an opportunity to observe surface Fermi level behavior free of exotic species introduced during metallization. In this paper, we introduce a direct method for recording surface Fermi level maps with lateral resolution better than 10 μm and energy resolution near 0.05 eV. Using this technique, excursions from bulk Fermi levels are found to be highly correlated with surface roughness as had been previously shown using a lower resolution and a less direct technique [1,6,7].

EXPERIMENTAL

The instrument used in the experiment is a magnetic projection photoelectron microscope operating at Beam Line 8-1 at SSRL. This unique imaging spectrometer is a magnetic analogue of field emission microscopy. Design and operation of the microscope is described elsewhere [8,9]. The base pressure of the main chamber was better than $5x10^{-10}$ Torr during the experiment. GaAs crystals were cleaved from 5x5 mm bars of n-type ($7x10^{17}$ cm^{-3} Si doped) and p-type crystal ($1x10^{19}$ cm^{-3} Zn doped) obtained from Bertram Laboratories, Inc., Somerville, NJ. Submonolayers of In were evaporated using a resistively heated evaporator with the evaporation rate monitored by a quartz crystal thickness monitor. Fermi level positions were followed by tracking the position of the Ga 3d core level at hv = 100 eV with checks made of the position of the As 3d and valence band to ensure that any changes seen were Fermi level shifts rather than of a chemical origin. Our ability to generate Fermi level maps relies on the fact that, due to variations in band bending, core level electrons are found over a range of kinetic energies. The measured kinetic

energy of a given core level of a p-type surface that is pinned due to defects will be measured having a lower kinetic energy than a nearby region that is unpinned. By setting the retarding potential judiciously, image contrast is generated such that the unpinned region is bright(more core electrons are allowed to pass) and the pinned region is dark (more core electrons are retarded). The case is reversed for n-type crystals, where pinned regions will appear brighter. Certain calibration procedures then translate raw image contrast into relative or absolute Fermi level positions. Additional normalization procedures may also be required if the x-ray flux is not homogeneous over the microscope's field of view or if topographic contrast (shadowing) is present. Given the angle at which x-rays intercept the sample(15 degrees off normal) and the nature of projection process, photoelectron microscopy of this form is largely insensitive to topology and contrast is almost wholly Fermi level variation. The photon energy of 100 eV was chosen such that the ratio of Ga 3d and valence band cross section is large and the impact of valence band electrons (which only serve to reduce useful contrast) is small.

RESULT AND DISCUSSION

Correlation of Fermi maps and surface topography Fig. 1a is the raw image of p-type GaAs surface taken at hv = 100 eV with the retarding potential set to 76.5 V to maximize Fermi level contrast at the Ga 3d peak. For p-type GaAs, defectrelated pinning brings core level electrons toward lower kinetic energies which are then retarded revealing the central low yield area as a pinned region. Fig. 1b is the calibrated B pinning map based on Fig. 1a. The middle area is pinned about 0.45 eV above the surrounding unpinned areas. The central pinned region is a smooth defect region. The pinned region stands out as a dark area in the opitcal micrograph, though it is barley visible in the SEM due to its smoothness. No steps are visible in this region using SEM even in its higher resolution modes. As measured by a stylus profilometer, this region is smooth with a small number of undulations. The largest angular deviations from the 110 normal are less than 10 degrees. By comparison, the surrounding region is relatively flat and smooth correlating well with the Fermi level map which is largely unpinned throughout this region. Fig. 1c shows the pinning map of the same region recorded after a 0.5 ML In evaporation. This small amount of In acts to bring the surface Fermi level in the formerly unpinned regions into the gap. Fermi level contrast is therefore reduced. A number of other cleaves have been observed using both synchrotron and He lamp excitation. Results are similar to those shown above. No defective regions appeared unpinned and no clean, defective free areas were observed to be pinned. Charaterization of cleaved quality by visual inspection proved to be somewhat problematic due to being highly sensitive to the positioning of the light source. The maximum pinning observed to date resulted in the surface Fermi level stabilizing 0.5 eV above the VBM for both n- and p-type crystals. The magnitude of this defect induced pinning is similar to that observed by Palau et al [1]. Although not directly observed, we suspect that, in the case of the heavily pinned, defective n-type crystal, there will actually be movement back toward the bulk Fermi level (recovery) upon metalization, so that final pinning positions match those after metalization of the clean, perfect surface near 0.7 eV above the VBM. Efforts to confirm this will be carried out during the next available beam time.

CONCLUSIONS

We have developed a new technique for mapping Fermi level inhomogeneities of semiconductor surfaces. Our evidence indicates a correlation between surface imperfection and surface pinning that approaches 100% up to the resolution of the Fermi mapping technique. For surfaces which are anything other than perfect 110 surfaces, some degree of pinning exists. This behavior is certainly defect-derived and must involve both acceptor and donor states to explain the movement into the gap for both n- and p-type crystals. It remains unclear whether these cleave-related defects are similar in nature to those proposed in defect models developed to explain the surface Fermi level behavior upon metalization [11,12]. One possiblity is that observed defects (steps/ledges and glassy areas) are directly responsible for new states within the gap. Distinct luminescence features have been associated with cleave quality in InP [13]. Another possibility is that the surface damage acts as nucleation sites for point defects that subsequently moved into the bulk and whose stability is determined by the Fermi level [12].

ACKNOWLEDGMENTS

This work was partially supported under Air Force Contract No. AF 49620-86K-0019 and was performed at the Stanford Synchrotron Radiation Laboratory which is supported by the Department of Energy, Office of Basic Energy Science, Division of Chemical Sciences. C. Kim and P. Pianetta acknowledge the support of that Office's Division of Material Science for this research. P.King would like to acknowledge support from the Stanford University Center for Materials Research under NSF-MRL grant DMR-87-217359.

REFERENCES

1. J. M. Palau, E. Testemale, and L. Lassabatere, J. Vac. Sci. Technol. 19, 192 (1981).
2. J. Van Laar and A. Huijser, J. Vac. Sci. Technol. 13, 769 (1976).
3. W. E. Spicer, I. Lindau, P. E.Gregory, D. M. Garner, P. Pianetta, and P. Chye, J. Vac. Sci. Technol. 13, 780 (1976).
4. W. Gudat and D. E. Eastman, J. Vac. Sci. Technol. 13, 831 (1976).
5. L. W. Auckerman, Semiconductors and Semimetals, edited by R. K. Willardson and A. C. Beer (Academic, New York, 1973), Vol. 4, p. 343.
6. L. Lassabatere, J. M. Palau, E. Vieujot-Testemale, A.Ismail, C. Raisi, J. Bonnet, and L. Soonckindt, J. Vac. Sci. Technol. B1, 540 (1983).
7. A. Ismail, A. Ben Brahim, J. M. Palau, and L. Lassabatere, Surf. Sci. 162, 195 (1985).
8. P. L. King, A. Borg, C. Kim, S. A. Yoshikawa, P. Pianetta, and I. Lindau, Ultramicroscopy 36, 117 (1991).
9. P. Pianetta, I. Lindau, P. L. King, M. Keenlyside, G. Knapped, and R. Browning, Rev. Sci. Instrum. 60, 1686 (1989).
10. K. K.Chin, T. Kendelewicz, C. McCants, R. Cao, K. Miyano, I. Lindau, and W. E. Spicer, J. Vac. Sci. Technol. A4, 969 (1986).
11. W. E. Spicer, Z. Liliental-Weber, E. Weber, N. Newman, T. Kendelewicz, C. McCants, R. Cao, P. Mahowald, K. Miyano, and I. Lindau, J. Vac. Sci. Technol. B5, 1062 (1987).
12. W. Walukiewicz, J. Vac. Sci. Technol. B5, 1062 (1987).
13. R. A. Street, R. H. Williams, and R. S. Bauer, J. Vac. Sci. Technol. 17, 1001 (1980).

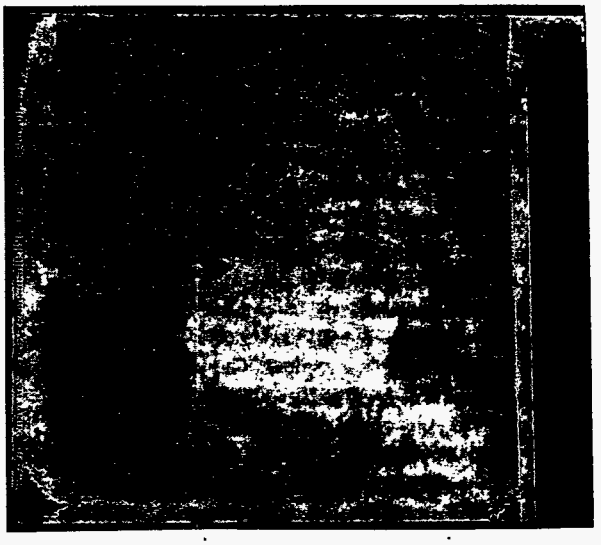

Fig. 1 (a) Raw image of p-type GaAs with RP=76.5 eV. (b) The Fermi level pinning position map for the same area. The gray shows the pinning position. (c) The Fermlevel pinning position map after evaporation of 0.5 ML In.

Spin Polarized Photoemission Studies of Gd(0001)

H. Tang, T. Walker, H. Hopster
Department of Physics, University of California, Irvine, CA 92717
D. P. Pappas, D. Weller and J. C. Scott
IBM Research Division, Almaden Research Center, San Jose, CA 95120

Gd is the *only* simple elemental ferromagnetic system consisting of localized (4f) moments. Its half filled 4f shell contains seven electrons whose spins are all aligned in the same direction at zero temperature. The ferromagnetism of Gd is predominently determined by these 4f electrons. Earlier experimental studies by Weller *et al.* [1,2] and by other groups [3-5] indicated that Gd exhibits ineteresting surface magnetic phenomena. In particular, experimental evidence indicated that the Gd surface orders magnetically at a higher critical temperature than its bulk, which orders at T_c = 293K, and that the Gd(0001) surface layer is antiferromagnetically coupled to its bulk magnetization. The strong spin polarization of the Gd 4f electrons coupled with the excellent surface sensitivity of photoemission makes spin-polarized photoemission an ideal technique for studying the surface magnetism of Gd. Due to the low efficiency of spin detectors and high chemical reactivity of Gd, however, satisfactory spin-polarized 4f photoemssion studies of Gd (and, in fact, of all other localized moment systems) have yet to be achieved. By taking advantage of the high beam intensity on the undulator beamline (5-2) at SSRL, we have successfully carried out a spin-polarized 4f photoemission study on epitaxial Gd(0001) grown on W(110). For the first time, we explored spin-polarized resonant 4f photoemission of Gd and obtained the temperature dependence of the spin polarization of Gd 4f electrons.

The experiments were carried out in a UHV system built for spin polarized angle resolved electron spectroscopy. The sample preparation and characterization chamber is equiped with a cylindrical mirror analyzer for-Auger electron spectroscopy and a rear-view LEED system. Following the method used by Weller *et al.* [1] high purity Gd (99.99%) was evaporated from a Knudsen cell at a typical rate of 1 Å/min and deposited onto a W(110) substrate held at 450 °C. The base pressure of the system was 5×10^{-10} torr, and during film growth the pressure remained below $\sim 2 \times 10^{-9}$ torr. The Gd film grows in the hcp (0001) orientation as revealed by the sharp (1×1) LEED pattern bearing six-fold symmetry. An in-plane magnetic field was applied while the sample was cooled from the growth temperature to ~150 K, and the sample was left in its remanent state for all photoemission measurements. The incident angle of the photon beam was 45°, and electrons photo-emitted normal to the sample surface were energy selected by a 90° spherical analyzer, and spin-analyzed using two Mott spin detectors capable of measuring all three spin components.

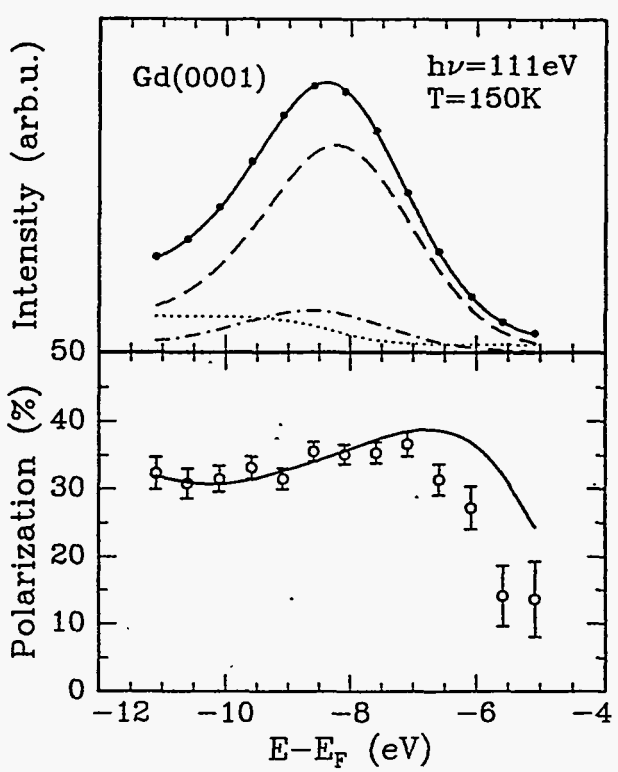

Fig. 1: Spin-polarized 4f photoemission results from a 500 Å Gd(0001) film at 150 K. Upper panel: experimental (filled circle) and fitted EDC's along with deconvoluted bulk (broken) and surface (dot- broken) contributions and background (dotted). Lower Panel: experimental (open circle) and calculated spin polarization.

The energy distribution curve (EDC) and the spin polarization across the Gd 4f peak measured for a 500 Å Gd(0001) sample at 150 K using 111 eV photons are shown in Fig. 1. The data were collected over a period of ~4 hours. The spin polarization of the Gd 4f electrons was about 35%. We fitted the EDC with an established scheme [6] that uses a bulk 4f component and a surface 4f component, whose binding energy is 0.5 eV higher than the bulk value, convoluted with instrumental broadening. Assuming an antiferromagnetic coupling between the surface and the bulk and using a temperature reduction factor of 0.55 for both the surface and bulk spin polarizations, we succeeded in reproducing the observed spin polarization curve (shown as solid curve in the lower panel of Fig. 1). The drop in the measured spin polarization and the dicrepancy between the calculated and measured values at lower binding energies can be attributed to the polarization dilution effect of a small amount of oxygen contaminants, which has an emission feature in that energy range.

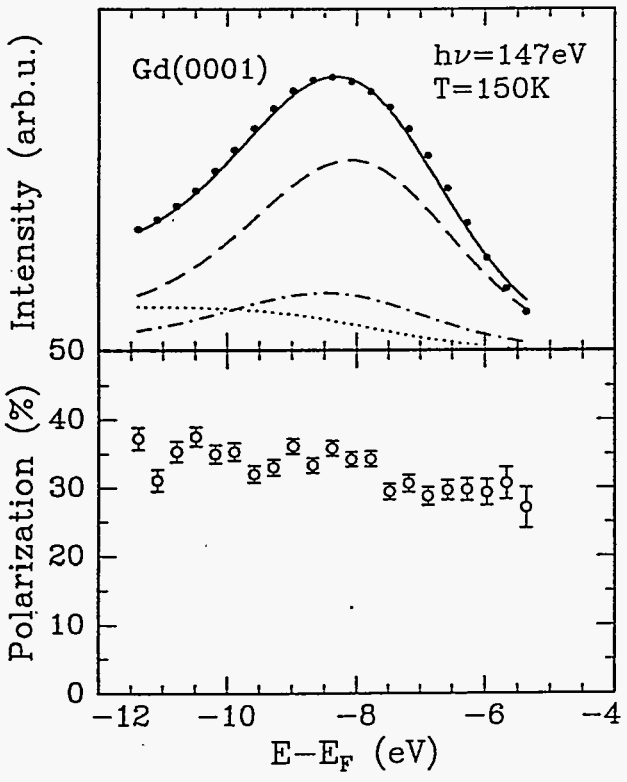

Fig. 2: Spin-polarized 4f resonant photoemssion results for Gd(0001). Upper panel shows measured and fitted EDC's, and lower panel shows measured spin polarization.

In order to minimize the adverse effect of surface contamination, we explored the possibility of spin polarized resonant 4f photoemission for Gd. Besides, it is also interesting in its own right to examine the spin polarization of Gd 4f photoelectrons resonantly emitted. We found that maximum resonant emission occured at a photon energy of 147 eV, resulting in a three-fold intensity enhancement, which enabled us to greatly shorten the measuring time. Fig. 2 shows the EDC and spin polarization data for another 500 Å Gd(0001) film at 150 K. The spin polarization at the 4f peak is, again, about 35%, which agrees very well with the value measured in the normal photoemission case. It follows, therefore, that the resonant photoemission process preserves the spin information of the 4f electrons and can be used as a magnetic probe for Gd.

By properly increasing the energy acceptance window on the analyzer (which is equivalent to integrating over the entire 4f peak), we were able to measure the temperature dependence of the 4f electron spin polarization with sufficient statistics. The result of such a measurement on a 500 Å Gd(0001) film is shown in Fig. 3. Distinctive temperature dependences can be seen in two temperature ranges: a slow, almost linear decrease in the spin polarization between 135 K to about 250 K, followed by a rapid drop characteristic of critical behavior between 250 K and the Curie temperature. An extrapolation to 0 K from a liear fit to the data in the temperature range of 135 K to 250 K yield-

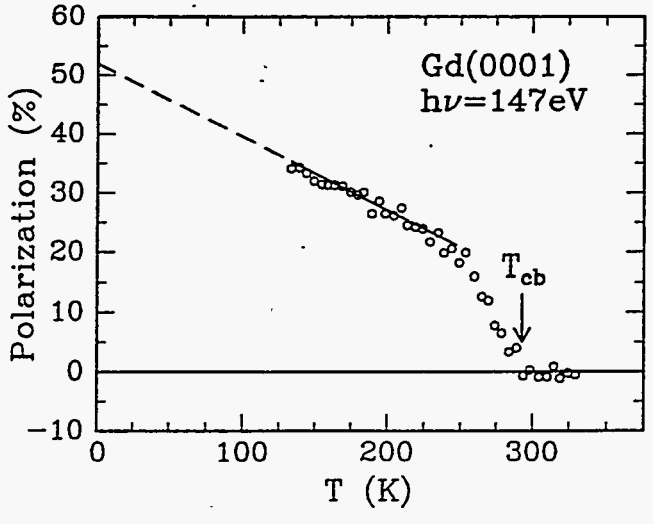

Fig. 3: Temperature dependence of the spin polarization of Gd 4f photoelectrons at resonant photoemission using 147 eV photons.

s a value of 53% for the ground state Gd 4f electron spin polarization. This value should be regarded as an upper bound as the temperature dependence may deviate from the fitted linear relation below 135 K. On the other hand, the spin polarization of the Gd 4f electrons is expected, and has also been reported [7], to be 100% at 0 K. The large discrepancy is, however, consitent with the notion of antiferromagnetic coupling between the Gd(0001) surface and bulk moments. Domain formation in the remanent state may also lead to a smaller measured spin polarization. This possibilty has been exluded based on the results of our complementary magneto-optical Kerr effect (MOKE) and spin-polarized secondary electron measurements performed recently [8].

In conclusion, we have successfully performed spin-polarized resonant as well as normal photoemission studies on epitaxial Gd(0001) films. We demeonstrated that the resonant photoemission process preserves the spin information of the 4f photoelectrons as in the normal process. The much increased emission intensity from the resonant photoemission enabled us to obtain the temperature dependence of the 4f electron spin polarization. An extrapolation of the temperature dependence data to 0 K yielded a spin polarization of 53% instead of 100% for the Gd 4f electrons, which can be explained by magnetic reconstruction on the Gd(0001) surface.

Work supported by NSF and IBM Almaden Research center.

References:

1. D. Weller, S. F. Alvarado, W. Gudat, K. Shröder, and M. Campagna, Phys. Rev. Lett. **54**, 1555 (1985).
2. D. Weller and S. F. Alvarado, J. Appl. Phys. **59**, 2908 (1986).
3. C. Rau, J. Magn. Magn. Mater. **31-59**, 874 (1983).
4. C. Rau and S. Eichner, Phys. Rev. B **34**, 6347 (1986).
5. A. Cerri, D. Mauri, and M. Landolt, Phys. Rev. B. **27**, 6526 (1983).
6. F. Gerken, J. Barth, and C. Kunz, Phys. Rev. Lett **47**, 993 (1981).
7. C. Carbone and E. Kisker, Phys. Rev. B **36**, 1280 (1987).
8. H. Tang *et al.*, to be published.

H_2S Adsorption on Cu(I) and Zn(II) Surface Sites: Bonding in d^{10} Metal Ions Related to Catalytic Poisoning[1]

Jianyi Lin, Paul M. Jones, Jeffrey A. Guckert, Jennifer A. May, Edward I. Solomon*
Department of Chemistry, Stanford University,
Stanford, CA 94305

INTRODUCTION

H_2S is a common source of sulfur poisoning in many catalytic processes. In particular, the Cu/ZnO catalysts for methanol synthesis and the water gas shift reaction are found to be more sensitive to H_2S poisoning than ZnO catalysts which contain no copper component. Studies of H_2S adsorption on surfaces relevant to methanol synthesis catalysis are therefore necessary for obtaining molecular level insight into the mechanism and increased sensitivity of the copper-promoted catalysts to sulfur poisoning. Our previous studies of the coordination chemistry of submonolayer coverages of copper on different ZnO single crystal surfaces and their interaction with CO have determined that a coordinatively unsaturated C_{3v} Cu(I) site appears to be the active center for high affinity CO binding which has been correlated to high activity for methanol synthesis[2]. Therefore, the adsorption of H_2S sites was performed on $Cu_2O(111)$, ZnO (0001) and $(10\bar{1}0)$ surfaces. The availability of oxide ions on both the Cu_2O and ZnO surfaces is important for comparison of H_2S chemisorption on these surfaces since oxide ions are Brønsted basic centers and can serve in the deprotonation of adsorbed H_2S.

RESULTS AND DISCUSSION

At room temperature, all surfaces react to form sulfide. At low temperature(140 K) and low H_2S coverages (0 - 0.3 L), H_2S chemisorbed on the $Cu_2O(111)$ surface is found to completely dissociate forming sulfide and hydroxide. At intermediate coverages (0.3 - 3.4 L), partial deprotonation of H_2S yields HS^- on the $Cu_2O(111)$ surface resulting in three valence band photoemission peaks at 17.0 (Cu-S-H σ), 13.8 (Cu-S pseudo -σ), and 10.3 eV (Cu-S π) below the vacuum level. At high coverages (> 3.4 L), H_2S is molecularly chemisorbed on the $Cu_2O(111)$ surface. Alternatively, higher H_2S exposures are required for chemisorption on the ZnO surfaces at low temperature (140 K), and only coordinated HS^- is observed. Thus the reactivity of H_2S on ZnO is fundamentally different than on Cu_2O. The valence band photoemission spectrum of HS^- / ZnO also differs from HS^- on Cu_2O. The former exhibits peaks at 18.2 (Zn-S σ), 13.8 (Zn-S pseudo-σ) and 11.8 eV (Zn-S π).

Photoemission spectra of the valence band region of the H_2S/ $Cu_2O(111)$ system at 1.8 L and 130 K have been recorded from 25-120 eV photon energy (experiments were conducted on Beam Line III-1 at SSRL) and are presented in figure 1. The clean surface spectrum at each photon energy is included for comparison. The surface HS^- group is the dominant adspecies at this coverage, exhibiting three peaks labeled A, B and C in the photoemission spectra. Figure 1 shows a significant and similar dependence of the intensity of peaks A and B on photon energy. Peak C also shows similar behavior but

is complicated due to overlap with the substrate oxide region. At low photon energies, the peak intensities increase with increasing photon energy and show a maximum at 30 eV. They then decrease with further increase in photon energy. The large intensity increase to lower photon energies demonstrate that peaks A and B are mainly of S 3p character, consistent with their assignment as photoemission from a surface bound HS^- species. Further, the occurrence of a decrease in intensity below 30 eV is characteristic of Cu 4s photoemission (due to its Cooper minimum at ~ 16 eV photon energy). Thus Cu 4s character is mixed into the molecular orbitals of the surface HS^- group via Cu-SH^- bonding. Since the interaction of the HS^- ligand with the filled 3d levels will not contribute to net bonding of HS^- to the Cu(I) surface site, the interaction with the unoccupied Cu 4s (and 4p) levels is of particular importance to bonding.

The energy dependence ($h\nu$ = 25- 120 eV) of valence band PES peaks of the chemisorbed HS^- species on ZnO (7.5 L H_2S exposure) at 130 K is presented in figure 2. The clean surface spectrum at each photon energy is included for comparison. The peaks (labeled L, M and N) are also quite dependent on photon energy. Both peaks L and M start relatively intense at low photon energy and drop rapidly with increasing photon energy as expected for ionization from the S 3p orbitals. In contrast to the H_2S /Cu_2O (111) system in figure 1, the intensity does not decrease at photon energies below 30 eV.

From variable photon energy PES studies, we find significant metal 4s character in the Cu(I)-HS^- system, but no measurable 4s mixing in the Zn(II)-SH^- system, indicating a stronger covalent bonding interaction for Cu(I)-SH. This is supported by the quantitative energy splittings of the three HS^- peaks for the two surfaces. Figure 3 presents difference spectra (covered minus clean) for HS^- binding to Cu(I) vs. Zn(II). The two spectra are aligned to the M-S π level for comparison. Note that the B-C splitting increases relative to the M-N splitting and the A-B splitting decreases relative to the L-M splitting. From Xα calculations[3] a stronger bonding interaction should result in larger energy stabilizations of the two deeper energy σ type orbitals relative to the S $3p_\pi$ orbital, the pseudo-σ being the more stabilized.

From an electronic structure point of view, both Zn(II) and Cu(I) have fully occupied 3d orbitals which can not contribute to HS^--metal ion bonding with ligand orbitals which are also fully occupied. Net bonding mainly derives from the interaction between the ligand orbitals, ϕ_{S3p}, and the unoccupied metal 4s (and 4p) levels, ϕ_{M4s}. The energy of bonding, $\Delta E_{M4s,S3p}$, depends on the resonance matrix element $H_{M4s,S3p} = \langle\phi_{M4s}|H|\phi_{S3p}\rangle$ and the energy difference ($E_{M4s} - E_{S3p}$): $\Delta E_{M4s,S3p} \simeq -(H_{M4s,S3p})^2 / (E_{M4s} - E_{S3p})$. Since, from CIS studies, the Zn(II) 4s orbital is lower in energy than the 4s orbital of Cu(I) (5.2 vs. 2.2 eV) it is energetically more accessible for bonding. The smaller covalent bonding interaction found for Zn(II) as compared to Cu(I) must therefore be due to a smaller $H_{M4s,S3p}$, which reflects the overlap between the ligand orbitals and metal 4s and 4p levels. Zn(II) has higher effective nuclear charge, consequently its 4s orbital is highly contracted, resulting in less overlap and thus a weaker covalent bonding interaction.

Coordination of the HS^- ligand to a metal ion results in mixing of metal 4s and 4p character into the HS^- bonding orbitals with the electron density being redistributed from the S-H bond. The stronger Cu(I)-SH^- interaction should remove more charge from the S-H molecular orbital weakening the S-H bond and activating it toward further deprotonation. Complete deprotonation therefore occurs more easily on the Cu_2O surface at low temperature and low coverages. Alternatively, complete

deprotonation of H_2S is observed on the ZnO surfaces at room temperature but not at 140 K, implying that there exists a higher activation barrier for the deprotonation of the surface bound HS^-, related to the weaker Zn(II)-SH^- interaction and thus stronger S-H bond. Accordingly, the strength of the metal-sulfur covalent bonding interaction is closely related to the catalytic sensitivity to sulfur poisoning.

REFERENCES

1. Lin, J.; May, J.A.; Didziulis, S.V.; Solomon, E.I., submitted.
2. Didziulis, S.V.; Butcher, K.D.; Cohen, S.L.; Solomon, E.I. *J. Am. Chem. Soc.*; **1989**; 111; 7110.
3. Penfield, K.W.; Gerwirth, A.A.; Solomon, E.I. *J. Am. Chem. Soc.* **1985**; 107; 4519.

ACKNOWLEDGMENTS

Financial support and facilities were provided by the Stanford Center for Materials Research, which is funded by the NSF Division of Materials Research, and by the Stanford Synchrotron Radiation Laboratory which is operated by the Department of Energy.

CAPTIONS

1. Photon energy dependence of the valence band spectra for the HS^--covered (1.8 L H_2S exposure at 130 K) (solid line) and clean $Cu_2O(111)$ surfaces (dashed line). In each set of spectra, clean data are normalized and aligned to the Cu 3d band. The adsorption-induced features are labeled as peaks A, B and C.

2. Photon energy dependence of the valence band spectra of the HS^--covered (7.5 L H_2S exposure at 130 K) (solid line) and clean ZnO(0001) surfaces (dashed line). In each set of spectra, clean data are normalized and aligned to the Zn 3d band.

3. Comparison of the difference spectra assigned to the surface HS^- species on the $Cu_2O(111)$ and $ZnO(10\bar{1}0)$ surfaces. Difference spectrum **i** is obtained by subtracting the clean $Cu_2O(111)$ surface spectrum from the spectrum of the H_2S (1.8 L) / $Cu_2O(111)$ system at 130 K; **ii** is the H_2S (5.0 L, 140 K) / ZnO(0001) minus clean ZnO(0001) difference spectrum. Difference spectra are aligned to the M-S π level (peak C in **i** and peak N in **ii**) for comparison, which corresponds to a shift of 2.1 eV to lower binding energy of the HS^- / Zn(II) system.

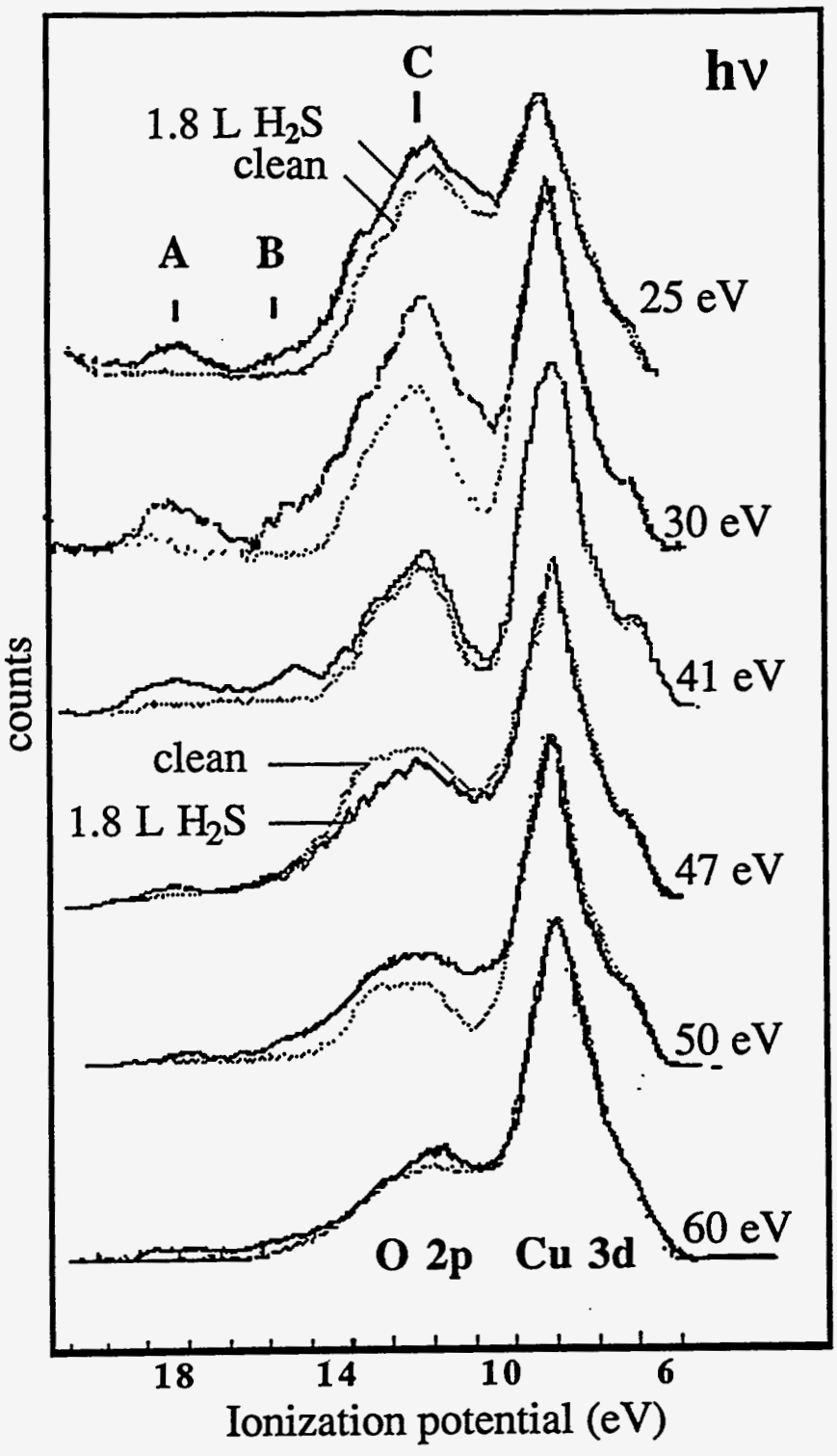
hν
C
1.8 L H_2S
clean
A
B
25 eV
30 eV
41 eV
clean
1.8 L H_2S
47 eV
50 eV
60 eV
O 2p
Cu 3d
counts
18
14
10
6
Ionization potential (eV)

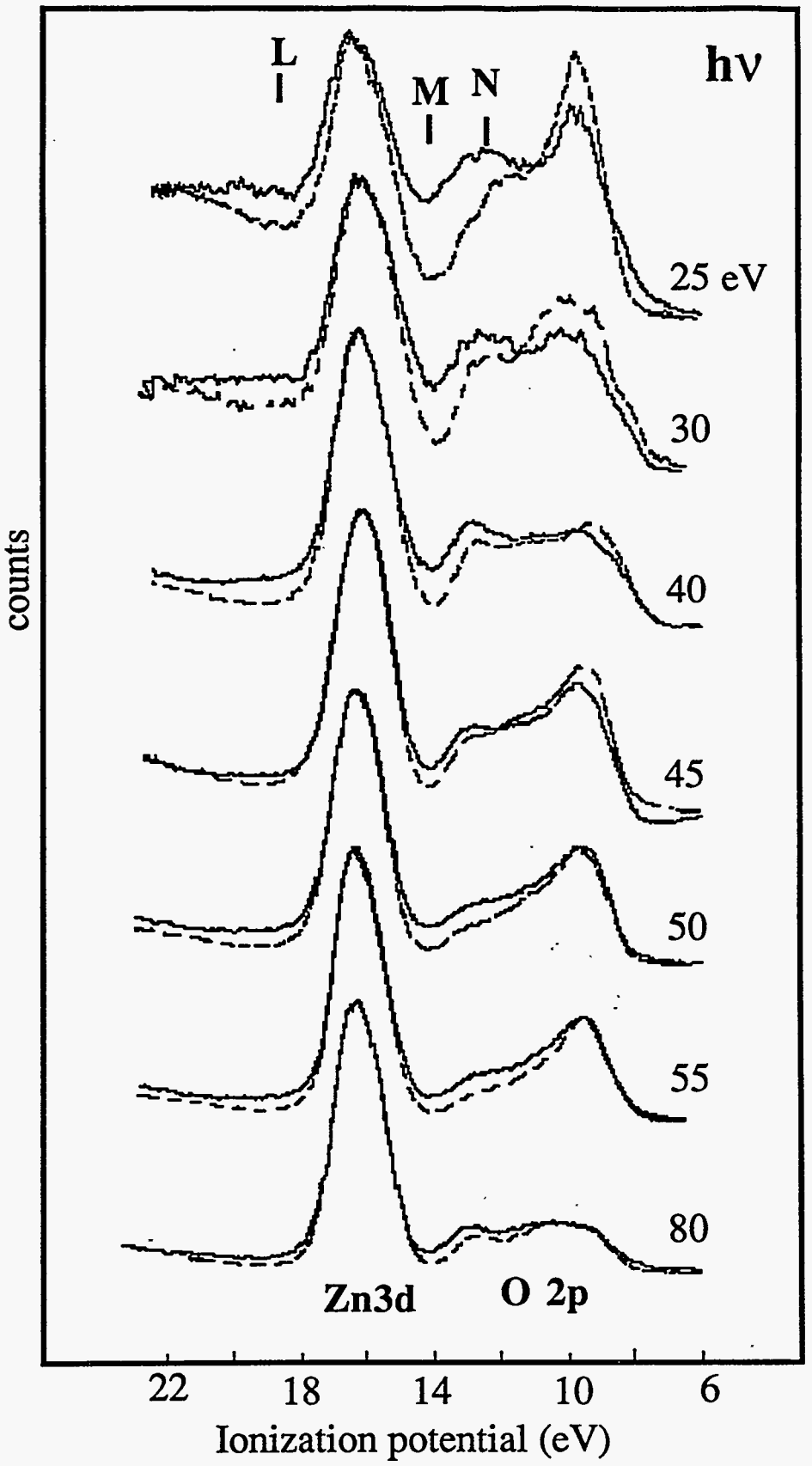
L
M
N
hν
25 eV
30
40
45
50
55
80
counts
Zn3d
O 2p
22
18
14
10
6
Ionization potential (eV)

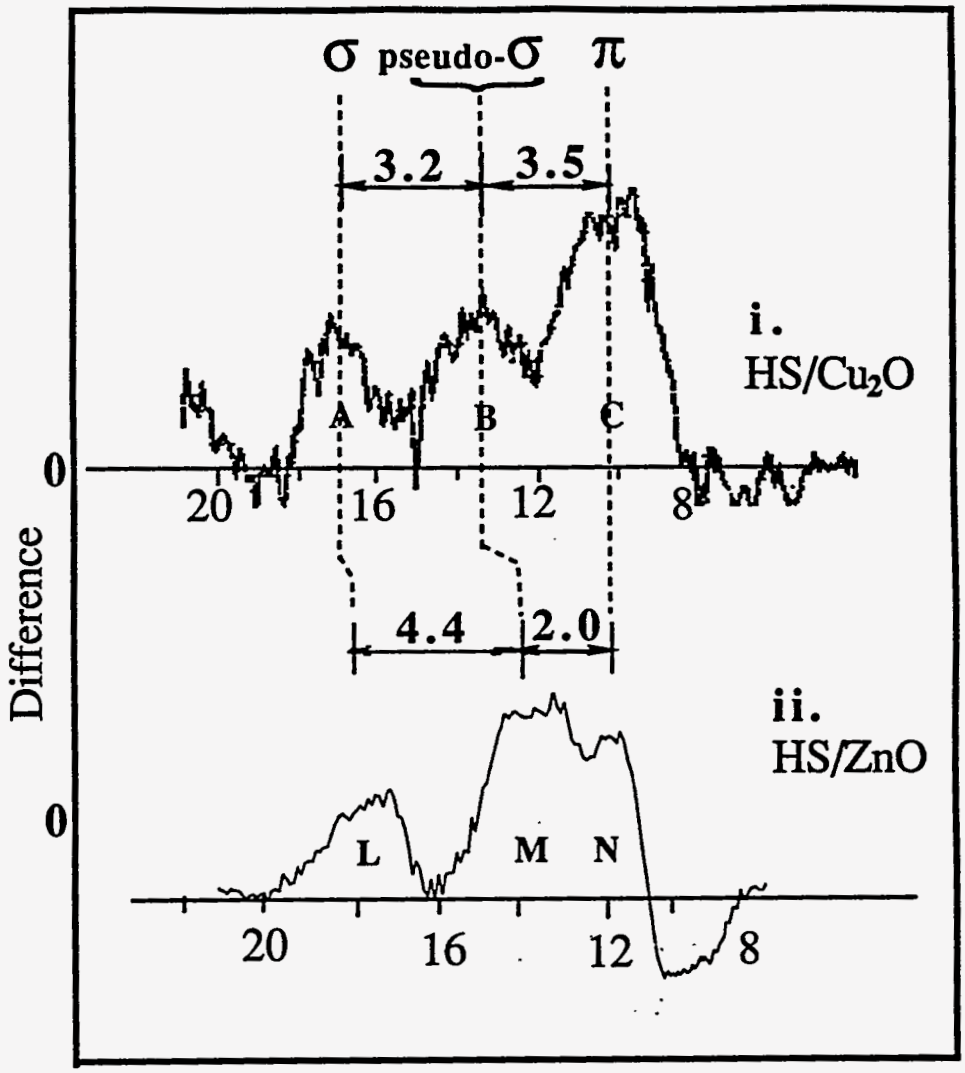
σ pseudo-σ π
3.2
3.5
i.
HS/Cu2O
A
B
C
0
20
16
12
8
4.4
2.0
ii.
HS/ZnO
0
L
M
N
20
16
12
8
Difference
Ionization potential (eV)

CORE LEVEL SHIFTS OF THE Ge AND Si(100)-(2x1) SURFACES AND THEIR ORIGINS

R. Cao, X. Yang, J. Terry, and P. Pianetta
Stanford Synchrotron Radiation Laboratory, P.O. Box 4349, Bin 69, Stanford, CA 94309-0210

INTRODUCTION

The Si(100)-(2x1) and Ge(100)-(2x1) surfaces have been extensively studied for decades due to practical importance and fundamental interest. Despite much progress, there remain a number of issues regarding these reconstructed surfaces. There is no concensus about how many surface related components in the core level photoemission spectra. A number of studies showed only one surface component but others reported two surface components [1-5]. A closely related issue, the nature of these surface components, also remains controversial. A number of theoretical calculations as well as experiments attribute the observed surface core level components to the atoms of the top layer surface dimers, which then favor strong charge transfer between the two atoms within the dimer, while the others suggests that the observed surface components may come from different layers, which implies that the charge transfer between the two atoms may not be so significant [1-8]. It should be pointed out that most experimental determinations up to now are considered as indirect. The key to resolve the core level shift is to obtain a core level lineshape that is close to its natural lineshape. In this study we used epitaxial Ge/Si and Si/Ge(100) system to achieve this goal. The epitaxial layers were grown with Sb as surfactant and showed excellent epitaxy.

EXPERIMENTAL

The experiment was carried out at the Stanford Synchrotron Radiation Laboratory on beam line I-2 with a 6-m toroidal grating monochromator. A VG ADES400 angle-resolved system equipped with a hemisphere analyzer was used. The combined resolution was about 0.2 eV, including contribution from both analyzer and the monochromator. In this particular study, photon energy was fixed. Thus, we eliminate potential complication in data analysis due to variation in monochromator resolution at different photon energies and in probing depth at different electron kinetic energies. The n-type Ge(100) and Si wafers were cleaned by thermal annealing. Sharp (2x1) diffraction patterns with two domains were observed from LEED optics on these surfaces. The pressure was kept in 10^{-10} torr range during evaporation with a base pressure around 1×10^{-10} torr.

After Ge (Si)(100) surface was thermally cleaned, a couple of monolayers (ML) of Sb were deposited on this surface. An afterward thermal annealing up to ~500°C leads to formation of one monolayer of Sb on the surface. This layer is ordered, as indicated by observed (2x1) LEED pattern with weak and diffuse half-order spots. It has been known that the Sb atoms occupy the epitaxial sites of the Si(100) surfaces and saturate the surface dangling bonds resulting from the surface dimers [9]. Similar structure is likely to exist for Sb/Ge(100) system. More importantly, this structure provides an excellent base for Si (Ge) epitaxial growth on the Ge (Si)(100) surface [10]. The epitaxial growth is achieved by depositing Si (Ge) on this surface at room temperature followed by thermal annealing to ~500°C or by depositing Si (Ge) on this surface at elevated temperature. The key in this growth process is the reduction of the surface energy induced by ordered Sb overlayer. Consequently, uniform epitaxial layer can be grown. Si and Ge are similar in many aspects, so one would expect that the substrate Ge (Si)(100) is nearly fully relaxed.

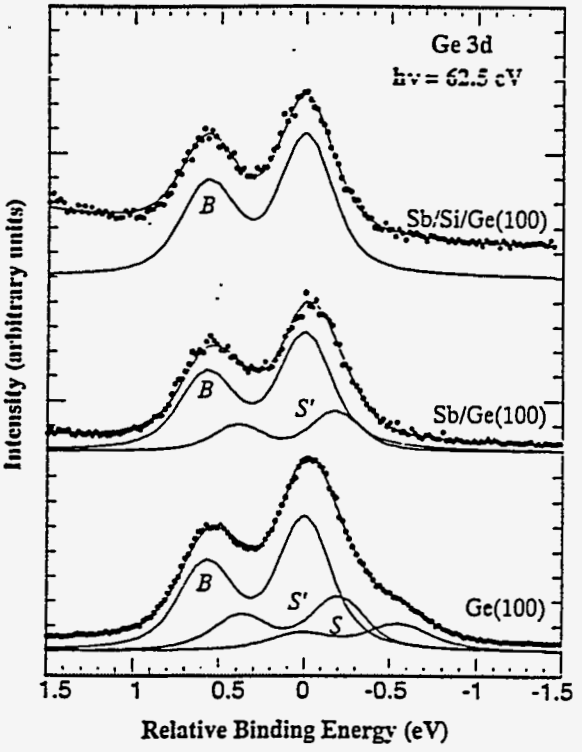

Figure 1. Experimental and computer fitted Ge 3d spectra of Ge(100)-(2x1) clean surface, Sb/Ge(100), and Sb/Si/Ge(100) interfaces.

RESULTS AND DISCUSSION

Figure 1 shows Ge 3d spectra for various surfaces taken at photon energy 62.5 eV. The spectra have been moved in such a way that the band bending of the substrate induced by the either Sb or Si overlayer has been removed. For the clean Ge(100)-(2x1) surface there is an obvious shoulder on the low binding energy direction relative to the main peak. This has been observed before and is attributed to the surface core level shift. When the surface is covered by an ordered Sb monolayer this shoulder vanishes from the spectrum, indicating that this surface component has been removed. But it does not represent the real bulk component as previous studies suggested. As we can see, after the Si layer is epitaxially grown on the Ge(100) surface, the Ge 3d core level is sharper than that obtained from that of the Sb/Ge(100) interface. Clearly, this lineshape is closer to the nature lineshape of the Ge 3d. Although it may not be the true bulk component, it certainly sets an upper limit of the linewidth of the bulk component. This is not surprising, given the fact that Si and Ge are similar in electronic and chemical properties so that Ge atoms don't feel much difference when the neighbor Ge atoms are replaced by Si atoms.

Based on previous argument, we assume that there is only single doublet in curve C. Voigt line shapes (convolution of a Guassian and a Lorentzian) was applied during the least square fitting, and a Gaussian width equal to 0.24 eV and Loretzian width of 0.12 eV were obtained. Other fitting parameters are as following: spin-orbit-splitting, 0.61 eV and branching ratio of $p_{1/2}/p_{3/2}$, 0.5. Using these parameters, we fit rest of the spectra in figure 1. During the fitting, both Gaussian (instrumentation broadening) and Lorentzian (lifetime of the core hole) were kept fixed, assuming all the surface components to have the same line shape as the bulk component. No asymmetric lineshape was used. The fits are indicated by the solid curves overlapping the data points, and the background noise is purely white noise (not shown here). For the clean Ge(100) surface, we have observed two surface components (indicated by S and S') in additional to the bulk component (B) for the clean surface spectrum. The shifts of the surface components from the bulk component are 0.56 and 0.22±0.02 eV for S and S', respectively. S corresponds to the shoulder seen in the spectrum and has been observed previously. The presence of S' is evidenced by the filling in the valley between the two spin-orbit-split peaks of the bulk component.

Using the similar method, we have also studied the surface core level shifts of the clean Si(100)-(2x1) surface. The Si 2p core levels taken at 125 eV at various surfaces are shown in figure 2 together with the fits. Here, two surface components are resolved with the shifts of 0.46 eV and -0.27±0.02 eV from the bulk component for S and S' component, respectively. They agree well with the results reported by the Lin *et al*, where Ge film was grown on the Ge(100) surface directly [3]. Again, here we observe S' component at the Sb/Si(100) interface while others haven't resolved that [11].

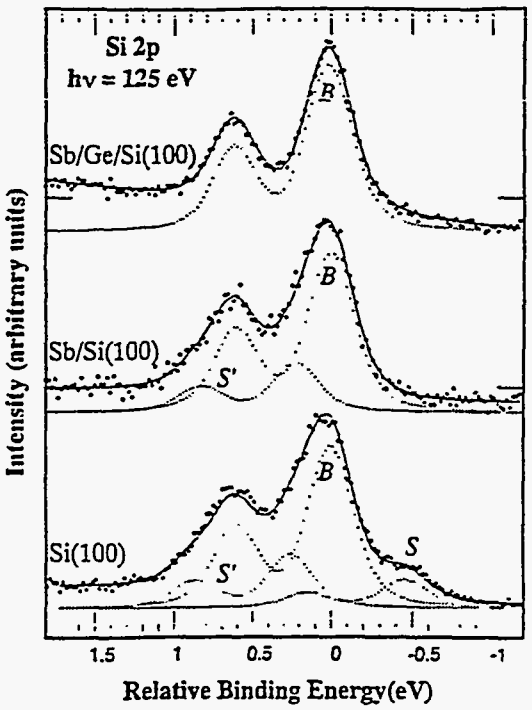

Figure 2. Experimental and computer fitted Si 2p spectra of Si(100)-(2x1) clean surface, Sb/Si(100), and Sb/Ge/Si(100) interfaces. The spectra were taken using the second order light from 62.5 eV primary source.

We have established that there are two core level shifts in additional to the bulk component in the Ge 3d spectrum of the Ge(100) surface and Si 2p of the Si(100) surface. Now we attempt to elucidate the nature of these components. Let's look at the clean surfaces covered by one ordered Sb monolayer first. Here, S component disappears, while S' component remains virtually intact. It clearly demonstrates that S component is contributed by the atoms on the top surface. This is in accordance with previous studies. We also noticed that previous photoemission studies of this interface failed to reveal existence of the S' component. Then, a much larger width of the bulk component had to be used in order to achieve reasonable fit. The key reason is that there was no means to obtain narrower lineshape (close to the natural lineshape) in these studies. In our work, existence of S' becomes obvious. Sb atoms, in these cases, occupy the epitaxially sites of Ge (Si)(100) surface and form dimer themselves. As a results, all the dangling bonds from the original top surface dimers are saturated, and the contribution from them are eliminated from the spectrum. The fact that the S' component remains virtually unchanged, particularly B/S' ratio roughly the same, is highly suggestive that this component does not come

from the top layer atoms, rather it is contributed by the submonolayer atoms . The observed slight shift of the S' between the clean surface and Sb covered surface may result from slight difference in electronegativity and size between Ge (Si) and Sb atoms. When more than one epitxial layer Si (Ge) is grown on the Ge (Si)(100) surface with Sb remaining on the top surface (notice that this Sb layer also occupies the epitaxial sites) the S' component also disappears from the spectrum, indicating that S' mainly originates from the second layer. This work, together with the work reported by Lin *et al*, strongly indicates that although there exist asymmetric dimers on Si(100) and Ge(100) surfaces charge transfer between the two atoms in the same dimer may be much less than what has been previously suggested if one accepts that assumption that approximately 2 eV core level shift should be observed with one electron charge transfer.

Although Ge(100) and Si(100) surfaces behave very similar to each other, there is a drastic difference between them. For the Si(100) surface, two surface components straddle the bulk component, while for Ge(100), the two surface components are located on the same side of the bulk component. Our result also differs from those reported by Lin *et al* [3], where the large separation of the two surface components implies that the configuration of the Ge(100) surface component is the same as that on the Si(100) surface. It is interesting to compare our findings with those from Si(111)-(2x1)/Ge(111)-(2x1) pair and Si(111)-(7x7)/Ge(111)-(2x8) pair, where one always sees different arrangement of S' relative to the bulk component for the Si surface with respect to the Ge surface [12,13]. So far, there is no theory which can successfully explain such a striking difference. A plausible explanation may involve the role of initial and final state effects on the surface core level shifts. As for the initial state effect, one can consider the surface dipole moment induced by the charge density accumulated on the surface atoms. Depending on where the dipole cuts through the atomic plane beneath the surface, the surface core level binding energy will be affected. The final state effect includes screening effect, particularly the screening from the surface electrons Strong screening effect can, indeed, induce drastic alternation of the measured binding energy of the surface atoms. There are some evidence that the binding energy of the surface atoms being influenced by both surface dipole and final state screening [8].

In summary, we have provided a positive identification of the Ge(100) and Si(100) surface states using epitaxial layer method. Two surface states, S and S', have been observed, and they are contribution from the top layer dimers and submonolayer atoms, respectively. Although Ge(100) surface is similar to Si(100) surface, the two surface components shift to one direction relative to the bulk component as opposed to the Si(100) surface, where the shifted surface components straddle the bulk component.

REFERENCES

1. F.J. Himpsel, P. Heimann, T.-C. Chiang, and D.E. Eastman, Phys. Rev. Lett. **45**, 1112 (1980).
2. G.K. Wertheim, D.M. Riffe, J.E. Rowe, and P.H. Citrin, Phys. Rev. Lett. **67**, 120 (1991).
3. D.-S. Lin, T. Miller, and T.-C. Chiang, Phys. Rev. Lett. **67**, 2187 (1991).
4. T. Weser, A. Bogen, B. Konrad, R.D. Schnell, C.A. Schug, and W. Steinmann, Phys. Rev. B **35**, 8184 (1987).
5. D.H. Rich, T. Miller, and T.-C. Chiang, Phys. Rev. Lett. **60**, 357, (1988).
6. D.J. Chadi, Phys. Rev. Lett. **43**, 43 (1979).
7. T. Yamazaki and K. Cho, Surf. Sci. **242**, 260 (1991).
8. E. Artacho, and F. Ynduráin, Phys. Rev. Lett. **62**, 2491 (1989).
9. J.M.C. Thornton, A.A. Williams, J.E. Macdonald, R.G. van Silfhout, J.F. van der Veen, M. Finney, and C. Norris, J. Vac. Sci. Technol. B **9**, 2146 (1991).
10. J. Nogami, A.A. Baski, and C.F. Quate, (to be published).
11. R.H. Rich, G.E. Franklin, F.M. Leibsle, T. Miller, and T.-C. Chiang, Phys. Rev. B **40**, 11804 (1989).
12. T. Miller, T.C. Hsieh, and T.-C. Chiang, Phys. Rev. B **33**, 6983 (1986).
13. S.B. DiCenzo, P.A. Bennett, D. Tribula, P. Thiry, G.K. Wertheim, and J.E. Rowe, Phys. Rev. B **31**, 2330 (1985).

PHOTOEMISSION STUDY OF THE SURFACTANT-ASSISTED Si AND Ge EPITAXIAL GROWTH

R. Cao, X. Yang, J. Terry, and P. Pianetta
Stanford Synchrotron Radiation LaboratoryP.O. Box 4349, Bin 69, Stanford, CA 94309-0210

INTRODUCTION

High quality growth of epitaxial Si, Ge film has attracted much attention recently. The driving force mainly comes from the potential application of SiGe alloy and Si, Ge strain layer structures in new generation semiconductor devices such as high speed devices, optoelectronics applications. It is also of fundamental importance to understand epitaxial growth process itself such as the interplay among surface, interface free energy and lattice strain relief. For the Si/Ge system, the preferred surface termination is Ge, determined by the free energy difference between the two species. Due to the lattice mismatch between the two, Ge can grow on the Si(100) surface following Stranski-Krastanov mode (layer-by-layer growth for ~3 monolayers followed by island formation) [1,2]. In contrast, Si starts islanding from the beginning of the growth on the Ge(100) surface. In order to achieve uniform growth, growth temperature has been pushed lower and lower in various growth techniques. However, the achievement of the uniformity is based on sacrifice of crystallinity of the grown layers. Therefore, there is urgency to look for other strategy. Recently, it has been demonstrated that when the growth front is terminated by a specific third species, so-called surfactant, which is energetically favored over either Ge or Si termination and always moves with the growth front, Si and Ge growth mode can be dramatically changed. There, three-dimensional (island) growth has been altered into two-dimensional (layer) growth up to a reasonable thickness, and the uniform epitaxial Si, Ge layer growth can be realized [3]. A number of atoms have been used as surfactant such as, As, Sb, and Te [3-5].

Although such growth process is under active investigation, the growth mechanism is not well understood. The goal of this work is to provide an microscopic description of the Si, Ge epitaxial growth process involving surfactant at the atomic scale. High revolution photoelectron spectroscopy has been used in this work. Here, we break the growth process down to various stages and investigate the morphology and particularly the electronic structures at these stages. Sb was used as a prototypic surfactant to examine such a growth process based on two reasons. First, Sb/Si(100) and Sb/Ge(100) have long been viewed as model systems and studied rather intensively. Second, Sb is relatively easier to handle with precise control compared with As, so that a quantitative study is feasible. We found that the ordered Sb layer occupies the epitaxial sites and saturates the surface dangling bonds of both Si(100) and Ge(100) surfaces. During the growth, Sb and incoming species exchange their positions. As a result, Sb moves to the growth front to form new ordered layer, while leaving epitaxially grown film behind.

EXPERIMENTAL

The experiment was carried out at the Stanford Synchrotron Radiation Laboratory on beam line I-2 with a 6-m toroidal grating monochromator. A ultra-high vacuum (UHV) VG ADES400 angle-resolved system with a hemisphere analyzer was used with combined resolution about 0.2 eV, including contribution from both analyzer and the monochromator. The n-type Si and Ge wafers used in this experiment were cut in (100) orientation with less than 1^{o} miscut. The Si(100) samples were chemically cleaned and etched in 48% HF solution for a fraction of a minute before introduced into the UHV system. The sample was then prebaked at ~500°C for about an hour and annealed to ~800°C. The Ge(100) samples were cleaned by thermal annealing at ~800°C. Sharp two-domain (2x1) diffraction patterns were observed from the low energy electron diffraction (LEED) optics on these surfaces. Sb and Ge were evaporated from tungsten filament evaporators, and Si was evaporated with a electron beam evaporator. Thorough outgassing was performed prior to deposition. The pressure was kept in 10^{-10} torr range during sample cleaning and evaporation with a base pressure around 1×10^{-10} torr. No trace of contamination was found within the sensitivity of photoemission.

The growth process is as the following: after the Si(100) [Ge(100)] surfaces were thermally cleaned, couple of monolayers of Sb were deposited on the surfaces at room temperature. The interface was then annealed to ~500°C. As will be seen later in this letter, such a treatment leads to formation of an ordered Sb monolayer residing on the top surfaces. The same type of structure can be also obtained by depositing Sb at elevated temperature (~500°C). Ge (Si) was then deposited on to this structure at room temperature followed by thermal annealing at ~500°C or at elevated temperature (~500°C). The observed LEED pattern and photoemission spectra indicates that the structure beneath the Sb layer is well ordered and occupy the epitaxial sites.

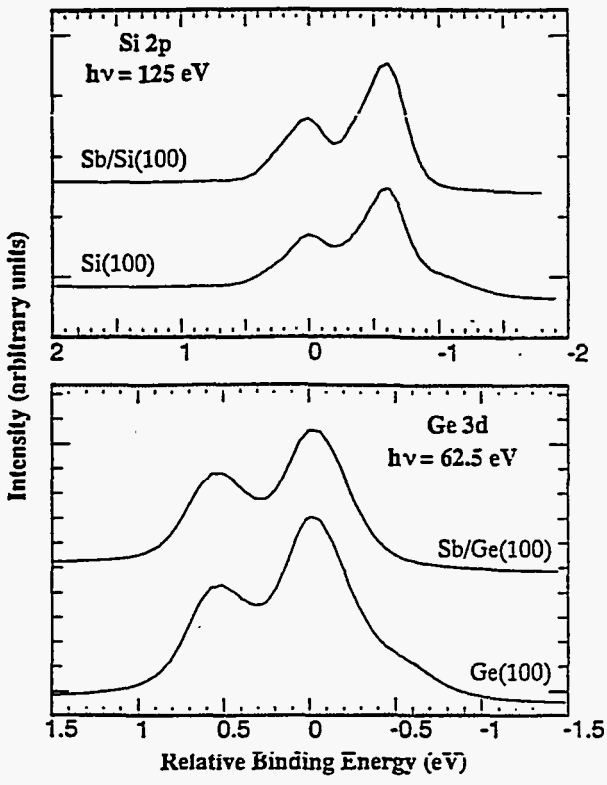

Figure 1. Si 2p and Ge 3d core level spectra from the Si(100), Ge(100) and their corresponding Sb-covered surfaces.

RESULTS AND DISCUSSIONS

Let us first take a look at the photoemission spectra taken at the clean and Sb-covered Si(100) and Ge(100) surfaces. Figure 1 shows Si 2p and Ge 3d spectra taken at photon energies 125 eV and 62.5 eV, respectively. The spectra have been moved in such a way that the band bendings of the substrate induced by the overlayer Sb have been subtracted out. The spectra of the clean Si(100)-(2x1) and Ge(100)-(2x1) surfaces exhibit obvious shoulders on the low binding energy direction relative to the main peaks. These have been identified as the surface related core-level shifts of these surfaces, and it is generally agreed that they are contributed by the atoms of the top surface dimers. When several monolayers of Sb were deposited on these surfaces at room temperature followed by thermal annealing around 500°C, only one monolayer of Sb remains on the surfaces [6]. A (2x1) LEED pattern with weak, diffuse half-order dots was observed. The Sb/Si(100) interface has been studied by Nogami et al using scanning tunneling microscopy (STM) [7], and they confirmed that only one monolayer of Sb was left on the surface as a result of thermal annealing. The study further showed that Sb atoms formed dimers rows which are perpendicular to the substrate Si dimer rows, and the substrate Si was relaxed. Note that the Sb dimers reside exactly where the Si dimers will be located in the case of Si homoepitaxial growth. The weak and diffuse half-order dots in the LEED pattern may results from break of Sb dimer rows. Nevertheless, to a large extent, Sb/Si(100) structures resemble that of the As/Si(100) [8,9]. Influence of the Sb overlayer over the electronic properties is reflected by the removal of the surface related core level shift from the clean surface spectrum, in accordance with the previous study [10]. This provides strong evidence that the surface dangling bonds are saturated. The behavior of Sb on Ge(100) surface is nearly identical to the Sb/Si(100) [11]. Here, we also observed a (2x1) LEED pattern with weak half-order dots. And the Ge(100) surface dangling bonds have been removed from the interface as evidenced by the spectrum in Fig. 1 (b). Therefore, we believe that Sb atoms also occupy the epitaxial sites of the Ge(100) surface, similar to that of the Sb/Si(100).

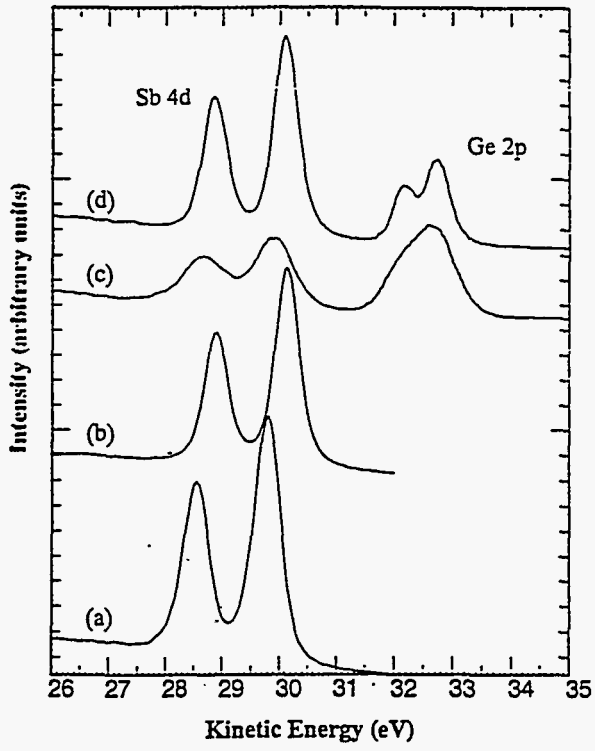

Figure 2. Sb 4d and Ge 3d core level spectra at various stages of Ge epitaxial growth on the Si(100) surface. The photon energy is 62.5 eV. (a) RT deposition of Sb on Si(100) surface; (b) after annealing; (c) RT deposition of Ge on 1ML Sb/Si(100); (d) the structure after 500°C annealing.

Figure 2 shows Sb 4d and Ge 3d spectra at various stages of Ge epitaxial growth on the Si(100) surfaces. The identical behavior of the Sb 4d has been observed in the case of the Si epitaxial growth on the Ge(100) surface. For sake of brevity, the spectra are not shown here. We are going to concentrate on discussion of the first case, and all the conclusion will be directly

applied to the latter one. Strong emission from the Sb 4d is observed when several monolayers of Sb is deposited on the clean Si(100) surface at room temperature. After mild annealing, the intensity decreases. The remaining amount of Sb is estimated about one monolayer, consistent with previous studies. The fact that Sb 4d spectrum in this case consists of only one component indicates occupation of a single type of Sb site. This is a direct result of the epitaxial Sb layer. Measurable core-level shift is also observed in the Si 2p spectrum (not shown here). This influence to the substrate Si electronic structure by Sb is analogous to As [9], in contrast with the previous study where Sb was deposited on the Si(100) surface at room temperature [12].

When Ge is deposited on this structure at room temperature, several changes take place. The first obvious change is the large decrease of the Sb 4d peak intensity. The degree of this intensity decrease is consistent with the uniform Ge overlayer on top of the Sb layer. In addition to the intensity decrease, Sb 4d becomes much broader compared with that without Ge overlayers. Ge 3d is also broader with unresolved spin-orbit splitting features. These changes in the photoemission spectra suggest that the deposited Ge is in amorphous state. Lack of crystallinity in the Ge layer is corroborated by disappearance of LEED pattern in this case. The situation is completely different when this structure undergoes a thermal annealing around 500°C. First, there is a recover of intensity of the Sb 4d spectrum. In fact, the intensity in this case is the same as that on the Sb/Si(100) surface. No obvious sign of Sb depletion has been detected within the limit of photoemission sensitivity. This clearly demonstrates that Sb layer now resides on the top surface. Second, the Ge 3d spectrum is much more defined. The filled valley in curve c reappears, indicating much improved crystallinity in Ge layer. In fact, this spectrum is nearly identical to spectrum shown in figure 1, when the single crystal Ge(100) surface is covered by an ordered monolayer of Sb. Finally, LEED pattern [(2x1) with weak, diffuse half-order dots] is restored again.

From this set of spectra, we can easily draw several conclusions. It is clear that during the annealing, Sb atoms and Ge atoms change their positions. As a result, Ge atoms move in and make direct contact with the Si substrate, while Sb atoms move out to the top surface, a typical behavior of surfactant. Moreover, Ge atoms are no longer arranged in a random fashion. Instead, they appear to occupy some ordered sites. The observed LEED pattern suggests that this layer of Ge actually occupies the epitaxial sites of the Si(100) surface. What has happened there is not hard to imagine. During the thermal annealing, Sb atoms move up, leaving their epitaxial site to the incoming Ge atoms. Consequently, an epitaxial Ge layer is formed and is covered by Sb layer again.

The identical Sb 4d and Ge 3d spectra seen in figure 2 and that of figure 1b also confirms that the segregated Sb atoms form a new ordered overlayer on top of the epitaxial grown Ge film. This makes the substrate ready for further epitaxial Ge epitaxial growth. In fact, We repeated the same process for several times and obtained thick Ge epitaxial film on the Si substrate. The epitaxial Ge film can also be obtained by direct depositing Ge on Sb/Si(100) structure at elevated temperature, which was used previously by other groups. The same method has been used for epitaxial Si growth on Ge(100) substrate, and we find that the grown film is uniform without much clustering.

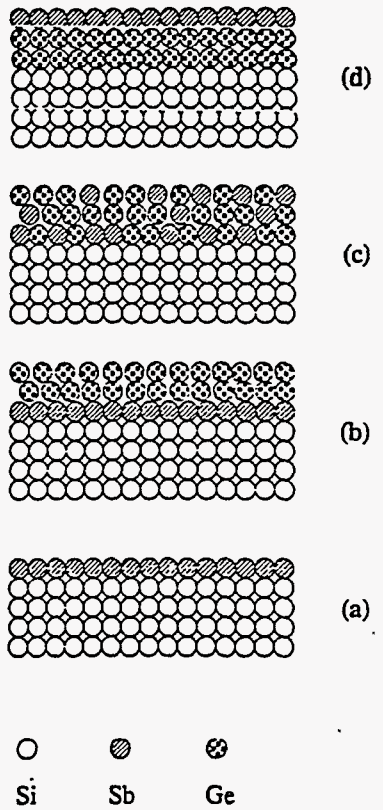

Figure 3. Schematic model of the Sb-assisted Ge epitaxial growth on the Si(100) surface: (a) 1ML Sb/Si(100); (b) RT deposition of Ge on Sb/Si(100); (c) Sb and Ge atoms change their positions during annealing; (d) Sb atoms form new ordered layer on top surface leaving epitaxial Ge layer behind.

CONCLUSION

To conclude our study, we show a schematic diagram to illustrate the surfactant-assisted Si, Ge epitaxial growth in figure 3. We have demonstrate that ordered Sb layer on the Si(100) and Ge(100) surfaces occupies the epitaxial sites and saturates the surface dangling bonds as shown in (a). As a result, the surface energy is reduced, providing a base for uniform growth. It has been shown that it is energetic favorable to form Si/Ge/As compared with Si/As/Ge. This relation is likely to hold in the case involving Sb. During the growth process, Sb atoms and the deposited Si (Ge) atoms change

their positions. Si (Ge) atoms move in and take the epitaxial sites emptied by the Sb atoms. This is illustrated in figure 4 (c). Consequently, an epitaxial film is formed. At the same time, Sb atoms move to the growth front and form a new ordered overlayer. Then the the whole system is ready for the further growth as fig. 4 (d) indicates.

REFERENCES

1. M. Asai, H. Ueba, and C. Tatsuyama, J. Appl. Phys. **58**, 2577 (1985).
2. P.M.J. Marée, K. Nakagawa, F.M. Mulders, and J.F. van der Veen, Surf. Sci. **191**, 305 (1987).
3. M. Copel, M.C. Reuter, and R.M. Tromp, Phys. Rev. Lett. **62**, 632 (1989); M. Copel, M.C. Reuter, M. Horn von Hoegen, and R.M. Tromp, Phys. Rev. B **42**, 11682 (1990); F.K. LeGoues, M. Copel, and R. Tromp, Phys. Rev. Lett. **63**, 1826 (1989).
4. J.M.C. Thornotn, A.A. Williams, J.E. MacDonald, R.G. van Silfhout, J.F. van der Veen, M. Finney, and C. Norris, J. Vac. Sci. Technol. B **9**, 2146 (1991).
5. S. Higuchi, and Y. Nakanishi, Surf. Sci. **254**, L465 (1991).
6. S.A. Barnett, H.F. Winters, and J.E. Greene, Surf. Sci. **165**, 303 (1986).
7. J. Norgami, A.A. Baski, and C.F. Quate, Phys. Rev. B **44**, 1415 (1991).
8. R.I.G. Uhrberg, R.D. Bringans, R.Z. Bachrach, and J.E. Northrup, Phys. Rev. Lett. **56**, 520 (1986).
9. R.S. Becker, T. Klitsner, and J.S. Vickers, J. Microscopy **152**, 157 (1988).
10. D.H. Rich, G.E. Franklin, F.M. Leibsle, T. Miller, and T.-C. Chiang, Phys. Rev. B **40**, 11804 (1989).
11. R. Cao, X. Yang, J. Terry, and P. Pianetta, (to be published).
12. D.H. Rich, F.M. Leibsle, A. Samsavar, E.S. Hirschorn, T. Miller, and T.-C. Chiang, Phys. Rev. B **39**, 12758 (1989).

INITIAL IMAGES WITH A NEW TYPE OF SOFT X-RAY MICROSCOPE

GREGORY HIRSCH
HIRSCH ASSOCIATES
365 TALBOT AVE. SUITE D8, PACIFICA, CA 94044

INTRODUCTION

Soft x-ray microscopy is currently being developed in many laboratories wordwide. The method holds the promise of high resolution imaging of biological samples in their natural, even living, state [1]. Fully hydrated (wet), unstained, unsectioned specimens are suitable samples for investigation. By using x-rays with a wavelength between the K-edges of oxygen and carbon (23-44Å), high contrast can be obtained without staining, due to the absorption difference between water and organic material. In addition, by tuning the wavelength above and below characteristic absorption edges, high spacial resolution elemental analysis is possible. Soft x-ray microscopy is a complementary technique to electron microscopy with both techniques having certain advantages and disadvantages.

The microscope being developed in this work is described in United States Patent 4,829,177. The technique can be thought of as contact microscopy with photoelectric conversion [2] in a field emission microscopy geometry [Fig. 1]. As in field emission microscopy, a conical emitter with a small spherical tip is positioned in a vacuum chamber with the tip facing an electron sensitive imaging surface. Instead of the usual solid emitter, a hollow emitter is used. The sample to be examined is placed inside the spherical tip of the hollow emitter. To produce an image, x-rays are beamed down the inside of the emitter, through the specimen, and onto the spherical tip. The tip is a thin x-ray transparent membrane coated with a highly efficient photoemissive layer on the outside. A contact image is produced on the emitter tip corresponding to the x-ray absorption of the specimen. This contact image produces photoelectrons on the outside surface of the tip which are then accelerated radially to the detector surface by a high voltage placed on the emitter. A highly magnified, real time, high resolution image results without the need for complicated x-ray or electron optics.

EXPERIMENTAL

A small viton-sealed chamber was attached to the back flange of the beamline 3-4 experimental chamber at SSRL. Beamline 3-4 has a differentially pumped section which allows operation up to a pressure of $2x10^{-5}$ Torr. The pressure in the chamber was typically an order of magnitude lower in these experiments. The chamber has a 40 millimeter diameter microchannel plate detector with a phospor screen output. Images were recorded by photography of the screen with a 35 mm single lens reflex camera. The hollow emitters were mounted inside the chamber at a distance of 7 centimeters from the detector. For these initial experiments, the inside of the emitter was open to the vacuum. X-rays were collimated with a pinhole of approximately 25 microns in lead foil . The pinhole was mounted over the end of a tube which was attached to the X-Y movement stage normally used for x-ray lithography sample movement. The pinhole was positioned a few centimeters behind the opening of the hollow emitter allowing close proximity of the pinhole to the emitter even though the movement stage was some distance away. A small beamstop was positioned directly above the detector surface to stop the x-ray beam which was transmitted through the emitter tip. The hollow emitters were mounted on the center of a 1/2 inch wide metal strip. A phosphor was deposited on the metal strip for alignment of the x-ray beam. Once the beam was lined up in one axis with the emitter center, it was then scanned across the other axis until a photoelectron image was observed from the tip. The metal strip was attached to a high voltage feedthrough which allowed up to 30 kV to be placed on the emitter, although 20 kV was the highest potential used. This was due to field emission from the support structure above 20 kV.

The shape of the hollow emitters is quite different from that of a typical field emitter, which has a very narrow taper angle and a small diameter. In these hollow emitters, the taper angle is 30-60 degrees, and the opening is 2 millimeters. Therefore, the emitter tip interior is quite accessible for introducing specimens. In the initial experiments, silver was used for the tip membrane material, with a thickness of 0.5-1.0 microns. A thin sputtered gold or evaporated cesium iodide layer was used for the photoemissive surface. The beamline 3-4 white beam was generally used with a 5 micron Be filter to remove the UV and very soft x-ray component. This radiation would not be transmitted by the silver membrane, but causes a background problem due to scattering from the pinhole.

RESULTS AND DISCUSSION

Images were produced using metal grids mounted

inside the emitters as test objects. Due to the high absorption of the silver membrane, there was very little transmission through the membrane below approximately 1500 electron volts. This eliminated the possibility of using biological objects in these initial experiments, due to insufficient contrast at these energies. The beamline toroidal mirror cuts off at roughly 3000 electron volts. Therefore, imaging was accomplished with photons between these two values. Nickel mesh with a period of 12.7 microns and a gold grating with a period of 0.85 microns were used. A typical image with the nickel mesh is shown [Fig. 2]. By using smaller radii tips, resolutions estimated to be approximately 1000Å were obtained. The resolution of the images is consistant with what is predicted from theory. Resolution improves with smaller tip radii, higher electric fields, and lower photoelectron energy distributions. The photoelectron energy distribution is a function of the photoemissive material and there are materials which are known to have lower energy distributions than cesium iodide. In addition, the electric field should be able to be increased by better preparation of the support structure to eliminate field emission sources. Therefore, the goal of routine imaging with a resolution better than 1000Å appears to be achievable.

Future work will extend this technology to softer x-rays and biological samples. The eventual goal is to produce routine imaging at the 100-500Å resolution range for biological samples. In addition to using synchrotron radiation as the source, this technique could be used with small laboratory soft x-ray sources for producing a table top size instrument.

ACKNOWLEDGMENTS

Partial support for this work was provided by Dr. B. G. Falk. The author wishes to acknowledge equipment loans from Balzers and Trufocus Corporation. Helpful discussions were provided by Drs. P. Pianetta and S. Rothman. The help of the SSRL staff was greatly appreciated.

REFERENCES

1. See for example, A.G. Michette, Reports on Progress in Physics 51 (12), 1525 (1988)

2. F. Polack, S.Lowenthal, D. Phalippou, P. Fournet, X-RAY MICROSCOPY II, ED. D.Sayre, M. Howells, J. Kirz, H. Rarback, Springer-Verlag (1988) P. 220

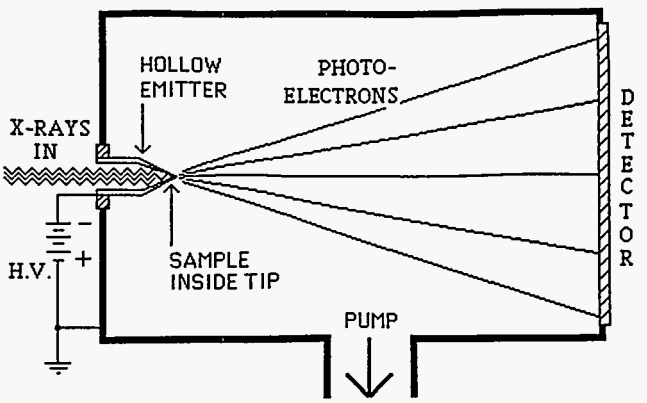

Fig. 1 Schematic diagram of microscope. The opening of the emitter can be open to atmosphere as shown or inside the vacuum chamber with a thin window to contain the sample at atmospheric pressure.

Fig 2 Soft x-ray micrograph taken at beamline 3-4. Sample is 2000 line/inch nickel mesh suspended inside emitter. Two of the roughly 8 micron openings are visible. Tip radius is approximately 15 microns. Voltage on emitter is 18 KV. The horizontal bar is the x-ray beamstop held in front of the detector. The resolution of this image is estimated to be 3000-4000Å.

"THE STRUCTURES AND PROPERTIES OF ULTRATHIN MAGNETIC FILMS"

J. G. Tobin,[A] G. D. Waddill,[A] D. P. Pappas,[B] S. Y. Tong,[C]
X. -Q. Guo,[C] and P. Sterne[A]

A. Lawrence Livermore Nat'l Lab, Livermore, CA 94550
B. IBM, Almaden Research Center, San Jose, CA 95120
C. Dept. of Physics, Univ. of Wis-Milw, Milwaukee, WI 53201

We are using a combination of approaches and techniques to study the structures and properties of ultrathin magnetic films of iron. Included in this are photoelectron diffraction with multiple scattering analysis and x-ray magnetic circular dichroism. The photoelectron diffraction variant utilizing the intrinsic spin-resolution of the multiplet split 3s state is also being developed. Additionally, spin-dependent densities of states are being calculated using LDA slab methods, for comparison to the MCD results.

Photoelectron Diffraction

The prefatory results of an ongoing investigation of Fe/Cu(001) are presented here. Energy dependent photoelectron diffraction is being used to investigate the nanoscale structures formed by near-monolayer deposits of Fe onto Cu(001). Core level photoemission from the Fe3p and Fe3s states has been generated using synchrotron radiation as the tunable excitation source. Initially, a comparison of the experimental Fe3p cross-section measurements with multiple scattering calculations over a narrow energy range indicated that the Fe is in a fourfold hollow site with a spacing of 3.6Å between it and the atom directly beneath it, in the third layer[1]. This is consistent with an FCC structure. However, questions remained concerning the exact bond lengths and the nature of the Fe nearest neighbors. Recently, we completed more extensive measurements at the Stanford Synchrotron Radiation Laboratory, using the spherical grating monochromator beamline (8-2) of the University of California/National Labs Participating Research Team (PRT) Facilities. An example of our data is shown in Fig. 1. Note the wide energy range over which the data were collected, as well as the oscillations in the cross sections, which are indicative of strong local order. Further data analysis is in progress. The possibility of utilizing spin-dependent photoelectron diffraction to investigate magnetic ultrathin films is also being pursued, using the multiplet-split Fe3s of near-monolayer Fe/Cu(001)[1]. Spin-dependent photoelectron diffraction with a full multiple scattering analysis including spin-effects, holds out promise as a probe of local magnetic order. It would thus be the nanoscale (10^{-9}m) counterpart of techniques such as those utilizing the surface-magneto-optic Kerr effect (SMOKE).

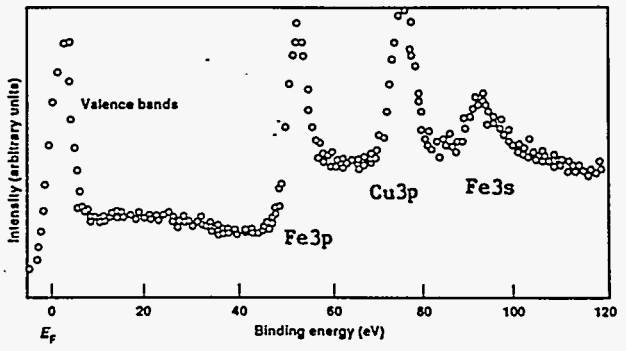

Photoelectron Spectrum

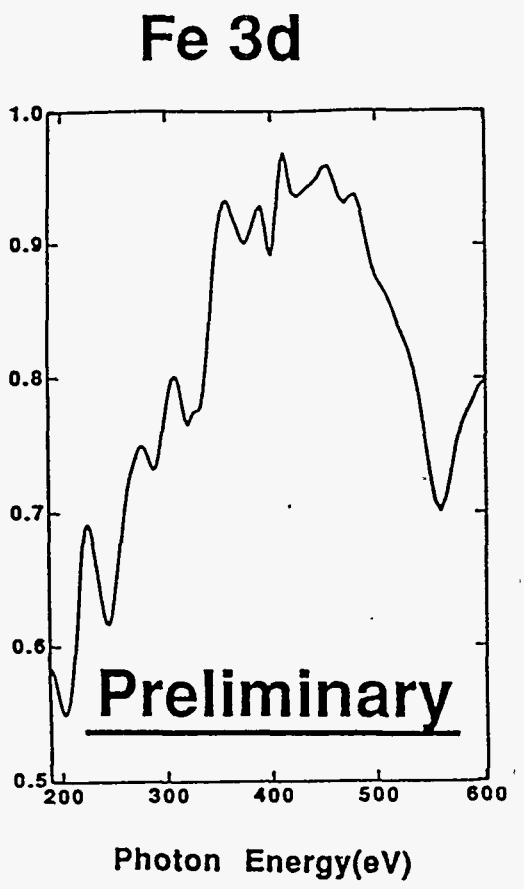

Fig. 1. A photoelectron spectrum at hν = 550 eV and a photoelectron diffraction curve, for Fe/Cu(001).

Magnetic Circular Dichroism in X-ray Absorption and Core Level Photoemission of Fe/Cu(oo1)

We report the first observation of magnetic circular dichroism in both x-ray absorption and core-level photoemission of ultra thin magnetic films using circularly polarized x-rays. Iron films (1-4 ML) grown on a Cu(001) substrate at 150 K and magnetized perpendicular to the surface show dramatic changes in the $L_{2,3}$ branching ratio for different x-ray polarizations. For linearly polarized x-rays perpendicular to the magnetic axis of the sample the branching ratio was 0.75. For films $\geq$ 2 ML, this ratio varied from 0.64 to 0.85 for photon spin parallel and anti-parallel, respectively, to the magnetic axis. This effect was observed either by changing the x-ray helicity for a fixed magnetic axis, or by reversing the magnetic axis for a fixed x-ray helicity (Fig. 2). Warming the films to ~300 K eliminated this effect indicating a loss of magnetization in the film over a temperature range of ~30 K (Fig. 3). Reversing the relative orientation of the photon spin and the magnetic axis from parallel to anti parallel allowed measurement of the exchange splitting of the Fe 2p core levels which was found to be ~0.2 eV (Figs. 4 and 5). We can compare. our experimental results to spin-specific calculations, an example of which is shown in Fig. 6. The MCD results are consistent with earlier studies, but the use of off-plane circularly polarized x-rays from a bending magnet monochromator offers ~2 orders of magnitude greater intensity than typical spin-polarization measurements.

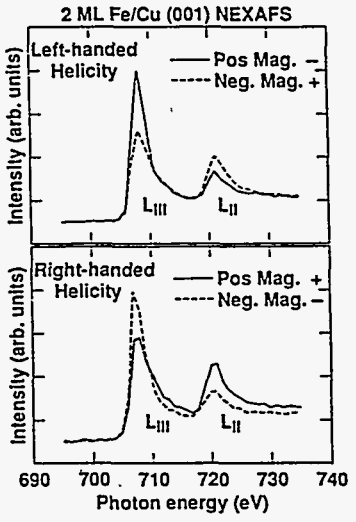

Fig. 2. The near-edge x-ray absorption fine structure (NEXAFS) dichroism of 2ML of Fe/Cu(001). These are plots of absorption vs photon energy. The upper panel shows the effect of reversing the magnetization while maintaining the left-handed helicity of x-rays. Similarly for the lower panel and right- handed helicity x-rays. Samples are perpendicularly magnetized either into (pos. mag.) or out of (neg. mag.) the surface. The symbol +(-) means that the helicity and magnetization are parallel (antiparallel). The $2p_{3/2}$ peak is at the L_{III} edge and the $2p_{1/2}$ peak is at the L_{II} edge. The spectra were normalized to each other by equating the pre-edge intensity, at energies below approximately 700 eV.

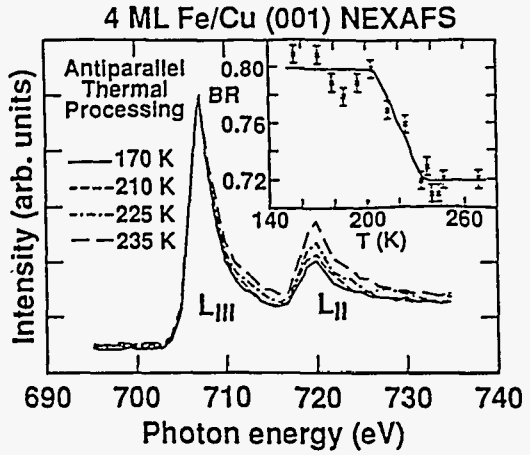

Fig. 3. The temperature dependence of the magnetization, using NEXAFS magnetic circular dichroism as the probe. Absorption vs energy spectra, similar to Fig. 2, are shown, as well as a plot of BR vs temperature. The spectra are normalized to the maximum of the L_{III} peak. Because of imperfect placement of the thermocouple on the sample plate, the sample temperature may be slightly higher than that shown. Error bars of approximately ±1% are included for comparison but the true time error estimate is probably higher.

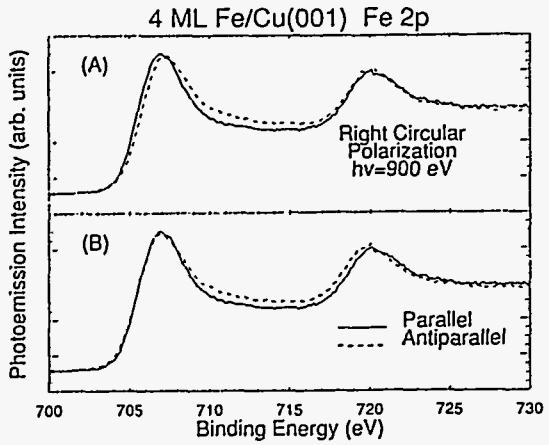

Fig. 4. Fe 2p spectra taken with hν = 900 eV and positive photon helicity. The solid lines are parallel orientation of photon spin and sample magnetization and the broken lines an antiparallel orientation. The two orientations were achieved by fixing the photon helicity and reversing the magnetization of the sample. The spectra in (a) are as collected and show the differences in binding energy for the $2p_{3/2}$ and $2p_{1/2}$ levels for the two helicity and magnetization orientations. The spectra in (b) are identical but have been shifted in energy to align the leading edge of the $2p_{3/2}$ level in order to emphasize lineshape differences between the two orientation extremes.

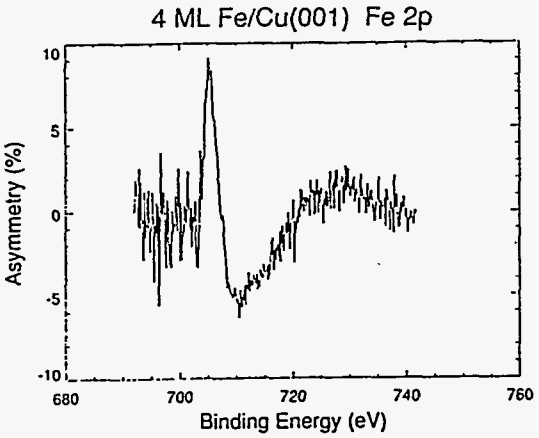

Fig. 5. Asymmetry of the photoemission intensity observed for parallel (I_P) and antiparallel (I_A) orientation of photon spin and sample magnetization, $A = (I_P - I_A)/(I_P + I_A)$. This curve is obtained for fixed photon helicity and two different sample magnetizations.

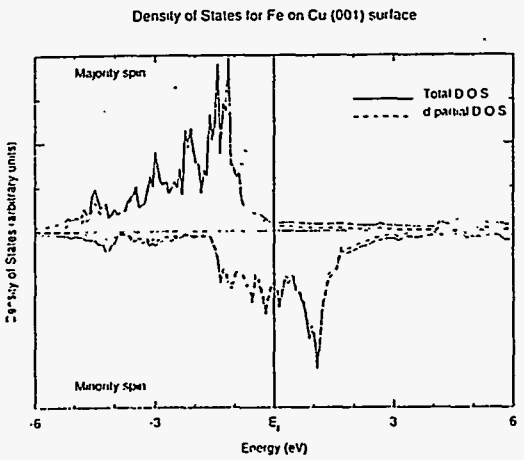

Fig. 6. Shown here are spin dependent density of states calculations for 1 MlFe/5MLCu(001)/1 MlFe. Both the total and d density of states are shown. Ef is the Fermi energy. Occupied states are to the left of E_F and unoccupied states to the right.

1. J. G. Tobin, M. K. Wagner, X.-Q. Guo and S. Y. Tong, Mat. Res. Soc. Symp. Proc., 208, 283 (1991).

Work performed under the auspices of the U.S. DOE by the Lawrence Livermore National Laboratory under contract No. W-7405-ENG-48.

HIGH-RESOLUTION OF THE TOROIDAL GRATING MONOCHROMATOR ON BEAM LINE 8-1

T. Reich, R. Fellers, Z. Hussain, M. Howells, O.B. Dabbousi, D.A. Shirley

Lawrence Berkeley Laboratory
1 Cyclotron Road
MS 2-300
Berkeley, CA 94720

A careful determination of the resolution of the toroidal grating monochromator (TGM) on beam line 8-1 at SSRL was performed. The high-resolution potential of the TGM can be realized by optimizing the focusing conditions and by a suitable illumination of the toroidal grating over a restricted area to emphasize its large radius (R=19.224mm) (see table 1).

Table 1. Ideal performance for R = 19.224m grating

Grating	Photon energy eV	Dispersion eV/mm	Resolution E/ΔE(FWHM)
2400 l/mm	200	0.746	26.700
	150	0.447	33.600
	100	0.222	45.000
	75	0.139	54.000
823 l/mm	80	0.338	23.700
	60	0.201	29.900
	40	0.099	40.400
	20	0.032	62.500
288 l/mm	25	0.096	26.000
	20	0.065	30.800
	15	0.039	38.500
	10	0.020	50.000

To test the resolution of the 823 l/mm grating, the higher members in the Rydberg series $1s^2 \rightarrow (2snp \pm 2pns)$ of the double-excitation spectra below the N=2 threshold of He^+ with a much smaller natural linewidth than the achieved monochromator resolution were studied. The photoionization measurements were performed with a two-plate ionization chamber filled with 15 mtorr He.

The measured spectra were fitted in two ways: by a least-squares fitting procedure with convoluted Fano and Gaussian profiles, and by a deconvolution with a Fano profile to yield the monochromator resolution. High-accuracy experimental data /1/ and theoretical results /2/ were used as a reference data set for the Fano profiles.The Gaussian linewidth was set equal to the monochromator resolution.

For the first time it was possible to show experimentally the dependence of the monochromator resolution on the exit slit position (see fig. 1). To obtain the highest resolution, the exit slit was positioned at the point of the perfect focus.

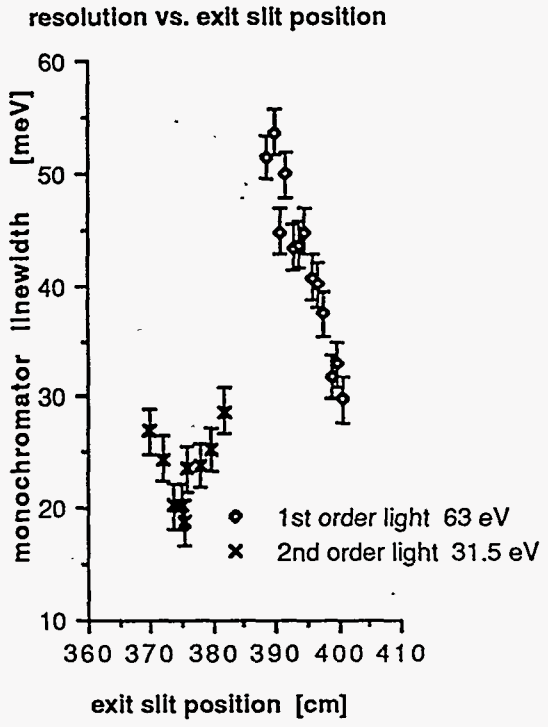

Fig. 1 Resolution vs. exit-slit position

The dependence of the monochromator resolution on the vertical entrance and exit slit opening is shown in fig. 2. During the experiments, the monochromator resolution was limited by the smallest possible vertical entrance slit opening of approximately 40 μm.

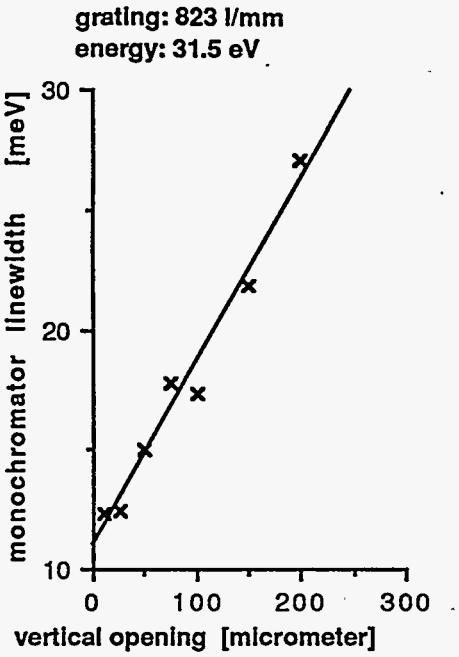

Fig. 2 Resolution vs. entrance- and exit-slit opening

For the optimal achievable conditions, the Rydberg states up to n=14 of the "+" series have been resolved (see fig. 3).

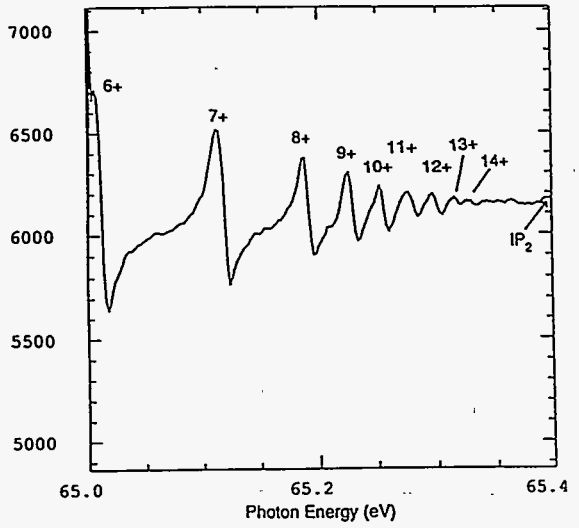

Fig. 3 Photoionization spectra of the N=2 series of the autoionization double-excitation states of He, $1s^2 \rightarrow (2snp + 2pns)$

At 63.5 eV the monochromator resolution was 24 meV and 12 meV for first and second order light, respectively (see fig. 4). This corresponds to a resolving power of 5200 with second order light.

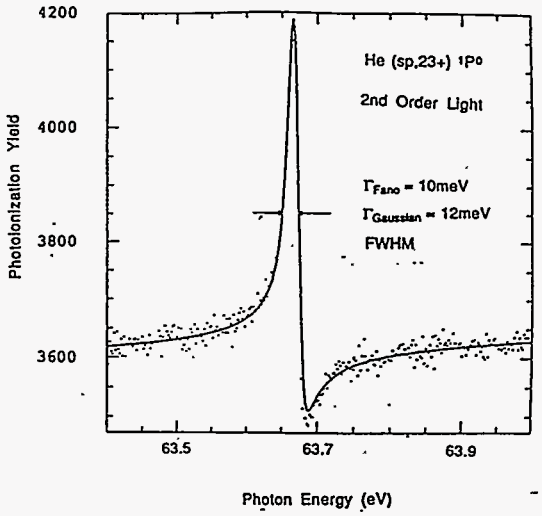

Fig. 4 Photoionization spectra of the autoionization double-excitation state $1s^2 \rightarrow (2s3p + 2p3s)$ of He

With an improved slit mechanism and a better stepping motor for the gratings, a significant higher resolving power of the TGM can be realized.

Acknowledgements

This work was supported by the Director, Office of Energy Research, Office of Basic Energy Sciences, Chemical Sciences Division of the U.S. Department of Energy under the Contract No. DE-AC03-76SF00098. It was performed at the SSRL which is supported by the Department of Energy's Office of Basic Energy Sciences. T.R. is pleased to acknowledge the Alexander von Humboldt Foundation for support through a Feodor-Lynen-fellowship.

References

/1/ M. Domke et al., Phys.Rev.Lett., v.66, 1991, p.1306

/2/ P. Hamacher and J. Hinze, J.Phys.B, v.22, 1989, p.3397

High Resolution Photoabsorption on the University of California/ National Laboratory Spherical Grating Monochromator Beamline

L.J. Terminello, G. D. Waddill, and J.G. Tobin
Lawrence Livermore National Laboratory, Livermore, California 94550

The nitrogen, carbon, and oxygen 1s photoabsorption of O_2, N_2 and CO gas was measured using the University of California/National Laboratory bend magnet beamline located at the Stanford Synchrotron Radiation Laboratory. The resolving power at the N 1s edge ranges from 8-12.5x10^3 based upon the vibrationally-resolved 1s - π^* transition. This indicates that this spherical grating monochromator is one of the highest-resolution monochromatic soft X-ray (SXR)/vacuum ultra-violet (VUV) photon sources yet reported.

We have recently demonstrated how the University of California/ National Laboratory (UC/NL) Participating Research Team (PRT) Beamline 8-2 (BL 8-2) at the Stanford Synchrotron Radiation Laboratory (SSRL) performs exceedingly well as a high energy resolution SXR/VUV facility with high photon flux. This beamline is part of a three beamline UC/NL PRT that includes a toroidal grating VUV monochromator and a hard X-ray wiggler beamline.[1] An excellent description of the UC/NL PRT Beamline 8-2 has been presented by K.G. Tirsell and V.P. Karpenko, thereby eliminating the need for an extensive review. In this study the 1s-π^* gas-phase photoabsorption measurements serve the useful purpose of allowing us to estimate the beamline 8-2 energy resolution.

Ion-yield gas-phase photoabsorption was measured on N_2 and CO. In particular, the N 1s - π^* photoabsorption transition was measured because its vibrational fine structure has proven to be a resolution benchmark for SXR/VUV beamlines.[2,3,4,5] We show, in Fig. 1, the N_2-gas 1s - π^* absorption spectrum taken with 10μ entrance and exit slits on BL 8-2. These data clearly show greater definition in the vibrational-spliting when compared to the results of this measurement made on other high resolution beamlines[2,4,5] and are comparable to those measured on BL X1B at the National Synchrotron Light Source.[3]

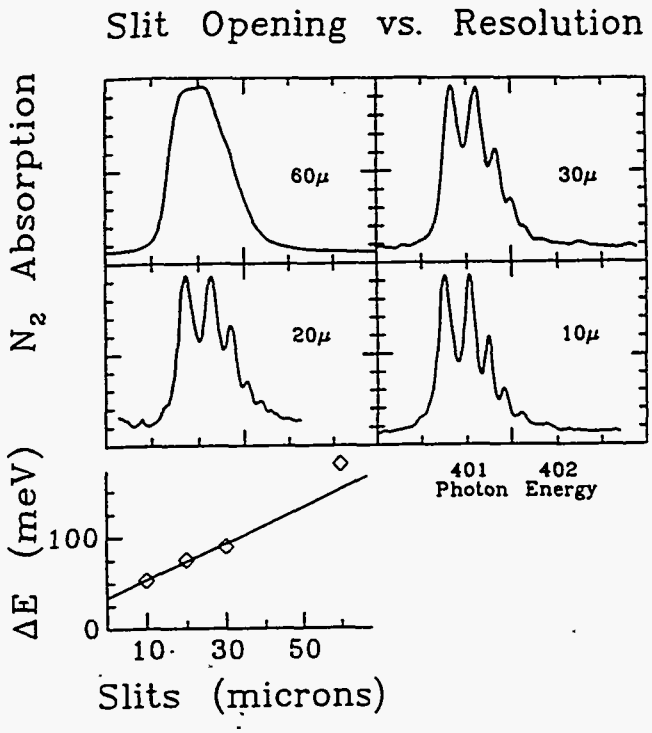

Figure 1. Photon energy resolution at 400 eV as a function of entrance and exit slit aperture. The top four panels are the raw N_2 1s-π^* photoabsorption spectra taken with slit openings indicated (entrance aperture equals exit). Photon energy resolution as a function of slit opening is shown in the bottom panel (open diamonds are data, solid line is linear fit).

Knowing the natural line width of the 1s - π^* spectral features should enable the deconvolution of the instrumental broadening from the spectrum and thus obtain the photon energy resolution. From linear least squares fits it was found that the photon energy resolution extracted from the N 1s photoabsorption data is better than 60 meV with a range of 32-50 meV giving the best fits. This range of Gaussian width parameters not only gave the best fits to the data, but also yielded the most rational distribution of Lorentzian widths within the series of Voigt line shapes. This distribution of vibrationally-resolved peak separations and widths correlates satisfactorally with previous results.[2,3,4] Thus, the resolving power of this beamline at the N 1s edge is measured to be $8\text{-}12.5 \times 10^3$.

Working from the highest-resolution N 1s spectrum as a reference, we calibrated the beamline resolution as a function of slit opening. Select results of this calibration are shown in Fig. 1. The slit aperture mechanism, which has been described previously[1], was actuated *ex-situ* by a ruled micrometer. This mechanical indicator of slit opening was linear with the aperture estimated by the photon flux reading over the range sampled and using the minimum aperature of 10m as a reference. The relationship of slit opening vs. resolution at 400 eV photon energy is shown in the insert of Fig. 1.

Carbon 1s photoabsorption of CO gas was measured on BL 8-2 using the 500 l/mm grating. The initial estimate of instrumental resolution taken from this spectrum is ~ 125 meV using a natural line width of 80 meV. It is worth noting that better photon energy resolution is anticipated when various beamline optical elements can be optimized (e.g. exit-slit positioning). Oxygen 1s photoabsorption was also measured from CO and O_2 (not shown) using the 1100 l/mm grating and resulted in absorption features of comparable resolution to that obtained on other high energy resolution synchrotron radiation monochromators.[3,4,7]

We would like to acknowledge R. Hanson for aid in obtaining the Al windows[8], E. Hudson and Z. Hussain for assistance with experimental equipment[9], and D. A. Shirley for valuable discussions regarding the photoabsorption measurements. This work was performed under the auspices of the U.S. Department of Energy by the Lawrence Livermore National Laboratory under contract No. W-7405-ENG-48 and was conducted at the Standford Synchrotron Radiation Laboratory which is supported by the Department of Energy, Office of Basic Energy Sciences.

References:

1. K.G. Tirsell and V. Karpenko, Nucl. Instum. and Methods in Phys. Research A 291, 511 (1990). V. Karpenko, J. H. Kinney, S. Kulkarni, K. Neufeld, C. Poppe, K. G. Tirsell, J. Wong, J. Cerino, T. Troxel, J. Yang, E. Hoyer, M. Green, D. Humphries, S. Marks, and D. Plate, Rev. Sci. Instrum. **60** (7), 1451 (1989).
2. P.A. Heimann, F. Senf, W. McKinney, M. Howells, R.D. van Zee, L.J. Medhurst, T. Lauritzen, J. Ching, J. Meneghetti, W. Gath, H. Hogrefe, and D.A. Shirley, Physica Scripta T31, 127 (1990).
3. W.R. McKinney, M.R. Howells, T. Lauritzen, J. Chin, R. DiGennaro, E. Fong, P.A. Heimann, L. Terminello, Z. Ji, D.A. Shirley, and S. Senf, Nucl. Instrum. and Meth. A 219, 221 (1990).
4. C.T. Chen and F. Sette, Rev. Sci. Instrum. 60(7), 1616 (1989).
5. K.J. Randall et al. Rev. Sci. Instrum. is Press, and this conference.
6. C.T. Chen, Y. Ma, and F. Sette, Phys-Rev. A 40, 6737 (1989).
7. M. Donke, C. Xue, A. Puschmann, T. Mandel, E. Hudson, D.A. Shirley, and G. Kaindle, Chem. Phys. Lett. 173, 122 (1990).
8. The Luxel Corp., Friday Harbor, WA 98250.
9. Z. Hussain, P.A. Heimann, D.A. Shirley, private communication.

BIOLOGY PROPOSALS

POLARIZED DISPERSION, GLIDE-RULE FORBIDDEN REFLECTIONS, AND PHASES OF STRUCTURE FACTORS

David H. Templeton and Lieselotte K. Templeton

Department of Chemistry, University of California, Berkeley, California 94720

Polarization-dependent absorption of X-rays has been observed in many materials now that synchrotron radiation provides polarized beams at the wavelengths near absorption edges where this dichroism is most significant (see review by Brouder[1]). With it comes polarized dispersion that requires that atomic scattering factors be represented by tensors rather than scalars.[2,3] The intensity of a Bragg reflection then depends both on the wavelength and the exact orientation of the crystal, and its change with azimuth can be used to determine phases of structure factors in much the same way as the change with wavelength in the MAD method.[4] The scattering may be different for atoms related by rotation or reflection, and the ordinary symmetry rules for absent Bragg reflections are violated. These forbidden reflections depend only on the anisotropic atoms, and their intensities give information about that substructure. Structure-factor phases were derived using screw-axis reflections in an earlier experiment at SSRL.[5]

In experiments at SSRL in 1990 and 1991 we measured reflections forbidden by a glide plane in barium bromate monohydrate, showed that they changed with azimuthal setting in accord with theory, and used their intensities to derive amplitudes and phases for the bromine atom contributions to structure factors of their second-order (allowed) reflections. The x and z coordinates of bromine determined from 11 such reflections agree with the known values within 0.02 Å.

Barium bromate monohydrate (space group $I2/c$) was chosen for this study because the bromate ion is strongly birefringent near the Br K edge and has its symmetry axis inclined to the glide plane and to the b axis in this crystal structure.[6,7] Glide-forbidden reflections ($h0l$, l odd) appear only if the scattering-factor tensor is not symmetric with respect to reflection in the glide plane. Integrated intensities were measured by standard techniques using the CAD-4 diffractometer on Line 1-5 with the double Si(111) monochromator set 3.6 eV below the peak of the bromate K-edge white line. The results indicate that the magnitude of the anomalous scattering anisotropy is $|\delta| = 2.6$ at this wavelength (0.91984 Å).

The intensity of a forbidden reflection is a complicated function of parameters defining the orientation of the atomic scattering tensor, the magnitude of its anisotropy, and the polarization state of the radiation.[8,9] Its dependence on azimuthal angle ψ contains terms proportional to $\cos^2\psi$, $\cos^2 2\psi$, $\cos\psi\cos 2\psi$, and $\sin^2 2\psi$. The relative magnitudes of these terms are different for various reflections, giving rise to a variety of profiles as illustrated in Figs. 1-4. The curves are calculated from theory.

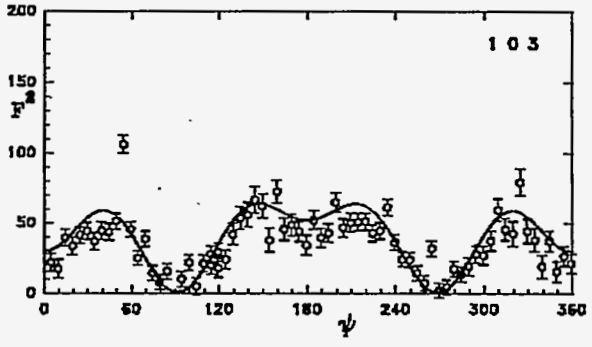

Fig. 1. Azimuthal profile for (103).

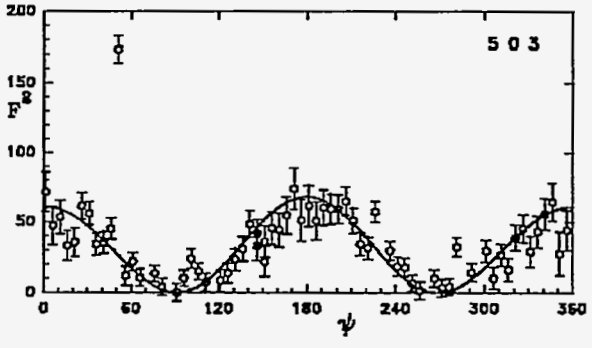

Fig. 2. Azimuthal profile for (503).

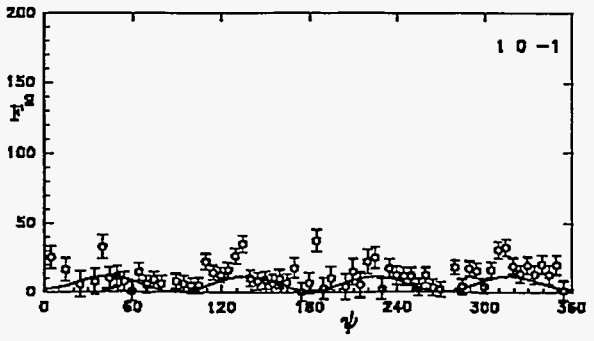

Fig. 3. Azimuthal profile for (1,0,-1).

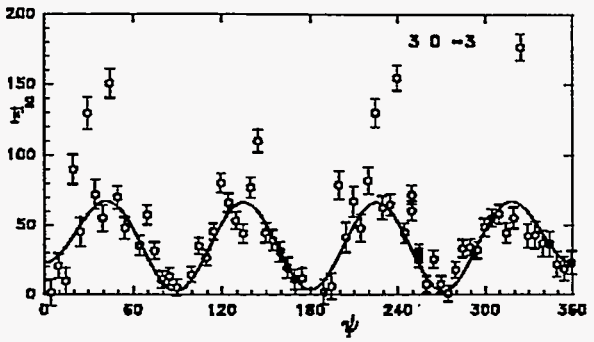

Fig. 4. Azimuthal profile for (3,0,-3).

With a single kind of anisotropic atom as in this case, the intensity is proportional to $|\delta U_{Br}|^2$, where $U_{Br} = \cos(2\pi(hx+lz))$ is the unitary structure factor for the unique bromine atom. Once the scale is determined, for example using Wilson's statistics, U_{Br}^2 can be determined for each forbidden reflection. Then both the magnitude and phase of $U_{Br}(2h,0,2l) = \cos[4\pi(hx+lz)]$ are given by the trigonometric identity

$$\cos 2A = 2\cos^2 A - 1.$$

For one atom the inequality of Harker & Kasper[10] for a center of inversion becomes this equality, thereby gaining the power to imply negative phases. The bromine structure factors for eleven allowed reflections, obtained from the intensities of eleven forbidden reflections were used in a Fourier synthesis to get coordinates $x = 0.249(1)$ and $z = 0.557(1)$, in good agreement with $x = 0.2510$ and $z = 0.5574$ from the two full structure determinations. Regardless of the scale, a negative phase is implied for 2**h** whenever the intensity of **h**, adjusted for Lorentz, absorption, and temperature effects and for these peculiar polarization factors, is less than half that of any other forbidden reflection. Thus the weakness of 1,0,-1 relative to 3,0,-3 (Figs. 3 and 4) implies a negative phase for 2,0,-2 without any further calculation.

We thank the many staff members of SSRL whose assistance made this work possible. We are particularly indebted to Dr. Michael Soltis. This research was supported by the National Science Foundation under Grant CHE-8821318.

1. C. Brouder, *J. Phys.: Condens. Matter* **2**, 701-738 (1990).
2. D.H. Templeton, L.K. Templeton, *Acta Cryst. A* **36**, 237-241 (1991); **38**, 62-67 (1982).
3. V.E. Dmitrienko, *Acta Cryst. A*, **39**, 29-35 (1983); **40**, 89-95 (1984).
4. D.H. Templeton, L.K. Templeton, *Acta Cryst. A* **47**, 414-420 (1991).
5. D.H. Templeton, L.K. Templeton, *Acta Cryst. A* **43**, 573-574 (1987).
6. H.D. Lutz, E. Alici, W. Buchmeier, *Z. anorg. allg. Chem.* **535**, 31-38 (1985).
7. L.K. Templeton, D.H. Templeton, *Acta Cryst. C* **45**, 672-673 (1989).
8. A. Kirfel, A. Petcov, K. Eichhorn, *Acta Cryst. A* **47**, 180-195 (1991).
9. D.H. Templeton, L.K. Templeton, *Acta Cryst. A*, (*submitted*).
10. D. Harker, J.S. Kasper, *Acta Cryst.* **1**, 70-75 (1948).

X-ray Absorption Spectroscopic Characterization of the Mn in Biological Systems

James E. Penner-Hahn, Pamela J. Riggs, Geoffry S. Waldo,
Richard M. Fronko, Rui Mei, and Charles F. Yocum
University of Michigan

I. Oxygen Evolving Complex

(Riggs, Mei, Yocum, Penner-Hahn)

Photosynthetic oxygen evolution requires Ca^{2+}, Cl^-, and a multinuclear Mn cluster. The Mn cluster cycles through 5 kinetically resolvable intermediates (S_0, S_1, S_2, S_3 and S_4) as it accumulates oxidizing equivalents for the oxidation of water to dioxygen.[1] Although it is generally agreed upon that the cluster contains 4 Mn^2, the nuclearity of this cluster remains a hotly debated issue. X-ray Absorption Spectroscopy can address two particularly important questions pertaining to this area of photosynthesis research: 1) Through which oxidation states does the Mn cluster cycle? 2) What is the geometry of the cluster in the various S states? We have focused our XANES and EXAFS studies on reduced derivatives of the Mn cluster to gain insight on its structure in the native state.

Treatment of the oxygen evolving complex (OEC) with micromolar concentrations of hydroxylamine results in a two flash delay in oxygen evolution.[3] This has been interpreted as arising from rapid reduction of Mn in the dark to a state formulated as S_{-1}.[4-6] This interpretation has been most recently questioned by Guiles et al.[7] They report, based on XANES, that NH_2OH does not cause reduction in the dark, but that reduction to a species formulated as S_0^* does occur following illumination. One difficulty in studying putative reduced states is that high (millimolar) concentrations of NH_2OH and/or longer exposure times result in an eventual inhibatory loss of Mn(II).[8-9] It has recently been demonstrated that high (millimolar) concentrations of Ca^{2+} stabilize the OEC reaction center with respect to NH_2OH- (and hydroquinone-) induced loss of activity.[10] This stabilization permits the study of reduced derivatives using XANES.

With both of the reductants used, NH_2OH (100μM, 3 minutes) and hydroquinone (200μM, 30 minutes), there was a shift in the Mn K edge spectrum to lower energy relative to control S_1 state (figure 1). However, quantitative analyses of the XANES spectra using linear combinations of spectra drawn from a library of Mn(II), Mn(III), and Mn(IV) models indicate that the hydroquinone treatment produces twice as much Mn(II) as the NH_2OH treatment. There is no evidence for Mn(II) in the control S_1 state. (We previously suggested[11] that S_1 contains ca. 25% Mn(II). We have since discovered[12] that a Mn(II) contamination was present in the Mylar windows covering these samples.)

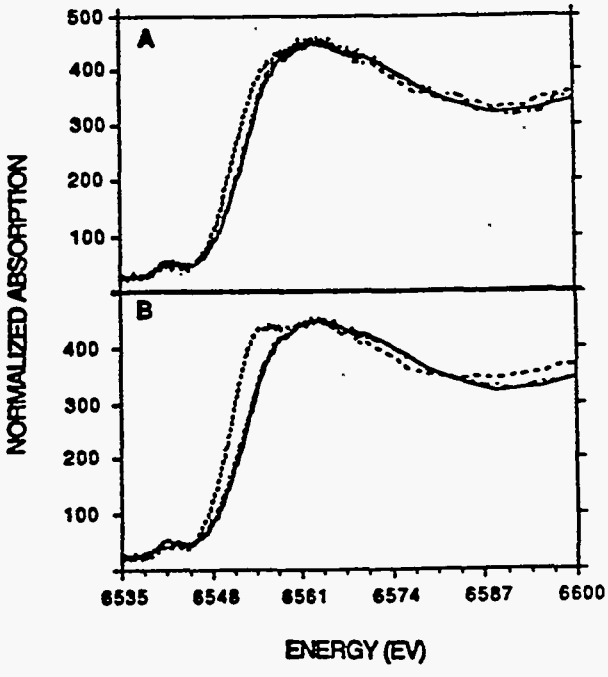

Figure 1: Normalized OEC XANES spectra. Solid line = S_1 control; Dashed line = reduced sample; Dotted-Dashed line = reduced sample followed by illumination and dark adaption. A. NH_2OH (100μM, 3 minutes) reduced sample. B. Hydroquinone (200μM, 30 minutes) reduced sample.

Incubation conditions were chosen to maximize reductant concentration and exposure time without compromising activity. Little activity (0-20%) is lost following treatment. In fact, both reductions are completely reversed by illumination, demonstrating that the observed changes are not the result of irreversible loss of Mn(II). The XANES spectra for reduced samples that were later illuminated and then dark adapted are identical to that of the control S_1 spectrum. This reversiblility is also observed in the EXAFS spectra of the reduced samples. For hydroquinone treated samples especially, there are dramatic changes in the EXAFS spectra. These changes are reversed completely after illumination and dark adaption.

Our results using NH_2OH as a reductant contradict the findings of Guiles et al.[7] These differences may be due in part to the use of different sample preparations (our reaction center complexes lack the smaller extrinsic polypeptides and might be more susceptible to reduction despite Ca^{2+} protection.) Guiles et al. also observe an edge shift in the dark after NH_2OH treatment, but the shift is attributed to the formation of inactive centers. Since we observe little loss of activity and since the reduction is reversible, the Mn(II) present in our samples cannot be due to inactive centers.

Hydroquinone treatment produces ca. twice as much Mn(II) as does the NH_2OH treatment. Perhaps this is not surprising considering the higher concentration and longer incubation time used for hydroquinone. As mentioned above, however, reaction conditions were chosen to maximize reduction without inactivating the sample. We have also generated a NH_2OH treated sample with a XANES spectrum and Mn(II) content identical to that of the hydroquinone sample. Under these conditions, however, the sample is inactive. This suggests that the original NH_2OH sample is not simply a mixture of ca. 50% S_1 and 50% of the more reduced derivative that is formed by hydroquinone. Chemical reactivity studies by Mei and Yocum also support this supposition. Hydroxylamine samples are EDTA sensitive[10] whereas hydroquinone samples are not.[13] The data presented here might be the first spectroscopic evidence for two functionally distinct Mn sites.

References

1. Kok, B.; Forbush, B.; McGloin, M. *Photochem. Photobiol.* **1970**, *11*, 457.

2. For a recent review, see Ghanotakis, D.; Demetriou, D.; Yocum, C. In *Progress in Photosynthesis Research;* Biggens, J., editor, **1986**, *1*, 681-684.

3. Bouges, B. *Biochim Biophys. Acta* **1971**, *234*, 103-112.

4. Beck, W.; Brudvig, G. *Biochemistry* **1987**, *26*, 8285-8295.

5. Beck, W.; Brudvig, G. *J. Am. Chem. Soc.* **1988**, *110*, 1517-1523.

6. Sivaraja, M.; Dismukes, G. *Biochemistry* **1988**, *27*, 3467-3475.

7. Guiles, R.; Yachandra, V.; McDermott, A.; Cole, J.; Dexheimer, S.; Britt, R.; Sauer, K.; Klein, M. *Biochemisty*, **1990**, *29*, 486-496.

8. Cheniae, G.; Martin, I. *Plant Physiol.* **1971**, *47*, 568-575.

9. Yocum, C.; Yerkes, C.; Blankenship, R.; Sharp, R.; Babcock, G. *Proc. Natl. Acad. Sci., USA* **1981**, *78*, 7507-7511.

10. Mei, R.; Yocum, C. *Biochemistry* **1991**, *30*, 7836-7842.

11. Penner-Hahn, J.; Fronko, R.; Pecoraro, V.; Yocum, C.; Betts, S.; Bowlby, N. *J. Am. Chem. Soc.* **1990**, *112*, 2549-2557.

12. Waldo, G.; Penner-Hahn, J., unpublished results.

13. Mei, R.; Yocum, C., manuscript in preparation.

II. Manganese catalase

(Waldo, Fronko, Penner-Hahn)

Disproportionation of hydrogen peroxide to water and oxygen, the so-called catalase reaction, is one of the principal pathways for hydrogen peroxide detoxification.[1] Though most catalases contain the protoporphyrin IX prosthetic group, Kono and Fridovich[2] isolated and purified the first of several non-heme, Mn containing catalases from *Lactobacillus plantarum* ATCC 14431. These Mn catalases have an apparent stoichiometry of 2 Mn per subunit. A low-temperature EPR spectrum in the as-isolated enzyme shows a 16-line signal which has been attributed to a Mn(III)/Mn(IV) mixed-valence binuclear structure.[3-5] This, together with a low-resolution crystal structure suggests that the enzyme has a binuclear active site.[6] In addition to this form, two other EPR spectra point to the existence of a Mn(II)/Mn(III) derivative and a Mn(II)/Mn(II) derivative.[3-4] The optical spectrum indicates the existence of a Mn(III)/Mn(III) form.[2]

Despite the identity of these derivatives, the catalytic cycle remains unclear. Given that the disproportionation of H_2O_2 is a two electron process and assuming only the Mn is redox active, possible cylces include:
1) Mn(II)/Mn(II)<-->Mn(III)/Mn(III)
2) Mn(II)/Mn(III)<-->Mn(III)/Mn(IV)
3) Mn(III)/Mn(III)<-->Mn(IV)/Mn(IV)
Studies were undertaken to identify which of the Mn oxidation states are involved in the catalase mechanism.

The oxidation state of the Mn atoms in three derivatives have been characterized using XANES (Figure 2) and EPR. The first, a hydroxylamine treated sample, has a XANES spectrum that can be fit quantitatively with Mn models using only Mn(II). NH_2OH treatment has no effect on catalase activity.[2,7-8] The same spectrum is observed when incubation is long (2 hours) or short (immediate freezing. NH_2OH in the presence of substrate inactivates the catalase[7-8,9]; concurrent with the inactivation is an increase in the intensity of the 16-line EPR signal. The XANES spectrum for this inactive form can be fit using only combinations of Mn(III) and Mn(IV), thus eliminating the speculation that the 16-line signal could arise from a Mn(II)/Mn(III) dimer.[10]

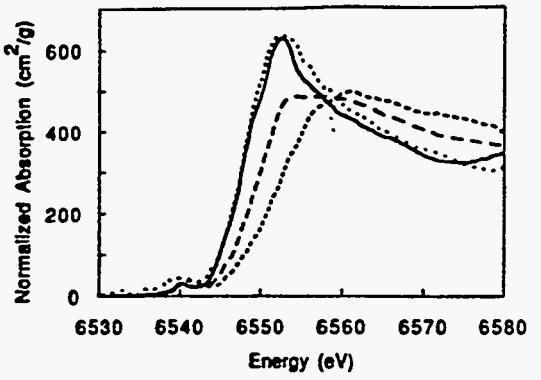

Figure 2: Normalized XANES spectra for Mn catalase. Solid line = long term NH_2OH reduced; dotted line = short term NH_2OH reduced; long dash = as isolated; short dash = $NH_2OH + H_2O_2$ inactivated.

In contrast to previous reports, we have found that it is possible to completely reactivate the Mn(III)/Mn(IV) form by long term anaerobic incubation with NH_2OH. Earlier efforts to reactivate the (III)/(IV) form involved the aerobic incubation with NH_2OH. Since NH_2OH is slowly autoxidized with the reduction of O_2 to H_2O_2, any reactivation would be immediately reversed. As expected, reactivation is accompanied by the complete disappearance of the Mn(III)/Mn(IV) EPR signal.

The XANES spectrum of the as- isolated enzyme is also included in Figure 2. It is of intermdiate oxidation state, most consistent with an average composition of Mn(III).

The XANES data demonstrate that the majority of the Mn in the as-isolated enzyme is rapidly reduced by NH_2OH, with no loss of activity. This indicates that the Mn(II) derivative must either be active or be readily convertible to the active protein. The spectra are most consistent with the catalytic cycle in equation 1, although equation 3 cannot be ruled out at this time. In order to be correct, the latter would require that both the Mn(II)/Mn(II) and the Mn(III)/Mn(III) derivatives be oxidized rapidly by H_2O_2. In addition, there is, as of yet, no

evidence for a Mn(IV)/Mn(IV) form of the enzyme.

References

1. Jones, P.; Wilson, I. *Metal Ions in Biol. Systems* **1978**, *7*, 185-240.

2. Kono, Y.; Fridovich, I. *J. Biol. Chem.* **1983**, *258*, 6015-6019.

3. Khangulov, S.; Barynin, V.; Melik-Adamyan, V.; Grebenko, A.; Voevodskaya, H.; Blumenfield, L.; Dobryakov, S.; Ilyasova, V. *Biorg. Khim.* **1986**, *12*, 741-748.

4. Khangulov, S.; Voevodskaya, H.; Barynin, V.; Grebenko, A.; Melik-Adamyan, V. *Biofizika* **1987**, *32*, 960-966.

5. Fronko, R.; Penner-Hahn, J.; Bender, C. *J. Am. Chem. Soc.* **1988**, *110*, 7554-7555.

6. Barynin, V.; Vagin, A.; Melik-Adamyan, V.; Grebenko, A.; Khangulov, S.; Popov, A.; Andrianova, M.; Vainshtein, B. *Sov. Phys.-Dokl. (Engl. Transl.)* **1986**, *31*, 457-459.

7. Kono, Y. *Biochem. Biophys. Res. Commun.* **1984**, *124*, 75-79.

8. Kono, Y. in *Superoxide and Superoxide Dismutase in Chemistry, Biology, and Medicine* **1986**, Potilio, G., editor, Elsevier, New York, 231-233.

9. Kono, Y.; Fridovich, I. *J. Biol. Chem.* **1983**, *258*, 13646-13648.

10. Mabad, B.; Tuchagues, J.; Huang, Y.; Hendrickson, D. *J. Am. Chem. Soc.* **1985**, *107*, 2801-2802.

An X-ray Absorption Edge Study of the Oxygen Intermediate in the Reaction of the Laccase Trinuclear Copper Active Site with Dioxygen

Grace O. Tan, Brooke L. Hemming, James L. Cole,
Keith O. Hodgson and Edward I. Solomon

Department of Chemistry, Stanford University, Stanford, CA 94305, USA.

The multicopper oxidases (laccase, ascorbate oxidase and ceruloplasmin) catalyze the four-electron reduction of dioxygen to water. Study of these oxidases allows insight into the function of cytochrome c oxidase, which plays a vital part in the respiratory cycle. Laccase, the simplest of the multicopper oxidases, contains four Cu atoms: a type 1, a type 2 and a binuclear type 3 center. Low-temperature MCD measurements have demonstrated that the type 2 and type 3 centers comprise a trinuclear Cu cluster site,[1] and this model has been supported in a recent X-ray crystal structure determination[2] of ascorbate oxidase. X-ray absorption edge spectroscopy has proven crucial in the study of laccase because it is the only direct probe of the oxidation states of the Cu atoms in the active site.

In Cu K edge absorption spectroscopy, a pre-edge 1s→4p transition near 8984 eV is present in the edge spectra of 2-coordinate and 3-coordinate Cu(I) compounds, but not in Cu(II) compounds[3]. Thus the degree of oxidation of the laccase derivatives may be determined against a scale obtained by subtracting the edge of a fully oxidized sample (reacted with H_2O_2) from that of a fully reduced sample.

In a previous study, X-ray absorption edge spectroscopy was used to determine Cu oxidation states following reaction of reduced laccase derivatives with dioxygen. It was established that the fully reduced trinuclear site in a type 1 Hg^{2+}-substituted laccase derivative (T1Hg) is fully reoxidized by dioxygen, while a fully reduced type 2-depleted (T2D) derivative was only one-third reoxidized by dioxygen (T1 was oxidized, but the two T3 Cu remained reduced), and that at an extremely slow rate. It was thus concluded that the trinuclear site represents the minimal structural unit capable of reducing dioxygen[4]. Also, in the course of this study, an intermediate in the reaction of T1Hg with dioxygen was detected.

The present study characterizes the oxidation states of the Cu atoms in the trinuclear site of T1Hg in this oxygen intermediate. We measured X-ray absorption spectra on the oxygen intermediate of T1Hg, frozen at 77 K. Three samples were run. Care was taken to ensure the integrity of each of these samples; no excess reductant was present after the initial reduction of T1Hg before reaction with dioxygen, and mixing with dioxygen was thorough and complete. Quantitating the oxidation states in the manner described above, we are able to conclude that in all three samples of the oxygen intermediate both the T3 Cu are oxidized, while the T2 Cu remains reduced (Figure 1).

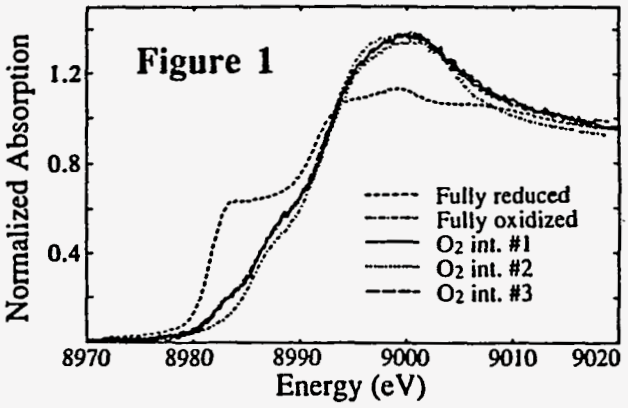

This XAS study confirms CD and MCD studies which suggest that two electrons are transferred to dioxygen when it binds to the trinuclear site, to give a peroxide-type intermediate. However, the uv-visible absorption spectrum of this intermediate is strikingly different from that of oxyhemocyanin, where the peroxide is bound either cis μ-1,2 or μ–η:η across the T3-like dicopper site (see Figure 2). It is also different from spectra of copper model compounds where the peroxide is bound terminally to one copper only, or in a trans μ-1,2 configuration. On the other hand, it shows some similarities to spectra of Cu(II) hydroperoxide complexes. Also, the XAS work comparing T1Hg and T2D reactivities to dioxygen strongly suggests that the T2 site (absent in T2D) is involved in the binding by dioxygen. Taking the evidence all together, we propose that dioxygen binds as a μ-1,1 hydroperoxide bridge between T2 and one Cu in the T3 site (see Figure 2)[5].

Figure 2

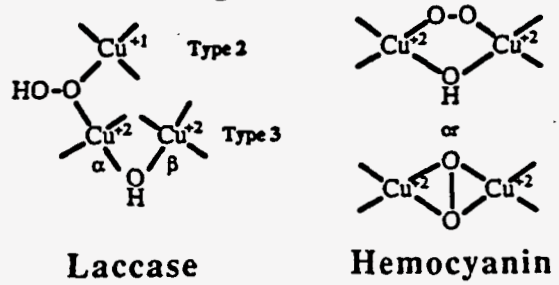

Acknowledgements. This work was supported by NSF Grant CHE 8817702 (KOH) and NIH Grant AM31450 (EIS). Data was collected at SSRL, which is operated by the US DOE, Division of Chemical Sciences, and used resources provided by the SSRL Biotechnology Program, which is supported by the NIH, Biomedical Resource Technology Program, Division of Research Resources (RR-01209) and by DOE's Office of Health and Environmental Research, and Office of Basic Energy Sciences, Division of Materials Sciences.

References

(1) (a) Allendorf, M.D.; Spira, D.J.; Solomon, E.I. *Proc. Natl. Acad. Sci. USA* **1985**, *82*, 3063-3067. (b) Spira-Solomon, D.J.; Allendorf, M.D.; Solomon, E.I. *J. Am. Chem. Soc.* **1986**, *108*, 5318-5328.

(2) Messerschmidt, A.; Rossi, A.; Ladenstein, R.; Huber, R.; Bolognesi, M; Gatti, G; Marchesini, A.; Petruzzelli, R; Finazzi-Agrò, A. *J. Mol. Biol.* **1989**, *206*, 513-529.

(3) Kau, L.-S.,; Spira-Solomon, D.J.; Penner-Hahn, J.E.; Hodgson, K.O.; Solomon, E.I. *J. Am. Chem. Soc.* **1987**, *109*, 6433-6442.

(4) Cole, J.L.; Tan, G.O.; Yang, E.K.; Hodgson, K.O.; Solomon, E.I., *J. Am. Chem. Soc.* **1990**, *112*, 2243-2249.

(5) (a) Cole, J.L.; Ballou, D.P.; Solomon, E.I. *J. Am. Chem. Soc.* **1991**, *113*, 8544-8546. (b) Clark, P.A., Solomon, E.I. *J. Am. Chem. Soc.*, in press (1992). (c) Solomon, E.I., Baldwin, M.J., Lowery, M.D. *Chem. Rev.*, submitted for publication (1992).

Nickel K-edge X-ray Absorption Studies of the Active Site of *Rhodospirillum rubrum* Nickel Carbon Monoxide Dehydrogenase

Grace O. Tan,[a] Scott A. Ensign,[b] Stefano Ciurli,[c] M. J. Scott,[c] Britt Hedman,[d] Richard H. Holm,[c] Paul W. Ludden,[b] Z. Richard Korszun,[e] Philip J. Stephens,[f] Keith O. Hodgson[a*]

[a] Department of Chemistry, Stanford University, Stanford, CA 94305, U.S.A.
[b] Department of Biochemistry, University of Wisconsin-Madison, Madison, WI 53706, U.S.A.
[c] Department of Chemistry, Harvard University, Cambridge, MA 02138, U. S. A.
[d] Stanford Synchrotron Radiation Laboratory, Stanford University, SLAC, Stanford, CA 94309, U. S. A.
[e] Department of Chemistry, University of Wisconsin-Parkside, Kenosha, WI 53141, U. S. A.
[f] Department of Chemistry, University of Southern California, Los Angeles, CA 90089, U. S. A.

Rhodospirillum rubrum nickel carbon monoxide dehydrogenase (Ni CODH) is an enzyme[1] containing 1 nickel atom per unit of protein[2], that converts CO to CO_2 in the presence of an electron acceptor (such as methyl viologen)[1] :

$$CO + H_2O \text{ ---> } CO_2 + 2H^+ + 2e^-$$

Assays on nickel-free Ni CODH show that nickel must be present in order to activate the enzyme[2], and EPR studies further suggest that the nickel is coupled in some fashion to Fe-S clusters[3]. We have used Ni K edge X-ray absorption spectroscopy to investigate the possibility that the active site may contain a $NiFe_3S_4$ cubane cluster, and also to draw some conclusions about the nature and geometry of the ligands coordinated to Ni.

Edges :

The Ni CODH edge was compared to the edges of several model compounds. Consistent with the results from EXAFS fits (see next section), only edges of compounds containing some Ni-S ligation were found to be at all close in appearance to the Ni CODH edge. Some such comparisons are shown in Figure 1, where the Ni CODH edge is shown in solid lines.

The magnitude of the 1s→3d transition at 8332 eV suggests that, in the case that the Ni is 4-coordinated, the coordination geometry about Ni is distorted from the square-planar (top of Fig. 1), being closer to the opposite limit of the tetrahedral (middle of Fig. 1). This feature is also consistent with a distorted 5-coordinated geometry (middle of Fig. 1), or even with a cubane-like geometry (bottom of Fig. 1). There is also a weak 1s→4p transition at ~8338 eV, and this, too, suggests a distorted tetrahedral or five-coordinate geometry.

However, none of the models we have examined thus far is a good model for the Ni CODH edge in all of its features.

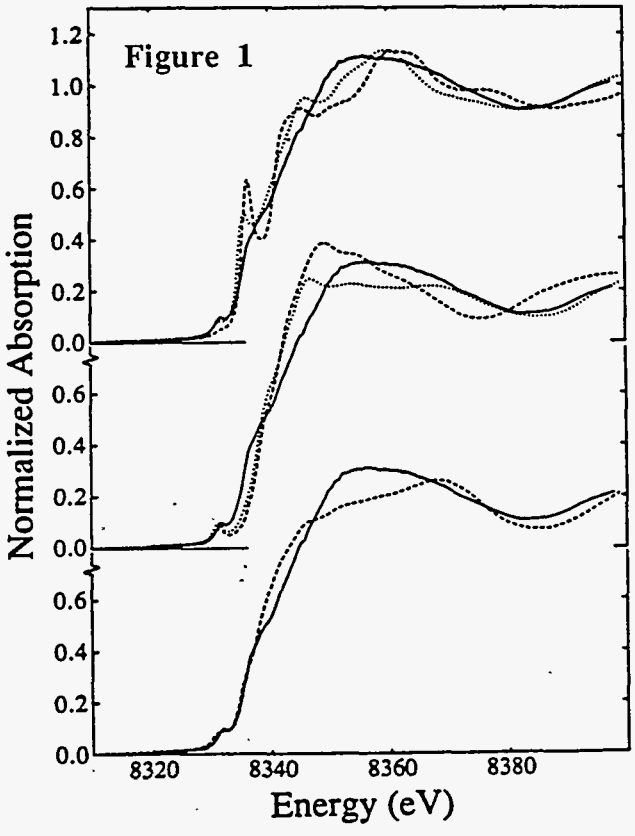

——— Ni CODH, oxidized
Top :
----- $Ni\text{-}S_4$ ligation, sq. planar
..... $Ni\text{-}N_2S_2$ ligation, sq. pl., slight T_d distortion
Middle :
----- $Ni\text{-}N_2S_3$ ligation, distorted trig. bipy.
..... $Ni\text{-}S_4$ ligation, T_d
Bottom :
----- $Ni\text{-}S_3P$ ligation, cubane, distorted T_d

EXAFS :

Fits were made to backtransformed data of Ni CODH and of $[Et_4N]_3[NiFe_3S_4(SEt)_4]$ over a range of k = 4 - 11 $Å^{-1}$. In all the fits shown below, numbers in brackets were held constant at the values shown. Also, note that the change in the relative Debye-Waller factor, $\Delta\sigma^2$, is with respect to σ^2 in the model compounds from which empirical Ni-N, Ni-S and Ni-Fe parameters were extracted.

The first shell of Ni CODH showed a strong beat and clearly could not be fitted with only 1 shell of atoms. The best fit to it was obtained using 1 shell of N and 1 shell of S. In contrast, a good fit to the first shell of the $NiFe_3S_4$ cubane could be obtained using only 1 shell of S.

	R_N	CN_N	$\Delta\sigma^2_N$	R_S	CN_S	$\Delta\sigma^2_S$	Fit Index
Ni CODH	1.87	2.7	(0)	2.23	1.8	(0)	0.529
Ni CODH	1.86	(2)	-0.0029	2.22	(2)	0.0009	0.487
Ni cubane	—	—	—	2.26	2.6	(0)	0.333

Thus, we can conclude that Ni in Ni CODH is coordinated either with 3 N and 2 S, or with 2 N and 2 S.

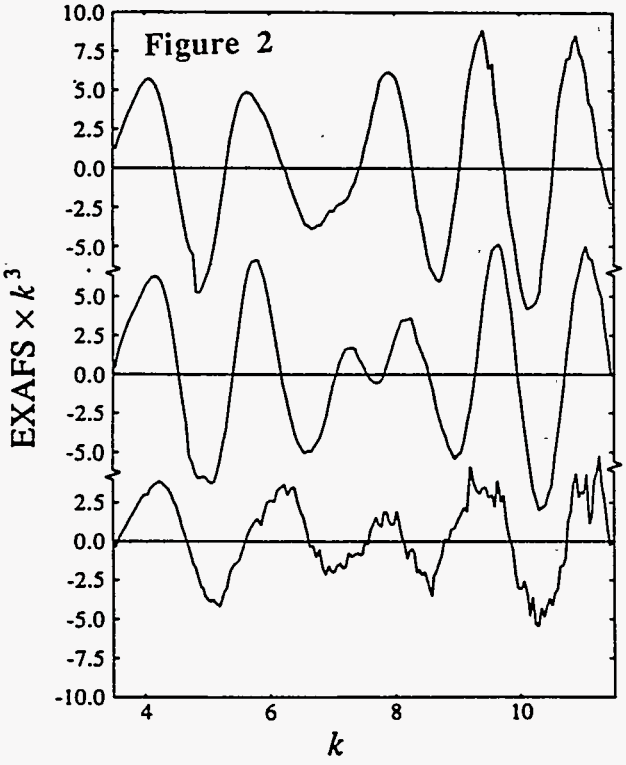

Top: $[Et_4N]_3[NiFe_3S_4(SEt)_4]$
Middle: $[Et_4N]_2[NiFe_3S_4(PPh_3)(SEt)_3]$
Bottom: Ni CODH, oxidized

As shown below, fits to the combined first and second shells of Ni CODH and $[Et_4N]_3[NiFe_3S_4(SEt)_4]$ showed that while 2.6 Fe at 2.74 Å were found in the cubane data, less than 0.1 Fe (at 2.93 Å) were found for Ni CODH. Although these fits therefore do not indicate the presence of any Fe near Ni, we do not exclude the possibility that there may be 1 Fe at longer distance from Ni.

(1) S + Fe fit to $[Et_4N]_3[NiFe_3S_4(SEt)_4]$:

R_S	CN_S	$\Delta\sigma^2_S$	R_{Fe}	CN_{Fe}	$\Delta\sigma^2_{Fe}$	Fit Index
2.25	2.7	(0)	2.74	2.6	(0)	0.521
2.26	(4)	0.0030	2.74	(3)	0.0006	0.751
2.26	(3)	0.0007	2.74	(3)	0.0011	0.499

(2) N + S + Fe fit to Ni CODH :

Fit (a) : Fixed σ^2's

R_N	CN_N	R_S	CN_S	R_{Fe}	CN_{Fe}	Fit Index
1.87	2.7	2.23	1.8	2.93	0.06	0.630

Fit (b) : Fixed CN's

$CN_N = 2$ $CN_S = 2$ $CN_{Fe} = 1$

R_N	$\Delta\sigma^2_N$	R_S	$\Delta\sigma^2_S$	R_{Fe}	$\Delta\sigma^2_{Fe}$	Fit Index
1.86	-0.0034	2.22	0.0005	2.73	0.0136	0.502

We may conclude from these fits that the active site of Ni CODH *does not* contain a $NiFe_3S_4$ cubane[4].

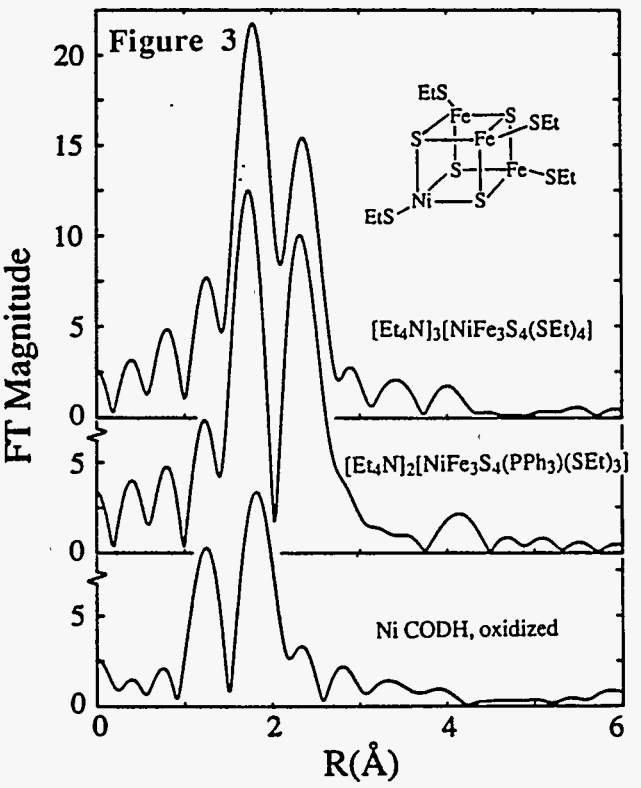

Acknowledgements :

We are grateful to Prof. Robert A. Scott of the University of Georgia, Athens, for sharing with us the data for many of his compounds. We are also grateful to NSF (Grant CHE 88-17702 to K.O.H.) for support of this work. Data was collected at SSRL, which is operated by the US DOE, Division of Chemical Sciences, and used resources provided by the SSRL Biotechnology Program, which is supported by the NIH, Biomedical Resource Technology Program, Division of Research Resources (RR-01209) and by DOE's Office of Health and Environmental Research, and Office of Basic Energy Sciences, Division of Materials Sciences.

References :

1. D. Bonam, S. A. Murrell, P. W. Ludden *J. Bacterio.* 1984, *159*, 693-699.
2. S. A. Ensign, D. Bonam, P. W. Ludden *Biochem.* 1989, *28*, 4968-4973.
3. P. J. Stephens, M.-C. McKenna, S. A. Ensign, D. Bonam, P. W. Ludden *J. Biol. Chem.* 1989, *264*, 16347-16350.
4. G. O. Tan, S. A. Ensign, S. Ciurli, M. J. Scott, B. Hedman, R. H. Holm, P. W. Ludden, Z. R. Korszun, P. J. Stephens, K. O. Hodgson, in press, *Proc. Natl. Acad. Sci. USA* (1992).

Small Angle X-ray Scattering Studies of the Molybdenum Iron Cofactor from Nitrogenase

D. Eliezer(1), P. Frank(2), N. Gillis(3), L. Chen(2),H. Tsuruta(4), W. E. Newton(5), S. Doniach (3), and K. O. Hodgson(2)

1 Department of Physics, Stanford University, Stanford, CA 94305

2 Department of Chemistry, Stanford University, Stanford, CA 94305

3 Department of Applied Physics, Stanford University, Stanford, CA 94305

4 Stanford Synchrotron Radiation Laboratory, SLAC, Bin 69, P.O. Box 4349, Stanford, CA 94309

5 Department of Biochemistry and Nutrition, Virginia Polytechnic Institute, Blacksburg, VA 24061

Introduction

The Nitrogenase enzyme complex, consisting of an iron-containing (Fe) protein and an iron and molybdenum-containing (MoFe) protein, plays a critical role in the reduction of dinitrogen to ammonia (nitrogen fixation). The nitrogen fixing site on the MoFe protein is an iron-molybdenum-sulfur cofactor (FeMoco) of roughly 1000 Dalton mass, but little is known about its structure. We measured small angle X-ray scattering (SAXS) data from isolated FeMoco in N-methylformamide (NMF) solution in order to determine its radius of gyration (R_g). Model compounds of known structure were also examined in a similar solvent, N,N-dimethylformamide (DMF) as a control and for calibration purposes. In addition we measured data on thiolated FeMoco solutions in order to observe the effects on the solution structure of FeMoco.

Experimental

SAXS Data were collected on beamline 4-2 using the biotechnology SAXS camera [1]. An X-ray energy of 7515 eV (Terbium L-III edge) was used. Samples were contained in 1 mm thin-walled fused quartz capillaries mounted on a goniometer head. Capillaries were filled with NMF for FeMoco background measurements and DMF for model compound backgrounds. Immediately after the background measurement each capillary was removed, emptied, and placed, still mounted on the goniometer head, in a nitrogen-filled inert atmosphere glove box. In the glove box the capillary was filled with FeMoco or model compound solutions (kept in dry ice until needed) and sealed. The goniometer head was remounted in the same position in which the background data was collected, and data was collected from the sample. Data were collected for 4 or 5 consecutive one hour cycles for each background and each sample. All of the FeMoco samples used in the first series of measurements maintained a dark black color throughout the experiment, indicating that no oxidation had taken place. For the second series of measurements, a thiol ligand was added to each of the FeMoco samples used in the first series.

Each data cycle was normalized using the integrated transmitted beam intensity. Cycles for the same sample were averaged together. Background data was then subtracted from the accompanying sample data. The data were represented in a Guinier plot ($\log I$ vs. S^2) and the fits obtained using a nonweighted linear least squares fitting procedure are shown in Figure 1. The high angle end of the fitting range was chosen so as to allow the fit to be independent of statistical noise in the data (the final fitting S^2 range was .0004 - .0001). Statistical error bars were calculated by propagating the statistical noise in the data throughout the above procedures.

Results

The forward scattered intensity and R_g obtained from the Guinier fits are summarized in Table 1. The forward scattered intensity is proportional to the square of the integral of the electron density of the sample in excess of the solvent electron density. In our case, where the sample constituents are heavy compared to those of the solvent, the forward scattered intensity can be taken as nearly proportional to the square of the mass of the sample.

Theoretical calculations for two model compounds ($Mo_2Fe_6S_8(SC_2H_5)_9$ and $Mo_2Fe_7S_8(SC_2H_5)_{12}$) using the Debye formula and the published crystal structures [2,3] gave calculated R_gs of 5.03 and 4.53 Å respectively. There is still some degree of discrepancy between the calculated and measured values, but on

the whole the agreement is rather good. The values of R_g and of the forward scattering intensity measured for the FeMoco samples are significantly higher than those measured for the model compounds. These values are not consistent with the expected molecular weight of FeMoco and the known molecular weights of the models. The most likely cause of such a result is the presence of other species in the sample, either impurities or aggregates. Since great care was taken to insure the purity of the samples, we suspect that the results we have obtained indicate that our samples, prepared using the standard method for FeMoco preparation [4] contained FeMoco aggregates. Unfortunately, the angular range of our data is not sufficient to warrant speculating upon such details as the shape and size distribution of the aggregates in the samples.

Measurements on thiolated samples were preformed in order to test the possibility that the previously observed effects of thiol ligation on cofactor EPR spectra [5] were due to some modification of the aggregation behavior observed in the unthiolated samples. Although two of the samples for these measurements were of suspect integrity (visually appeared to be partially oxidized), the results obtained were quite similar to the data obtained before the addition of thiol. No significant difference was observed.

Sample	C (mM)	R_g (Å)	$\sigma(R_g)$	I(0)	Mw
FeMoco	1.93	6.51	0.18	0.031	2.44
	1.61	7.83	0.14	0.030	2.85
	1.21	6.65	0.22	0.023	2.87
Mo_2Fe_7	6.17	4.45	0.16	0.041	1.00
	3.20	4.72	0.23	0.027	1.26
	2.13	4.41	0.28	0.023	1.61
	6.00	4.14	0.24	0.016	1.00
Mo_2Fe_6	14.40	3.74	0.08	0.039	1.05
FeMoco	1.86	6.12	0.29	0.015	3.04
+ thiol	1.55	7.97	0.36	0.015	3.65
	1.15	6.68	0.66	0.010	3.48

Table 1: R_g and molecular weights (relative to the Mo_2Fe_7 model) derived from the Guinier fits for unthiolated FeMoco, thiolated FeMoco, Mo_2Fe_7 model, and Mo_2Fe_6 model.

References

1. Wakatsuki, S. et. al. Rev. Sci. Instrum. **63** (1) 1068 (1992).
2. Wolff, T. E. et. al. J. Am. Chem. Soc. **101** (15) 4140 (1979)
3. Wolff, T. E. et. al. Inorg. Chem. **19** (2) 430 (1980)
4. Brigle, K. E. et. al. J. Bacteriol. **169** 1547 (1987) and ref. therein.
5. Rawlings, J. et. al. J. Biol. Chem. **253** 1001 (1978)

Acknowledgements

The measurements were preformed at SSRL which is supported by the Department of Energy, Office of Basic Energy Sciences. Support was also provided by the NIH Biomedical Research Technology Program Grant RR1209. D. Eliezer was supported under an NSF Graduate Fellowship.

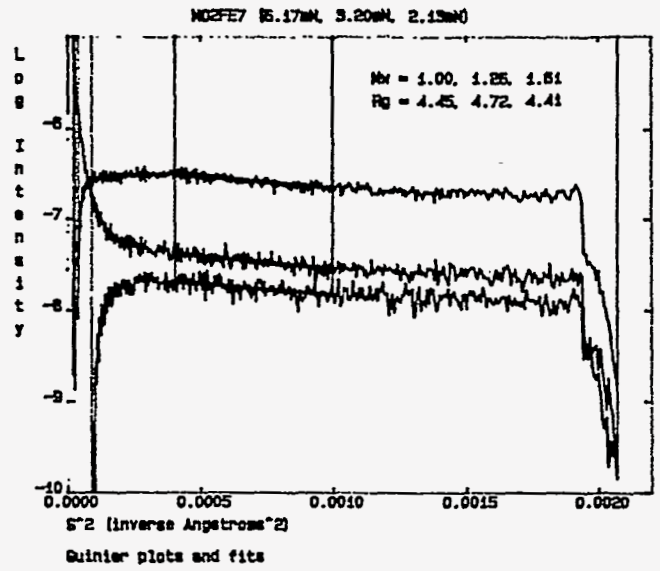

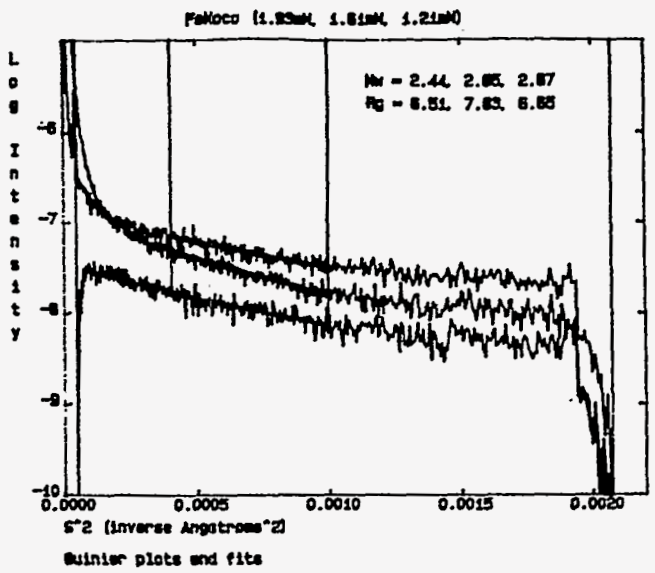

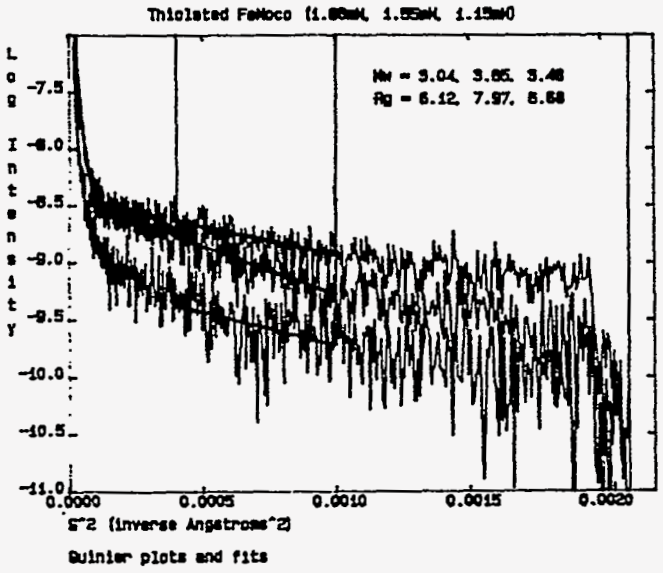

Figure 1: Guinier plots ($\log I$ vs. S_2) and fits for a) Mo_2Fe_7 model compound, b) unthiolated FeMoco samples, and c) thiolated FeMoco samples. The high reproducibility of the data after thiolation indicates the lack of a detectable effect.

Protein Folding observed by Time Resolved Small Angle X-ray Scattering

D. Eliezer(1), K. Chiba (2), H. Tsuruta (3), R. L. Baldwin (4) S. Doniach (5), K. O. Hodgson(6) and H. Kihara (2)

1 Department of Physics, Stanford University, Stanford, CA 94305

2 Department of Physics, Jichi Medical School, Yakushiji, Tochigi, Japan

3 Stanford Synchrotron Radiation Laboratory, SLAC, Bin 69, P.O. Box 4349, Stanford, CA 94309

5 Department of Applied Physics, Stanford University, Stanford, CA 94305

6 Department of Chemistry, Stanford University, Stanford, CA 94305

Introduction

We have been continuing our efforts to use small angle X-ray scattering (SAXS) and time-resolved SAXS to observe the change in size of a protein as it folds from a chemically denatured state into its native state.

Experimental

Static SAXS data were measured at 25°C for 3 different concentrations (26, 13 and 6.5 mM) of purified bovine pancreatic ribonuclease A (RNase A, from Sigma) in 50mM sodium formate, pH 4.0, at 11 concentrations of urea and 7 concentrations of GuHCl. Data were collected using a 20 cm Rigaku gas-filled linear detector, at a wavelength of 1.5 Å and a sample to detector length of 1100 mm on beamline X15A at the Photon Factory. A more complete data set of 15 urea concentrations was later collected using camera lengths of 1084 mm and 2285 mm to obtain data over a larger angular range. All samples were contained in flat 20 μm quartz window cells. Background data were collected immediately preceding each sample. Typical sample volume was 50 μl.

In addition, kinetic data were collected from horse myoglobin (Mb, from Sigma) samples. A camera length of 2298 mm was used. Various conditions were examined in initial experiments. The most promising results were obtained with samples prepared in 100mM NaCl, 40mM NaCN, at 8M urea concentration and at 8°C, made fresh before the experiment. The sample solution was diluted, using a rapid mixing stopped flow machine, into a dilution buffer containing no urea. Collection of SAXS data was started simultaneously with the mixing event and was accumulated in 20 20ms, 20 50ms, 20 200ms, 20 500ms and 14 2000ms time slices. This process was repeated 90 times to improve statistics. The initial protein concentration was 68 mg/ml and the mixing volume ratio was 1 to 3.5, resulting in a final protein concentration of 15 mg/ml in 1.78M urea. Some problems were encountered with urea crystallizing out of solution at such a high initial concentration at this temperature.

Results

The plot of radius of gyration (R_g) versus urea concentration obtained from the first set of static RNase A data (fig. 1) is lacking the sigmoidal shape usually associated with melting curves obtained by such techniques as UV absorption and fluorescence and CD. It may be possible that while the localized chemical environment of the areas probed by other techniques follow a two state behavior upon unfolding of the protein, the protein as a whole unfolds in a more continuous fashion under the influence of chemical denaturants. The data could be taken as an indication of the pretransition swelling. Alternatively, it is possible that a dense layer of urea molecules adheres to the protein as the urea concentration increases, causing a continuous rise in the observed R_g. The second set of data, taken to verify the initial results, have not been processed yet.

The signal to noise level of the individual time slices collected in the kinetic Mb experiments was too low to allow for standard data analysis. Instead, the total integrated intensity scattered into the small angle region was examined for each time slice. The plot shows a clear signal (fig. 2), indicating that a significant fraction of the protein is still unfolded after the mixing dead time of the stopped flow machine, and that it takes approximately one second for most or all of this fraction to refold. The curve suggests a single exponential process, but a detailed analysis has not been preformed. We speculate that the rate constant

being measured here is associated with one or more pathways for the protein to assume the correct initial folding state, after which we believe folding occurs very rapidly.

Acknowledgements

The measurements were preformed at the Photon Factory. Support was provided by the NIH Biomedical Resource Technology Program Grant RR1209 and by the Department of Energy, Office of Basic Energy Sciences and Office of Health and Environmental Research. D. Eliezer was also supported under an NSF Graduate Fellowship.

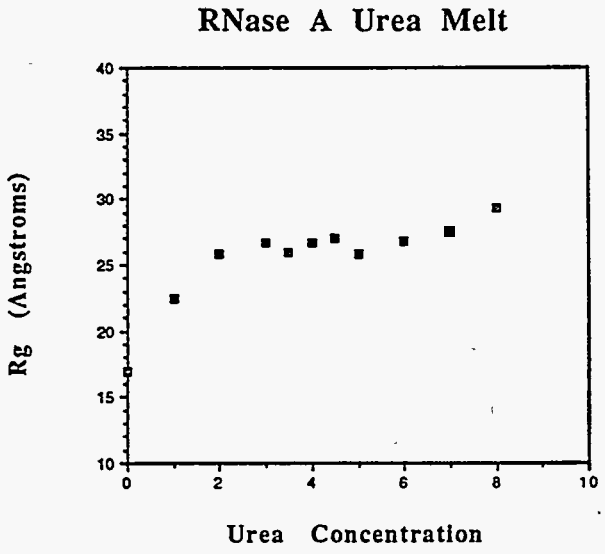

Figure 1: R_g of RNase A as a function of Urea concentration.

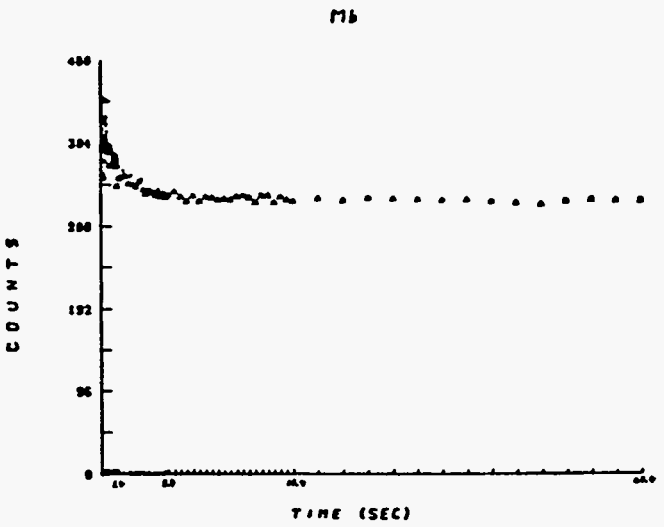

Figure 2: Integrated intensity scattered into the small angle region plotted as a function of time elapsed after introduction of denatured Myoglobin into a refolding environment.

EXAFS and WAXS Studies of Rhenium Hydroxyethylidene - A Novel Palliative Agent For Metastatic Bone Disease

R.C. Elder and Edward Deutsch*

Department of Chemistry and the
Biomedical Chemistry Research Center
University of Cincinnati
Cincinnati, Ohio 45221-0172

Complexes with the radioactive isotopes ^{99m}Tc, ^{186}Re, and ^{188}Re have been used for several years as diagnostic, palliative and recently as therapeutic agents. Each of these isotopes emits high energy short lived gamma rays which are used to image specific sites in vivo. The rhenium isotopes have the added advantage that low energy beta particles are emitted which can be used to destroy cancerous tissue. However, in order for these agents to be efficacious they must be directed to the afflicted area in a safe and rapid manner. A great deal of effort has been put forth to design various chelation complexes with such site specificity and low toxicity in mind.

One such agent, ^{186}Re(HEDP) (HEDP= Hydroxyethylidene 1,3-diphosphonate) has been designed in our laboratories with collaboration from Mallinckrodt Medical Inc. This palliative agent is currently under multi-clinical evaluation for the relief of pain associated with metastatic bone cancer.[1-4] Approximately 80% of the patients being administered an average dose of 35 mCi of ^{186}Re(HEDP) have responded with partial or complete pain relief. In addition to reducing the pain, it is suspected that the same complex might act as a therapeutic agent and eliminate tumor cells themselves. Clearly it is advantageous to fully understand the properties of this agent so that future generations of drugs can be designed which are even more efficacious and less toxic.

To understand the binding of this drug, its molecular structure must be determined. Unfortunately, we have been unable to grow high quality single crystals suitable for single crystal X-ray diffraction. Analysis by HPLC suggests that the agent is a mixture of many complexes similar to the analogous ^{99m}Tc-diphosphonates.[5] Therefore EXAFS and WAXS studies were undertaken to obtain structural information on the drug and several of its analogues.

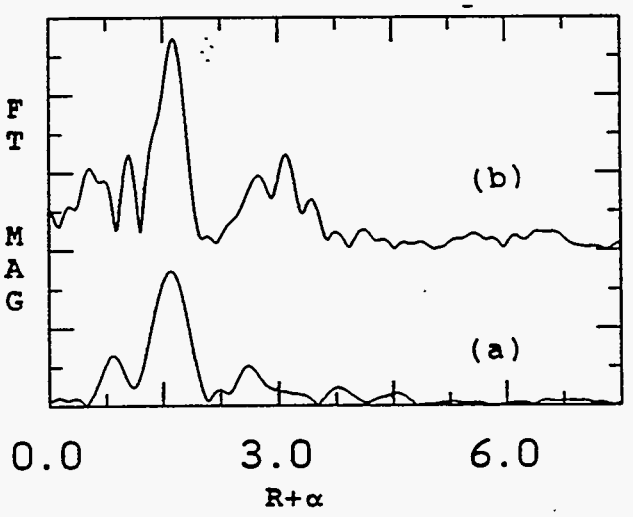

Figure 1: PRDF for a) the substitution product and b) the tin reduced product of Re(HEDP) from EXAFS data.

*Current Address:
Mallinckrodt Medical Inc.
675 McDonnell Blvd.
St. Louis, Missouri 63134

We have performed EXAFS and WAXS experiments on Re(HEDP) containing a non-radioactive isotope of rhenium. Two different synthetic routes were used to prepare these drugs, the first involved adding the HEDP ligand to a rhenium(V) complex, while the second used stannous chloride to reduce ReO_4^- in the presence of the ligand. The EXAFS data were collected at liquid helium temperature in an attempt to elucidate any metal-metal interactions which may be present in the proposed oligomeric form of the drug.

The dominant peak in the PRDF's (Figures 1a and b) for each of these materials occurs at 1.6 Å R+α. This peak has been attributed to approximately 4-5 Re-O bonds at 2.02 Å and 1 Re=O bond at 1.69 Å. This is consistent with many known technetium and rhenium octahedral and square pyramidal complexes. A second less intense peak occurs at about 2.7 Å R+α and corresponds to either a Re-O, Re-P interaction, or some combination of the two. We have speculated that this is due to close non-bonded interactions with the ligand. The filtered EXAFS signal from this peak was fit with phosphorus and oxygen theoretical phase and amplitude functions and the distance calculated to be 3.2 Å.

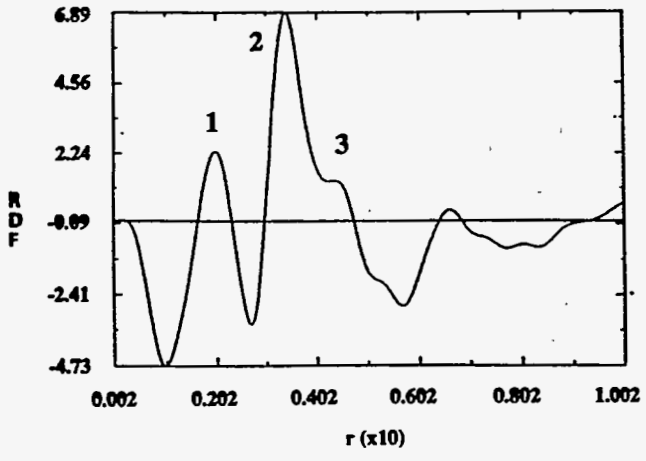

Figure 2: Radial Distribution function of the tin reduced form of Re(HEDP) from WAXS data.

Perhaps the most interesting distinction between the two PRDF's is the presence of two peaks between 3.0 and 3.8 Å in the tin reduced form of the drug and the absence of these same peaks in the PRDF for the substitution product. The filtered EXAFS spectra calculated for both peaks in the tin reduced material exhibited an amplitude envelope which maximized very high in K space. We have tentatively assigned these two peaks to a Re-Re and Re-Sn interaction. The presence of this interaction suggests an oligomeric structure similar to that found in technetium diphosphonates.[5] Further evidence for this type of structure was observed in the data from WAXS/DAS experiments performed on this complex. Peaks occurring in the RDF (Figure 2) at 2.0, 3.2, and 4.3 Å support the idea of an oligomeric species. The peak at 2.0 Å arises from the first shell of oxygen neighbors while the latter two peaks are likely to correspond to rhenium-rhenium and rhenium-tin interactions.

Three additional complexes were studied to further our knowledge of how these drugs interact with bone tissue. The tin reduced product of the drug was precipitated from solution using Ca^{2+}, Sr^{2+} and finely ground calcium hydroxyapatite. These cations should closely mimic the active binding site of the drug in vivo. Strontium is isostructural with calcium and has the added advantage that its K absorption edge is at 16107 eV, well within the useable energy range at SSRL. This allows us to obtain complementary information by comparing data collected at the Re L_{III} edge and the Sr K edge.

The PRDF's for the calcium and strontium Re(HEDP) were identical to that for the tin reduced product with one notable exception, the presence of a large peak at ca. 2.28 Å R+α (Figure 3). When this peak is Fourier filtered the amplitude envelope maximizes toward high K space which is characteristic of a heavy backscattering atom. We conclude that this peak is caused by Re-Ca and a Re-Sr interaction in the corresponding samples. The modeling performed using theoretical phase

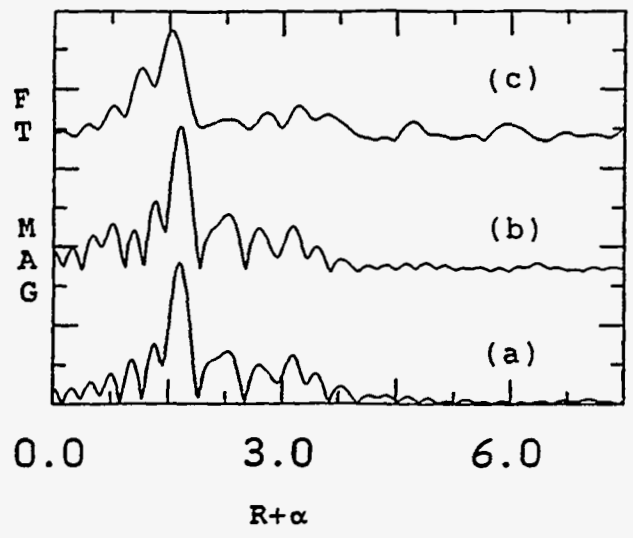

Figure 3: PRDF for the a) Sr^{2+} precipitate b) Ca^{2+} precipitate and c) calcium hydroxyapatite precipitate.

and amplitude functions indicates that the interactions occur at 2.5 and 2.6 Å for the calcium and the strontium respectively. The data collected about the Sr K edge yielded very little information because the data were very noisy. Also a large spike at high K in the data occurred due to an anomaly in the monochromator crystal.

Calcium hydroxyapatite is a major component in bone tissue and therefore makes an excellent model for the binding of Re(HEDP). Very finely ground hydroxyapatite was reacted with a solution containing Re(HEDP). However, the amount of the drug that we were able to load on the substrate was much lower than we had expected <1% by mass. Therefore the EXAFS data for this sample were very noisy. A qualitative comparison shows features in the PRDF that are very similar to the PRDF for the calcium precipitated form of the drug.(figure 3) Further EXAFS data will have to be measured once we have solved the loading problem to obtain any quantitative results.

Preliminary examination of these drugs using WAXS/DAS techniques was performed on beamline VI-2. The low loading of the Re(HEDP) on hydroxyapatite precluded the measurement of data that was high enough in quality to interpret. The precipitation of the tin reduced Re(HEDP) with calcium and strontium does show some differences in the RDF. These changes may lend support to the Re-Ca and Re-Sr interactions seen in the EXAFS data. Currently mechanical and sample problems are being eliminated so that high quality WAXS/DAS data may be measured during future experiments.

From these synchrotron radiation studies we have deduced that the rhenium center is bound to 5-6 oxygen atoms. A peak in the PRDF at 2.7 Å R+α corresponding to a phosphorus or oxygen backscatterer supports binding to the diphosphonate ligand. The discovery of a Re-Re and Re-Sn interaction suggests that the structure is an extended polymer with oxygen atoms bridging between the metal atoms. The calcium and strontium precipitated forms of the drug show a strong interaction between rhenium and the cations at very close distances ca. 2.5 Å.

More synchrotron studies have been planned including further WAXS/DAS studies and data measured on the drugs in solution. Efforts are currently under way in our laboratories to use vibrational spectroscopy, NMR and molecular synchrotron radiation.

Acknowledgements: The materials described here were all synthesized by Dr. David Pipes of Mallinckrodt Medical. The X-ray studies were performed by Dr. John D'Amore and Mr. W. B. Jones. Grant support was from Mallinckrodt Medical to RCE.

1.a) Maxon, H.; Deutsch, E.A.; Thomas, S.R.; Libson, K.; Lukes, S.J.; Williams, C.C.; Ali, S.; Radiology, **1988**, 166, 501. b) Maxon, H.; Schroeder, L.E.; Thomas, S.R.; Hertzberg, V.S.; Scher, H.I.; Samaratunga, R.C.; Deutsch, E.A.; Libson, K.; Williams, C.C.; Moulton, J.S.; Schneider, H.J.; Radiology, **1990**, 176, 155.

2.a) Maxon, H.; Schroder, L.; Hertzberg, V.; Thomas, S.; Englaro, E.; Samaratunga, H.; Smith, H.; Moulton, J.; Williams, C.; Schneider, H.; J. Nuc. Med., 1991, 32(5), 963. Maxon, H., "Therapy of Painful Osteoblastic Metastases with ^{186}Re HEDP", Science and Nuclear Medicine Continuing Education Course June 14th, 1991, Cincinnati, OH.

3.a) Zonnenberg, B.A.; de Klerk, J.M.H.; van Rijk, P.P.; Quirijnen, J.M.S.P.; van het schip A.D.; van Dijk, A.; ten Kroode; N.F.J.; J. Nuc. Med. 1991, 32(5), 1082. b) de Klerk, J.M.H.; van Rijk, P.P.; Zonnenber, B.A.; van het Schip, A.D.; J. Nuc. Med. 1991, 32(5), 1083.

4. Pipes, D.W.; D'Amore, J.; Deutsch, K.; Elder, R.C.; Deutsch, E.A.; J. Nuc. Med., 1991, 32(5), 1089.

5. Martin Jr., J; Yuan, J.; Lunte, C.; Elder, R.C.; Heineman, W.; Deutsch, E.; Inorg. Chem. 1989, 28(15), 2899.

SYNCHROTRON RADIATION DETECTOR DEVELOPMENT PROGRAM

W.K. Warburton & S.R. Russell
X-ray Instrumentation Associates
1300 Mills Street, Menlo Park, CA 94025-3210

Our experimental effort this past year was divided into two parts. In the first we attempted to collect and digitize scattered x-rays synchronously with their arrival from SPEAR. In the second we collected preamplifier output data from two common energy dispersive detectors to establish a baseline for our development program.

The synchronous data collection effort was undertaken in conjunction with our NIH SBIR project to develop a 2-D detector for time resolved protein crystallography which would be capable of collecting a full frame of data once every 150 nsec. This time was chosen because it was sub-microsecond, was considered long enough to allow the contemplated data storage operation and was shorter than the inter-bunch time when SPEAR is operated in the 4-by-4 mode. As part of our SBIR Phase I effort we had developed a single pixel detector whose output could be digitized at this rate and we wished to discover what problems would arise in attempting to synchronize its operation to the arrival of x-rays from SPEAR. In this effort we were sufficiently successful that we were unable to collect any data. The first problem is that SPEAR timing signals are not routinely supplied to the experimental stations. In building 120, for example, the signals are on free cables which must be located and dragged to the desired stations. The second problem is that these signals are not well conditioned, being essentially the analog signals produced by current sensors in SPEAR. As such, considerable processing is required to produce good digital signals with sharp enough rise times and short enough durations to be good for timing applications. These problems we were able to cope with. The final problem was that the fill pattern in SPEAR had been changed since its last run and this situation was not advertized. Instead of 4-by-4 we found about 30 buckets separated by about 30 nsec intervals followed by a single 300 nsec dark space. This pattern was useless for our purposes so we terminated our run after determining that we could at least synchronize to the first bucket following the dark space.

The preamplifier output data collection was both successful and enlightening. The two detectors we studied were: 1) one channel of the Biotechnology program's Canberra 13 element detector array; and 2) an Ortec HPGe detector in a Gamma Gage cryostat. The Canberra preamplifier used pulsed optical feedback and has a nominal energy resolution (noise) of about 180 eV. The Ortec detector was optimized for high count rates using a high rate feedback resistor and has a nominal gain of about 300 eV. Data were collected from these preamplifiers using wide bandwidth, high speed digital oscilloscopes. Sampling rates were varied from about 1 MSA (10^6 samples/sec) to 50 MSA in order to study both how these signals could be filtered to achieve enhanced noise reduction and to investigate the effect of sampling rate on the deduced noise spectra of the two preamplifiers.

Typical data from both preamps for 5.9 keV x-rays are shown in Figure 1 below. It is quite clear that the Canberra preamp is much less noisy than the Ortec preamp, as expected. What was not anticipated was the great difference in the risetimes of the signals from the two detectors. As shown in Figure 2, the Ortec risetime is about 140 nsec or so, while the Canberra detector's risetime is well over a microsecond, almost 10 times slower. We impute the observed risetimes to charge collection times in the detectors themselves because risetimes in the preamplifiers is typically 10 nsec or less. The slow Canberra risetime means that even with improved noise filtering there is an inherent limit on the count rates which could be processed with this detector. We are currently analyzing these data and studying the possibilities of developing digital filtering techniques to replace the analog electronics currently used in high quality spectroscopy amplifiers. Our goal in this effort is to lower both the cost and physical size of the filters so that detector arrays with 100s of elements can become economically feasible.

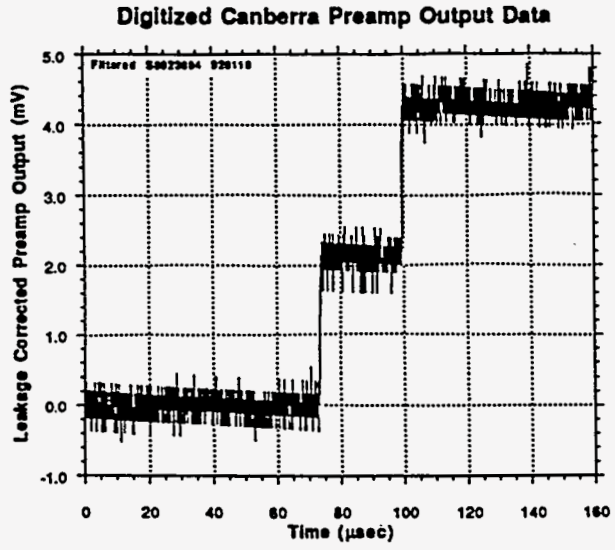

Figure 1a: Output from a pulsed optical feedback preamp, from a Canberra 13-element Ge detector array, for 5.9 keV x-rays.

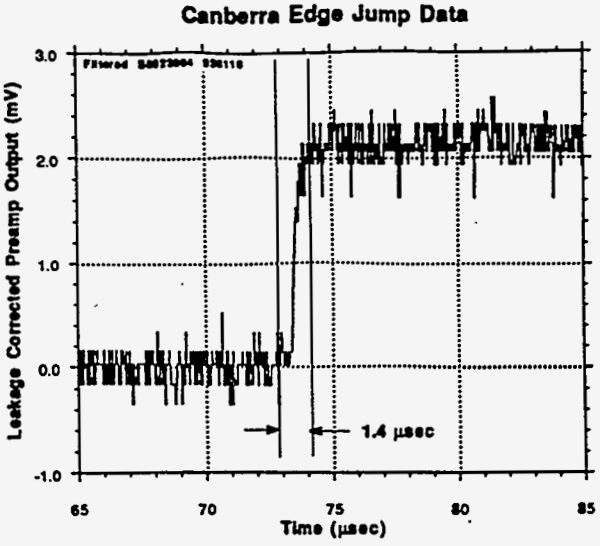

Figure 2a: Expanded region of Figure 1a showing charge collection time following absorption of a single 5.9 keV x-ray.

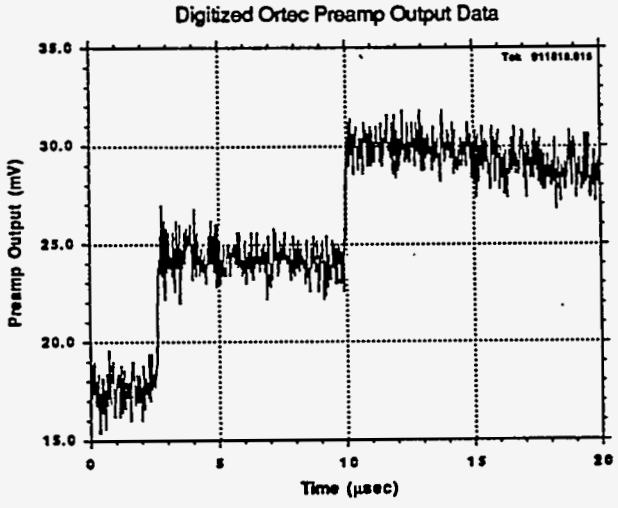

Figure 1b: Output of the preamp on an Ortec GLP Ge detector using a high count rate resistor feedback, for 5.9 keV x-rays.

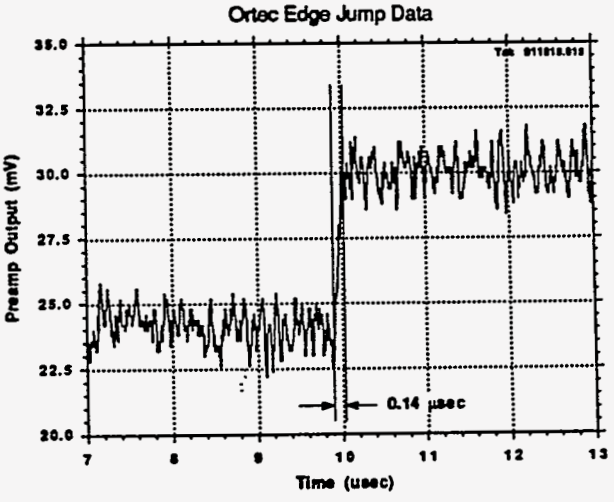

Figure 2b: Expanded region of Figure 1b showing charge collection time following absorption of a single 5.9 keV x-ray.

XAS LIGAND EDGE STUDIES OF BLUE COPPER PROTEIN ELECTRONIC STRUCTURE

Susan E. Shadle, Keith O. Hodgson, Edward I. Solomon
Department of Chemistry, Stanford University, Stanford, CA 94305

Britt Hedman
Stanford Synchrotron Radiation Laboratory, Stanford, CA 94309

Introduction

Blue copper proteins are characterized by several unique spectral features. The blue color of these proteins results from an intense absorption feature ~600 nm, the extinction coefficient of which is two orders of magnitude greater than in normal tetragonal (D_{4h}) copper complexes in the same region. The EPR of blue copper centers exhibit an unusually small $A_{||}$ hyperfine splitting. A detailed understanding of the origin of these features and the electronic structure of these systems has been the goal of many experimental and theoretical studies. One proposed explanation for the small $A_{||}$ hyperfine in blue copper has been a 12% Cu p_z mixing into the Cu $d_{x^2-y^2}$ ground state.[1]. Because the $4p_z$ orbital will have a spin dipolar contribution which opposes that of the $d_{x^2-y^2}$ orbital, the hyperfine coupling between the unpaired electron spin and the nuclear spin would be thus reduced. In order to determine the nature of the contribution of 4p mixing to the blue copper ground state, we have conducted a polarized single crystal X-ray absorption spectroscopy (XAS) study at the copper K-edge.[2]

An alternative explanation for the small $A_{||}$ splitting has come from Xα-SCF-SW calculations on the structurally characterized plastocyanin site. They show the site to have a highly covalent Cu-S(Cysteine) bond.[3]. A high degree of covalency would delocalize the unpaired electron spin onto the sulfur ligand, thereby reducing its coupling to the nuclear spin. Ligand XAS has been shown to be an effective probe of the covalency of a metal-ligand bond.[4]. As reported here, our recent studies at the S K-edge provide a direct experimental probe of the electronic structure of the blue copper active site.

Experimental

Cu K-edge XAS data were measured at SSRL on beam line II-2. Details of the measurements, including the orientation of the single crystals has been described previously .[5] Sulfur K-edge XAS data were measured at SSRL using the 54-pole wiggler beam line VI-2 at low magnetic fields (5kG), using a Si(111) double crystal monochromator at a Pt-coated focusing mirror. The entire experimental beam path was in He atmosphere. Measurements were made in fluorescence detection mode, using a N_2-filled Lytle detector. Model compounds were measured as very thin powders on mylar tape to avoid self-absorption. Protein solutions were contained in a teflon cell with a polypropylene window during data collection.

Results and Discussion

Polarized single crystal Cu K-edge spectra of plastocyanin (Fig. 1) show a preedge feature at ~8987 eV in the xy-polarized spectrum, while the z-polarized spectrum has no preedge feature. This feature at ~8987 eV has been assigned as a Cu 1s-->$3d_{x^2-y^2}$ transition, which gains intensity from 4p mixing into the d-orbital. The intensity of this transition reflects the 4p character in the plastocyanin ground state wave function. The fact that there is preedge intensity in only the xy-polarized spectrum indicates that the ground state contains $4p_{xy}$ character and not $4p_z$ character. Therefore, $4p_z$ mixing cannot explain the EPR hyperfine splitting.

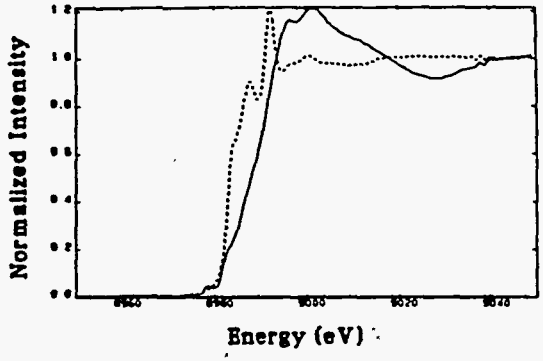

Figure 1. Plastocyanin single crystal polarized Cu K-edges. The solid line corresponds to the xy-polarized orientation; the dashed line to the z-polarized orientation. (This figure has been previously published in reference 5)

For a comparison to the blue copper protein center, the X-ray absorption S K-edge spectrum of the blue copper model, [Cu(tet-b)(o-$SC_5H_4CO_2$)]·H_2O (tet-b)[6] (Fig.2) is shown in Figure 3.

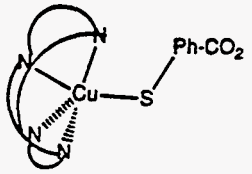

[Cu(tet-b)(o-$SC_6H_4CO_2$)]·H_2O

Figure 2. Schematic structure of the blue copper model, tet-b.

The EPR solution spectrum of tet-b has normal copper hyperfine splitting.[7]. This indicates that tet-b is an inorganic complex having a normal degree of covalency. Tet-b exhibits a S K-edge preedge feature at 2470.3 eV with a normalized intensity of 0.460. This is assigned as a S 1s--> ψ^* (Cu $3d_x2\text{-}y2$ + S 3p) transition. The intensity of this transition reflects the S 3p character in the Cu -S(Cys) antibonding orbital. The intensity of the tet-b preedge feature, then, reflects a degree of delocalization characteristic of normal copper complexes. In contrast, the S K-edge spectrum of the blue copper protein, plastocyanin, (Fig. 1) exhibits a preedge feature at 2469.0 eV with a scaled intensity of 1.140[8], i.e. more than twice that of the tet-b model (Fig 3, inset).

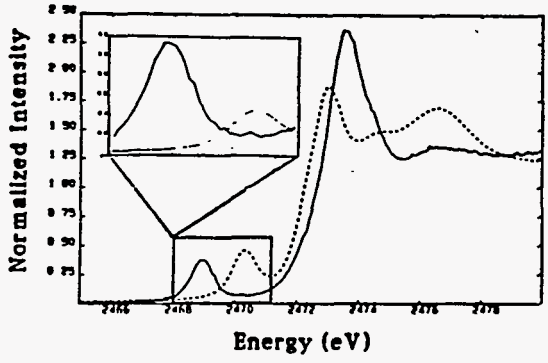

Figure 3. Normalized sulfur K-edges of tet-b (---) and plastocyanin (——). Inset: Preedge region of the tet-b (-----) and plastocyanin (——) spectra, where the edge jump and thus preedge height is rescaled to show the contribution of the cysteine sulfur.

The increased intensity of the protein preedge relative to that of tet-b shows experimentally that the blue copper site in plastocycanin is highly covalent. It is this experimentally observed covalency in blue copper centers that is responsible for the reduced $A_{||}$ hyperfine splitting in the EPR spectrum. This large degree of overlap between the Cu and S(Cys) is consistent with the assignment of the intense ~600 nm band as a S(Cys)-->Cu charge transfer transition.

The 1.3 eV shift between tet-b and plastocyanin in the energy of the preedge feature can be understood in terms of the energy of their respective $d_x2\text{-}y2$ orbitals, whose energies are determined by antibonding interactions with the ligands. The Cu center in tet-b experiences a higher ligand field strength than in plastocyanin, causing its preedge transition to occur at higher energy.

Acknowledgments

Grant support was provided by NSF (CHE88-17702, KOH), (CHE89-19687, EIS). The measurements were performed at SSRL, which is supported by the US DOE, Office of Basic Energy Sciences, Divisions of Chemical and Material Science, and Office of Health and Environmental Research; and by the NIH, Biomedical Resource Technology Program, Division of Research Resources.

References

1 a) Bates, C.A.; Moore, W.S.; Standley, K.J.; Stevens, K.W.H. Proc. Phys. Soc. **1962**, 79, 79-83.
b) Sharnoff, M. J. Chem. Phys. **1965**, 42, 3383-3395.
2. Schulman, R.G.; Yafet, Y.; Eisenberger, P.; Blumberg, W.E. Proc. Natl. Acad. Sci. USA **1976**, 73, 1384-1388.
3. Penfield, K.W.; Gewirth, A.A.; Solomon, E.I. J. Am. Chem. Soc. **1985**, 107, 4519-4529.
4. Hedman, B.; Hodgson, K.O.; Solomon, E.I. J. Am. Chem. Soc. **1990**, 112, 1643-1645.
5. Scott, R.A.; Hahn, J.E.; Doniach, S.; Freeman, H.C.; Hodgson, K.O. J. Am. Chem. Soc. **1982**, 104, 5364-5369.
6. Hughey IV, J.L.: Fawcett, T.G.; Rudich, S.M.; Lalancette, R.A.; Potenza, J.A.; Schugar, H.A.; J. Am. Chem. Soc. **1979**, 101, 2617-2623.
7. H. Schugar, unpublished results.
8. Only sulfur atoms which undergo bonding interactions with the vacant $d_x2\text{-}y2$ orbital contribute to the preedge intensity. Of the three sulfurs in the protein, only the cysteine bonds in this way.

STRUCTURAL CHARACTERIZATION OF Hg METALLOPROTEINS

Kimber Clark, Timothy Stemmler, James Penner-Hahn
Department of Chemistry
University of Michigan

Thomas V. O'Halloran
Department of Chemistry
Northwestern University

Susan Miller
Department of Biological Chemistry
University of Michigan

A central component of the bacterial mercury detoxification system is the cooperation between the MerR metalloregulatory protein and the MerA mercuric reductase protein. MerR is an intercellular heavy metal receptor of mercury and acts as a metal-responsive genetic switch in the production of proteins which transport and reduce mercury. MerA catalyzes the actual two-electron reduction of Hg(II) to Hg(0) using NADPH and FAD.

A) MerR

MerR is converted from a repressor to an activator of prokaryotic mercury resistance genes in the presence of mercuric ions. Although MerR is activated by the binding of mercuric ions, it also binds other metals, including Zn and Co, without transcription activation occuring. This may be due to Zn and Co having a higher preference than Hg to bind low molecular weight ligands. In addition, Cd both binds and activates MerR, albeit at concentrations ca. 1000 times as high as needed for Hg. [1] Even at Cd concentration levels this large, the transcription rate for Cd-MerR is lower than for Hg-MerR, suggesting separate binding sites. This is somewhat surprising because of similarities in Cd and Hg coordination chemistry.

Previous results for Hg-MerR suggest a three-coordinant sulfur environment with an average Hg-S distance of 2.43 A. [2] This tridentate coordination environment is in agreement with the thermodynamic stability of $[Hg(SR)_3]^-$ complexes. In contrast, other group IIB metals appear more likely to adopt tetrahedral environments with thiolate coordination. [2,3,4] A $Hg(S\text{-}Cys)_3$ binding site may explain how MerR discriminates between Zn(II) or Co(II), Cd(II), and Hg(II).

X-ray absorption data for both Zn(II) and Cd(II) forms of MerR have provided further evidence for this mechanism of discrimination. The EXAFS and corresponding Fourier transform spectra for Zn-MerR show a single resolved shell of scatterers.[fig. 1]

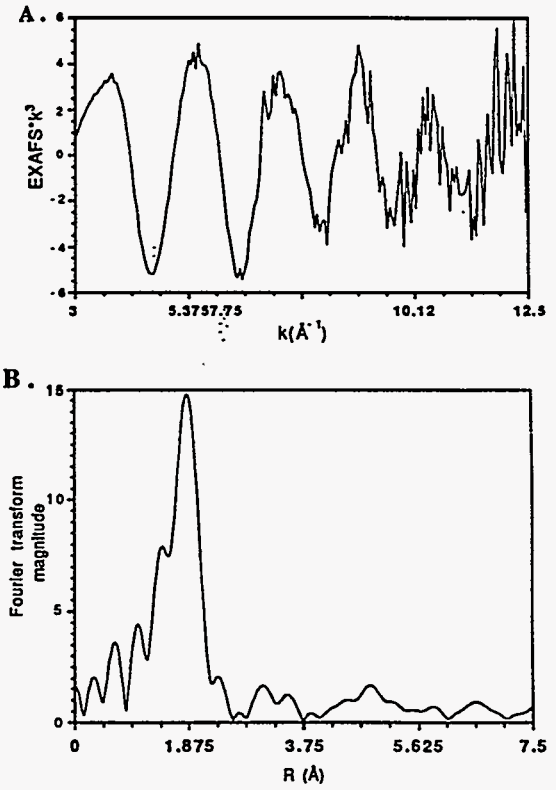

Figure 1. (A) MerR Zn k3-weighted EXAFS spectrum. (B) Fourier transform for Zn-MerR

This shell was fit using theoretical parameters [5] and allowing the distance and Debye-Waller factor to vary. The data are consistent with a tetradentate sulfur environment with an average Zn-S distance of 2.34A. This distance is consistent with crystallographic data on four coordinate Zn-S complexes. [6] Furthermore, no significant improvement in quality of fit is observed for inclusion of a second shell of low-Z ligands.

The EXAFS and Fourier transform spectra for Cd-MerR also depict a single shell of scatterers. [fig. 2] Preliminary analysis of the Cd EXAFS again suggests that the metal is coordinated only to thiolate ligands. Further analysis of these data is in progress.

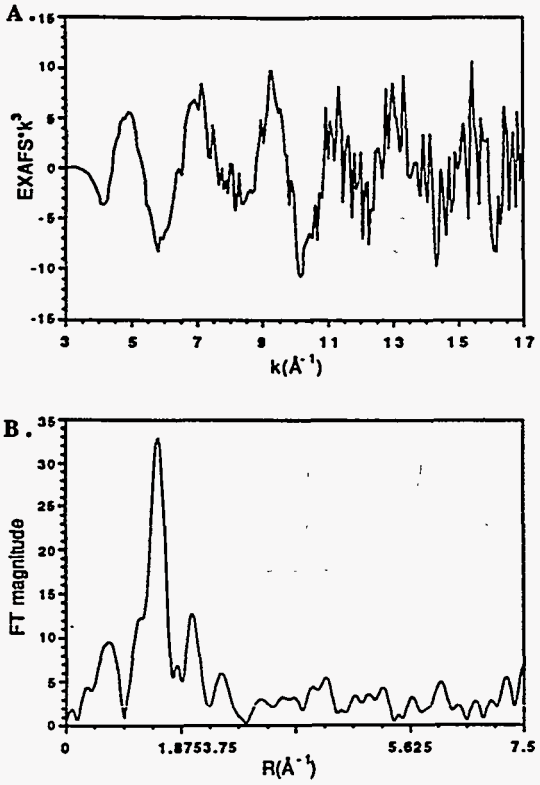

Figure 2. (A) MerR Cd k3-Weighted EXAFS spectrum. (B) Fourier tranform for Cd-MerR.

B) MerA

The ultimate step in bacterial detoxification of mercuric ions is their two electron reduction to elementary mercury catalyzed by MerA. This enzyme contains FAD, a reducible active site disulfide, and a C-terminal pair of cysteines. Walsh and co-workers have found that all 4 cysteines are required for efficient Hg(II) reduction [7]. As noted previously [7], MerA must bind Hg tightly to prevent damage to other proteins, but this tight binding, by stabilizing Hg(II), is inconsistent with facile reduction of Hg(II) to elemental Hg. Recent data from pyridine nucleotide binding studies suggest that the dimeric enzyme is asymmetric when complexed to pyridine nucleotide substrates/products. EXAFS has been used to test the alternating sites hypothesis [8] which states that the MerA dimers may function asymmetrically and that different Hg(II) binding modes may coexist on the asymmetric dimer. This so-called "alternating sites hypothesis" suggests that one site within the dimer functions to bind Hg(II) while the other site catalyzes the reduction to elemental Hg. Following reduction, the Hg(0) is released and the functional roles of the sites change.

Previous EXAFS studies of MerA containing one Hg per dimer found an average Hg-S bond length of 2.30 Å, consistent with two-fold Hg-S coordination. [7] We have recently measured EXAFS data for MerA containing only a single Hg(II) per dimer in order to test the alternating sites hypothesis. Samples were studied in the presence and absence of pyridine nucleotides. The EXAFS spectra and their Fourier Transforms are shown in Fig. 2. The data are consistent with Hg-S coordination and an average Hg-S distance of 2.34 Å. This is slightly, but probably significantly higher than the distance found by Walsh et al. Experiments to test this difference are in progress. If confirmed, this would be consistent with the proposal [8] that the two Hg sites are structurally distinct. In addition, it appears from Fig. 3 that addition of NADP causes a structural change at ca. 3.0 Å from the Hg. Analysis of these data are in progress.

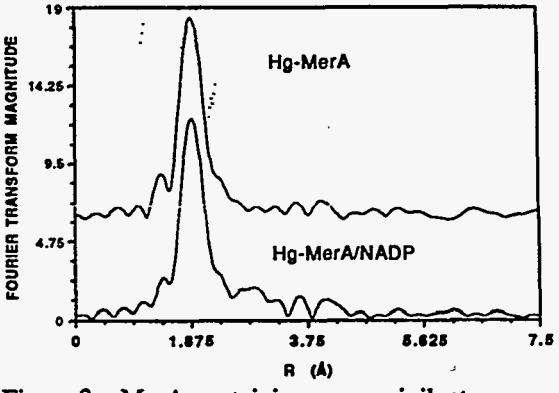

Figure 3. MerA containing one equivilent Hg(II) per dimer in the presence and absence of NADP.

REFERENCES:
(1) D. M. Ralston and T. V. O'Halloran, *Proc. Natl. Acad. Sci. USA*, **1990**, *87*, 3846-3850.
(2) J. G. Wright, H. T. Tsang, J. E. Penner-Hahn, and T. V. O'Halloran, *J. Am. Chem. Soc.*, **1990**, *112*, 2434-2435.

(3) I. Persson and F. Zintl, *Inorg. Chim. Acta.*, **1987**, *129*, 21-26.
(4) B. V. Cheesman, A. P. Arnold, D. L. Rabenstein, *J. Am. Chem. Soc.*, **1988**, *110*, 6359-6364.
(5) D. L. Rehr and A. Zabinsky, *J. Am. Chem. Soc.*, **1991**, *113*, 5135.
(6) E. S. Gruff and S. A. Koch, *J. Am. Chem. Soc.*, **1989**, *111*, 8762-8763.
(7) M. Moore and C. Walsh, *Biochemistry*, **1989**, *28*, 1183-1194.
(8) Miller,S.M.; Massey, V.; Williams, C. H.; Ballou, D.P.; Walsh, C.T. *Biochemistry*, **1991**, *30*, 2600-2612.

STRUCTURAL STUDIES OF MYOSIN SUBFRAGMENT-1

Ivan Rayment, Diana Tomchick, Robert Smith, Gary Wesenberg, and Hazel Holden

Institute for Enzyme Research, University of Wisconsin,
1710 University Avenue, Madison, WI 53705

The objective of this research is to improve our understanding of the molecular basis of muscle contraction by determining the three-dimensional structure of myosin subfragment-1 using single-crystal X-ray diffraction. Myosin is the major protein in muscle, in which it plays both a structural and enzymatic role. The myosin rod forms the backbone of the thick filament, whereas the myosin head is responsible for the generation of movement through the hydrolysis of ATP and its interaction with actin.

Crystals of chicken pectoralis myosin subfragment-1 that diffract to 2.6 Å resolution have been grown reproducibly and at least seven heavy atom derivatives have been prepared, five of which have been solved at 3 Å resolution. The crystals belong to space group $C222_1$ and have unit cell dimensions of a = 98.8 Å, b = 123.8 Å, and c = 274.9 Å. There is one molecule of molecular weight 130,000 daltons per asymmetric unit. The crystals have a low mosaic spread and diffract isotropically. A 1° oscillation photograph can be recorded in eight hours using radiation from a conventional rotating anode equipped with double focusing mirrors, whereas the same data can be recorded in 3-6 minutes on the SSRL rotation camera beam line.

During the last data collection run at SSRL, seven data sets were recorded on film for myosin subfragment-1. Two of these were improved native data sets, whereas the others represented the final high resolution data sets for five heavy atom derivatives. The heavy atom derivative data sets collected were: 20 mM Trimethyllead acetate--20 days, 2 mM Uranyl Fluoride--2 days, 0.08 mM 2-Chloromercuri 4,6-Dinitrophenol/1.6 mM Mercaptosuccinic acid--36 hours, 0.2 mM Tetrakis (acetomercuri) Methane/1 mM Mercaptosuccinic acid--24 hours and a saturated Pt-acetoacetamide derivative. The last three derivatives were collected in an effort to locate the positions of the three reactive cysteine residues known to exist in chicken skeletal myosin subfragment-1 and cannot be collected with an in-house radiation source, since the crystals are far more sensitive to radiation damage. In addition, these derivatives are sensitive to oxidation so that it is not possible to collect their data within the time-scale of a normal data collection run.

All of these films have now been processed, reduced and scaled. The quality and extent of the data is far better than had been recorded previously either from an in-house area detector or from the CHESS B1 beam line. The improvement in the data arises not only from the lower wavelength available at SSRL, but also from the superb stability of the experimental station and X-ray beam at Stanford. At this time, we are refining the heavy atom positions and preparing a final merged data set. A preliminary electron density map at 3.5 Å resolution shows that 35% of myosin subfragment-1 is built from α-helices and that it contains one α-helix that is over 90 Å long. In addition, this map gives a good indication of the arrangement of the domains in this molecule. It is expected that once the data merging and refinement is complete, it will be possible to locate most of the 1,200 amino acid residues in this molecule and that this will form the basis for developing a model that describes the molecular basis of muscle contraction.

Until our last trip to SSRL it was believed that the crystals diffracted only to 2.8 Å resolution. To our surprise, some films show diffraction to beyond 2.6 Å. Even though data appears to be very radiation sensitive, it will clearly be important for the final high resolution structure. To overcome this problem,

we are attempting to both slow cool and rapid cool crystals in an effort to be able to record this data. In addition, we would like to collect data from crystals that contain ATP or nucleotide analogues. It is already known that they can be soaked into the crystals without damage and that they bind specifically to the active site. Future experiments at SSRL will be focused toward collecting higher resolution data and collecting data on myosin/ATP derivatives. Together, these will provide the information necessary to confirm the hypotheses of how chemical energy is transduced into mechanical force that are emerging from the data collected at SSRL in 1991.

CONTINUED HEAVY ATOM DERIVATIVE SCANNING ON PILIN

H. E. Parge, E. D. Getzoff and J. A. Tainer
Department of Molecular Biology,
The Scripps Research Institute,
La Jolla, California 92037

Introduction

Pilus fibers are long protein filaments on many pathogenic bacteria that participate in attachment to host cells (1). These fibers are constructed from the self-assembling pilin protein. The pilin protein from *Neisseria gonorrhoeae* has a molecular mass of about 18 kDa and consists of approximately 160 amino acids depending on strain variation (2-4). We have published the biochemical purification and crystallization procedures for pilin from *Neisseria gonorrhoeae* (5) and have applied these techniques to obtain crystals of pilin from *Bacteroides Nodossus* and the PGH3.2 strain of *Neisseria gonorrhoeae* (unpublished results). Analysis of native data previously collected at the Stanford Synchrotron Radiation Laboratory (SSRL) has provided us with our current model of the pilin subunit as an anti-parallel α-helix bundle similar to tobacco mosaic virus coat protein and myohemerythrin (6,7). We have used the SSRL facility extensively for data collection and to screen heavy atom derivatives since these crystals are usually small.

Experimental

Three-dimensional needle- and plate-shaped crystals of purified *N. gonorrhoeae* pilin (strain MS11 variant C30) grew from 36-40% polyethylene glycol 400, pH 8.0–9.0, in space group C222, with cell dimensions $a = 126.4$, $b = 121.2$, $c = 26.7$ Å and $V_m = 2.84$ Å^3/dalton for one molecule per asymmetric unit (2). Crystals were mounted in glass capillaries along with their mother liquor for experiments conducted at ambient temperatures and on glass fibres after immersion in a hydrocarbon for low temperature experiments. For heavy atom screening, crystals were soaked in 10μ drops of stabilising solution made 1-10mM in heavy atom reagent. Data were collected at SSRL on beamline 7-1 using an Arndt-Wonacott rotation camera with a crystal to film distance of 10 cm, 0.2 mm collimator, and rotation increments of 2.0-3.5° and 1.54 and 1.08 Å radiation.

Results

Pilin crystals grown form PEG 400 are obtained in two morphologies, thin plates and long thin needles. In the previous allocated beamtime (1989) we established that the plate morphology was unsuitable for data collection and thus renewed our efforts to reproducibly obtain the needle shaped crystals. For the beamtime assigned in 1991 we therefore had a good supply of suitable crystals. In the 1991 run using these crystals we screened 21 heavy atom reagents and extensively tested the feasibility of collecting pilin diffraction data at cryogenic temperatures.

The screening of heavy atom reagents involved collecting three to five rotation photographs around the major zones and subsequent comparison of the processed data with native diffraction data also collected at SSRL. The results of these experiments have indicated eight potential heavy atom derivatives. The results of the cryogenic data collection experiments have shown that crystal beam-lifetime can be extended significantly to the point of obtaining a complete data set on a single crystal of pilin. However, it is very important to insure that crystals are adequately supported during the flash freezing procedure.

In addition to these experiments we also collected a complete data set to 4.0 Å on crystals of pilin from *Bacteroides Nodossus* and a partial data set to low resolution on pilin from the PGH3.2 strain of *Neisseria gonorrhoeae*.

Acknowledgements

This work was supported by a National Institute of Health grant AI-22160 to E. D. Getzoff and J. A. Tainer and funding from the U. S. Army Medical Research and Development Command (DAMD17-88-C-8015).

References

1. Stromberg, N., Deal, C., Nyberg, G., Normark, S., So, M. and Karlsson, K. (1988) *Proc. Natl. Acad. Sci. U.S.A.* **85**, 4902-4906.

2. Schoolnik, G. K., Fernandez, R., Tai, J. Y., Rothbard, J. and Gotschlich, E. C. (1984) *J. Exp. Med.* **159**, 1351-1370.

3. Meyer, T. F., Billyard, E., Haas, R., Storzbach,

S. and So, M. (1984) *Proc. Natl. Acad. Sci. U.S.A.* **81**, 6110-6114.

4. Hagblom, P., Segal, E., Billyard, E. and So, M. (1985) *Nature* **315**, 146-158.

5. Parge, H. E., Bernstein, S. L., Deal, C. D., McRee, D. E., Christensen, D., Capozza, M. A., Kays, B. W., Fieser, T. M., Draper, D., So, M., Getzoff, E. D. and Tainer, J. A. (1990) *J. Biol. Chem.* **265**, 2278-2285.

6. Getzoff, E. D., Parge, H. E., McRee, D. E. and Tainer, J. A. (1988) *Reviews of Infectious Disease* **97**, 211-216.

7. Parge, H. E., McRee, D. E., Capozza, M. A., Bernstein, S. L., Getzoff, E. D. and Tainer, J. A. (1987) *J. of Microbiology* **53**, 447-453.

Crystal Structure of PhoE Porin

Thomas N. Earnest, Edward A. Berry, Li-shar Huang, and Bing K. Jap
Cell and Molecular Biology Division
Lawrence Berkeley Laboratory
University of California
Berkeley, CA 94720

ABSTRACT - We seek to determine the structure of PhoE porin, an integral membrane protein from the outer membrane of gram negative bacteria using x-ray crystallographic methods. Using the rotation camera on beam line 7-1 at SSRL we have so far collected a partial native data set which we plan to phase using the structure determined at medium resolution by electron crystallography of two-dimensional crystals.

The determination of the three dimensional structure of integral membrane proteins remains a difficult problem in light of the difficulty in obtaining large,well-ordered crystals of this important class of proteins.

Porins are integral membrane proteins which exist in the outer membrane of gram negative bacteria and exhibit a wide range of functions. PhoE porin is an anion channel which is selective for phosphate and is produced by *E. coli* under conditions of phosphate starvation. We have recently used electron crystallographic methods applied to two-dimensional crystals in DMPC to determine the structure of PhoE porin to approximately 3.4 Å. The inability to tilt the sample in the electron microscope beyond 60 degrees leads to an incomplete data set. This missing cone of data leads to a loss of resolution perpendicular to the plane of the membrane. Thus we have crystallized PhoE porin in three dimensions with the intent of a) collecting higher resolution data, and b) filling in the missing cone of data.

We have recently been able to grow large crystals of PhoE porin and begun subjecting them to x-ray crystallographic analysis. We have been unable to collect data to high resolution using a rotating anode x-ray source, thus we required synchrotron radiation in order to investigate these crystals adequately.

Two crystal forms have so far been obtained. By far the most predominant form are hexagonal plates which grow up to .6 mm in the largest dimension. These give x-ray diffraction patterns which suggest a hexagonal space group with unit cell dimensions of a=b=240 Å and c=158 Å. These crystals diffract to a resolution of approximately 3.2 Å. Another form, which grows in the morphology of rods with a hexagonal cross section diffract to a much higher resolution of approximately 2.0 Å, but they rarely occur and exhibit twinning and a great deal of mosaicity (as evidenced by the shape and size of the diffraction spots). Both forms exhibit rapid beam induced radiation damage.

Presently we are continuing to attempt to improve the crystallization conditions in order to grow larger, more well-ordered crystals which will hopefully lead to higher resolution data. We then plan to use our density map derived from electron microscopy and/or the model based on this map to provide phases for the x-ray diffraction data. This will allow for an higher resolution, isotropic electron density map to be calculated, and thus supply a more accurate determination of the atomic positions in PhoE porin. We also plan to use rapid freezing of the crystals in liquid ethane and the subsequent data collection at liquid nitrogen temperatures in order to decrease beam induced damage to the crystals.

SURVEY OF CRYSTALS FOR SYNCHROTRON DATA COLLECTION

David B. McKay
Stanford University

This report summarizes our work on surveying crystals for suitability of data collection at SSRL. Since the work was preliminary in nature and took only a few hours (significantly less than one 8-hour shift) of beam time, the report is commensurately brief.

The most exciting result we obtained was from crystals of catalytic hammerhead RNAs. The hammerhead RNAs we are working with are approximately 13 kDa in molecular weight. We have purified the necessary RNA and have grown several (at least four) crystal forms of these RNAs. During the past run at SSRL, during some "free" time slots, we took some small angle (0.1°) oscillation pictures of the different crystal forms to see whether they diffracted well enough to pursue; we cannot see adequate diffraction on our in-house facilities to pursue data collection on conventional facilities. Two of the crystal forms showed diffraction to approximately 3.5-3.2 Å. From small-angle oscillation pictures at two orientations separated by 90° in spindle rotation, we have made estimates of the unit cell parameters. One of the crystal forms has cell parameters of ~ 70 x 70 x 90 Å; the other has cell edges of ~ 90 x 90 x 200 Å. We should be able to collect data on these crystals at SSRL to an adequate resolution for a structure determination. We have several difficulties which make it uncertain precisely when we would have crystals for collecting full datasets: (i) the RNA is difficult to purify in milligram quantities, and the crystals are difficult to grow reproducibly to large size; (ii) the crystals seem to be temperature- and radiation-sensitive; we plan to put effort into trying to stabilize them by freezing or cooling. However, we are putting substantial effort into sorting out these difficulties at this time. We imagine that in the future, this project will proceed in three stages, all of which will require beam time at SSRL: (1) determination of space group of the crystals--this can be done with a precession camera, if available, probably during one 24-hour period; it is the type of thing that could be squeezed into 8-hour periods between other users, if necessary. (2) collecting native data; we do not have an accurate estimate for how much actual beam time this will take; from the time required for the oscillation photographs we took, we would estimate ~48 hours of beam time per dataset, but this could be off by a factor of two one direction or the other. Once the image plate is available, it is conceivable that we could take a partial dataset over an 8-hour period and process it, in order to see what sort of resolution and statistics we are getting. We could then judge accurately how much time would be required for complete data. (3) Once we have usable native datasets, we will collect three or four heavy atom derivative datasets for each of the two crystal forms.

Structure of the Envelope Glycoprotein from Tick-borne Encephalitis Virus (TBE)

Stephen C. Harrison
Harvard University

We have crystallized the external domain of the envelope glycoprotein from TBE. This protein is critical for viral antigenicity and viral infectivity. TBE is a medically important virus in central Europe, and it is closely related to viruses important worldwide (Yellow fever, Dengue, etc.). Understanding the detailed structure of this protein will be valuable for subunit vaccine design, for working out how the virus binds to its receptor, and for elucidating the mechanism by which the virus enters a cell. The only other viral glycoproteins whose structures are known are those from influenza virus. The TBE virus glycoprotein should therefore give significant additional information about the architecture of a class of proteins that includes retroviral envelope antigens such as HIV gp120. The data collected at SSRL, together with data collected at other synchrotron sources, should permit a full structure determination during 1992.

Evaluation/Data Collection of Cytochrome Reductase Crystals

Bing K. Jap, Li-shar Huang, Edward A. Berry, and Thomas N. Earnest

Cell and Molecular Biology Division
Lawrence Berkeley Laboratory
University of California
Berkeley, CA 94720

Summary- The rotation camera on beam line 7-1 was used to take x-ray diffraction patterns from crystals of a membrane protein, cytochrome reductase. The patterns showed the crystals to be ordered and suitable for x-ray structure analysis, but of limited resolution and very sensitive to radiation damage. The space group and unit cell parameters were obtained.

Introduction- Cytochrome reductase (E.C. 1.10.2.2), also known as the cytochrome bc_1 complex, ubiquinol:cytochrome c oxidoreductase, or Complex III, is the middle part of the mitochondrial respiratory chain. Reducing equivalents from various substrates get funnelled into the ubiquinone pool by NADH and succinate dehydrogenases. Cytochrome reductase oxidizes ubiquinol and reduces cytochrome c, using part of the energy released to translocate protons across the mitochondrial inner membrane. Cytochrome c is then oxidized by cytochrome oxidase at the expense of molecular oxygen, with further energy conservation in the proton gradient. Cytochrome reductase is thus vital for aerobic metabolism. Defects in the respiratory chain lead to mitochondrial myopathies such as Kearns-Sayre Syndrome.

Cytochrome reductase is a large membrane protein, with 11 subunits (for the beef enzyme) and a total molecular weight of 230 kDA. Recently we developed a procedure for growing crystals of cytochrome reductase. However, we were unable to demonstrate x-ray diffraction using a conventional rotating anode x-ray source. Because we suspected radiation damage and the low power of the conventional x-ray source were limiting, we applied for time at SSRL to measure diffraction with a synchrotron source.

Purpose- The original purpose was to see if the crystals diffract, and if so to what resolution and with what space group and unit cell parameters. Once this was achieved, the purpose was extended to testing different forms of crystals and some possible heavy atom derivatives.

Results-When tested with the high energy synchrotron radiation at 1.08 Å wavelength collimated to 0.2 mm, the cytochrome reductase crystals diffracted x-rays to a resolution of 5-6 Å, with some spots as high as 4.5 Å. From the diffraction the space group was determined to be $P6_122$ or $p6_522$. The unit cell parameters.were a=b=212 Å, c=352 Å.

The protein content of the crystals was determined from protein assay of crystals whose volume had been estimated from light micrographs. This indicated that the asymmetric unit contains a single monomer of the 11-subunit complex.

The crystals are very sensitive to radiation damage, with the moderate resolution spots visible only in the first exposure or two on any crystal.

Future plans- These results have been reported to the Journal of Molecular Biology (in press). They have also been used in an NIH grant application for support to improve the crystals and collect data. This grant has been funded for three years with a start date of March 1992. We are now working on improving the order of the crystals and on obtaining heavy atom derivatives.

Because of the large size of the protein and the large number of cysteine and other reactive residues, obtaining suitable heavy atom derivatives may be difficult. Our main effort is directed at synthesizing tightly binding inhibitors with heavy atoms incorporated in the inhibitors.

The order of the crystals at present is probably good enough to obtain a structure with 5-6 Å resolution. Although this is not high enough to locate atoms, larger details such as transmembranous helices may be discernable. In view of the fact that the best current structure for the enzyme is at the 20-25 Å resolution level, a 5-6 Å structure may be a worthwile intermediate step in out project. The ultimate goal, however, is an atomic structure, so we need to improve the crystalline order.

THE STRUCTURES OF HIV PROTEASE COMPLEXED WITH NON-PEPTIDE INHIBITORS AND THE CRYSTAL STRUCTURE OF COLICIN Ia

Partho Ghosh, Earl Rutenber, Eric Fauman, and Robert Stroud
University of California, San Francisco

HIV PROTEASE COMPLEXED WITH NON-PEPTIDE INHIBITORS

The protease of the Human Immunodeficiency Virus (HIV) is required for the expression of viral proteins and subsequent viral replication. We are attempting to design non-peptide inhibitors of the HIV protease, and we are relying on x-ray crystal structures of the protease complexed with potential inhibitors to guide our attempts. We have found that a derivative of haloperidol inhibits the protease with an IC_{50} of 10 μM and have solved the structure of the protease-inhibitor complex to 2.2 Å. Based on this structure, we have designed and synthesized many other derivatives of haloperidol.

Synchrotron radiation is necessary for these experiments since the co-crystals of protease and inhibitor are too small (less than 250 μm in length, only 50 μm in diameter) for data collection in the lab. From a previous experiment at SSRL, we have determined that these small co-crystals diffract to 1.96 Å, better resolution than observed in the lab with larger crystals.

To date we have collected two full data sets on HIV protease at SSRL. The first data set confirmed the presence of a halide counter-ion binding site which appears to be crucial for inhibitor binding. A chloride binding-site was initially suggested by a rotating-anode derived data set and was confirmed at the synchrotron with a co-crystal containing bromide (manuscript in preparation). The second data set was collected on HIV protease bound to a second haloperidol derivative with a promising inhibitory effect. We were able to collect 80% of the diffraction data to 2.0 Å from two small crystals, and refinement of this structure is currently in progress.

CRYSTAL STRUCTURE OF COLICIN Ia

Colicin Ia, a 70 kD bacterial protein, forms relatively non-selective, voltage-dependent ion channels in bacterial membranes. The molecule is synthesized and secreted as a cytoplasmic, soluble protein, but functions as a transmembrane protein. In order to understand the mechanism of conversion from soluble to transmembrane protein, we have crystallized the soluble form of the molecule. The soluble form may also have implications for the mechanism of action of ion channels.

Crystals of colicin Ia are extremely sensitive to radiation. They diffract to only 7.0 Å using a laboratory, rotating-anode source of X-rays, but diffract to 3.4 Å using a synchrotron source, making data collection at the synchrotron a necessity. Furthermore, the fact that the crystals have a large unit cell (a=66.0 Å, b=176.2 Å, c=290.2 Å) also makes the synchrotron requisite for data collection.

We have collected a full, native data set at SSRL and have within the last year collected four useful isomorphous derivatives. One of these is a mercury derivative of a site-directed mutant of colicin Ia with a unique cysteine. The other three are thallium, niobium, and platinum derivatives of the wild-type protein. The derivatives appear to have sufficient phasing power to allow the solution of the structure. Initial multiple isomorphous derivative maps appear promising and confirm a low resolution electron micrographic structure of the protein (manuscript in preparation). We are currently building into the solvent-flattened, multiple isomorphous derivative map.

VII ACTIVE PROPOSALS

SSRL accepts a variety of proposal types. These include a) full peer-reviewed proposals, b) letters of intent, c) rapid turn-around EXAFS proposals and d) rotation camera proposals for protein crystallography. Beam time is also given by the Participating Research Teams on their beam lines based on application to the PRT. As of January 1, 1992 there were 146 active proposals; 103 peer-reviewed, 3 Rapid Turn-Around EXAFS, 25 Imaging Plate, 11 Letters of Intent and 4 active PRTs. The letter suffix appended to the proposal number indicates the sub-panel of the Proposal Review Panel to which the proposal is assigned: Materials (M), Biology (B) or Vacuum Ultra-Violet (V). The small p denotes a program proposal. The date is the original date of receipt. Peer-reviewed single project proposals remain active for two years after their initial rating, while program proposals can be renewed for an additional two years. Many proposals have received extensions in the last few years due to the limited availability of beam time at SSRL

943Vp	9/06/84	**Electron Spectroscopy of Gases, Solids, and Surfaces**
		David A. Shirley Philip A Heimann Zheng-Qing Huang Tony Huff Zahid Hussain Laura Medhurst Eddie Moler Li-Quing Wang Alexis Schach V Wittenau (LAWRENCE BERKELEY LABORATORY)
1021Mp	3/03/86	**Synchrotron X-ray Polycrystalline Diffractometry**
		George Castro Maurizio Bellotto Curt Erickson Michael Hart Ting C Huang George Will (IBM RESEARCH LABORATORY)
1046Bp	9/03/86	**Iodine Dichromography with Monochromatic X-ray Beams for Angiography**
		Edward Rubenstein George S Brown Donald C Harrison Robert Kernoff John Otis W Thomlinson Albert C Thompson Herbert D Zeman (STANFORD UNIVERSITY)

1048Mp	9/11/86	**High Resolution Compton Profiles of Iron and Silicon**	
		Caroline Stahle Sean Brennan Douglas Osheroff (NASA/GODDARD SPACE FLIGHT CENTER)	
1066Mp	3/01/87	**X-Ray Spectroscopy of Electrochemically Generated Species**	
		Richard C Elder William R Heineman (UNIVERSITY OF CINCINNATI)	
1067Bp	3/01/87	**Active Site Structures of Cytochrome *c* Oxidase**	
		Robert A Scott Mitchell C Brenner Sunney I Chan Robert Kertayasa (UNIVERSITY OF GEORGIA)	
1080Vp	3/01/87	**Adsorption Structure of Heteroatom-Containing Molecules on Transition Metal Surfaces**	
		Robert J Madix B Factor C M Friend A C Liu J T Roberts J Solomon (STANFORD UNIVERSITY)	
1084Bp	3/01/87	**Polarized X-Ray Spectroscopy of the Oriented Chloroplast Water-Oxidizing Complex**	
		Graham N George Stephen P Cramer Roger C Prince (EXXON RESEARCH & ENGINEERING)	
1085Bp	3/01/87	**X-Ray Absorption Spectroscopic Characterization of the Manganese in Biological Systems**	
		James E Penner-Hahn W D Frasch D Ghanotakis J T Groves V L Pecoraro M Stern Him-Tai Tsang C F Yocum (UNIVERSITY OF MICHIGAN)	
88M	3/01/87	**Polarized X-Ray Absorption Near Edge Structure**	
		James E Penner-Hahn Geoffrey Waldo Shengke Wang Glenn A Waychunas (UNIVERSITY OF MICHIGAN)	

1093Mp	8/07/87	**Structure of Superconducting Thin Films** Stephen Laderman Malcolm Beasley Alice Fischer-Colbrie Theodore H Geballe R D Jacowitz Aharon Kapitulnik J Moll R Smith (HEWLETT PACKARD LABORATORIES)
1095Mp	8/07/87	**EXAFS and NEXAFS Investigation of OMPVE Growth of II-VI Compounds** Paul H Fuoss Sean Brennan D W Kisker (AT&T BELL LABORATORIES)
1096Mp	8/20/87	***In-Situ* X-Ray Scattering Studies of OMVPE Growth of II-VI Compounds** Paul H Fuoss Sean Brennan J Kahn D W Kisker (AT&T BELL LABORATORIES)
1097Mp	8/20/87	**Anti-Site Disorder in High T_c Superconductors** Farrel W Lytle Robert B Greegor (BOEING COMPANY)
2010Bp	9/17/87	**X-Ray Spectroscopy Of Manganese And Iron In Chloroplasts** Melvin P Klein Melissa Grush Matthew Latimer Wenchan Liang Vittal K Yachandra J L Zimmerman (LAWRENCE BERKELEY LABORATORY)
2023Mp	9/21/87	**High T_c Superconducting Materials: Their Structural and Electronic Characterization by XAS** Steve D Conradson Zachary Fisk Ian D Raistrick Antonio Redondo (LOS ALAMOS NATIONAL LABORATORY)
2029Bp	9/29/87	**Mo and Se XAS Studies of Small-Molecule Binding to Nitrogenas** Keith O Hodgson Barbara K Burgess Britt Hedman C Stanfel (SSRL)

2030Bp 9/29/87 **XAS Structural Characterization of the Binuclear Iron-Center in Methane Monooxygenase**

Keith O Hodgson
Jane Dewitt
Britt Hedman
Stephen J Lippard
Amy Rosenzweig
(SSRL)

2031Bp 9/29/87 **X-Ray Absorption Studies of Coupled Binuclear Copper Sites in Proteins**

Keith O Hodgson
Britt Hedman
Kent Nakagawa
Edward I Solomon
Grace Tan
(SSRL)

2032Bp 9/29/87 **Xas Studies Of Heme-Iron Enzymes: Cytochrome P-450 And Peroxidases**

Keith O Hodgson
John H Dawson
Britt Hedman
Masanori Sono
(SSRL)

2033Mp 9/29/87 **Sulfur K Edge XAS Studies of Photographic Sensitizing Centers**

Teresa A Smith
Britt Hedman
Keith O Hodgson
(EASTMAN KODAK COMPANY)

2044Mp 11/05/87 **Direct Scattering Studies of Surface Premelting**

J Kahn
Arthur Bienenstock
Sean Brennan
Paul H Fuoss
Frank Lamelas
Laura Norton
(STANFORD UNIVERSITY)

2055M 3/15/88 **Shallow and Deep Donors in $Ga_{1-x}Al_xAs$ Semiconducting Alloys**

T M Hayes
P Gibart
D L Williamson
(RENSSELAER POLYTECHNIC INSTITUTE)

2074Vp 9/13/88 **Electronic And Geometric Properties Of Impurities On/In Carbon**

Brad Pate
Ingolf Lindau
William E Spicer
J Wu
(WASHINGTON STATE UNIVERSITY)

2076Mp	9/13/88	**Investigation of Short Range Order in Mineralogical Solid Solutions** Glenn A Waychunas Wayne A Dollase Richard J Reeder Charles R Ross (STANFORD UNIVERSITY)
2077M	2/01/89	**SEXAFS and Surface X-Ray Diffraction Study of Self-Assembled Monolayers on Gold Surfaces** M Samant Gary Borges Charles A Brown Joseph G Gordon (IBM RESEARCH LABORATORY)
2079Bp	3/01/89	**XAS Structural Characterization of the Active Center in the *Rhodospirillum rubrum* Carbon Monooxide Dehydrogenase Enzyme** Keith O Hodgson Scott Ensign Britt Hedman Paul W Ludden Marie-Claire Mckenna Philip J Stephens (SSRL)
2091Mp	3/15/89	**Strain Mapping and Crystal Characterization Using Synchrotron Radiation Polychromatic Topography** S R Stock Y H Chung T S Gross A B Lee J D Plummer Zophia U Rek (GEORGIA INSTITUTE OF TECHNOLOGY)
2097B	9/10/89	**Structural Investigation of Terbium Chelates in Aqueous Solution by X-Ray Absorption Spectroscopy** John E Kuo Cong-Yuan Guo (UNIVERSITY OF MISSOURI)
2098B	9/10/89	**Mo K and L Edge Spectroscopy of Cyandie Inhibited Sulfite Oxidase and Model Compounds** J H Enemark M D Carducci Stephen P Cramer (UNIVERSITY OF ARIZONA)

2099M	9/10/89	**Study of Framework Demetallation of COAPO and FAPO Molecular Sieves by X-Ray Absorption Spectroscopy, X-Ray Diffraction and Diffuse Reflectance Spectroscopy** Guang Zhang Gary S Mondo (CHEVRON RESEARCH COMPANY)
2100Mp	9/10/89	**X-Ray Absorption Investigation of Metal Binging Sites in Crude Oil and Petroleum Products** Guang Zhang Gary S Mondo (CHEVRON RESEARCH COMPANY)
2101B	9/10/89	**Structural Studies of the Blue Form of The Purple Membranes** Sebastian Doniach D Eliezer N Gillis Keith O Hodgson S Wakatsuki (STANFORD UNIVERSITY)
2102B	9/10/89	**Anomalous Dispersion Scattering Studies of Metal Clusters in Biological Systems** Keith O Hodgson Sebastian Doniach D Eliezer N Gillis S Wakatsuki (SSRL)
2103Vp	9/10/89	**Photoemission Study of High T_c Superconductors and Related Materials** Z X Shen Ingolf Lindau William E Spicer (STANFORD UNIVERSITY)
2104Bp	9/10/89	**XAS Structural Characterization of Vanadium Bromoperoxidase** Ulrich Kuesthardt Britt Hedman Keith O Hodgson Hans Vilter (TÜ MUNCHEN)
2105Mp	9/19/89	**Damage and Crack Closure in Composite and Monolithic Materials** S R Stock S D Antolovich T M Breunig Zophia U Rek (GEORGIA INSTITUTE OF TECHNOLOGY)

2106B	9/19/89	**Measurement of Nitrogenase Multiwavelength Anomalous Diffraction Data** Jeffrey T Bolin Nino Campobasso Wladek Minor R Paul Phizackerley (PURDUE UNIVERSITY)
2107M	9/28/89	***In-Situ* EXAFS Transition Metal Macrocycles Adsorbed on Electrode Surface** Daniel A Scherson Philip N Ross (CASE WESTERN RESERVE UNIVERSITY)
2108B	3/01/90	**X-ray Tomographic Microscopy of Human Dentin** John H Kinney Ulrich Bonse Greyson W Marshall Sally J Marshall Monte Nichols (LAWRENCE LIVERMORE NATIONAL LABORATORY)
2109M	3/01/90	**Structural Investigation of Metal Contaminants in Fluid Catalytic Cracking Catalysts using X-ray Absorption Spectroscopy** Guang Zhang Gary S Mondo (CHEVRON RESEARCH COMPANY)
2110B	3/01/90	**XAS Structural Characterization of a Novel Molybdenum Site in 2-Hydroxycarboxylate Viologen Oxidoreductase** Ulrich Kuesthardt Britt Hedman Keith O Hodgson (TÜ MUNCHEN)
2111Vp	3/01/90	**Structural Studies of Thiols and Alcohols on Mo and Rh Surfaces** C M Friend Joachim Stohr Benjamin C Wiegand Xueping Xu (HARVARD UNIVERSITY)
2112M	3/01/90	**Development of an 8 keV Synchrotron Microscope** Richard M Bionta Ken Skulina (LAWRENCE LIVERMORE NATIONAL LABORATORY)
2113B	3/01/90	**Static Structures of Associating Polymers via Small Angle X-ray Scattering** Alice P Gast Cathy Cogan Robert Ju Jenni Raeder (STANFORD UNIVERSITY)

2114Bp	3/01/90	**Structural Interactions in Respiratory Proteins** James O Alben Craig F Hemann John Hill Kimerly A Powell Jianhong Pu Zhouhong Shi (OHIO STATE UNIVERSITY)
2115Mp	3/21/90	***In-Situ* Determination of Surface and Interface Structure of Sputter Deposited Films** Bruce M Clemens Sean Brennan (STANFORD UNIVERSITY)
2116M	3/21/90	**Solution Structures of Lanthanide-CMPO Complexes in Organic Solvents by SAXS and ASAXS Techniques** P Thiyagarajan H Diamond J E Epperson Keith O Hodgson E P Horwitz (ARGONNE NATIONAL LABORATORY)
2117Bp	3/21/90	**Kinetic Intermediates on the Pathway of Protein Folding: SAXS Studies** Keith O Hodgson R L Baldwin Sebastian Doniach D Eliezer A Robertson (SSRL)
2118Mp	3/21/90	**Anomalous X-ray Diffraction Studies of Crystal Structure and Valence Ordering** George Kwei Joyce A Goldstone Jon M Lawrence Andrew C Lawson Robert B Von Dreele (LOS ALAMOS NATIONAL LABORATORY)
2119M	8/11/90	**EXAFS Investigations of Metal Multilayers** Geraldine M Lamble Bruce M Clemens Steve M Heald (BROOKHAVEN NATIONAL LABORATORY)

2120M	8/28/90	**Local Atomic Structure of High T_c Superconductors** Frank Bridges James B Boyce Tord Claeson Theodore H Geballe Guoguang Li (UNIVERSITY OF CALIFORNIA)
2121Vp	8/28/90	**Spin Polarized Photoemission Studies of Magnetic Surfaces and Ultra-Thin Films** Herbert Hopster C R Brundle D E Fowler A C Luntz D P Pappas Z X Shen (UNIVERSITY OF CALIFORNIA)
2123Vp	9/04/90	**Growth, Structure & Electrical Properties of Large Bandgap Materials** Don Kania Lawrence Pan Brad Pate Piero Pianetta (LAWRENCE LIVERMORE NATIONAL LABORATORY)
2124M	9/04/90	**Structural and Charge-transfer High Pressure Transitions in Perrhenates** Robert L Ingalls Daryl Crozier L Huang (UNIVERSITY OF WASHINGTON)
2125M	9/05/90	**Determination of the Strain Distribution in Aluminum Thin Films Using GIXS** John C Bravman Sean Brennan (STANFORD UNIVERSITY)
2126M	9/05/90	**X-ray Absorption Studies of Perovskites as a Function of Pressure** Robert L Ingalls B Houser (UNIVERSITY OF WASHINGTON)
2127V	9/10/90	**Heteroepitaxial Interface Formation Between Insulators and Metals** Marjorie Olmstead Jonathan Denlinger Eli Rotenberg Gerard Wong (UNIVERSITY OF WASHINGTON)
2128Bp	9/11/90	**Technetium and Rhenium Imaging Agents and Therapeutic Radiopharmaceuticals** Richard C Elder Edward A Deutsch (UNIVERSITY OF CINCINNATI)

2129Bp	9/14/90	**Synchrotron Radiation Detector Development Program** William K Warburton J S Iwanczyk S R Russell (X-RAY INSTRUMENTATION ASSOCIATES)
2130V	9/14/90	**The Role of Fluorine in Fluoride/Silicon Interface Formation** Marjorie Olmstead Jonathan Denlinger Eli Rotenberg Gerard Wong (UNIVERSITY OF WASHINGTON)
2131M	9/17/90	**Off-center Displacement of Cu^+ in KCl** Frank Bridges James B Boyce Guoguang Li Xun Wang (UNIVERSITY OF CALIFORNIA)
2132M	9/17/90	**"Glitch" Formation in XAFS Spectra** Frank Bridges James B Boyce Guoguang Li Xun Wang (UNIVERSITY OF CALIFORNIA)
2133Mp	9/19/90	**Determination of Local Epitaxy and Strain in Sputter-Deposited Films** Bruce M Clemens Sean Brennan (STANFORD UNIVERSITY)
2134V	4/11/91	**Determination of the Ellipsoidal Polarization Parameters of VUV Radiation** S V Bobashev O S Vasyutinskii (A F IOFFE INSTITUTE)
2135Mp	2/06/91	**Structure/Activity Relationships in the Vanadium-Phosphorous-Oxide System** Robert M Friedman Farrel W Lytle Michael Thompson (MONSANTO COMPANY)
2136Mp	2/06/91	**Investigation of the Structure and Chemistry of Surface Layers for Corrosion Protection** Robert B Greegor Farrel W Lytle (BOEING COMPANY)

2137Bp	2/18/91	**X-ray Absorption Spectroscopic Studies of Nickel-Containing Metalloenzymes** Robert A Scott Mitchell C Brenner Li Ma (UNIVERSITY OF GEORGIA)
2138Mp	2/27/91	**Local Atomic Structure of High-T_c Superconductors** James B Boyce Frank Bridges Tord Claeson Theodore H Geballe (XEROX)
2139Mp	2/25/91	**Chemical Vapor Infiltration of Ceramic Matrix Composites** John H Kinney C A Lundgren Monte Nichols T L Starr S R Stock (LAWRENCE LIVERMORE NATIONAL LABORATORY)
2140Mp	2/28/91	**X-ray Diffraction Studies on AX_2 Compounds: Example BeH_2** J Akella L C Ming G S Smith S T Weir (LAWRENCE LIVERMORE NATIONAL LABORATORY)
2141M	3/01/91	**High Pressure Transition Mechanisms in Iron Via EXAFS** Robert L Ingalls Daryl Crozier Fuming Wang (UNIVERSITY OF WASHINGTON)
2142Mp	3/04/91	**Anomalous Scattering of X-rays** David H Templeton L K Templeton (LAWRENCE BERKELEY LABORATORY)
2143Mp	3/12/91	**XAS Study of Cation Chemisorption at Oxide-Water Interfaces** Gordon E Brown John R Bargar Singfoong Cheah Farrel W Lytle P O'day George A Parks Per Persson Steve Towle N Xu (STANFORD UNIVERSITY)

2144M	3/02/91	**X-ray Absorption Study of Metal Ion Reactions at Semiconductor Surfaces** N S Lewis (CALIFORNIA INSTITUTE OF TECHNOLOGY)
2145Vp	3/02/91	**Photoelectron Spectroscopic Studies of Inorganic Materials as Active Sites in Catalysis** Edward I Solomon Jeff Guckert Paul Jones J A May (STANFORD UNIVERSITY)
2146Bp	3/14/91	**XAS K-Edge Studies of Ligands Bound to Open-Shell Metal Ions in Proteins and Model Compounds** Keith O Hodgson Bittt Hedman Susan Shadle Edward I Solomon (SSRL)
2147M	3/14/91	**Small Angle X-ray Scattering Studies of Microvoids in Amorphous Semiconductors** D L Williamson Yan Chen Richard Crandall G David Mooney (COLORADO SCHOOL OF MINES)
2148Bp	3/15/91	**Structure↔Function Studies of the Intrinsic Metal Sites in RNA Polymerase from *E. coli*** Linda S Powers G L Eichhorn Robert Sinclair (UTAH STATE UNIVERSITY)
2149Bp	3/15/91	**Structure↔Function Studies of the Active Sites of Lignin Peroxidase, Peroxidases, and Models** Linda S Powers Robert Sinclair (UTAH STATE UNIVERSITY)
2150B	3/15/91	**X-Ray Absorption Studies of the Structure of Cytochrome-c Oxidase** James E Penner-Hahn Kimber Clark Timothy Dawes Olof Einarsdottir Katy Georgiadis Pamela Riggs Timothy Stemmler (UNIVERSITY OF MICHIGAN)

2151Bp 3/15/91 **Structural Characterization of Mercury Metalloproteins Using XAS**

James E Penner-Hahn
Kimber Clark
Susan Miller
Thomas V O'halloran
Pamela Riggs
Timothy Stemmler
(UNIVERSITY OF MICHIGAN)

2152Mp 3/15/91 **XAS Study of Metal Ion Partitioning at Water/Mineral Interfaces**

Kim F Hayes
Lynn E Katz
James E Penner-Hahn
(UNIVERSITY OF MICHIGAN)

2153Mp 3/15/91 **Composition Fluctuations in Amorphous Films**

Michael Regan
Arthur Bienenstock
(STANFORD UNIVERSITY)

2154V 3/15/91 **Photoelectron Microscopy**

Piero Pianetta
Changyoung Kim
Paul King
Ingolf Lindau
(SSRL)

2155M 3/15/91 **EXAFS Study of Cordierite Crystallization in Presence of Bi_2O_3 Flux**

Gordon E Brown
K B Schwartz
Glenn A Waychunas
(STANFORD UNIVERSITY)

2156Vp 3/15/91 **Passivation of GaAs and InP by Sb Interlayers**

Tom Kendelewicz
Al Green
Alberto Herrera
William E Spicer
Masao Yamada
(STANFORD UNIVERSITY)

2157M 3/15/91 **Structural Characterization of Ferrihydrite Surface Sites, Structure, and Absorbate Geometries**

Glenn A Waychunas
James A Davis
Christopher C Fuller
Brigid A Rea
(STANFORD UNIVERSITY)

2158M	3/15/91	**Structures for Silver(I)-Crown Complexes in Liquid and Solid Phases** Nolan Mangelson Robert B Greegor Max W Hill Farrel W Lytle Lawrence B Rees (BRIGHAM YOUNG UNIVERSITY)
2159Bp	4/11/91	**Kinetic Structural Studies of Isocitrate Dehydrogenase Using Laue Crystallography** Barry Stoddard Daniel Koshland Michael Soltis (UNIVERSITY OF CALIFORNIA)
2160B	7/12/91	**Multiwavelength X-ray Analysis of Gene V Protein Crystals Containing Selenomethionine** Thomas C Terwilliger Henry Bellamy R Paul Phizackerley Andrew Wang Hong Zhang (LOS ALAMOS NATIONAL LABORATORY)
2161B	8/29/91	**Structural Studies of the *E. coli* Single Strand Binding Protein** David Ollis John J Barton Nicholas Dixon Jennifer Thorn (THE AUSTRALIAN NATIONAL UNIVERSITY)
2162Bp	8/30/91	**Kinetic X-Ray Crystallography of Carbonmonoxy Myoglobin** Joel Berendzen Kelvin Chu Gregory Petsko Dagmar Ringe Ilme Schlichting (LOS ALAMOS NATIONAL LABORATORY)
2163Mp	9/04/91	**The Effect of Dilute Impurities on Bulk Melting** E A Stern Matthew Newville Bruce Ravel (UNIVERSITY OF WASHINGTON)
2164M	9/04/91	**EXAFS Studies of Deformed Ionomers** B P Grady Stuart L Cooper R J Goddard (UNIVERSITY OF WISCONSIN)

2165Mp 9/10/91 **Ultra-High Strength-High Temperature Surface Coatings**

John C Bilello
Zofia Rek
Jun Tao
Mark Vill
Steve Yalisove
Zhen Zeng
(UNIVERSITY OF MICHIGAN)

2166Vp 9/16/91 **Calibration of M.S.S.T.A. Instruments**

Maxwell Allen
Troy W Barbee, Jr.
Craig De Forest
Richard Hoover
Charles Kankelborg
Joakim F Lindblom
Ray O'neal
Arthur Bc Walker
Thomas Willis
(STANFORD UNIVERSITY)

2167B 9/13/91 **Laue Studies of *Rb. Sphaeroides* Photosynthetic Reaction Center**

Douglas C Rees
Art Chirino
George Feher
R Paul Phizackerley
Michael Soltis
(CALIFORNIA INSTITUTE OF TECHNOLOGY)

2168Mp 9/16/91 **Environmental and Energy-Related Science at LANL**

Steve D Conradson
(LOS ALAMOS NATIONAL LABORATORY)

2169Vp 9/16/91 **X-Ray Standing Wave Studies of Adsorption Geometries at Selected Metal III-V Semiconductor Interfaces**

Tom Kendelewicz
Piero Pianetta
William E Spicer
Joe Woicik
(STANFORD UNIVERSITY)

2170Mp 9/16/91 **X-Ray Absorption Spectroscopy of Transformation-Toughend Zirconia Ceramics**

James E Penner-Hahn
I-Wei Chen
Ping Li
(UNIVERSITY OF MICHIGAN)

2171M 9/16/91 **X-Ray Scattering Studies of Epitaxial Calcium Fluoride on Silicon**

C A Lucas
Jeffrey B Kortright
D Loretto
I M Tidswell
Gerard Wong
(LAWRENCE BERKELEY LABORATORY)

2172M 9/18/91 **Interlayer Forces Between Tethered Chains**

Alice P Gast
Mark Fair
(STANFORD UNIVERSITY)

THE ROTATION CAMERA PROPOSALS

2A11B	9/14/90	**Crystal Structure of PhoE Porin** Thomas Earnest Ed Berry Bing Jap (LAWRENCE BERKELEY LABORATORY)
2A13B	2/18/91	**α_2-Macroglobulin Complexes Suitable for Crystallographic Studies Using Synchrotron Radiation** Soren S Thirup Morten Kjeldgaard Gregers Rom Andersen Soren Bogestrand (AARHUS UNIVERSITY)
2A14B	3/01/91	**Structural Studies of *E. coli* DNA Topoisomerase I** Alfonso Mondragon Christopher Lima (NORTHWESTERN UNIVERSITY)
2A15B	3/01/91	**Structural Studies of *E. coli* Strand Binding Protein** David Ollis John Barton Nicholas Dixon Jennifer Thorn (THE AUSTRALIAN NATIONAL UNIVERSITY)
2A16B	4/23/91	**Structure Determination of Various Viruses** Michael G Rossmann Mavis Agbandje Jodi Bibler Michael S Chapman Ho[illegible]-Kin Choi Vi[illegible]ent L Ciranda Leodevico L Ilag Walter Keller (PURDUE UNIVERSITY)
2A18B	4/22/91	**Summary of Pt-pseudoazurin Experiment** Ethan A Merritt (UNIVERSITY OF WASHINGTON)
2A19B	4/22/91	**Summary of Human Recombinant Factor XIII Experiment** Ethan A Merritt (UNIVERSITY OF WASHINGTON)
2A20B	4/22/91	**Summary of *D. Gigas* Hydrogenase Experiment for Rotation Camera** Ethan A Merritt (UNIVERSITY OF WASHINGTON)

2A21B	4/25/91	**Data Collection from Radiative Sensitive Fc Receptor Crystals** Pamela Bjorkman (CALIFORNIA INSTITUTE OF TECHNOLOGY)
2A22B	6/01/91	**Feasiblity Study for 15-Liopxygenase Structural Studies** Michelle Browner (UNIVERSITY OF CALIFORNIA)
2A23B	6/01/91	**X-Ray Diffraction Studies of Macrophage Colony Stimulating Factor** Jay Pandit (UNIVERSITY OF CALIFORNIA)
2A24B	5/06/91	**HMG CoA Reductase Study** Marjorie Wilke (UNIVERSITY OF TEXAS)
2A25B	6/28/91	**Survey of Crystals for Synchrotron Data Collection** David Mc Kay (STANFORD UNIVERSITY)
2A26B	7/09/91	**Crystal Data Collection** Stephen C Harrison (HARVARD UNIVERSITY)
2A27B	7/15/91	**Evaluation/Data Collection of Cytochrome Reductase Crystals** Bing Jap (LAWRENCE BERKELEY LABORATORY)
2A28B	9/12/91	**Proposal to Collect High Resolution Data on Human and Yeast Superoxide Dismutase** Hans E Parge Elizabeth D Getzoff C F Kuo Duncan E Mcree S Mylvaganam John A Tainer (RESEARCH INSTITUTE OF SCRIPPS CLINIC)
2A29B	9/12/91	**Proposal to Collect and Screen Heavy Atom Data on Pilin** Hans E Parge Elizabeth D Getzoff C F Kuo Duncan E Mcree S Mylvaganam John A Tainer (RESEARCH INSTITUTE OF SCRIPPS CLINIC)
2A30B	10/14/91	**110 K Structure of Alpha-Lytic Protease** Stephen Rader (UNIVERSITY OF CALIFORNIA)

2A31B	9/20/91	**Structural Studies of TMEV, HAV and Flu NA** Ming Luo M N Janakiraman Ken Toth Jun Tsao Clint White Carl Zhang Lan Zhou (UNIVERSITY OF ALABAMA)
2A32B	10/11/91	**RNA Crystals** C D Stout H Lauble (RESEARCH INSTITUTE OF SCRIPPS CLINIC)
2A33B	10/24/91	**Structure of Yeast RNA Polymerase II** Aled Edwards Peter David Roger Kornberg (STANFORD UNIVERSITY)
2A34B	10/25/91	**X-Ray Structures of Antibody-Antigen Complexes and Receptors** Ian Wilson Jairo Arevalo Ping Chen Robyn Stanfield Enrico Stura (RESEARCH INSTITUTE OF SCRIPPS CLINIC)
2A35B	10/25/91	**The Crystal Structure of Colicin Ia and The Structures of HIV Protease Complexed with Non-Peptide Inhibitors** Partho Ghosh V. Ramalingam Earl Ruttenber Robert M Stroud Michael Wiener (UNIVERSITY OF CALIFORNIA)
2A36B	11/01/91	**Oscillation Data Collection of *E. coli* β-galactosidase Crystals** Brian W Matthews Enoch Baldwin Rick Faber Ray Jacobson (UNIVERSITY OF OREGON)
2A38B	10/01/92	**Crystal Structure Analysis of the Hydroxylase Component of Methane Monooxygenase** Stephen J Lippard Christine Fredericks Amy Rosenzweig (MASSACHUSETTS INSTITUTE OF TECHNOLOGY)

9050	1/01/91	**The Local Microscopic Structure of Oxygen Perovskite Systems Undergoing Structural and Superconducting Phase Transitions** E A Stern (UNIVERSITY OF WASHINGTON)
9051	1/01/91	**Critical Behaviour of the Structure Correlation Function of Perovskite Crystals in the Bulk and on the Surface** E A Stern (UNIVERSITY OF WASHINGTON)
9054	8/20/91	**Detector Test** Joseph G Gordon (IBM RESEARCH LABORATORY)
9055	9/03/91	**Protein Crystal Data Collection** Robert Glaeser (LAWRENCE BERKELEY LABORATORY)
9056V	9/09/91	**The Mechanism of Inactivation of Glyceraldehyde 3-Phosphate Dehydrogenase by Hydrogen Perioxide *in vitro*** Linda S Powers (UTAH STATE UNIVERSITY)
9057V	11/11/91	**Doped Fullerene Molecules** Z X Shen (STANFORD UNIVERSITY)
9058	11/18/91	**Characterization and Modification of Dentin** Sally J Marshall John H Kinney Greyson W Marshall (UNIVERSITY OF CALIFORNIA)
9059M	11/18/91	**Examination of Amorphous-Carbon Thin Films with Synchrotron Radiation** Michael A Capano (US AIR FORCE)
9060	5/01/91	**X-ray Tomographic Microscopy of the Conductive Anodic Filament Corrosion Mechanism in Printed Wiring Boards** S R Stock (GEORGIA INSTITUTE OF TECHNOLOGY)
9062M	12/03/91	**Determination of Conformational Properties of Proteins of Random Amino Acid Sequence** David Baker (UNIVERSITY OF CALIFORNIA)
9063	9/23/91	**Olivine-spinel Transition in $(Mg,Fe)_2Si0_4$** L C Ming (UNIVERSITY OF HAWAII)

RAPID TURN-AROUND EXAFS PROPOSALS

1E07B	11/13/91	**Europium Valence in $EuCo_{2-x}Ni_xP_2$ and $EuNi_{2-x}Cu_xP_2$: an L_{III}-edge X-ray Absorption Spectroscopy (L_{III}-XAS) Study** Robert M Bomick George Kwei Angelica M Stacy (UNIVERSITY OF CALIFORNIA)
1E08B	11/18/91	**Lanthanum Copper Oxides** Sarah L Stoll George Kwei Angelica M Stacy (UNIVERSITY OF CALIFORNIA)
1E09B	12/18/91	**Fluorescence EXAFS Study of Heavily-Doped III-V and II-VI Compound Semi-Conductors** Kin Man Yu J Jaklevic Carolyn Rossington Wladyslaw Walukiewicz (LAWRENCE BERKELEY LABORATORY)

PRT PROPOSALS

The spokesperson only is listed on the PRT proposals.

9500	01/01/91	**EXXON PRT Time - BL 6** Graham N George (EXXON RESEARCH & ENGINEERING)
9600	9/01/88	**Lawrence Berkeley Laboratory PRT Time - BL 6** Philip N Ross (LAWRENCE BERKELEY LABORATORY)
9700	9/01/88	**SEL PRT Time - BL 5** William E Spicer (STANFORD UNIVERSITY)
9900	1/01/85	**National Labs/University of California PRT Time - BLs 8 & 10** Marvin J Weber (LAWRENCE LIVERMORE NATIONAL LABORATORY)

VIII SSRL EXPERIMENTERS AND PROPOSALS BY INSTITUTION

As of January 1, 1992 there were 389 experimenters from 81 institutions officially listed on active proposals at SSRL. In addition, well over 100 others (graduate students, etc.) participated in work at the laboratory in collaboration with these scientists. The 65 United States institutions included 36 universities, 14 corporations and 15 government laboratories.

U.S. CORPORATIONS

AT&T Bell Laboratories, Boeing Company, Chevron Research Company, Dana Farber Cancer Institute, E.I. Du Pont de Nemours & Company, Eastman Kodak Company, EXXON Research & Engineering, Hewlett Packard Laboratories, IBM Research Laboratory, Monsanto Company, Raychem Corporation, X-Ray Instrumentation Associates, XEROX, XSIRIUS, Inc.

U.S. LABORATORIES

Argonne National Laboratory, Brookhaven National Laboratory, Lawrence Berkeley Laboratory, Lawrence Livermore National Laboratory, Los Alamos National Laboratory, NASA/Marshall Space Flight Center, NASA/Goddard Space Flight Center, National Institutes of Health, National Institute of Standards and Technology, Pacific Northwest Laboratory, Sandia National Laboratories, Solar Energy Research Institute, Stanford Synchrotron Radiation Laboratory, US Air Force, US Geological Survey Water Resources Division

U.S. UNIVERSITIES

Brandeis University, Brigham Young University, California Institute of Technology, Case Western Reserve University, Colorado School of Mines, Eastern Washington University, Georgia Institute of Technology, Harvard University, Massachusetts Institute of Technology, Northwestern University, Ohio State University, Princeton University, Purdue University, Rensselaer Polytechnic Institute, Research Institute of Scripps Clinic, Stanford University, State University-New York, University of Alabama, University of Arizona, University of California, University of Cincinnati, University of Georgia, University of Hawaii, University of Illinois, University of Michigan, University of Missouri, University of New Hampshire, University of Oregon, University of South Carolina, University of Southern California, University of Tennessee, University of Texas, University of Washington, University of Wisconsin, Utah State University, Washington State University

FOREIGN INSTITUTIONS

A F Ioffe Institute *(Russia)*, Aarhus University *(Denmark)*, The Australian National University *(Australia)*, Chalmers Institute of Technology *(Sweden)*, CNRS *(France)*, Fudan University *(Peoples Republic of China)*, Max Planck Insitute *(Germany)*, Max Laboratory *(Sweden)*, Simon Fraser University *(Canada)*, The University Manchester *(England)*, TU München *(Germany)*, Universita di Brescia *(Italy)*, Universitat Bayreuth *(Germany)*, Universitat Bonn *(Germany)*, Universitat Dortmund *(Germany)*, University of Oxford *(England)*

AMERICAN CORPORATIONS

AT&T BELL LABORATORIES

Paul H Fuoss	1095, 1096, 2044
Frank Lamelas	2044
Laura Norton	2044

BOEING COMPANY

Robert B Greegor	1097, 2136, 2158
Farrel W Lytle	1097, 2135, 2136, 2143, 2158

CHEVRON RESEARCH COMPANY

Gary S Mondo	2099, 2100, 2109
Guang Zhang	2099, 2100, 2109

DANA FARBER CANCER INSTITUTE

Christine Fredericks	2A38

E.I. DU PONT DE NEMOURS & CO.

C A Lundgren	2139

EASTMAN KODAK COMPANY

Teresa A Smith	2033

EXXON RESEARCH & ENGINEERING

Graham N George	1084, 9500
Roger C Prince	1084
Grayson H Via	9500

HEWLETT PACKARD LABORATORIES

Alice Fischer-Colbrie	1093
R D Jacowitz	1093
Stephen Laderman	1093
J Moll	1093
R Smith	1093

IBM RESEARCH LABORATORY

Gary Borges	2077
Charles A Brown	2077
C R Brundle	2121
George Castro	1021
Curt Erickson	1021
D E Fowler	2121
Joseph G Gordon	2077
Ting C Huang	1021
D W Kisker	1095, 1096
A C Luntz	2121
D P Pappas	2121
M Samant	2077
Joachim Stöhr	2111

MONSANTO COMPANY

Robert M Friedman	2135

RAYCHEM CORPORATION

K B Schwartz	2155

X-RAY INSTRUMENTATION ASSOCIATES

S R Russell	2129
William K Warburton	2129

XEROX

James B Boyce	2120, 2131, 2132, 2138
G A N Connell	9800

XSIRIUS, INC.

J S Iwanczyk	2129

AMERICAN LABORATORIES

ARGONNE NATIONAL LABORATORY

J E Epperson	2116
E P Horwitz	2116
P Thiygarajan	2116

BROOKHAVEN NATIONAL LABORATORY

Steve M Heald	2119
Geraldine M Lamble	2119
W Thomlinson	1046

LAWRENCE BERKELEY LABORATORY

John J Barton	2161
Thomas Earnest	2A11, 2A41
Melissa Grush	2010
Philip A Heimann	943, 9600
Tony Huff	943
Zahid Hussain	943, 9600, 9900
J Jaklevic	1E09
Bing Jap	2A11, 2A27, 2A40
Melvin P Klein	2010, 9600
Jeffrey B Kortright	2171, 9600
Matthew Latimer	2010
Wenchan Liang	2010
D Loretto	2171
C A Lucas	2171
Eddie Moler	943
A Robertson	2117
Philip N Ross	2107, 9600
Carolyn Rossington	1E09
David A Shirley	943, 9900
David H Templeton	2142
L K Templeton	2142
Albert C Thompson	046
I M Tidswell	2171
Wladyslaw Walukiewicz	1E09
Li-quing Wang	943

FOREIGN INSTITUTIONS

SIMON FRASER UNIVERSITY

Daryl Crozier	2124, 2141

TU MUNCHEN

Ulrich Kuesthardt	2104, 2110

UNIVERSITA DI BRESCIA

Maurizio Bellotto	1021

UNIVERSITAT BAYREUTH

Charles R Ross	2076

UNIVERSITAT BONN

Hans Vilter	2104
George Will	1021

UNIVERSITAT DORTMUND

Ulrich Bonse	2108

THE UNIVERSITY MANCHESTER

Michael Hart	1021

IX PUBLICATIONS BASED ON WORK AT SSRL

JOURNAL ARTICLES

P.G. Allen, J. Mustre de Leon, S.D. Conradson and A.R. Bishop, "Characterization of a Split Axial-Oxygen Site in $TlBa_2Ca_3Cu_4O_{11}$ by Extended X-ray Absorption Fine Structure Spectroscopy", Phys. Rev. B 44, 9480 (1991)

J. Arthur, W.H. Tompkins, C. Troxel Jr., R.J. Contolini, E. Schmitt, D.H. Bilderback, C. Henderson, J. White and T. Settersten, "Microchannel Water Cooling of Silicon X-ray Monochromator Crystals", Rev. Sci. Instrum. 63, 433 (1992)

J.A. Bain, B.M. Clemens and S. Brennan, "Interfacial Composition and Structure in Pt/Ni and Pt/Nb Multilayer Films", MRS Symp. Proc. 187, 315 (1991)

J.A. Bain, L.J. Chyung, S. Brennan and B.M. Clemens, "Elastic Strains and Coherency Stresses in Mo/Ni Multilayers", Phys. Rev. B 44, 1184 (1991)

T.W. Barbee Jr., J.W. Weed, R.B. Hoover, M.J. Allen, J.F. Lindblom, R.H. O'Neal, C.C. Kankelborg, C.E. DeForest, E.S. Paris, A.B.C. Walker et al., "Multi-Spectral Solar Telescope Array II Soft X-ray/EUV Reflectivity of the Multilayer Mirrors", Optical Engineering 30, 1067 (1991)

P. Besser, R. Venkatraman, S. Brennan and J. Bravman, "Calculation of Stress Gradients in Thin Al-0.5% Cu/Ti Lines from Strain Gradients Measured as a Function of Temperature Using Grazing Incidence X-ray Scattering", submitted to Mat. Res. Soc.

A. Borg, P.L. King, P. Pianetta, I. Lindau, D.B. Mitzi, A. Kapitulnik, A.V. Soldatov, S. Della Longa and A. Bianconi, "Ca 3d Unoccupied States in $Bi_2Sr_2CaCu_2O_8$ Investigated by Ca $L_{2,3}$ X-ray Absorption Near Edge Structure", submitted to Phys. Rev.

J.B. Boyce, F.G. Bridges, T. Claeson, T.H. Geballe, G.G. Li and A.W. Sleight, "Local Structure of $BaBi_xPb_{1-x}O_3$ Determined by X-ray Absorption Spectroscopy", Phys. Rev. B 44, 6961 (1991)

S. Brennan and P.L. Cowan, "A Suite of Programs for Calculating X-ray Absorption, Reflection and Diffraction Performance for a Variety of Materials at Arbitrary Wavelengths", Rev. Sci. Instrum. 63, 850 (1992)

S. Brennan, "A Data Collection Program for X-ray Diffractometry", Rev. Sci. Instrum. 63, 992 (1992)

F. Bridges and G. Li, "Distorted Local Environment About Zn and Transition Metals on the Copper Sites in $YBa_2Cu_3O_7$", accepted by SPIE

F. Bridges, X. Wang and J.B. Boyce, "Minimizing 'Glitches' in XAFS Data: A Model for Glitch Formation", Nucl. Instrum. & Methods A 307, 316 (1991)

K. Cantwell and P. Pianetta, "SSRL Operations and Research", Rev. Sci. Instrum. 63, 1609 (1992)

R. Carr and B. Kincaid, "Correlation Between Measured Undulator Magnetic Fields and X-ray Spectra", Rev. Sci. Instrum. 63, 347 (1992)

R. Carr and H.-D. Nuhn, "Design Study for an Adjustable Phase Undulator", accepted by Nucl. Instrum. & Methods

R. Carr and R. Thomson, "Device for High Resolution Positioning", submitted to Ultramicroscopy

R. Carr, "Adjustable Phase Insertion Devices as X-ray Sources", Nucl. Instrum. & Methods A 306, 391 (1991)

L.J. Chyung, B.M. Clemens and S. Brennan, "Determination of the Strain Source in Mo/Ni Multilayers", MRS Symp. Proc. 187, 327 (1991)

A.D. Cox, "The SSRL Beamline Data Acquisition System", Rev. Sci. Instrum. 63, 854 (1992)

H.D. DeWald, "Use of EXAFS to Probe Electrode - Solution Interfaces", Electroanalysis 3, 145 (1991)

J.G. DeWitt, J.G. Bentsen, A.C. Rosenzweig, B. Hedman, J. Green, S. Pilkington, G.C. Papaefthymiou, H. Dalton, K.O. Hodgson and S.J. Lippard, "X-ray Absorption, Mössbauer, and EPR Studies of the Dinuclear Iron Center in the Hydroxylase Component of Methane Monooxygenase", J. Am. Chem. Soc. 113, 9219 (1991)

D.M. Dooley, M.A. McGuirl, A.C. Rosenzweig, J.A. Landin, R.A. Scott, W.G. Zumft, F. Devlin and P.J. Stephens, "Spectroscopic Studies of the Copper Sites in Wild-Type Pseudomonas stutzerio N_2O Reductase and in an Inactive Protein Isolated from a Mutant Deficient in Copper-Site Biosynthesis", Inorg. Chem. 30, 3006 (1991)

A.S. Fischer, J.C. Gallardo, H.-D. Nuhn, R. Tatchyn, H. Winick and C. Pellegrini, "40-Å FEL Designs for the PEP Storage Ring", accepted by Nucl. Instrum. & Methods

D.A. Fischer, R.M. Wentzcovitch, R.G. Carr, A. Continenza and A.J. Freeman, "Graphitic Interlayer States: A Carbon K Near-Edge X-ray Absorption Fine-Structure Study", Phys. Rev. B 44, 1427 (1991)

R. Frahm, T.W. Barbee Jr. and W. Warburton, "In Situ Structural Study of Thin-Film Growth by Quick-Scanning X-ray Absorption Spectroscopy", Phys. Rev. B., Rap. Commun. 44, 2822 (1991)

R. Frahn, J. Wong, J.B. Holt, E.M. Larson, B. Rupp and P.A. Waide, "Real-Time Probe of Reaction Centers in Solid Combustions by QEXAFS on the Sub-Second Time Scale", submitted to Phys. Rev.

J. Freund, R. Ingalls and E.D. Crozier, "Extended X-ray Absorption Fine Structure of Alkali Halides under Pressure", Phys. Rev. B 43, 9894 (1991)

J. Freund, "On the Determination of Interatomic Potential Anharmonicities from EXAFS Measurements", Phys. Lett. A 157, 256 (1991)

B. Hellquist, L.A. Bengtsson, B. Holmberg, B. Hedman, I. Persson and L. Elding, "Structures of Solvated Cations of Palladium(II) and Platinum(II) in Dimethyl Sulfoxide, Acetonitrile and Aqueous Solution Studied by EXAFS and LAXS", Acta Chemica Scandinavica 45, 449 (1991)

B. Houser, R. Ingalls and J.J. Rehr, "The Separable Spherical Wave Approximation: Application to XAFS Multiple Scattering in ReO_3", Phys. Rev. B 46, XX (1992)

T.C. Hufnagel, A.P. Payne, S. Brennan and B.M. Clemens, "In-Situ X-ray Diffraction Observation of Amorphization Reaction During Sputer Disposition", submitted to Phys. Rev.

D.H. Igo, R.C. Elder and W.R. Heinemann, "EXAFS Solid-State Spectroeletrochemistry: Effects on Supporting Electrolyte on the Electrochemical and Structural Behavior of $Cu(bcp\text{-}s)_2^{3-}$", J. Electroanal. Chem. 314, 45 (1991)

D.T. Jiang, E.D. Crozier and B. Heinrich, "Structure Determination of Metastable Epitaxial Cu Layers on Ag(001) by Glancing-Incidence X-ray Absorption Fine Structure", Phys. Rev. B 44, 6401 (1991)

T. Kendelewicz, J.C. Woicik, K.E. Miyano, P.L. Cowan, B.A. Karlin, C.E. Bouldin, P. Pianetta and W.E. Spicer, "Synchrotron X-ray Standing-wave Study of Sb on GaAs(110) and InP(110)", J. Vac. Sci. Tech. B 9, 2290 (1991).

T. Kendelwicz, K.E. Miyano, P. Meissner, R. Cao and W.E. Spicer, "Photoemission Study of the Annealed Pd/GaAs(110) Interface", J. Vac. Sci. Technol. A 9, 990 (1991)

S. Kim, I-T. Bae, M. Sandifer, P. Ross, R. Carr, J. Woicik, M. Antonio and D. Scherson, "In Situ XANES of an Iron Porphyrin Irreversibly Adsorbed on an Electrode Surface", J. Am. Chem. Soc. 113, 9063 (1991)

P.L. King, A. Borg, C. Kim, S.A. Yoshikawa, P. Pianetta and I. Lindau, "Synchrotron-Based Imaging with a Magnetic Projection Photoelectron Microscope", Ultramicroscopy 36, 117 (1991).

P. Li, I.-W. Chen, J.E. Penner-Hahn and T.-Y. Tien, "X-ray Absorption Studies of Ceria with Trivalent Dopants", J. Am. Ceram. Soc. 74, 958 (1991)

J. Lin, J.A. May, S.V. Didziulis and E.I. Solomon, "Variable Energy Photoelectron Studies of H_2S Chemisorption on Cu_2O and ZnO Single Crystal Surfaces: HS^- Bonding to Cu(I) and Zn(II) Sites Related to Catalytic Poisoning", in press J. Amer. Chem. Soc.

J. Lin, P.M. Jones, M.D. Lowery, R.R. Gay, S.L. Cohen and E.I. Solomon, "Coordination Chemistry of NH_3 on ZnO(0001) and CuCl(111) Surfaces: σ-Bonding Interactions with d^{10} Metal Ion Sites", Inorg. Chem. 31, 686 (1992)

J. Lin, P.M. Jones, J.A. Guckert and E.I. Solomon, "Variable Energy Photoelectron Spectroscopic Study of CO Adsorption to Coordinatively Unsaturated Tetrahedral Cu (I) and Zn (II) Sites on CuCl(111) and ZnO(1010) Surfaces: d^{10} Contributions to CO Bonding &Activation", J. Am. Chem. Soc. 113, 8312 (1991)

K.E. Miyano, D.M. King, C.J. Spindt, T. Kendelewicz, R. Cao, Z. Yu, I. Lindau and W.E. Spicer, "Potential-Barrier-Measurements at Clustered Metal-Semiconductor Interfaces", Phys. Rev. B 43, 806 (1991)

K.E. Miyano, R. Cao, C.J. Spindt, T. Kendelewicz, I. Lindau and W.E. Spicer, "Band Bending at Low-Temperature Metal/III-V Semiconductor Interfaces: The Overshoot Phenomenon", J. Vac. Sci. Technol. B 9, 2100 (1991)

J. Mustre de Leon, S.D. Conradson, I. Batistic and A.R. Bishop, "Correlation Between Axial-Oxygen Anharmonicity and T_c in $YBa_2Cu_3O_7$ and Related Compounds", Phys. Rev. B 44, 2422 (1991)

J. Mustre de Leon, S.D. Conradson, I. Batistic and A.R. Bishop, "Evidence for an Axial Oxygen-Centered Lattice Fluctuaton Associated with the Superconducting Transition in $YBa_2Cu_3O_7$", Phys. Rev. Lett. 65, 1675 (1991)

J. Mustre de Leon, S.D. Conradson, I. Batistic, A.R. Bishop, I.D. Raistrick, W.E. Jackson, G.E. Brown, Jr. and G. Waychunas, " "XAFS of Systems in the Anharmonic Limit:, SPIE 1550, 85 (1991)

J. Mustre de Leon, S.D. Conradson, I. Batistic, A.R. Bishop, I.D. Raistrick, M.C. Aronson and F.H. Garzon, "Lattice Instabilities in the Axial Oxygen in YBa2Cu3O7; An Application of the Analysis of EXAFS in Anharmonic Systems", Phys. Rev. B 45, 2250 (1992)

J. Mustre de Leon, I. Batistic, A.R. Bishop, S.A. Trugman, and S.D. Conradson, "A Polaron Origin for Anharmonicity of the Axial Oxygen in $YBa_2Cu_3O_7$, submitted to Phys. Rev. Lett.

K.H. Nakagawa, C. Inouye, B. Hedman, M. Karin, T.D. Tullius and K.O. Hodgson, "Evidence from EXAFS for a Copper Cluster in the Metalloregulatory Protein CUP2 from Yeast", J. Am. Chem. Soc. 113, 3621 (1991)

H.-D. Nuhn, R. Tatchyn, H. Winick, A.S. Fisher, J.C. Gallardo and C. Pellegrini, "Short Wavelength FELs on Large Storage Rings", accepted by Rev. Sci. Instrum.

L.S. Pan, D.R. Kania, P. Pianetta, M. Landstrass, J.W. Ager, S. Han and O.J. Landen, "Electrical Transport Properties In Undoped CVD Diamond Films", Science 255, 830 (1992)

L.S. Pan., D.R. Kania, P. Pianetta, O.L. Landen and L.S. Plano, "Photoconductive Measurements on Microwave-assisted Plasma-enhanced Chemically Vapor Deposited Diamond Films", Surf. and Coatings Tech. 47, 356 (1991)

D.P. Pappas, K.-P. Kamper, B.P. Miller, H. Hopster, D.E. Fowler, C.R. Brundle, A.C. Luntz and Z.-X. Shen, "Magnetism of Ultra-Thin Films of Fe on Cu (100)", submitted to J. Mag. & Mag. Mat.

D.P. Pappas, K.-P. Kamper, B.P. Miller, H. Hopster, D.E. Fowler, C.R. Brundle, A.C. Luntz and Z.-X. Shen, "Spin Dependent Electron Attenuation by Transmission through Thin Ferromagnetic Film", Phys. Rev. Lett. 66, 504 (1991)

H.E. Parge, R.A. Hallewell and J.A. Tainer, "Atomic Structure of Wild-Type and Thermostable Mutant Recombinant Human Cu, Zn Superoxide Dismutase", in press Proc. Natl. Acad. Sci. USA

A.P. Payne, B.M. Clemens and S. Brennan, "An Apparatus for Studying Sputter Deposition with X-rays", Rev. Sci. Instrum. 63, 1147 (1992)

R. Redaelli, P. Pianetta, F. Rousseaux, A.M. Haghiri-Gosnet, B. Kebabi and A. Madouri, "X-ray Induced Damage Studies in SiC X-ray Lithography Mask Membranes", Microelectronic Engineering 13, 263 (1991).

M. Rice, S. Wakatsuki and A. Bienenstock, "Composition Modulation in Amorphous Metal-Germanium Alloys Detected by Anomalous Small Angle X-ray Scattering", J. Appl. Cryst. 24, 598 (1991)

M. Richter, J.C. Woicik, P. Pianetta, K.E. Miyano, T. Kendelewicz, C.E. Bouldin, W.E. Spicer and I. Lindau, "Surface Extended X-ray Absorption Fine Structure Studies of the Si(001) 2x1-Sb Interface", J. Vac. Sci. Technol. A 9, 1951 (1991)

A.L. Roe, K.F. Hayes, C.J. Chisholm-Brause, G.E. Brown Jr., G.A. Parks, K.O. Hodgson and J.O. Leckie, "X-ray Absorption Study of Lead Complexes at α-FeOOH/Water Interfaces", Langmuir 7, 367 (1991)

J. Safranek and H. Wiedemann, "A Low-Emittance Lattice for SPEAR", accepted by Nucl. Instrum. & Methods

S.J. Schaphorst, A.F. Kodre, J. Ruscheinski, B. Crasemann, M.H. Chen, J. Tulkki, T. Aberg, Y. Azuma and G.S. Brown, "Multiple Deep Inner-Shell Photoexcitation", Bull. Am. Phys. Soc. 36, 1286 (1991)

Z.-X. Shen, D.S. Dessau, B.O. Wells, W.E. Spicer, C.G. Olson, D.B. Mitzi, R.S. List and A.J. Arko, "Evidence for Chemical Potential Shift with Doping in $Bi_2Sr_2CaCu_2O_{8+\delta}$", accepted by Phys. Rev. B.

Z.-X. Shen, R.S. List, D.S. Dessau, B.O. Wells, O. Jepsen, A.J. Arko, R. Bartltlet, C.K. Shih, F. Parmigiani, J.C. Huang and P.A.P. Lindberg, "Electronic Structure of NiO: Correlation and Band Effects", Phys. Rev. B 44, 3604 (1991)

Z.-X. Shen, R.S. List, D.S. Dessau, A.J. Arko, R. Barttlet, O. Jepsen, B.O. Wells and F. Parmigiani, "Angle Resolved Photoemission of NiO(001)", Solid State Commun. 79, 623 (1991)

Z.-X. Shen, R. Cao, D.S. Dessau, X. Yang, P. Pianetta, D.S. Marshall, B.O. Wells, D. King, and J. Terry, "Angle-Resolved Photoemission of Single Crystal C_{60}", submitted to Phys. Rev. B

S.L. Sorenson, S.J. Schaphorst, S.B. Whitfield, B. Crasemann and R. Carr, "L-Shell Coster-Kronig Transition Probabilities in Ni, Cu, and Mo Measured with Synchrotron Radiation", Phys. Rev. A 44, 350 (1991)

C.J. Spindt, R. Cao, K.E. Miyano, I. Lindau and W.E. Spicer, "Morphological Study of Ag, In, Sb and Bi Overlayers on GaAs(100)", accepted by J. Vac. Sci. Tech.

C.K. Stahle, D. Osheroff, R.L. Kelley, S.H. Moseley and A.E. Szymkowiak, "Adapting Calorimetric X-ray Detectors for Compton Scattering Experiments Performed at High Energies", submitted to Nucl. Instrum & Methods

G.B. Stephenson, W.K. Warburton, W. Haller and A. Bienenstock, "Real-Time Small-Angle X-ray Scattering Study of the Early Stage of Phase Separation in the SiO_2-BaO-K_2O System", Phys. Rev. B 43, 13417 (1991)

D.H. Templeton and L.K. Templeton, "Phase Determination by Polarized Dispersion in Vanadyl Sulfate Pentahydrate", Acta Cryst. A 47, 414 (1991)

S.A. Vierkotter, C.E. Barnes, T.L. Hatmaker, J.E. Penner-Hahn, C.M. Stinson, B.A. Huggins, A. Benesi and P.D. Ellis, "Characterization of Rhodium-Olefin Complexes Chemisorbed onto λ–Alumina by Solid State ^{13}C-NMR and EXAFS Spectroscopies", Organometallics 10, 3803 (1991)

S. Wakatsuki, K.O. Hodgson, D. Eliezer, M. Rice, S. Hubbard, N. Gillis, S. Doniach and U. Spann, "Small-Angle X-ray Scattering/Diffraction System for Studies of Biological and Other Materials at the Stanford Synchrotron Radiation Laboratory", Rev. Sci. Instrum. 63, XX (1992)

G.S. Waldo, R.M. Fronko and J.E. Penner-Hahn, "Characterization of the Mn Oxidation States in Manganese Enzymes. Evidence for a Mn(II)/Mn(II)-Mn(III)/Mn(III) Catalytic Cycle in L.plantarum Mn Catalase", Biochem. 30, 10486 (1991)

G.S. Waldo, R.M.K. Carlson, J.M. Moldowan, K.E. Peters and J.E. Penner-Hahn, "Sulfur Speciation in Heavy Petroleums. Information from X-ray Absorption Near Edge Structure", Geochim. Cosmochim. Acta 55, 801 (1991)

W.K. Warburton and P. Pianetta, "*In Situ* Optical Element Cleaning with Photon Activated Oxygen", accepted by Nucl. Instrum. & Methods

H. Wiedemann, P. Kung and H.C. Lihn, "Ultra Short Electron and Photon Pulses", accepted by Nucl. Instrum. & Methods

J.C. Woicik, T. Kendelewicz, K.E. Miyano, C.E. Bouldin, P.L. Meissner, P. Pianetta and W.E. Spicer, "Structure of the Si(111) $\sqrt{3}X\sqrt{3}$-Sb Interface by Surface X-ray Absorption Fine Structures and Photoemission", J. Vac. Sci. Tech. A 9, 1956 (1991)

J.C. Woicik, T. Kendelewicz, K.E. Miyano, P.L. Cowan, C.E. Bouldin, B.A. Karlin, P. Pianetta and W.E. Spicer, "Determination of the Sb/Si(111) Interfacial Structure by Back-reflection X-ray Standing Waves and Surface Extended X-ray Absorption Fine Structure", Phys. Rev. B 44, 3475 (1991).

J.C. Woicik, C.E. Bouldin, M.I. Bell, J.O. Cross, D.J. Tweet, B.D. Swanson, T.M. Zhang, L.B. Sorensen, C.A. King, J.L. Hoyt, P. Pianetta and J.F. Gibbons, "Conservation of Bond Lengths in Strained Ge-Si Layers", Phys. Rev. B 43, 2419 (1991)

J.C. Woicik, T. Kendelewicz, K.E. Miyano, C.E. Bouldin, P. Pianetta and W.E. Spicer, "Local Bond Structure of Sb on Si(111) by Surface EXAFS and Photoemission", Phys. Rev. B 43, 4331 (1991)

J.C. Woicik, T. Kendelewicz, K.E. Miyano, P.L. Cowan, C.E. Bouldin, B.A. Karlin, P. Pianetta and W.E. Spicer, "X-ray Standing Wave Measurement of the InP(110) Surface Relaxation", accepted by J. Vac. Sci. Technol.

M. Yamada, A. Green, A.K. Wahi, T. Kendelewicz and W.E. Spicer, "Effects of an Sb Interlayer on Schottky Barrier Formation on InP(110) Surfaces", accepted by Electrochem. Soc.

M. Yamada, C.J. Spindt, K.E. Miyano, P.L. Meissner, A. Herrera-Gomez, T. Kendelewicz and W.E. Spicer, "Effects of Annealing InP Surfaces on Schottky Barrier Heights at Pd/InP(110) Interfaces", Phys. Rev. B 44, 3475 (1991)

M. Yamada, A.M. Green, A. Herrera-Gomez, T. Kendelewicz and W.E. Spicer, "Annealing Out of Thermal Process-Induced Defects at InP(110) Surfaces - A Novel Method", Jap. J. Appl. Phys. 11B, L1982 (1991)

M. Yamada, A.K. Wahi, P.L. Meissner, A. Herrera-Gomez, T. Kendelewicz and W.E. Spicer, "Effect of Annealing Sb/InP(110) Interfaces and Schottky Barrier Formation of Ag on Annealed Sb/InP(110) Surfaces", Appl. Phys. Lett. 58, 2243 (1991)

CONFERENCE PROCEEDINGS AND BOOKS

M.M. Baltay, W. Brunk, J. Cerino, R. Hettel, W. Leonard, J. Safranek, J. Voss, H. Wiedemann, K. Zuo, T. Sanchez, J. Jagger, "The Ring Magnets for a Dedicated Injector for SPEAR Injector" in Conference Record IEEE Particle Acclerator Conference 1991, May 6-9, 1991, pp. 2369-2371.

A. Bienenstock, R.D. Lorentz, M. Rice, "XANES, Anomalous Small-Angle Scattering and Fine Scale Composition Fluctuations in Amorphous Fe_xGe_{100-x} Films" in S.S. Hasnain, ed., X-ray Absorption Fine Structure, (Ellis Hoorwood, Chichester,1991), p. 709-14.

A. Bienenstock, "An Overview of Synchrotron Radiation Utilization in Applications of Synchrotron Radiation to Chemical Engineering Science, Workshop Report, ANL/APS/TM-9. pp. 46-56.

M. Borland, J.N. Weaver, M. Baltay, L. Emery, R. Hettel, H. Morales, J. Sebek, B. Youngman, R. Anderson, A.S. Fisher, R.H. Miller, "Design and Performance of the Traveling-Wave Beam Chopper for the SSRL Injector" in Conference Record IEEE Particle Accelerator Conference 1991, May 6-9, 1991, pp. 976-978.

S. Brennan, S. Baird, W. Lavender, H.-D. Nuhn, C. Wermelskirchen, J. Yang, "The Control and Operation of the Programmable Waveform Generator for the SSRL Injector" in Conference Record IEEE Particle Accelerator Conference 1991, May 6-9, 1991, pp. 1476-1477.

J. Cerino, M. Baltay, R. Boyce, S. Harris, R. Hettel, M. Horton, K. Zuo, "Extraction Septum Magnet for the SSRL Injector" in Conference Record IEEE Particle Accelerator Conference 1991, May 6-9, 1991 pp. 2328-2330.

C.J. Chisholm-Brause, G.E. Brown Jr., G.A. Parks, "In-situ EXAFS Study of Changes in Co(II) Sorption Complexes on γ-Al_2O_3 with Increasing Sorption Densities" in S. S. Hasnain, ed., X-ray Absorption Fine Structure, (Ellis, Horwood, Chichester, 1991) pp. 263-265.

J.-M. Combes, G.E. Brown Jr., G.A. Waychunas, "X-ray Absorption Study of the Local Ca Environment in Silicate Glasses" in S. S. Hasnain, ed., X-ray Absorption Fine Structure, (Ellis, Horwood, Chichester, 1991) pp. 312-314.

S.D. Conradson, J. Mustre de Leon, I.D. Raistrick, I. Batistic, and A.R. Bishop, "The Axial Oxygen and Superconductivity in Cuprates", in Y. Bar-Yam et al., Lattice Effects in High-Temperature Superconductors, (in press 1992).

W.J. Corbett, M.J. Lee, Y. Zambre, "Automatic Beamline Calibration Procedures", submitted to Third European Particle Accelerator Conference, Berlin, March 1992.

M. Cornacchia, W.J. Corbett, K. Halbach, "Modified Octupoles for Damping Coherent Instabilities", in Conference Record IEEE Particle Accelerator Conference 1991, May 6-9, 1991, pp. 1797-1799.

J.G. DeWitt, J.G. Bentsen, B. Hedman, A.C. Rosenzweig, J. Green, S. Pilkington, K.O. Hodgson, S.J. Lippard, H. Dalton, "X-ray Absorption Spectroscopy of Diferrous and Differric Protein A of Soluble Methane Monooxygenase from Methylococcus capsulatus (Bath)" in S.S. Hasnain, ed., X-ray Absorption Fine Structure, (Ellis Horwood, Chichester, 1991) pp. 128-130.

L. Emery, "Energy Feedback System for the SSRL Injector Linac" in Conference Record IEEE Particle Accelerator Conference 1991, May 6-9, 1991 pp. 1413-1415.

L. Emery, "Further Feasibility Studies on a Wiggler-Based Ultra-Low-Emittance Damping Ring Lattice" in Conference Record IEEE Particle Accelerator Conference 1991, May 6-9, 1991 pp. 1633-1635.

F. Farges, J.A. Peck, G.E. Brown Jr., "X-ray Absorption and Raman-UV/visible Spectroscopic Study of Au(III) Complexes in Chloride Solutions, Direct Evidence for Chlorine and Oxychlorine Complexes" in S. S. Hasnain, ed., X-ray Absorption Fine Structure, (Ellis Harwood, New York, 1991) pp. 478-480.

F.A. Farges, G.E. Brown Jr., C.W. Ponader, "EXAFS Study of the Structural Environments of Trace Levels of Zr^{4+}, Mo^{6+} and $U^{6+}/U^{5+}/U^{4+}$ in Silicate Glass/Melts Systems" in S. S. Hasnain, ed., X-ray Absorption Fine Structure, (Ellis, Horwood, Chichester, 1991) pp. 309-311.

A. Fisher, S. Baird, H.-D. Nuhn, R. Tatchyn, H. Winick, C. Pellegrini, "Coherent X-rays from PEP" in Conference Record IEEE Particle Accelerator Conference 1991, May 6-9, 1991, pp. 2748-2750.

J. Freund and R. Ingalls, "EXAFS of Alkali Halides under High Pressure and Interatomic Potentials" in S. S. Hasnain, ed., X-ray Absorption Fine Structure, (Ellis, Horwood, Chichester, 1991) p. 429.

B. Hedman, P. Frank, B.J. Feldman, S.F. Gheller, F.A. Schultz, W.E. Newton, K.O. Hodgson, "Sulfur K and Molybdenum L Edge XAS of the Nitrogenase Iron-Molybdenum Cofactor under *in-situ* Electrochemical Control" in S. S. Hasnain, ed., X-ray Absorption Fine Structure, (Ellis Horwood, Chichester, 1991) pp. 168-170.

R. Hettel, R. Averill, M. Baltay, S. Brennan, C. Harris, M. Horton, C. Jach, J. Sebek, J. Voss, "The 10 Hz Resonant Magnet Power Supply System for the SSRL 3 GeV Injector" in Conference Record IEEE Particle Accelerator Conference 1991, May 6-9, 1991, pp. 926-928.

R.O. Hettel, D. Mostowfi, R. Ortiz, J. Sebek, "Triggers and Timing System for the SSRL 3 GeV Injector" in Conference Record IEEE Particle Accelerator Conference 1991, May 6-9, 1991, pp. 1478-1480.

G.P. Huffman, F.E. Huggins, N. Shah, "XAFS Spectroscopy Studies of Critical Elements in Coal and Coal Derivatives" in H.L.C. Meuzelaar, Advances in Coal Spectroscopy, (Plenum Press, 1991)

F.E. Huggins, G.P. Huffman, S. Mitra, N. Shah, "Determination of Sulphur Forms in Coal by XAFS Spectroscopy" in S. S. Hasnain, ed., X-ray Absorption Fine Structure, (Ellis, Horwood, Chichester, 1991) pp. 610-612.

W.E. Jackson, G.E. Brown Jr., G.A. Waychunas, J. Mustre de Leon, S.D. Conradson, J.M. Combes, "*In-situ* High-Temperature X-ray Absorption Study of Ferrous Iron in Orthosilicate Crystals and Liquids" in S. S. Hasnain, ed., X-ray Absorption Fine Structure, (Ellis, Horwood, Chichester, 1991) pp. 298-301.

W. Lavender, S. Baird, M. Borland, S. Brennan, R. Hettel, H.-D. Nuhn, R. Ortiz, J. Safranek, J. Sebek, C. Wermelskirchen, J. Yang, "The SSRL Injector Beam Position Monitoring Systems" in Conference Record IEEE Particle Accelerator Conference 1991, May 6-9, 1991, pp. 1151-1153.

M. Lee, Y. Zambre, W. Corbett, "Accelerator Simulation Using Computers", submitted to the International Conference CUM Workshop on Current Trends in Data Acquisition and Control of Accelerators, Calcutta, India, November 19-21, 1991.

H. Morales, U. Cummings, N. Hower, W. Li, J. Safranek, J. Voss, H. Wiedemann, "Vacuum Chamber for the 3 GeV SPEAR Injector Synchrotron" in Conference Record IEEE Particle Accelerator Conference 1991, May 6-9, 1991, pp. 2278-2280.

J. Mustre de Leon, S.D. Conradson, P.G. Allen, I. Batistic, A.R. Bishop, "The Role of the Axial Oxygen in High-T_c Materials, in J. Ashkenazi and G. Vezzoli, eds. Electronic Structure and Mechanisms for High Temperature Superconductivity, (NY, Plenum, 1991).

J. Mustre de Leon, S.D. Conradson, A.R. Bishop, I.D. Raistrick, I. Batistic, W. E. Jackson, G.E. Brown, Jr., G.A. Waychunas, "XAFS Analysis in the Anharmonic Limit; Application to High T_c Superconductors and Ferrosilicates", in S. S. Hasnain, ed., X-ray Absorption Fine Structure, (Ellis, Horwood, Chichester, 1991)

J. Mustre de Leon, S.A. Trugman, I. Batistic, A.R. Bishop, S.D. Conradson, "Polaron Tunneling as a Mechanism for the Double-Well Anharmonicity of the Axial Oxygen in $Yba_2Cu_3O_7$" in Y. Bar-Yam et al., eds., Lattice Effects in High-Temperature Superconductors, (in press, 1992).

H.-D. Nuhn, R. Boyce, J. Cerino, T. Hostetler, "The SSRL Injector Kickers" in Conference Record IEEE Particle Accelerator Conference 1991, May 6-9, 1991 pp. 973-975.

H.-D. Nuhn, Y. Sun, H. Winick, W. Xie, R. Yotam, H. Schwarz, P. Friedrichs, "A Longitudinal Multibunch Feedback System for PEP" in Conference Record IEEE Particle Accelerator Conference 1991, May 6-9, 1991, pp. 1410-1412.

P.A. O'Day, G.E. Brown Jr., G.A. Parks, "EXAFS Study of Aqueous Co(II) Sorption Complexes on Kaolinite and Quartz Surfaces" in S. S. Hasnain, ed., X-ray Absorption Fine Structure, (Ellis, Horwood, Chichester, 1991) pp. 260-262.

L.S. Pan, P. Pianetta, D.R. Kania, O.L. Landen, M. Landstrass, "Temperature Dependent Photoconductivity Measurements on Type IIa Diamonds and Polycrystalline Diamond Films" in Y. Tzeng Applications of Diamond Films and Related Materials, (Elsevier Science Publ., New York, 1991) p. 341.

L.S. Pan, D.R. Kania, P. Pianetta, O.L. Landen, M. Landstrass, "Intrinsic Photoconductivity in Polycrystalline CVD Diamond Films and in Natural and Synthetic Bulk Diamonds" in R. Messier New Diamond Science and Technology, (MRS, Boston, 1991) p. 729.

J.E. Penner-Hahn, S. Wang, G.S. Waldo, "Polarized X-ray Absorption Spectroscopy of Biological Molecules" in S. S. Hasnain, ed., X-ray Absorption Fine Structure, (Ellis, Horwood, Chichester, 1991) pp. 146-151.

J.E. Penner-Hahn, "Structural Properties of the Mn Site in the Mn Catalases" in V.L. Pecoraro, Manganese Redox Enzymes, (VCH Publishers, 1991)

I. Persson, J.E. Penner-Hahn, K.O. Hodgson, "An EXAFS Study on Mercury (II) Halide Complexes in Dimethyl Sulfoxide and Pyridine Solution" in S. S. Hasnain, ed., X-ray Absorption Fine Structure, (Ellis, Horwood, Chichester, 1991) pp. 559-561.

J. Safranek, H. Wiedemann, "Low-Emittance in SPEAR" in Conference Record IEEE Particle Accelerator Conference 1991, May 6-9, 1991, pp. 1104-1106.

J. Safranek, S. Baird, "Commissioning the SSRL Injector" in Conference Record IEEE Particle Accelerator Conference 1991, May 6-9, 1991 pp. 2865-2867.

J. Sebek, M. Baltay, M. Borland, J. Cerino, L. Emery, R. Hettel, H. Morales, D. Mostowfi, M. Rowen, J. Safranek, et al., "Diagnostic Instrumentation for the SSRL 3 GeV Injector for SPEAR" in Conference Record IEEE Particle Accelerator Conference 1991, May 6-9, 1991, pp. 1243-1245.

T.A. Smith, J.G. DeWitt, B. Hedman, K.O. Hodgson, "Sulfur K-edge XAS Studies of Photographic Materials" in S. S. Hasnain, ed., X-ray Absorption Fine Structure, (Ellis Horwood, Chichester, 1991) pp. 607-609.

G.O. Tan, J.L. Cole, E.K. Yang, K.O. Hodgson, E.I. Solomon, "Reactivity of the Laccase Trinuclear Copper Active Site with Dioxygen, An X-ray Absorption Edge Study" in S. S. Hasnain, ed., X-ray Absorption Fine Structure, (Ellis Horwood, Chichester, 1991) pp. 156-158.

G.A. Waychunas, B.A. Rea, C.C. Fuller, J.A. Davis, "Fe and As K-edge EXAFS Study of Arsenate $(AsO4)^{-3}$ Adsorption on 'Two-Line' Ferrihydrite" in S. S. Hasnain, ed., X-ray Absorption Fine Structure, (Ellis, Horwood, Chichester, 1991) pp. 215-217.

J.N. Weaver, S. Baird, M. Baltay, M. Borland, C. Chavis, L. Emery, R. Hettel, S.J. Mello, H. Morales, H.-D. Nuhn, et al., "The Linac and Booster RF System for a Dedicated Injector for SPEAR" in Conference Record IEEE Particle Accelerator Conference 1991, May 6-9, 1991, pp. 769-771.

C. Wermelskirchen, S. Brennan, T. Goetz, W. Lavender, R. Ortiz, M. Picard, J. Yang, "The SSRL Injector Control System" in Conference Record IEEE Particle Accelerator Conference 1991, May 6-9, 1991 pp. 1383-1385.

H. Wiedemann, "3 GeV Injector Synchrotron for SPEAR" in Conference Record IEEE Particle Accelerator Conference 1991, May 6-9, 1991, pp. 2688-2690.

J.C. Woicik, P. Pianetta, "Studies of Si-Ge Interfaces with Surface EXAFS and Photoemission" in R.Z. Bachrach, ed., Synchrotron Radiation Research (Plenum Press, New York, 1991).

D.Y. Wang, F.C. Younger, H. Wiedemann, "Incorporation of a 5 T Superconducting Wiggler in an MLI Synchrotron Light Source", in Conference Record IEEE Particle Accelerator Conference, 1991, May 6-9, 1991, pp. 2727-2729.

R. Yotam, J. Cerino, R. Garoutte, R. Hettel, M. Horton, J. Sebek, E. Benson, K. Crook, J. Fitch, N. Ipe, et al., "Personnel Protection and Beam Containment Systems for the SSRL 3 GeV Injector" in Conference Record IEEE Particle Accelerator Conference, 1991, May 6-9, 1991, pp. 1028-1030.

THESES BASED ON RESEARCH AT SSRL

To date 182 theses from 25 universities have been granted based on work at SSRL. The 1991 and early 1992 theses are listed below.

1992

T.M. Breunig *Georgia Inst. of Tech*	"Nondestructive Evaluation of Damage in SiC/Al Metal Matrix. Composite Using X-ray Tomographic Microscopy" (Advisor - S. Stock)
W. B. Jones *Univ of Cincinnati*	"X-ray Studies of Gold Anti-Arthritis Drugs and Related Compounds" (Advisor - R.C. Elder)

1991

D.H. Igo *Univ of Cincinnati*	"Applications of X-ray Absorption Spectroelectrochemistry" (Advisor - R.C. Elder)
S. Wang *Univ of Michigan*	"Polarized X-ray Absorption Spectroscopic Studies of Iron Porphyrins and Metal Hexammines" (Advisor - J.E. Penner-Hahn)
G.S. Waldo *Univ of Michigan*	"Spectroscopic and Kinetic Chracterization of Lactobacillus Plantarum Manganese Catalase" (Advisor - J.E. Penner-Hahn)
B. Factor *Stanford University*	"Grazing Incidence X-ray Scattering Studies of Thin Polymer Films" (Advisor - A. Bienenstock)
C. Kilbourne-Stahle *Stanford University*	"The Development of High Resolution Calorimetric X-ray Detectors for Compton Scattering Experiments" (Advisor - A. Bienenstock)
M. Borland *Stanford University*	"A High Brightness Thermionic Microwave Electron Gun" (Advisor - H. Wiedemann)
J. Safranek *Stanford University*	"SPEAR Lattice for High Brightness Synchrotron Radiation" (Advisor - H. Wiedemann)
T. Tyson *Stanford University*	"X-ray Absorption Spectroscopy: K, L and KL Spectra with Quantitative Models" (Advisor - K.O. Hodgson)
D.T. Jaing *Simon Fraser University*	"Structural Investigations of Metastable Epitaxial Metallic Layers by Glancing Incidence X-ray Absorption Fine Structure" (Advisor - E.D. Crozier)
J.E. Silk *Brigham Young Univ*	"Chemical Characterization of Power-Plant and Sludge-Incinerator Emissions using Pixel and X-ray Absorption Techniques and Improvements in Data Analysis" (Advisor - N. Mangelson)